Design and modelling of low speed high torque motors

Chapple, Peter John

Award date:
1991

Awarding institution:
University of Bath

DESIGN AND MODELLING OF LOW SPEED HIGH TORQUE MOTORS

Submitted by:

PETER JOHN CHAPPLE

for the degree of PhD

of the University of Bath

1991

ProQuest LLC
789 East Eisenhower Parkway
P.O. Box 1346
Ann Arbor, MI 48106-1346

SUMMARY

Hydraulic motors that are available on the market fall basically into the two principal categories of low speed, high torque (*LSHT*) and high speed low torque (*HSLT*) coupled with gear reducers. The constructional features of these types of motors are discussed together with an examination of some of their major differences. As would be supposed, a significant demarcation between these categories is their maximum speed of operation. The lower speed of *LSHT* motors has allowed the creation of many different designs which is mostly reflected in the reciprocating components.

A major aspect of the thesis concerns the modelling of a particular type of radial piston motor of the eccentric type with which the author has been involved over a number of years. A comparison between the predictions from the model and measured results shows that changes in the level of friction in the sliding joints are principally a result of changes in the internal geometry during the pressure cycle.

The results of an examination of squeeze film effects suggests that these play a major role in the performance of the motor even when operating at speeds of less than 5 *rev/min*. This examination includes an investigation of the possibility of hydrodynamic lubrication from which it is concluded that its existence over a major part of the operating speed range is unlikely.

The level of component distortion is shown to be of critical importance to the motor performance in its effect on the lubrication of the sliding faces. In some components this could create the conditions necessary for hydrodynamic lubrication to occur but in others this has the opposite effect.

On the basis that the sliding faces at low speeds experience boundary lubrication, the model was shown to predict the performance of the motor with reasonable accuracy. This incorporated a variation in the friction coefficients with the changes in the motor geometry during a pressure cycle. The range of these variations was found to agree substantially with that obtained from the results of experimental work of other researchers in the field.

The model is then used to examine the effect of changes in various motor design parameters on the motor performance. A major conclusion of the work is that the mechanical efficiency at low speed is principally affected by the type of spherical joint used in the motor. The thesis is concluded with the examination of the performance of a motor design that uses a pressure balanced bearing to avoid the problems of low mechanical efficiency at low speed. This design of the author is compared with some recent developments in high torque motors which have adopted similar methods.

ACKNOWLEDGEMENTS

The author would like to express his thanks to Kevin Edge for his invaluable assistance in reading the transcript and for his advice and encouragement. Thanks also to all those colleagues who gave their assistance with various aspects of the work.

CONTENTS **PAGE NO**

CHAPTER 3

PRACTICAL TESTS

CHAPTER 4

REGIMES OF LUBRICATION AND THEIR EFFECT ON FRICTION

CHAPTER 5

THE INFLUENCE OF THE MOTOR DESIGN ON PERFORMANCE

NOTATION

α - Con Rod Angle

A_P - Pressure Area

A_B - Pressure Area

A_s - Slipper Mean Effective Area

B - Temperature Viscosity Coefficient

C_P - Specific Heat

D - Motor Displacement

D_P - Piston Diameter

d_o - Restrictor Diameter

d_c - Cylinder Diameter

d_1 - Slipper Pocket Diameter

d_s - Outside Diameter of the Slipper

d_2 - Spherical Bearing Pocket Diameter

d_u - Outside Diameter of the Spherical Bearing

e_C - Difference between the Slipper and Eccentric Radii

f_c - Slipper Friction Coefficient

f_P - Piston Friction Coefficient

f_B - Con Rod Bearing Friction Coefficient

F - Piston Force

F_{B1} - Con Rod Contact Force

F_{B2} - Con Rod Force

F_{C1} - Slipper Contact Force for Contact Angle β_1

F_{C2} - Slipper Contact Force for Contact Angle β_2

F_1 - Inner Piston Force

F_2 - Outer Piston Force

F_P - Hydrostatic Slipper Pressure Force

F_N - Radial Force at Con Rod Bearing Centre

F_T - Normal Force at Con Rod Bearing Centre

F_T - Total Squeeze Film Force

F_D - Hydrostatic Force

F_H - Con Rod Hydrostatic Force

F_I - Squeeze Film Force - Inner Region

F_o - Squeeze Film Force - Outer Region

F_K - Spring Force

F_s - Seal Force

F_u - Hydrostatic Force

h - Leakage Clearance between the Slipper and the Eccentric

h_1 - Movement between the Piston and the Con Rod

H_1 - Minimum Film Thickness - Tapered Plate

H_o - Maximum Film Thickness - Tapered Plate

K_o - Viscosity Pressure Coefficient

L - Con Rod Bearing to Eccentric Centre distance

L_R - Distance on Con Rod Centreline to Slipper Face

L_w - Slipper Width (straight edge)

L_P - Slipper Feed Restrictor Length

L_1 - Inner Piston Length

L_2 - Outer Piston Length

L_4 - Con Rod Bearing Centre to Cylinder opening distance at *TDC* ($\theta = 0$)

L_C - Spherical Cup to Eccentric Centre Distance

L_D - Spherical Cup to Shaft Centre Distance

L_o - Spherical Cup to Eccentric Centre Length ($\theta = 0$)

M - Con Rod Frictional Moment

M - Motor Mass (Chapter 1)

M_g - Gearbox Mass

N - Rotational Speed

n - Gearbox Ratio

P - Motor Cylinder Pressure

P_S - Supply Pressure

P_P - Hydrostatic Slipper Pocket Pressure

P_m - Maximum Squeeze Film Pressure

p - Pressure

P_r - Hydrostatic Slipper Pocket Pressure Ratio - P_P/P

P_o - Power

Q_I - Ideal Torque from one Cylinder

Q - Actual Torque from one Cylinder

Q_{MI} - Ideal Motor Torque

Q_M - Actual Motor Torque

Q_G - Gearbox Output Torque

Q_{MT} - Theoretical Mean Torque

ΔQ_F - Slipper Friction Torque Loss

ΔQ_G - Geometric Torque Loss

ΔQ - Total Torque Loss

Q_S - Slipper Leakage Flow

R_D - Eccentric Radius

R_E - Distance between the Eccentric and Shaft Centres

R_S - Slipper Face Radius

R_B - Con Rod Bearing Radius

R_C - Con Rod Bearing Cup Radius

r - Radius from Con Rod Bearing Centreline

r_o - Inner Radius from Con Rod Bearing Centreline

r_C - Radius of Con Rod Bearing Contact from Con Rod Bearing Centreline

r_1 - Outer Radius from Con Rod Bearing Centreline

S_1 - Outer Cup Contact Force

T - Temperature

T_o - Supply Temperature

t - Time

x - Piston displacement from TDC position

β_1 - Slipper Contact Angle - $0 < \theta < 90^0$

β_2 - Slipper Contact Angle - $90^0 < \theta$ 180^0

β_c - Angular Contact in Con Rod Bearing

β_m - Angle subtended between the Slipper Centre and its Edge

β_m - Con Rod Bearing Contact Angle for
Maximum Squeeze Film Pressure (Chapter 4 Appendix I)

β_s - Reference Angle for Tilting of the Slipper

ϕ - Shaft Twist Angle

γ - Angle

λ - Angle

μ - Dynamic Viscosity

μ_o - Dynamic Viscosity of Supply Fluid

μ_1 - Dynamic Viscosity at given Temperature

η_m - Mean Mechanical Efficiency

η_I - Instantaneous Mechanical Efficiency

ρ - Fluid Density

θ - Shaft Angle

θ_C - Con Rod Bearing Contact Angle

ω - Width of the Slipper Lands

LIST OF FIGURES

CHAPTER 1

CHAPTER 2

CHAPTER 3

CHAPTER 4

CHAPTER 5

CHAPTER 1

HYDROSTATIC MOTORS

1.0 BACKGROUND

The author has been involved over a number of years with various aspects of the design and performance of the radial piston eccentric type of motor and its application. In 1969, whilst working with a design consultancy organisation, he was engaged in a number of projects on behalf of Chamberlain Industries who, at that time, manufactured a range of motors under the name of Staffa.

During 1975-1977, when the author was a lecturer at the University of Bath, he was engaged on further work including some practical tests on the Staffa motor itself. Later, whilst working with the company as Technical Director during 1977-1981, this work continued in order to develop more fully and improve the motor design. As is discussed in detail in the thesis a major problem related to difficulties in modelling the effect of friction in the various sliding components and the oil flow through the pressurised hydrostatic slipper bearings.

Such a model was required in order to obtain an improved understanding of the mechanical losses and how these were related to the observed motor performance. Modelling techniques would provide improved methods of predicting how the motor behaves at different conditions of speed and pressure. Their use could also indicate where component manufacture could be changed to improve the performance and/or reduce the product cost.

The author was subsequently involved with motor design whilst working with Commercial Hydraulics who were contemplating producing a radial piston motor for which the company had manufacturing rights. This motor employed a similar principle of operation as that used in the Staffa motor and as a consequence of experiences with the motor and work on possible alternative designs the author completed a design using a different method of operation.

This design, which was related to ideas developed at Staffa and to a motor type produced by an Italian company, was intended to have improved operating characteristics particularly at starting and at low speed. It also provided an opportunity of reducing the cost of manufacture.

Eventually the company discontinued its interest in this type of motor and the author subsequently returned to the University of Bath with the Fluid Power Centre. Since that time the author has continued work on modelling techniques which has also included the use of the hydraulic simulation package developed at the University. This package has been used to examine the problem of motor speed regulation at low speeds on which topic the author presented a paper[1] at the 8th *BHRA* International Fluid Power Symposium.

The radial piston eccentric motor as commonly produced is of the low speed high torque type. In the field of application these need to be compared with high speed motors that are derived from pump designs. These have lower displacements and are generally used at high speed, the lower torque, as a consequence, requiring a reduction gear box to meet the same torque requirements of the final drive. Such a comparison, which involves a number of parameters, was presented by the author in a paper[2] at the 7th BHRA International Symposium in 1986 and is discussed in the thesis.

There is, then, a sharp distinction between high and low speed motors which tends to be dominated by product price. Because every type of hydraulic system requires a pump, their manufacture is a significantly large proportion of the total production of hydraulic units. As a consequnce additional use of the same type of units for motors serves to improve the unit cost of manufacture.

The development of the low speed motor really started in the 1950's for specific applications in all the market sectors. The numbers produced did become significant where such motors were, in the main, produced by manufacturing companies that were not involved with other hydraulic products. This reflected an entreprenurial activity to satisfy a perceived market need. However, the considerable demand to improve the operating speed and pressure of the high speed units, particularly for pump use, coupled with the growth of available low cost gear reducers, has resulted in a sizeable loss of market share for low speed motors.

The disparity in the relative positions of low and high speed motors in the market place and the difference in commercial scale of the manufacturing organisations involved is reflected in the number of technical papers on aspects of pump and motor design and their performance. There has been, particularly in recent years, a considerable amount of university research mostly in Japan, the UK and W.Germany involving specialised test rigs and applications of *FE* methods to examine in detail the lubrication mechanism between all the sliding surfaces. In contrast to this there is hardly any published work relating to such investigations for low speed motors.

As was demonstrated by the author[2], the low speed motor has some significant advantages in relation to high speed motors and there are areas of development that could make a useful contribution to both the component manufacturers and the user industries.

2.0 OBJECTIVES

A major objective of this thesis is, therefore, to collect together the accumulated experience of the author in respect of work on a particular type of radial piston motor and methods for modelling to provide information on the design, performance and use of the motor. The results of tests carried out both at the University of Bath and in industry at various times are used for comparision with the model. They are also used in conjunction with the model to investigate the mechanisms of friction that act in the sliding components.

The work also makes a comparative assessment of the different types of motors that are available together with a detailed analysis of a motor design method proposed by the author.

3.0 A COMPARISION OF THE AVAILABLE TYPES OF HYDRAULIC MOTORS

3.1 Introduction

The development of high pressure hydraulic water systems during the 19th Century saw many innovations. One of these was a radial piston motor[3], manufactured in 1875, which is shown in Fig 1. This was used for driving a rotary saw of 5*m* diameter for cutting steel rails. Hitherto the saw was driven directly from a steam engine. The major advantage claimed by the inventor was the reduction in shock damage afforded by the use of a hydraulic drive.

However, aside from such isolated developments, hydraulic motors generally speaking were essentially the same units as pumps requiring, for the majority of applications, gear reducers to provide the requisite load torque. For piston units the type mostly used are of the axial swash or bent axis design shown in Figs 2 and 3.

3.2 Design considerations for the distribution valve in low speed motors

The development of low speed radial piston motors allowed considerable freedom in the method used for converting the linear movement of the piston to rotational movement of the shaft because of the relatively low maximum speed, the main consideration being the achievement of high mechanical efficiency during starting and low speed operation.

Pumps are designed to run at high speed which in most applications is either constant when driven by an electric motor or over a small range of speeds when driven by, say, a diesel engine. In the bent axis and swash units it is normal to allow the rotating cylinder block to be free in the axial direction so that a proportion of the cylinder pressure force is used to force the block against the valve plate. This provides a seal against leakage as the fluid is transferred from the stationary casing containing the inlet and outlet ports to the rotating cylinders. The great majority of both industrial and university research has been directed at gaining a greater understanding of the processes involved in the valve seal operating interface in order to allow increases in operating speeds and pressures. Notable work on this aspect was that in the UK carried out by BHRA some results of which are summarised in the book by Turnbull[4].

In most low speed radial piston motors it is necessary to transfer the fluid from the stationary port casing through a shaft driven valve into the stationary cylinder housing. Obviously the design requirements of this type of valve are different to those in the high speed units and this geometric constraint would appear to require the design to be of a more complex nature. However whilst this is the case it does allow the diameter of the valve to be kept small which is of considerable benefit as it minimises the frictional torque from this component.

In the high speed units this freedom does not apply and at low speeds this frictional loss can be quite appreciable. On the other hand for high flow rates the valve size becomes important and it is often the case that the high speed limitation in low speed motors arises as a consequence of the pressure loss in the distributor valve and/or a limit of the surface rubbing speeds in the component.

This difference in design can be seen by comparing the low speed axial swash type motor shown in Fig 4 with the high speed motor of Fig 2. In the low speed motor the valve is made integral with the shaft thus allowing it to be of much smaller diameter. However there is an additional reason for the differences in the design which relates to the location of the rotating cylinder block in the low speed motor.

As low speed motors can transmit torque directly to the driven unit it is necessary to make the shaft sufficiently strong to carry side loads on the shaft end. For example in applications such as winches or vehicle drives the motor bearings are often used to provide partial, or complete, structural support for the driven load. This usually prevents using the cylinder block to provide a seal with the distributor valve as in high speed units.

3.3 Types of available low speed motors

Various types of radial piston motors are shown in Figs 5 to 11 all of which employ different methods for transferring the piston force to the output shaft and distributing the fluid to the cylinders. The motors shown are in two groups comprising those using eccentrics in Figs 5 to 9, and those using a cam in Figs 10 and 11.

3.3.1 Eccentric motors

The principal difference between the eccentric types lies in the method used to convert the reciprocating motion of the piston to rotary motion of the shaft. In Fig 5 this is facilitated by the use of a con rod that incorporates a spherical bearing between the con rod and the piston. The type shown in Fig 8 uses an oscillating cylinder that is mounted in trunnion bearings.

The slipper in this motor bears against a sleeve that rotates on the eccentric by means of needle roller bearings. Thus the slipper only has to move a small amount relative to the sleeve during one rotation of the shaft. In the unit of Fig 5 the slipper contains a hydrostatic bearing to reduce the friction between this and the eccentric. Here the relative velocity between the slipper and the eccentric is much higher than in that of Fig 8 but this can be advantageous in the avoidance of stiction at low speeds.

The distributor valves in these motors employ quite different principles. The motor in Fig 5 uses a rotating spool containing internal passages that direct the flows from the motor ports to the appropriate cylinder ports. That of Fig 8 has a plate valve having equal pressure areas to maintain a force on the valve regardless of which supply port is at high pressure.

The motor of Fig 7 has a cylinder body that rotates on the eccentric. This is located radially by an Oldhams' Coupling that is shown by dotted lines behind the shaft at the bearing on the drive shaft end. The pistons slide against the flat pad inside the outer casing. Distribution of the flow is made by the grooves on the eccentric which are connected by drillings in the shaft from slip ring connections at the supply ports.

The motors in Figs 6 and 9 are similar to that of Fig 8 except that they each use different methods for obtaining the oscillatory motion of the cylinders. Fig 6 uses a spherical joint which also acts as the seal for the piston. The motor in Fig 9 uses telescopic cylinders to transfer the pressure force to the eccentric. These are both mounted at their ends in spherical bearings that employ hydrostatic bearings.

3.3.2 Cam motors

Both the motors of Figs 10 and 11 convert the piston force into torque by means of cams. That of Fig 10 has a fixed cylinder body with a rotating case whereas that of Fig 11 has a rotating cylinder that is connected to the output shaft. The motor in Fig 11 employs a single roller between the piston and the cam but that in Fig 10 uses rotating element bearings for this purpose.

These motors have an advantage over the eccentric types in that they can be designed to produce zero torque ripple with no hydraulic loads on the shaft bearings. However their maximum operating speed tends to be limited by the cam roller bearing. It is not possible to obtain variable displacement from these motors as in the eccentric type.

4.0 DESIGN CONSIDERATIONS FOR THE RECIPROCATING COMPONENTS

The conversion of the piston movement to rotational movement of the shaft requires an oscillating joint which, because of the relatively low sliding velocities, is a major source of friction losses particularly at low operating speeds. This frictional loss is likely to increase when the velocity falls to zero during the pressure cycle.

For both types of high speed units this joint is effected by a ball and spherical cup but there is an important difference in their mode of operation. In the bent axis unit of Fig 3 the cup component on the output shaft rotates which creates sliding between the cup and the ball, the amount of which depending on whether or not the piston rotates in the cylinder. Rotation of the piston in the cylinder will depend on the relative values of the friction coefficients and the exact position at which the resultant force from the piston can be said to act in relation to the ball centre. Whether or not such rotation occurs, some form of sliding motion will take place in the ball joint.

For the swash plate unit it is possible for, say, the vertical axis of the slipper pad to maintain itself parallel to the vertical axis of the swashplate in which case it, and the piston, can act as a solid body with the piston rotating in its cylinder once per revolution of the cylinder block; if this were the case there would be no movement in the ball joint. At the other extreme if the piston is irrotational with respect to the cylinder it will rotate with respect to the swash plate and as a consequence sliding motion in the ball joint will take place.

Such aspects have been investigated by Hooke[5] together with work on measurement of the film thickness between the slipper face and the swash plate. Ikeya with Ezato and Kobayashi[6,7] have investigated variously the levels of friction and leakage between the piston and the cylinder and the effects of distortion between the slipper and swash plate.

During starting and low speed when frictional forces are at their maximum it is probable that localised contact will occur between the slipper and the swash plate in order to provide sufficient force to overcome the frictional forces that are acting in the various sliding faces. As is described in Chapter 2 the model derived for a particular type of radial piston eccentric motor considers this force and the effect of slipper leakage on the slipper hydrostatic bearing pressure.

For the axial piston units this is a very complex 3 dimensional problem with a large number of possible relative movements between the various components which are dependent on the amount of friction present.

In the radial piston eccentric motors there is no possibility of rotation of the slipper which consequently eliminates possible alternative movements. A further significant difference is that the engagement of the slipper with the eccentric provides, at worst, line contact as compared to that for the swash plate unit described previously. Here the localised contact could be considered to act at a point between the slipper and the swashplate which probably creates higher frictional losses during starting and at low speeds.

In both types of the axial units the reaction force that acts through the centre of the ball joint creates a bending moment on the piston. This action causes reaction forces between the piston and the cylinder which increase as the piston moves out to its maximum position. These forces give rise to friction which has been measured by Ezato and Ikeya[6] at different pressures and speeds using a special purpose test rig.

In most of the radial piston motors such overhang is avoided with a consequent reduction in the piston to cylinder friction. The friction in the ball joint itself creates reaction forces in both the piston and the slipper and the differing geometry in all of the various types of motors will be affected by this to varying extents.

5.0 OTHER PARAMETERS AS A BASIS OF COMPARING MOTORS

Users of hydraulic motors obviously need to be aware of how their application affects the performance of the motor which may predetermine, to a degree, the type of motor that is selected for the drive. However, of prime consideration in the selection process are the overall dimensions of the motor including its installed weight and the need or desirability of using a gear reducer.

The comparision made by the author in a paper[2] is discussed in the next section.

5.1 A Performance Comparision of Hydrostatic Piston Motors

The operating speeds obtained from an examination of the data for a selection of major European, American and Eastern motor manufacturers are shown in relation to their displacement in Fig 12. In this and subsequent figures the types of motor indicated by number are shown in Table 1. Any point on a graph of speed against displacement represents a flow, this being the product of speed and displacement. Thus a line of constant flow is given by:

Speed x Displacement = Constant

or N = Constant/D

On logarithmic scales this becomes:

$Log\ N$ = Constant - $Log\ D$

For a given operating pressure this line represents one of constant power. Fig 12 shows lines for power levels of 105 and 255 kW at a pressure of 210 bar.

It can be seen from Fig 12 that in general low speed machines produce a given power at displacements in the range six to ten times greater than those of the high speed machines. If a range of motors having different displacements for machines employing identical design principles are obtained by dimensional scaling, for a given sliding velocity in the motor, the corresponding motor speed will vary inversely with the linear size. For this situation and taking motor displacement to vary as the cube of the linear size, the relationship of speed with displacement is represented by:

$$N(D)^{1/3} = \text{Constant} \qquad (1)$$

This relationship is shown in Fig 12. For each type of motor the position of the line may be located to correspond to a particular machine size selected as a datum. The importance of the relationship lies in its slope and it can be seen that, in general terms, the different types of machine follow this relationship quite closely. A typical value of $N D^{1/3}$ for an aero outward radial pump is shown on Fig 12 for comparision.

5.2 Machine Size

The size of the various machines, bearing in mind the different shapes of each type, is best represented by their mass.

The masses of the motor types shown in Fig 12 are presented in Fig 13 as a function of displacement. It can be seen that for a given displacement there is a wide variation in mass between the different types considered.

For a family of similar machines the mass, M, would be proportional to the displacement, D. From Fig 13, it can be seen that the high speed machines generally follow this relationship quite well whereas the mass of the low speed radial machines increases at the lower rate that is approximately proportional with $D^{2/3}$.

5.3 Specific Performance

Considering the varying shapes of the different types of motors a very effective way of making a performance comparison is to present the torque and power to mass ratios (ie specific torque and power) as a function of the machine displacement. For the machine types identified by number on Figs 14 and 15 these parameters are shown for an operating pressure of 210 bar.

This information presents quite a different picture from that previously shown in Figs 12 and 13. It can be seen that the low speed motors have specific torque values of between four and fifteen times greater than those of the high speed motors and at low displacements some of the high speed machines have values of specific power which are between one and four times greater than that of the low speed machines.

For a family of similar machines having the same maximum sliding velocity as described by equation 1, the ratios of the torque, Q_M, and power, P_o, to the mass at a given pressure would be given as follows:

$$Q_M/M = \text{Constant} \qquad (2)$$

$$\text{and } (P_o\, D^{1/3})/\, M = \text{Constant} \qquad (3)$$

It can be seen from Fig 14 that for each of the machines the specific torque tends to a constant value. The trend of specific power variation with displacement for the different machines generally follows the relationship of equation 3 even though the machines employ distinctly different design principles. Many of the machines can be operated at pressures much greater than 210 bar and where such pressures are used the machines will show higher performance values.

5.4 Constructional Features

The data presented in Figs 12 to 15 demonstrates that, to a large extent, the different types of motors considered have clearly defined characteristics in terms of their mass and performance parameters. The high speed machines have, in general, similar operating speeds but there is a significant distinction between the mass values of the swash and bent axis types of motors. There is also a marked difference in the relationship of the specific performance parameters with displacement which must be considered as a reflection on the principles of construction.

The variation in mass of the low speed motors for a given displacement is very much less than that of the high speed machines and their speeds tend to have the same trend with displacement. The specific performance characteristics of the eccentric and cam motors show a distinctly different trend in that the cam motor peaks at a much higher value of displacement than does the eccentric motor.

5.5 Scale Factors

It is interesting to note that whilst the high speed machines have, for a given displacement, operating speeds of the order of four to five times greater than those of the low speed machines, the relatively light weight of the low speed machines results in the values of specific power of both types being similar. Also, the fact that all the types considered tend to follow the same scale relationship for specific power in respect to displacement could be taken to indicate that there is a natural limit for this parameter. However, it is more than likely that machines employing different design principles will have different constraints on their maximum performance, and such conformity to the scale relationship of specific power for all the types of machines would not necessarily be expected.

The fact that different types of aero pumps[8] achieve much higher values of specific power indicates that the apparent performance similarity between the various motors is to some extent coincidental. The reason for the similarity is more likely to lie in the aims of manufacturers to meet the same performance specifications. The fact that the levels of development effort expended have varied enormously between manufacturers shows that improvements in the performance of some machines can be still be made.

Linear scaling may be used to increase motor displacement but the technique cannot be applied universally since consideration must be given to particular design principles. For example, where there are bending moments arising from pressure forces the deflections will increase proportionally with the linear scaling factor. Such deflections may be unacceptable in instances where shape is important, as for example at the faces of pressure supported bearings and sealing lands. These limits to linear scaling together with the use of common components in machines of different capacity are probably the significant factors in the deviation of machine performance from the various scale relationships used in the analysis.

5.6 Geared Drives

The use of multi ratio gearboxes provides a very attractive method of increasing the effective displacement, since, by selection of the appropriate gear ratio, a range of torque and speed requirements can be covered by a given motor frame size. It was observed previously in relation to Fig 12, that high speed motors produce a given power at displacements between one tenth and one sixth of the values in low speed motors. In general terms, the effect of adding a gearbox will be to increase the value of specific torque and to reduce the value of specific power.

The epicyclic gearboxes commonly used are, in practical terms, limited to a maximum ratio of around 7:1 per stage. As can be seen from Table 2, which has incorporated typical gearbox mass values, the use of the same gearbox frame size to cover a range of gear ratios can result in the overall mass of the combined drive not being as favourable as it otherwise might be. The values of specific torque and power for the combined drive are as follows:

$$(Q_G/M)_{com} = (n\,Q_M) \,/\, (M_g + M) = n\,(Q_M \,/\, M)_{motor}) \,/\, (1 + M_g \,/\, M) \qquad (4)$$

$$(P_o \,/\, M)_{com} = P_o \,/\, (M_g + M) = (P_o \,/\, M)_{motor} \,/\, (1 + M_g \,/\, M) \qquad (5)$$

n = reduction ratio, M_g = gearbox mass

Thus in terms of torque, power and mass for the same operating pressure, the high speed combined drive can be roughly equivalent to the best low speed motor for gear ratios up to about 10:1.

However, this does depend on the way that the parameter $n \,/\, (1 + M_g \,/\, M)$ varies with the gear ratio and output torque level. Therefore, the values will depend on the particular machines and gearboxes in question. The information of Table 2 is shown by the dotted lines on Figs 12 to 15 for comparision with the values obtained for the low speed motors.

6.0 CONCLUDING REMARKS

As described in the opening section, the purpose of the work is to present a model of a particular type of low speed motor to allow an evaluation of the sensitivity of the motor performance to:

a) Various design parameters in order to provide information for optimising the performance.

b) Values of friction coefficients which may be either static or dynamic (stiction, coulomb, velocity dependent etc) or variable with time due to squeeze film effects.

The comparison of the different motors shows that the low speed types, whilst of lower mass and weight, are limited in terms of their maximum speed capability in relation to that of high speed motors. The reasons for this disparity will be explored together with an investigation of the various factors that affect the lubrication of the contacts where relative sliding takes place.

For low speed motors high efficiency at low speed is obviously of paramount importance but it would be advantageous to examine areas in which improvements can be obtained to increase their maximum operating speed.

TABLE 1

Identification of motors types used in the Figures

1. Variable displacement axial swash plate
2. Fixed displacement axial piston swash plate
3. Variable displacement bent axis

4.5 Fixed displacement bent axis

6. Axial piston swash plate LSHT

7.8 Radial piston eccentric LSHT

9. Radial piston cam LSHT

TABLE 2

High Speed Motor			Gear Ratio ; Gearbox mass ; Effective Displacement					
			7:1; 40 kg; 1260 cm^3/rev		22.5:1; 170kg; 4050 cm^3/rev		45:1; 180 kg 8100 cm^3/rev	
Displacement	Mass (kg)	Speed (rev/min)	Mass	Speed	Mass	Speed	Mass	Speed
180 (cm^3/rev)	45	2750	85	393	215	122	225	61
	160	2250	200	321	330	100	340	50
Low Speed Motor			105	380	270	185	425	150
			145	275	455	135	700	100
High Speed Motor			7:1; 70kg; 2520 cm^3/rev		22.5:1; 180kg; 8100 cm^3/rev			
360 (cm^3/rev)	140	2200	210	314	320	98		
	330	1850	400	264	510	82		
Low Speed Motor			190	260	425	150		
			280	185	700	100		

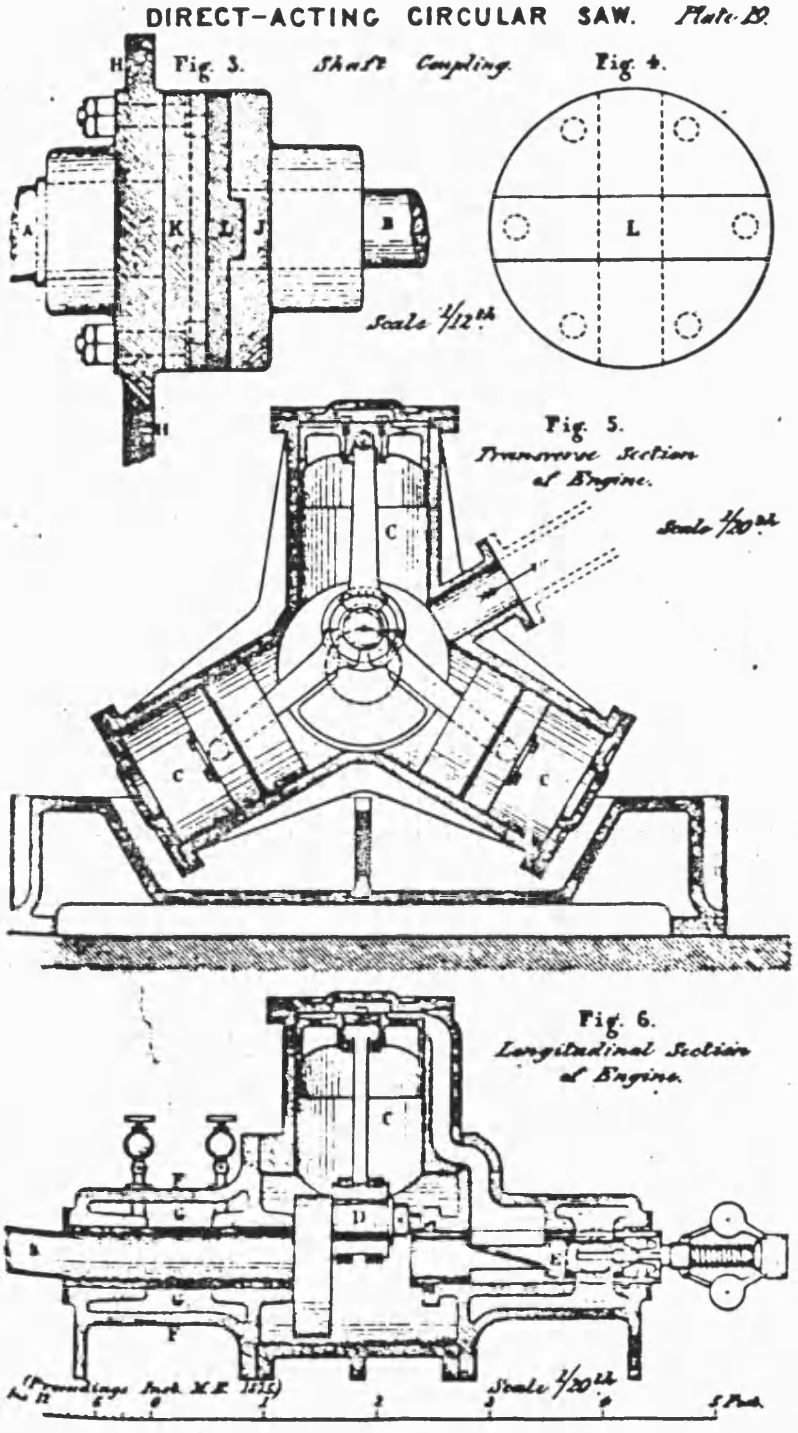

Fig 1 EARLY WATER POWERED HYDRAULIC MOTOR

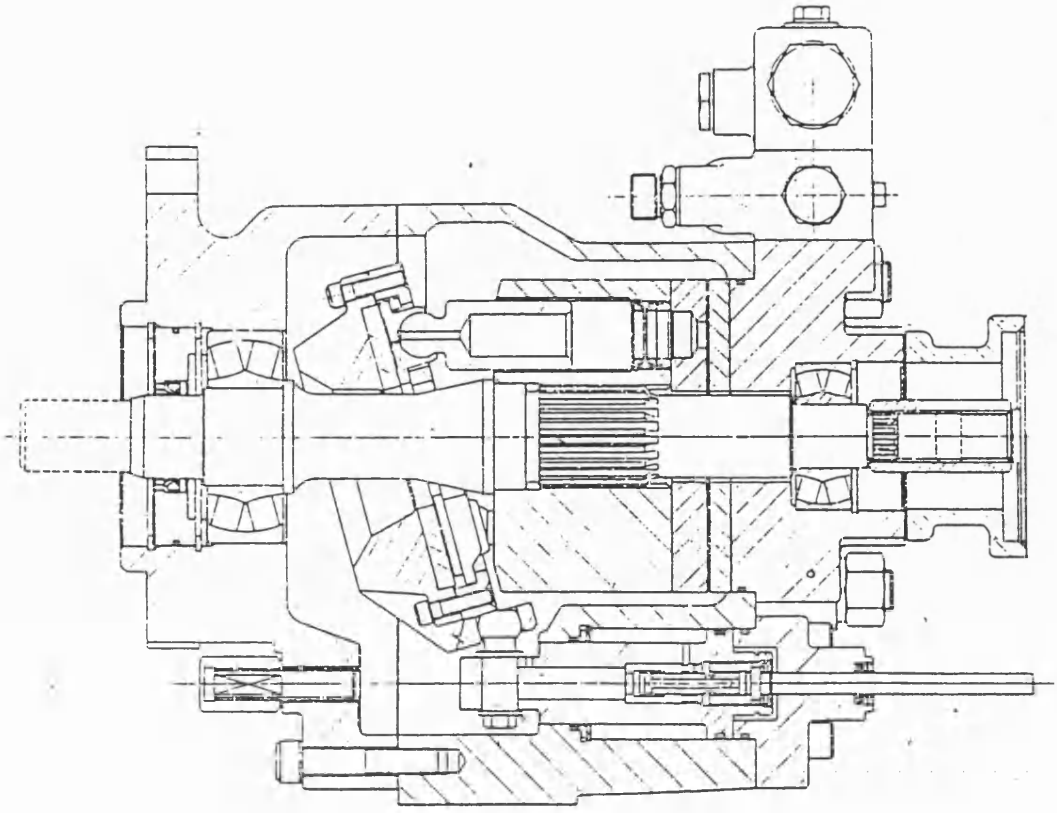

Fig.2 COMMERCIAL AXIAL PISTON MOTOR

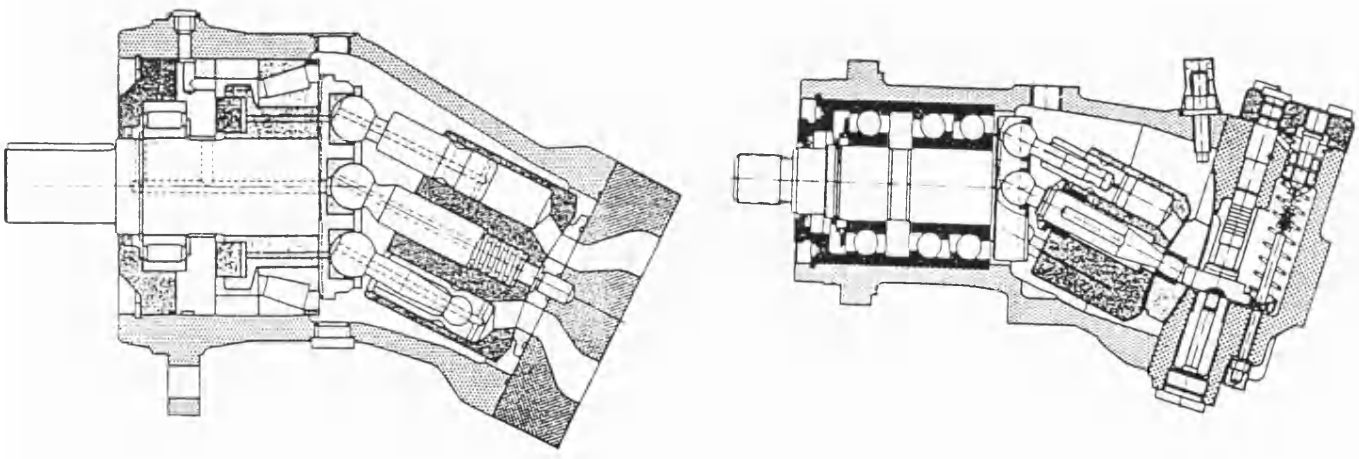

Fig.3 REXROTH BENT AXIS MOTORS

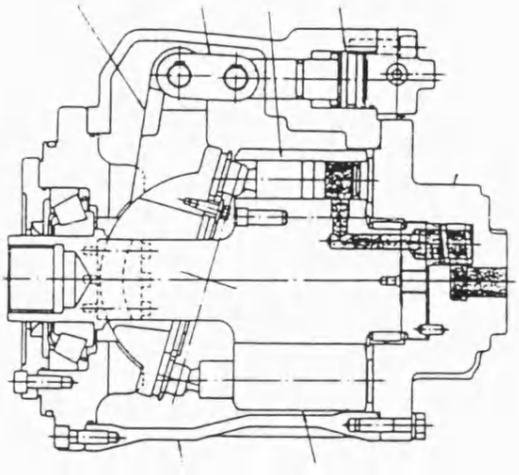

Fig.4 TOSHIBA AXIAL PISTON MOTOR

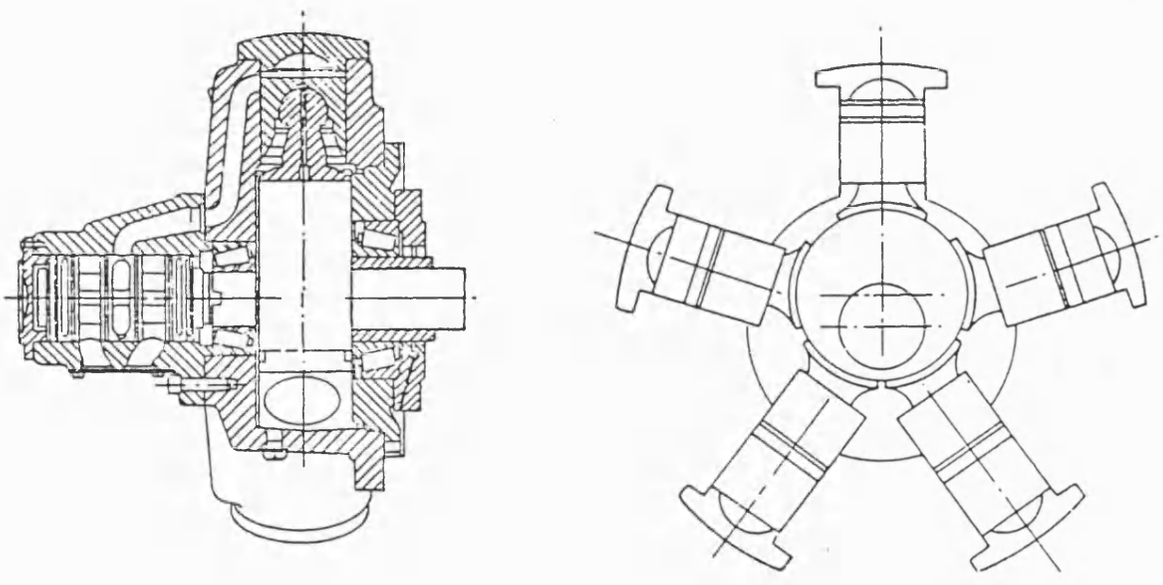

Fig.5 STAFFA RADIAL PISTON ECCENTRIC MOTOR

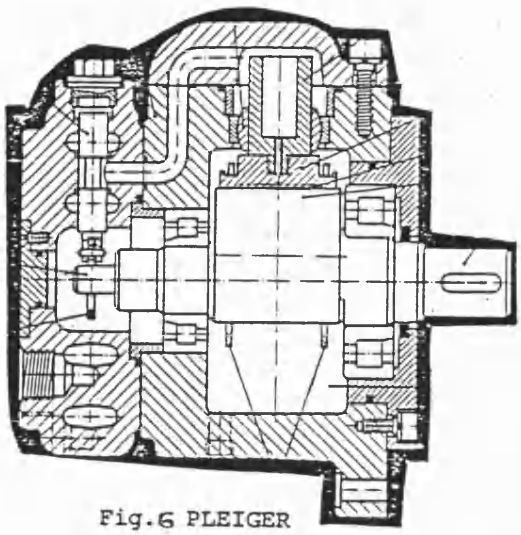

Fig.6 PLEIGER

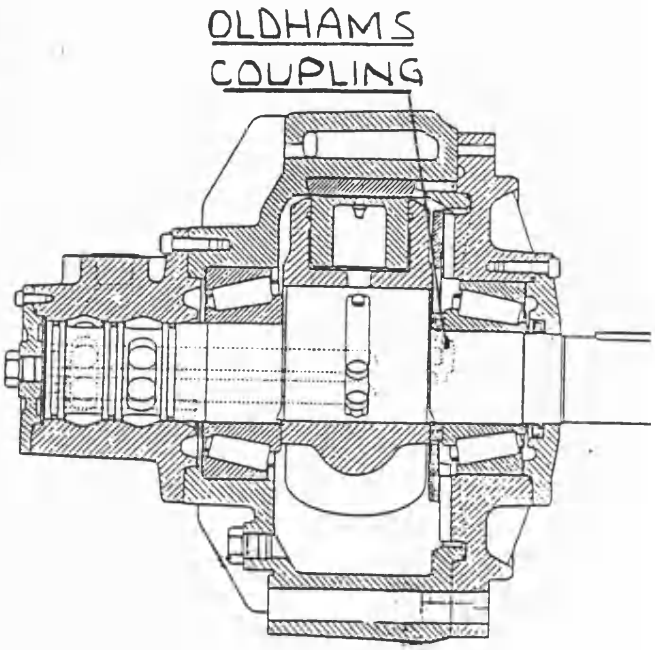

Fig.7 SAUER

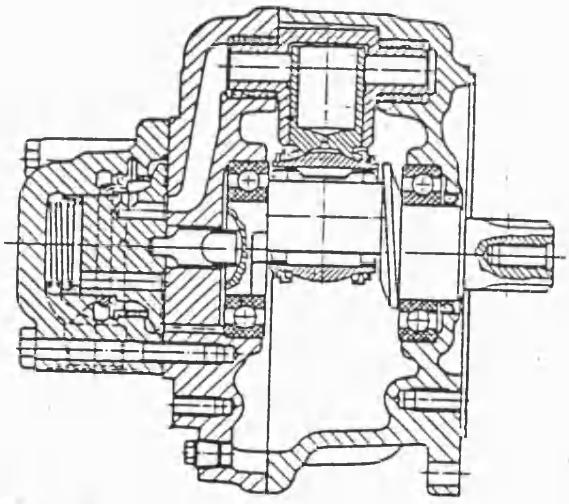

Fig.8 SAI

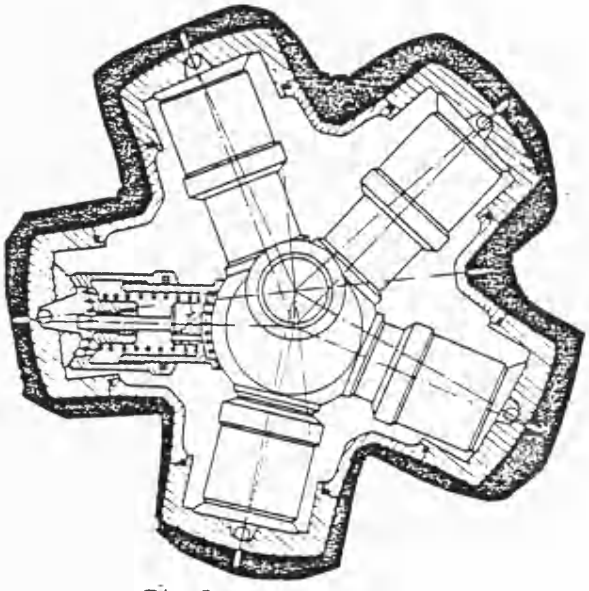

Fig.9 CALZONI

Figs 6 TO 9 RADIAL PISTON ECCENTRIC MOTORS

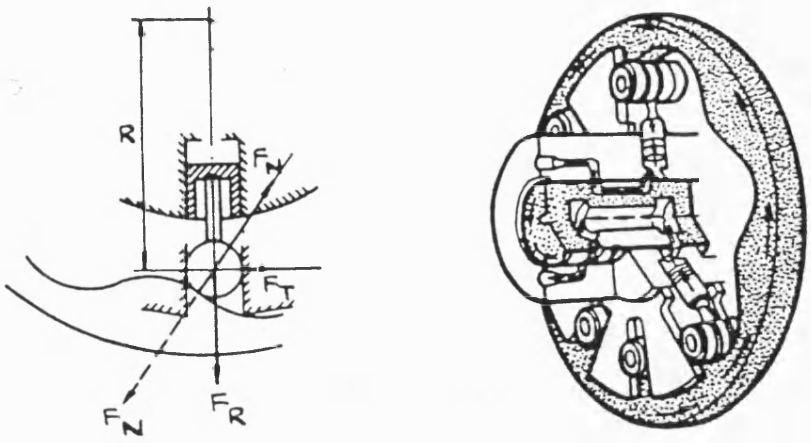

Fig.10 HAGGLUND RADIAL PISTON CAM MOTOR

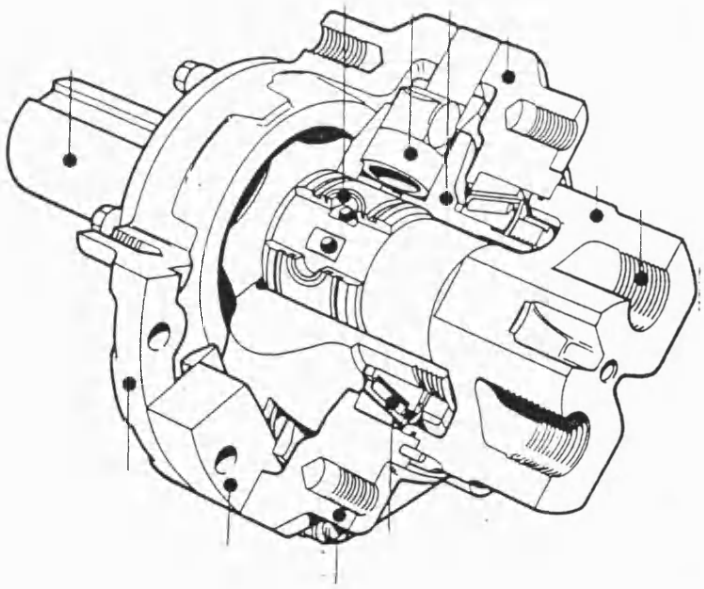

Fig.11 RENOLD RADIAL PISTON CAM MOTOR

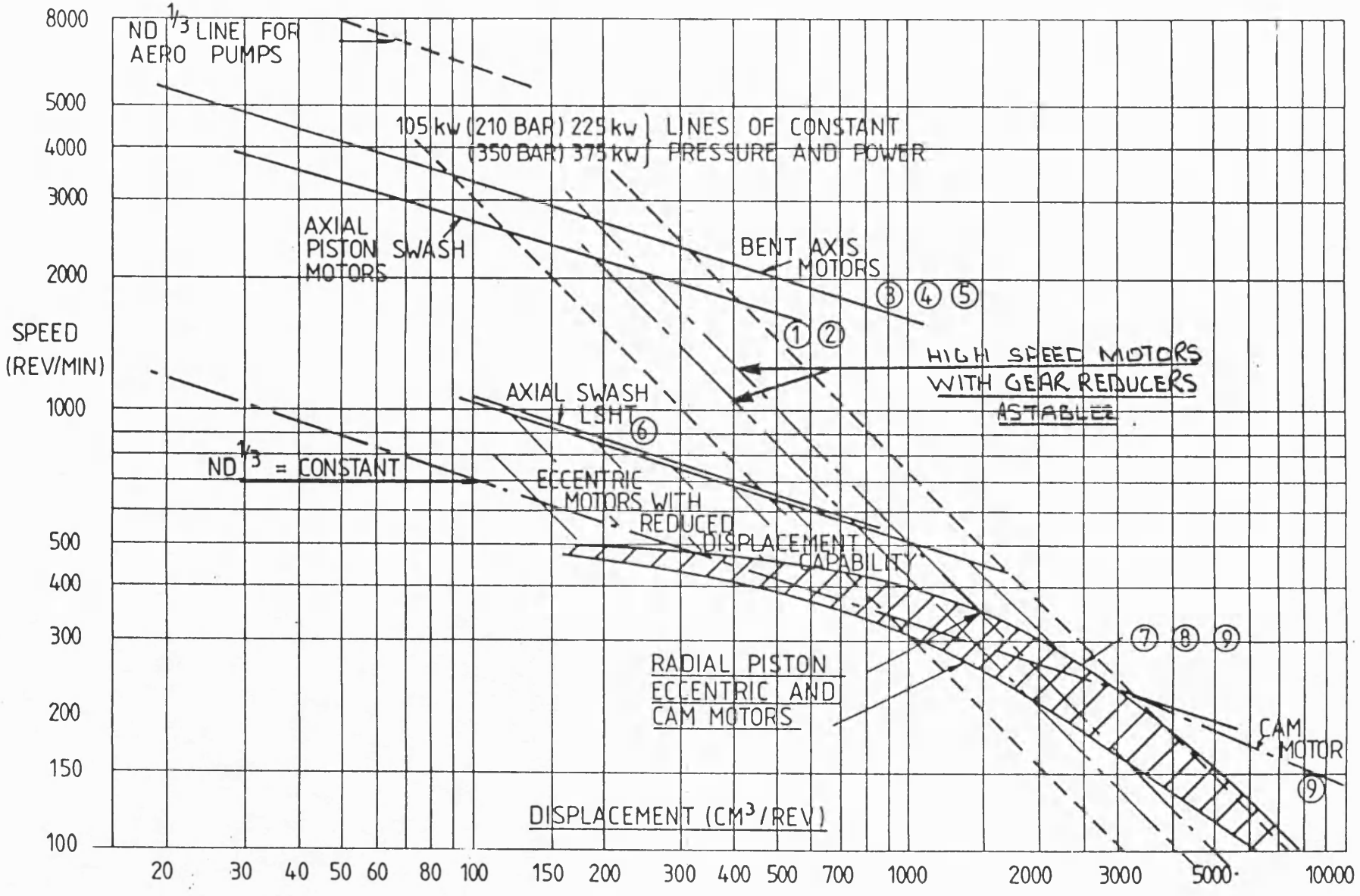

FIG.12 RANGE OF MOTOR OPERATING SPEEDS WITH DISPLACEMENT

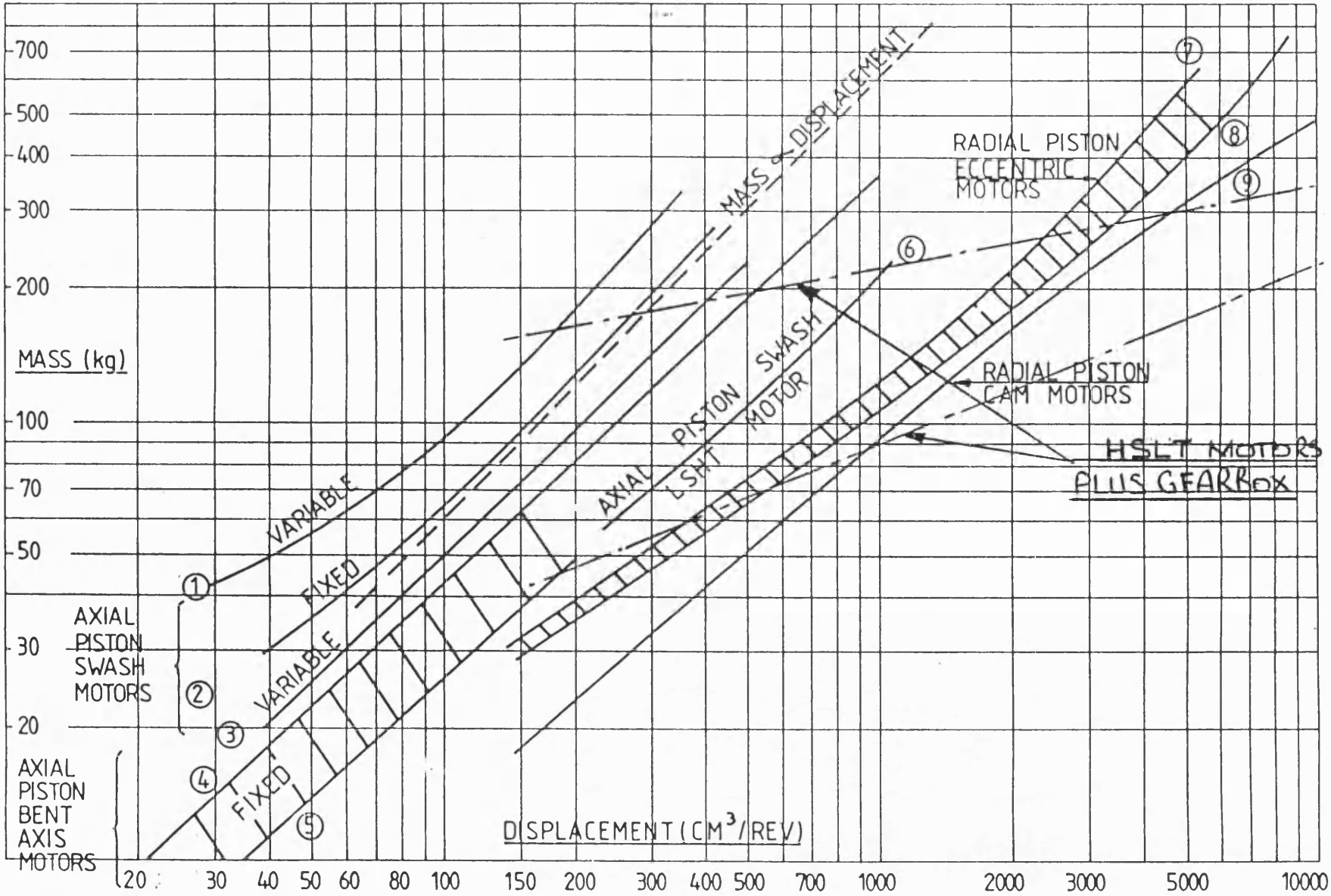

FIG.13 VARIATION OF MOTOR MASS WITH DISPLACEMENT

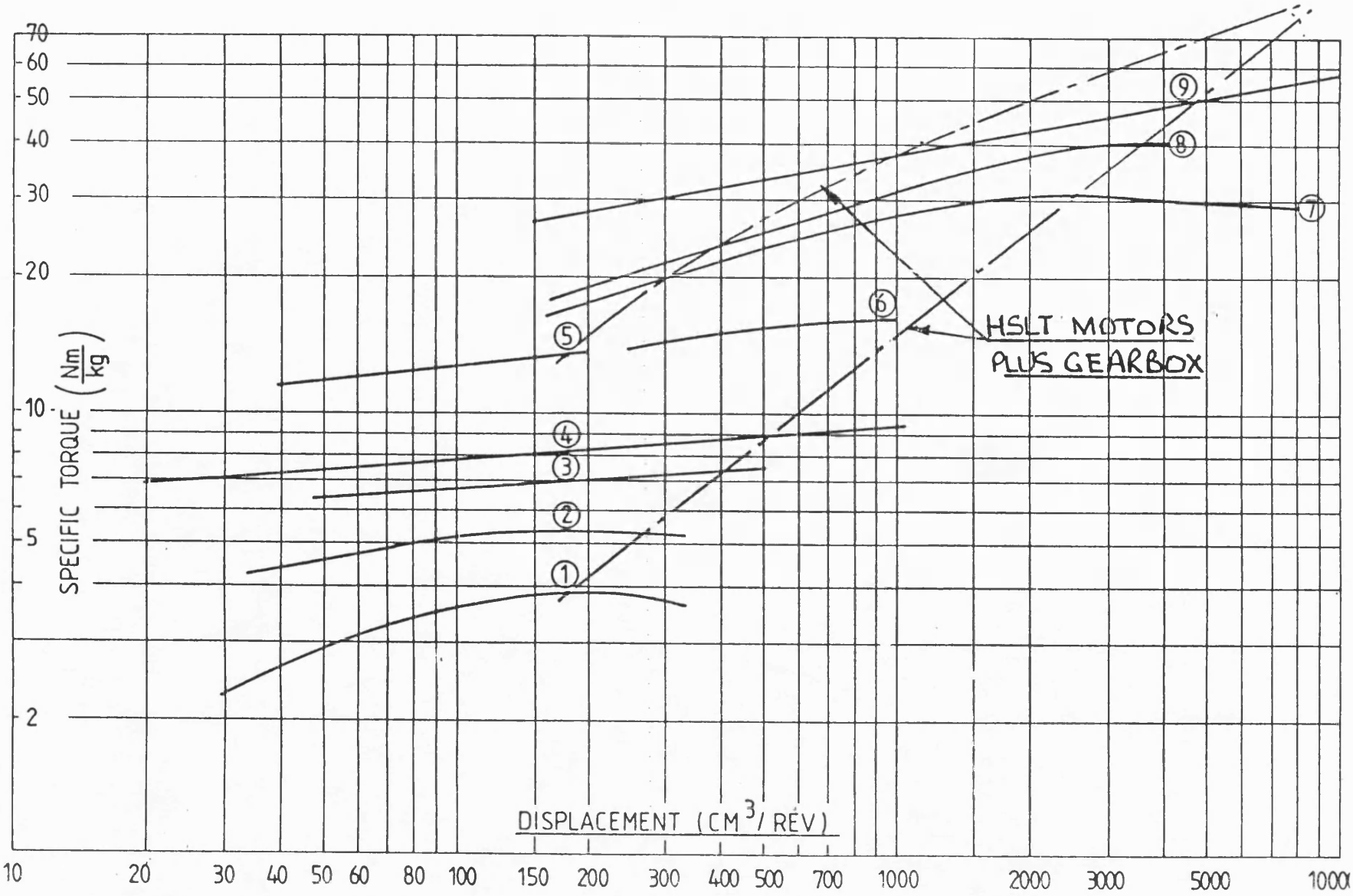

FIG.14 VARIATION OF MOTOR SPECIFIC TORQUE WITH DISPLACEMENT

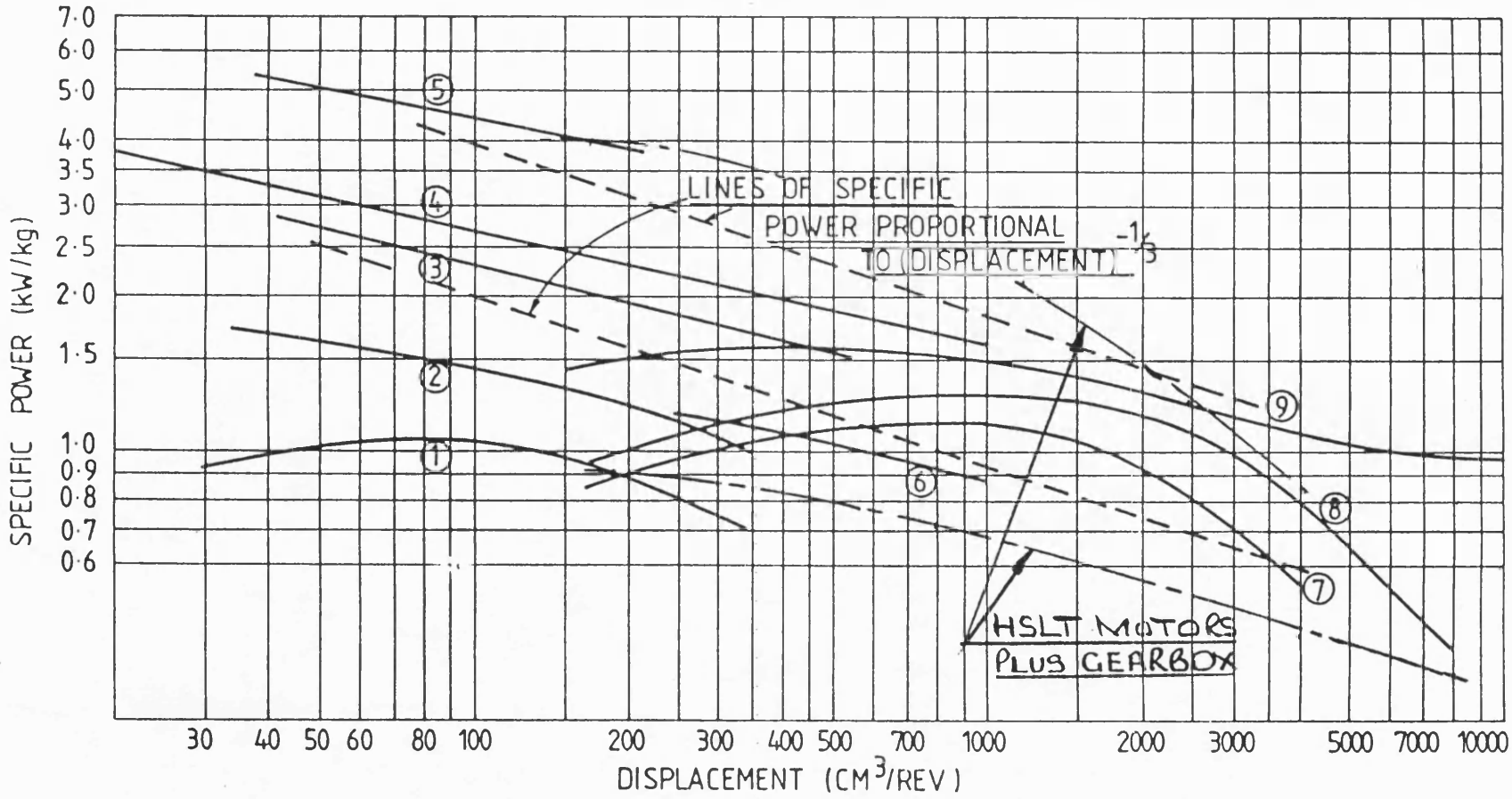

FIG.15 VARIATION OF MOTOR SPECIFIC POWER WITH DISPLACEMENT

CHAPTER 2

MATHEMATICAL MODELLING OF THE HYDRAULIC MOTOR

1.0 INTRODUCTION

As described in Chapter 1 radial piston eccentric motors are manufactured in forms that embody many different principles of operation. In this study a mathematical model of the motor type shown in Fig 1, is developed in which it is assumed that the components are inelastic. This analysis is aimed principally to establish the geometrical relationships for the forces acting including those due to friction which are assumed to be represented by friction coefficients.

2.0 FORCE TRANSFER TO THE ECCENTRIC

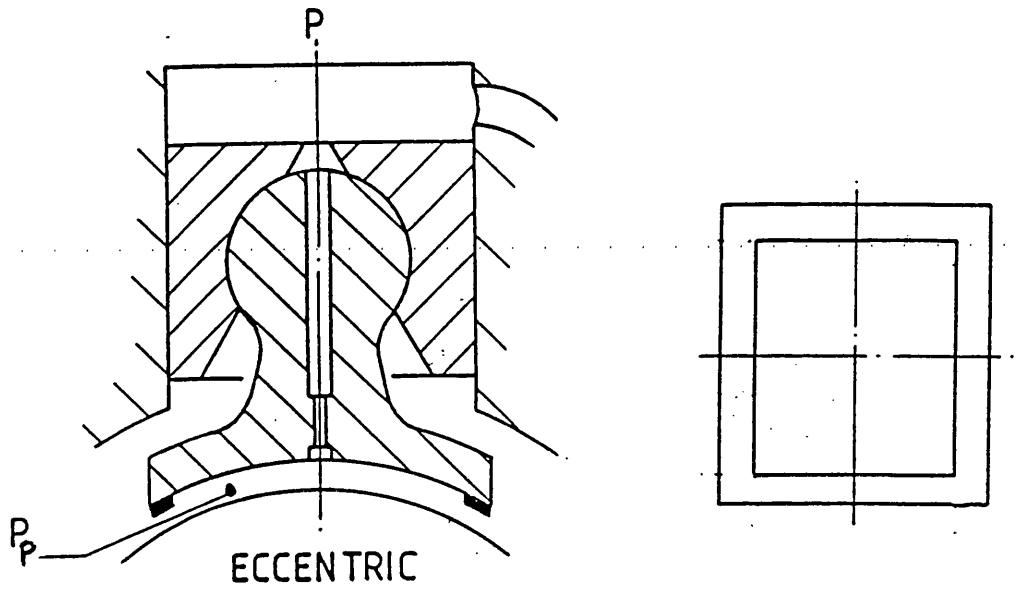

In the motor the force from the piston is transferred to the eccentric through the spherical joint in the piston to the connecting rod and the slipper. The slipper is hydrostatically balanced by feeding high pressure fluid from the cylinder to the slipper pocket through a restrictor. The effective projected area of the slipper face is greater than that of the piston and consequently the slipper lifts off from the surface of the eccentric until the oil leakage through the clearance space has reduced the pocket pressure to a level such that the slipper force just equals that of the piston. This is an ideal situation and assumes that there is no tilting of the slipper face. If the problem is further simplified to a flat bearing, the pocket pressure can be obtained by equating the flow through the restrictor and the slipper lands.

For a flat bearing assuming laminar flow:

$$Q = \frac{\pi d_0^4 (P - P_P)}{128\,\mu L_P} = \frac{P_P h^3 L_L}{12\,\mu\omega} \qquad (2.1)$$

where d_0 = restrictor diameter

L_L = total mean length of the slipper lands

ω = width of the slipper lands

L_P = restrictor length

The height of the leakage space (h) is the lift or clearance between the slipper and eccentric faces and this is taken to be constant at all points around the slipper. The effects of the corners of the rectangular slipper are assumed to have a negligible effect on the flow and pressure distribution across the lands. The flow through the clearance space will thus produce a pressure that varies linearly across the slipper lands as shown thus:

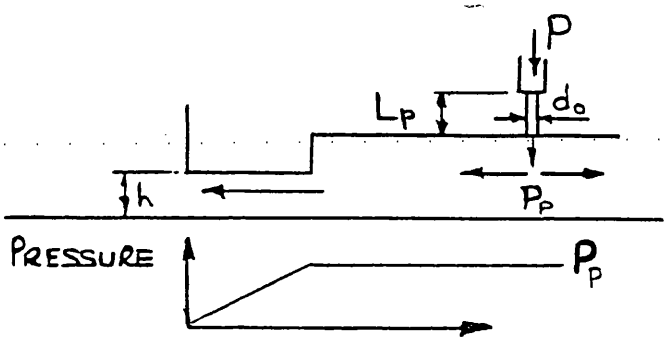

The pressure force on the slipper lands will therefore be equal to the land area x $P_P/2$. Thus the total slipper pressure force $F_P = P_P A_S$, where A_S is the mean effective slipper area. For this force to balance that from the piston (PA_P) we get:

$$P_P = PA_P/A_S \qquad (2.2)$$

Hence from equation (2.1) assuming that the dynamic viscosity is the same in the restrictor and the slipper leakage path.

$$h^3 = \frac{12\,\omega\pi d_o^4}{128 L_L L_P}\left(\frac{P}{P_P} - 1\right) \qquad (2.3)$$

Taking the dimensions for the motor from the data in Table 1 we get

$$\frac{A_P}{A_S} = 0.925 = \frac{P_P}{P} \qquad (2.4)$$

And $h = 0.016$ mm

For the case of a circular slipper and eccentric having the same radii, h will be a radial clearance the value of which will reduce with the distance from the centre line that is common to both of these components. Thus the maximum bearing lift will be slightly greater than 0.016 mm.

The slipper force is directed along the centre line of the eccentric and, in the absence of any other forces acting on the connecting rod and changes to the viscosity in the slipper clearance space, the clearance would be sustained during rotation of the motor shaft.

3.0 THE EFFECT OF FRICTION IN THE SLIDING COMPONENTS

The spherical joint being of a smaller diameter than the piston provides only a limited amount of hydrostatic balance against the force from the piston. The design of the piston cup is such that in the unpressurised state there is line contact between the surfaces at an angle of 45°. As a consequence there will be distortion of the spherical faces and high pressures in the region of contact.

During rotation of the shaft sufficient torque needs to be provided to overcome the frictional moment created by this bearing. Thus for movements from Top Dead Centre (T.D.C.) when the con rod angle is increasing ($0<\theta<90°$) there needs to be a force distribution around the slipper face to provide a torque about the spherical joint centre.

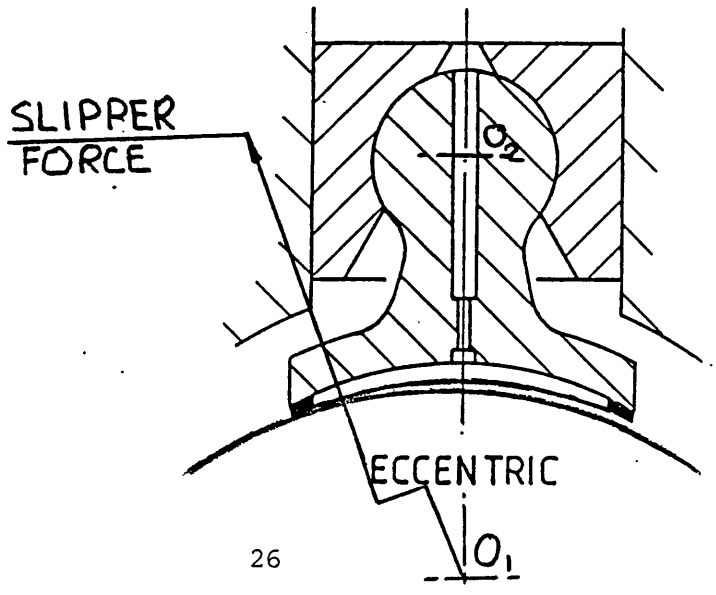

For the analysis it is assumed that a single force acts at an angle β_1 to the vertical centre line O_1O_2. This force would be the resultant of the force distribution that arises from contact between the slipper and eccentric faces.

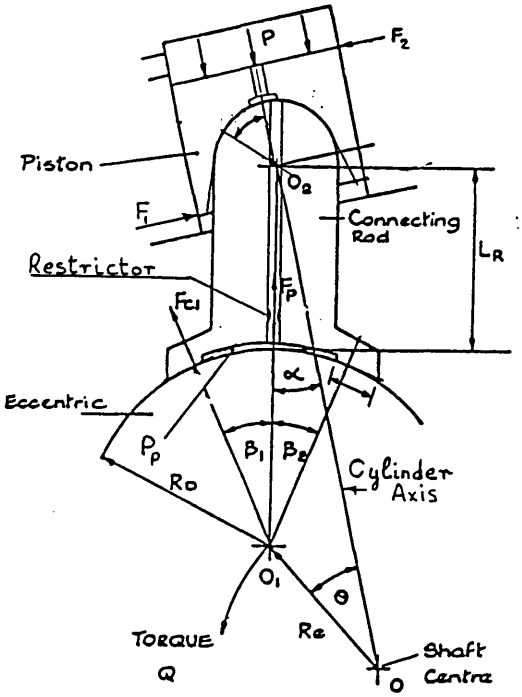

CYLINDER CROSS-SECTION

In the absence of a frictional torque in the con rod bearing the slipper would be able to lift away from the eccentric surface so that the hydrostatic force is equal to that of the piston as described in Section 2.0. Referring to the diagram if the slipper makes contact with the eccentric along the line O_1O_2 (ie $\beta_1 = 0$), the hydrostatic pressure (P_p) will increase because of the reduced leakage area between the slipper and the eccentric. If β_1 is then increased, there will be an increase in this leakage area thus causing the hydrostatic pressure to reduce because of the increased flow through the restrictor.

For a given value of β_1, the leakage area will depend on the difference between the slipper and eccentric radii (e_C) (not shown on the diagram). Thus for a given value of e_C, when β_1 increases beyond a certain value, the hydrostatic pressure force will fall below that required for equilibrium with the piston force. This will result in a force (F_{C1}) at the contact point and as β_1 is increased further, F_{C1} will also increase.

Referring to the diagram it can be seen that as β_1 increases the length of the torque arm between the line of action of F_{C1} and the con rod bearing centre O_2 also increases. The value of F_{C1} that is required to overcome the con rod bearing frictional torque is thus reduced. As a consequence of these variations with β_1, the

operating value of F_{C1} will be that which satisfies both radial equilibrium and the con rod bearing frictional torque.

4.0 THE CONDITIONS FOR CONTACT

As stated the so-called 'contact' force occurs at a position which satisfies equilibrium but, as a consequence, creates frictional resistance between the slipper and rotating eccentric. For static and low speed conditions (0<N<5 rev/min) it is likely that the fluid film in the 'contact region' will be extremely thin when the frictional process will pertain to that of boundary lubrication.

The objective of the analytical method that is developed in Section 5 is to establish how the motor torque varies with the shaft angle θ. This involves the determination of β_1 in the way described in Section 3.0. Before this method can be effected it is therefore necessary to determine the magnitude of the shaft movements that are associated with changes in the value of β_1.

The curvature of the slipper will be a function of manufacturing tolerances and the level of distortion created by the imposed forces. Experience has shown this to have a radius in the region of ±75 micron in the unloaded condition relative to that of the eccentric. The slipper leakage flow analysis contained in Appendix II deals with the effect of such variations in this curvature. In the following analysis the slipper is assumed to have a slightly larger curvature than that of the eccentric the geometry of which is shown exaggerated in the following diagram.

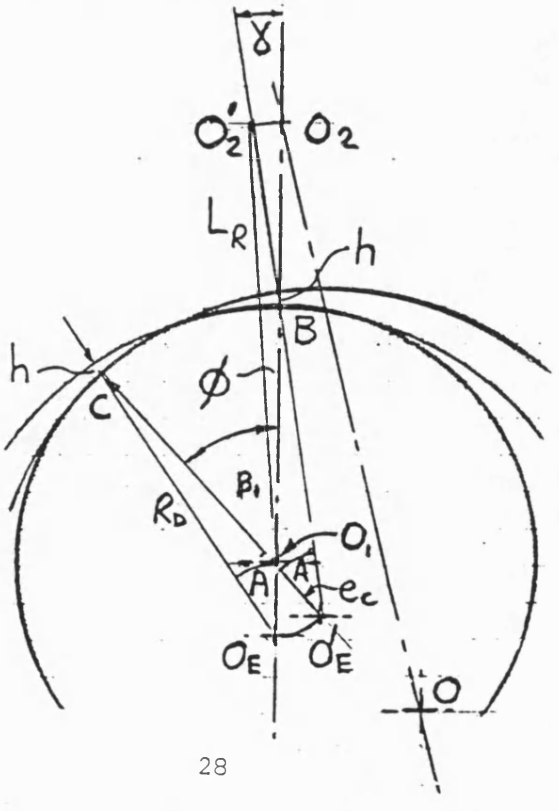

For changes in the angle β_1 from zero, movement of the contact point from B to C is achieved by the slipper rolling around the eccentric. This causes a vertical movement of the con rod bearing centre O_2 by the distance 'h' and a rotational movement to O'_2 away from the cylinder axis by the angle ϕ where $e_C << R_D$.

The slipper radius centre O_e will rotate around O_1 by the angle β_1 and in order to cancel the movement of O_2 the motor casing including the shaft centre will have to be rotated by the angle ϕ about the centre O_1. Thus by geometry the angular shaft movement ϕ can be determined.

From the diagram we have:

$$R_D \beta_1 \approx (R_D + e_C)A$$

$$\therefore A \approx \frac{\beta_1 R_D}{R_D + e_C}$$

For $\Delta O'_E O_1 B$

$$A + \gamma + 180 - \beta_1 = 180$$
$$\therefore \gamma = \beta_1 - A$$

For $\Delta B O_2 O'_2$ and $\Delta O_2 O'_2 O'_e$

$$L_R \gamma \approx (R_D + L_R)\phi$$

$$\therefore \phi = \frac{L_R \gamma}{(R_D + L_R)} = \frac{L_R \beta_1 e_C}{(R_D + L_R)(R_D + e_C)}$$

$$\therefore \phi \approx \frac{L_R \beta_1 e_C}{R_D(R_D + L_R)} \qquad (2.5)$$

Take $e_C = 75\ \mu m$ and $\beta_1 = 10^o$

and for $L_R = 63.5mm$

$R_D = 79.4mm$

gives $\phi = 4.2 \times 10^{-3}(\text{deg})$

and $\gamma = 9.4 \times 10^{-3}(\text{deg})$

Note that $h \approx e_C(1 - \cos(\beta_1 + \beta_M))$ at the extreme edge

For $\beta_m = 28^o$

$h = 12 \times 10^{-3}$mm

Thus it is shown that to establish a value of $\beta_1 = 10^o$ incurs negligibly small movements of the shaft and the con rod axes.

5 THE MATHEMATICAL MODEL OF THE MOTOR

5.1 Introduction

Equations are developed in Appendices I to V for the forces in the motor components and the output torque in terms of the angular position of the motor shaft and the contact angle β_1. The analysis assumes quasi steady state conditions for low motor speeds when dynamic effects can be neglected. The equations are summarised in this section together with a description of the methods used in the software developed for their solution.

5.2 Piston displacement and con rod angle

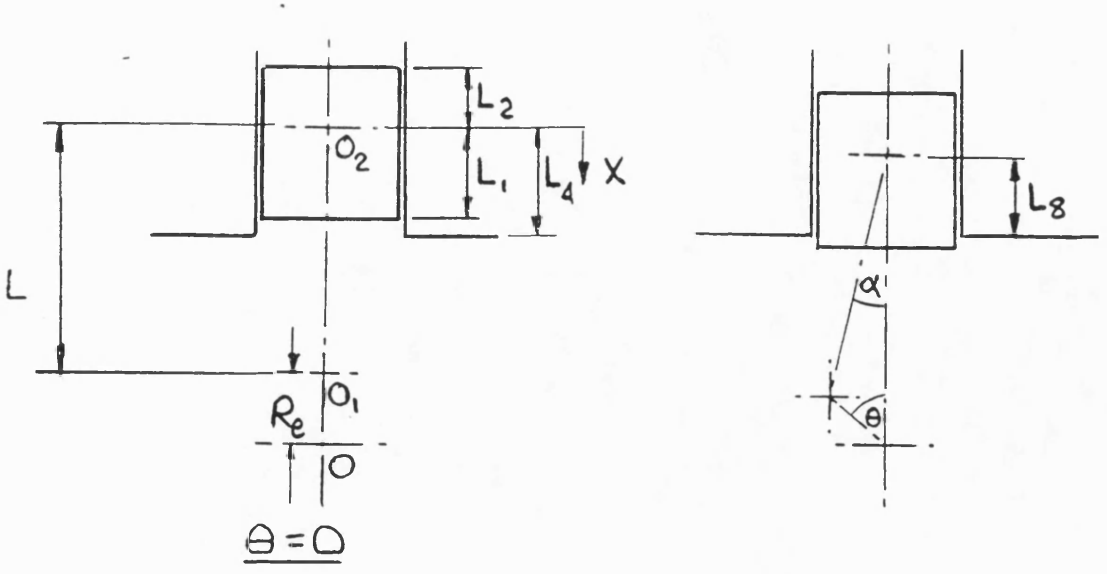

The piston displacement and con rod angle are related to the shaft angle by the following equations:

$$\sin \alpha = \frac{R_e}{L} \sin \theta \qquad (2.6)$$

and $$X = L(1 - \cos \alpha) + R_e(1 - \cos \theta) \qquad (2.7)$$

These relationships are shown in Fig.2 for the motor dimensions given in Table 1.

The dimension L_1 is the distance between the con rod bearing centre and the inner edge of the piston. The initial distance (TDC when $\theta = 0$). between the con rod bearing centre and the inner edge of the cylinder is denoted by L_4.

When $X > L_4 - L_1$, the inner piston edge emerges from the cylinder and the distance between the con rod centre and the cylinder edge is denoted by L_8 where $L_8 = L_4 - X$.

The significance of the dimension L_1 or L_8 relates to the piston forces which are discussed in Section 5.5. In this particular motor the con rod bearing centre eventually emerges from the cylinder and L_8 becomes negative.

5.3 Slipper forces

As described in Section 3.0 and 4.0 the slipper is considered to contact the eccentric at an angle β_1 to the line connecting the eccentric and con rod bearing centres (O_1O_2). The analysis in Appendix I is concerned with the resolution of the slipper forces parallel (F_N) and normal (F_T) to the centre line of the cylinder axis passing through the shaft centre.

The equations for these forces (Equations 9 and 12 Appendix I) are:

$$F_N = F_P \cos \alpha + KF_{C1} + J_2F_{C2} \qquad (2.8)$$

and $$F_T = F_P \sin \alpha + JF_{C1} + J_3F_{C2} \qquad (2.9)$$

where F_P = slipper hydrostatic bearing pressure force

F_{C1} and F_{C2} are the slipper contact forces where $F_{C2} = 0$ for $0 \leq \theta \leq 90°$ with the contact angle = β_1

and $F_{C1} = 0$ for $90° \leq \theta \leq 180°$ with the contact angle = β_2.

The coefficients K and J_2 are functions of α, β_1 and f_C and the coefficients J and J_3 are functions of α, β_2 and f_C.

5.4 Forces acting on the con rod bearing

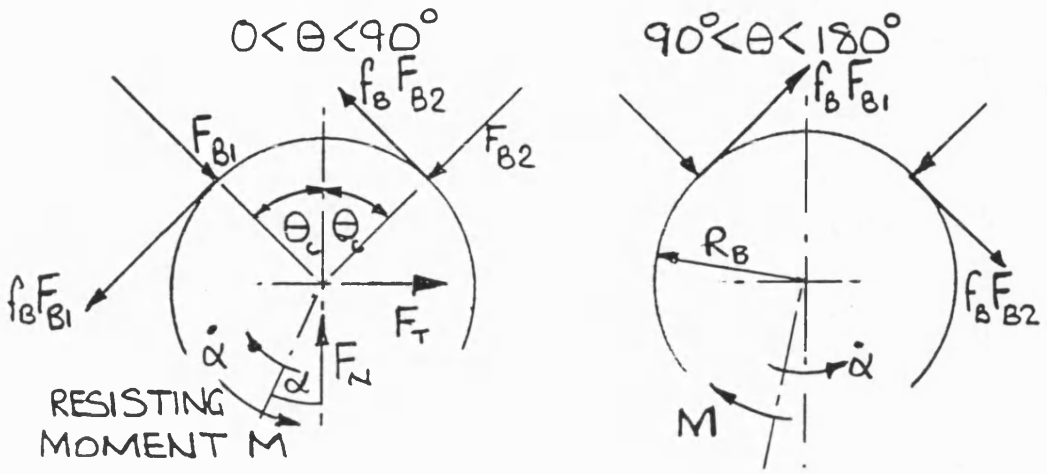

The con rod bearing is subjected to the forces exerted on the slipper which, together with the frictional forces thus created in the bearing, determine the normal forces between the spherical bearing and the piston cup as described in Appendix III.

The shape of the cup is such that contact with the sphere is over a narrow band at a nominal angle θ_C. The pressures acting around the contact band would have to be integrated over the line of contact in order to equate for vertical and horizontal equilibrium and obtain the frictional moment about the spherical joint axis through O_2 and parallel to that of the motor shaft. Here the bearing is treated as cylindrical and inelastic in order to simplify the analysis. As a consequence it is assumed that there are two forces F_{B1} and F_{B2} acting at an angle θ_C to the cylinder axis. The analysis in Appendix III is concerned with establishing the magnitude of $F_{B1} + F_{B2}$ as this determines the friction in the bearing. These are given by equations (45) and (49) Appendix III which are:

$$F_{B1} + F_{B2} = B_8 F_M + B_9 F_T \qquad (2.10)$$

for $0 \le \theta \le 90°$

and $$F_{B1} + F_{B2} = E_8 F_M + E_9 F_T \qquad (2.11)$$

for $90° \le \theta \le 180°$

Here $F_M = F_N - F_H$

where F_H = Hydrostatic force on the con rod bearing

and $$F_H = P\pi(R_B \sin \theta_C)^2 \qquad (2.12)$$

The coefficients B_8, B_9, E_8,E_9 are functions of f_B and θ_C

5.5 Forces acting on the piston

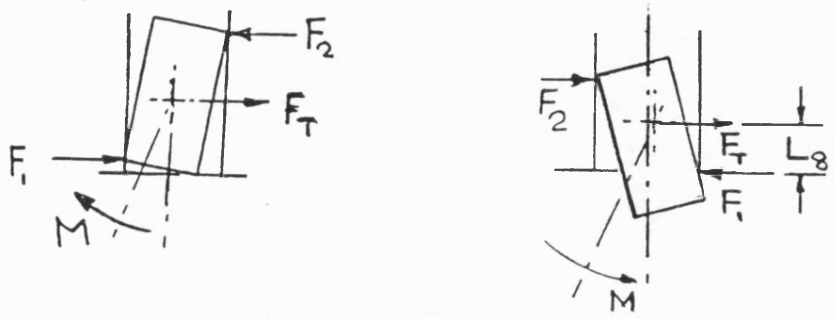

As a result of the frictional forces in the con rod bearing the piston will experience a torque about the con rod bearing centre which will be resisted by the piston forces F_1 and F_2 shown in the diagram. When the con rod angle α reaches its maximum value at $\theta = 90^o$, the direction of this torque will reverse thus changing the direction of the forces F_1 and F_2.

The magnitude and direction of F_1 and F_2 will however be dependent on the con rod bearing friction coefficient f_B and to a lesser extent the slipper friction coefficient f_C. Both of these affect the magnitude of the contact force F_C and the contact angle β.

The magnitudes of F_1 and F_2 are also affected by the distance from the con rod bearing centre to the outer and inner edges of the piston. As described in 5.2 the inner piston length L_1 changes to L_8 as the piston emerges from the cylinder when

$L_8 = L_4 - X$. As a consequence the action of the piston forces needs to be considered in regions that are related to the shaft angle.

The piston forces are derived in appendix IV and are as follows:

For $0 \leq \theta \leq 90°$

$$F_1 = D_1 F_M + D_2 F_T \qquad (2.13)$$

and $$F_2 = F_1 + F_T \qquad (2.14)$$

where the coefficients D_1 and D_2 are dependent on f_B. For $X > L_4 - L_1$, these coefficients are also dependent on L_8 (which is a function of θ).

For $90° \leq \theta \leq 180°$

$$F_1 = G_1 F_M + G_2 F_T \qquad (2.15)$$

$$F_2 = F_1 - F_T \qquad (2.16)$$

Here G_1 and G_2 are dependent on f_B and L_8. In this region the con rod centre emerges from the cylinder when L_8 becomes negative.

5.6 Equilibrium of the radial forces

There has to be equilibrium of the forces acting at the con rod bearing. In Appendix IV this condition is satisfied by equation 54 which applies in the region $0 \leq \theta \leq 90°$. Restating this equation and dividing by the piston force F we get.

$$\frac{F_{c1}}{F} = \frac{\left(1 - D_3\frac{F_P}{F} + 2D_1 f_B \frac{F_H}{F}\right)}{D_4} \qquad (2.17)$$

The coefficients D_3 and D_4 are dependent on D_1, D_2 and f_P but D_4 is additionally dependent on β_1, θ and f_C.

For the region $90° \leq \theta \leq 180°$, F_{C2} is given by:-

$$\frac{F_{C2}}{F} = \frac{\left(1 - H_3\frac{F_P}{F} + 2G_1 f_P \frac{F_H}{F}\right)}{H_4} \qquad (2.18)$$

The coefficients H_3, H_4 and G_1 are related to the motor geometry and friction coefficients in a similar way as D_1, D_3 and D_4. H_4 is also dependent on β_2, θ and f_P.

Thus, at a given shaft angle and for given values of the friction coefficients, the contact force F_C will vary with β and F_P/F.

5.7 Hydrostatic bearing pressure and force

The pressure in the hydrostatic bearing is dependent on the leakage flow across the slipper lands. This creates a pressure drop in the bearing restrictor which is supplied from the cylinder pressure.

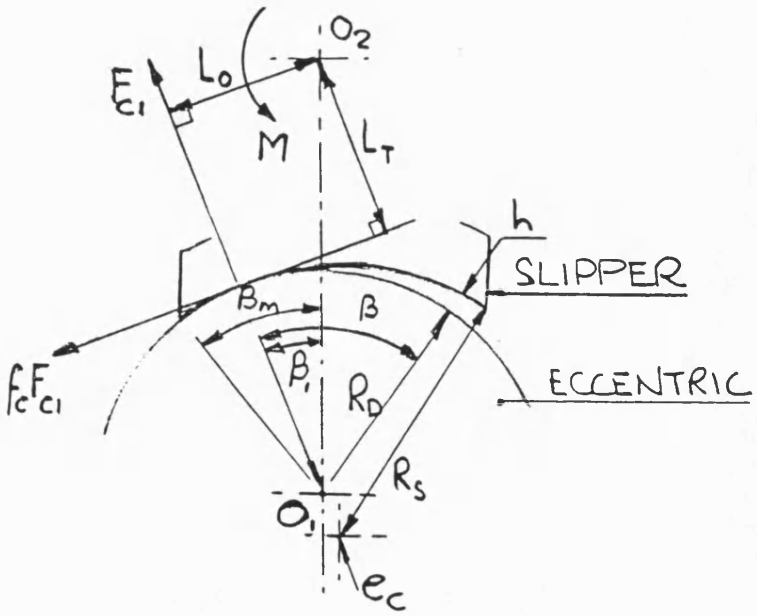

For the slipper contact angle β_1, shown in the diagram, the leakage area between the slipper and the eccentric will depend on the difference between the slipper and eccentric radii (R_S and R_D) which is denoted by e_C.

The analysis of the leakage flow in Appendix II therefore considers three conditions which are as follows:

(a) $R_S > R_D$ with tangential contact at $\beta_1 < \beta_M$ where β_M is the maximum angle subtended by the slipper around the eccentric as shown in the diagram.

(b) $R_S > R_D$ but with non-tangential contact when $\beta_1 = \beta_M$. In this situation small rotations of the eccentric will be associated with contact of the slipper at its edge against the eccentric. The geometrical relationships required to obtain the area are different from those used for (a).

(c) $R_S < R_D$ with non tangential contact between the slipper and the eccentric. This condition is deliberately contrived in an attempt to minimise the effects of distortion of the slipper face. The geometrical relationships required to obtain the leakage area are different, and more complex, than those required for (a) and (b).

Taking condition (a) by way of example, the relationships in Appendix II obtained for the hydrostatic bearing pressure P_P as a function of the contact angle β_1 can be summarised as follows:

$$\frac{P_P}{P} = \frac{1}{1 + K_6 f(\beta_1)} \qquad (2.19)$$

where $K_6 = \dfrac{128 e_C^3 L_P}{12 \pi \omega d_0^4}$

L_P is the length of the feed orifice
ω is the width of the slipper lands
d_0 is the feed orifice diameter

also $$f(\beta_1) = 2R_D(I_R + I_L) + \frac{L_\omega}{e_C^3}\left(h_R^3 + h_L^3\right) \qquad (2.20)$$

where L_ω is the mean peripheral length of the slipper lands
I_R and I_L are the values of the integral I given by equation 19 Appendix II.
These and the edge clearances h_R and h_L are dependent on β_1.

Thus knowing P_P the hydrostatic bearing pressure force is given by:

$$F_P = P_P A_S \tag{2.21}$$

where A_S is the effective slipper area

$$\therefore \quad \frac{F_P}{F} = \frac{P_P}{P}\frac{A_S}{A_P} \tag{2.22}$$

The variation of $\frac{F_P}{F}$ with β_1 can now be established by equations 2.19 and 2.22. As a consequence, the variation of the contact force with β can be obtained from equations 2.17 for $0 \leq \theta \leq 90°$. In the region $90° \leq \theta \leq 180°$, F_{C2} is obtained from equation 2.18.

5.8 Con rod bearing frictional torque

(a) $0 \leq \theta \leq 90°$

As described in 3.0 the magnitude of F_{C1} that is required to rotate the con rod will be dependent on the contact angle β_1. The relationship between F_{C1} and β_1 derived in Appendix V is given by:

$$\frac{F_{C1}}{F} = \frac{D_5}{D_6}\frac{F_P}{F} - \frac{B_8 f_P R_B}{D_6}\frac{F_H}{F} \tag{2.23}$$

where D_5 is dependent on f_B and α

and D_6 is dependent on f_C, f_B, α and β_1.

At a given value of β_1 we thus have the value of F_{C1} from equation 2.17 that will result from radial equilibrium of the forces and the value of F_{C1} from equation 2.23 that is required to overcome the frictional moment in the con rod bearing.

For the sake of clarity the force F_{C1} in equation 2.23 will be referred to as F_{C3} because it has a different functional relationship with β_1 than the value given by F_{C1} in equation 2.17. Equilibrium conditions are obtained when $F_{C3} = F_{C1}$.

Denoting the force F_{C1} in equation 2.23 that is required to rotate the con rod by F_{C3}, the angle β_1 at which equilibrium conditions will be achieved is that which makes the quantity $F_{C3} - F_{C1} = 0$.

This is achieved in the software by calculating F_{C1} and F_{C3} at two arbitrary values

of β_1. These are then used to estimate the value of β_1 that gives $F_{C3} - F_{C1} = 0$ using a straight line approximation (see diagram).

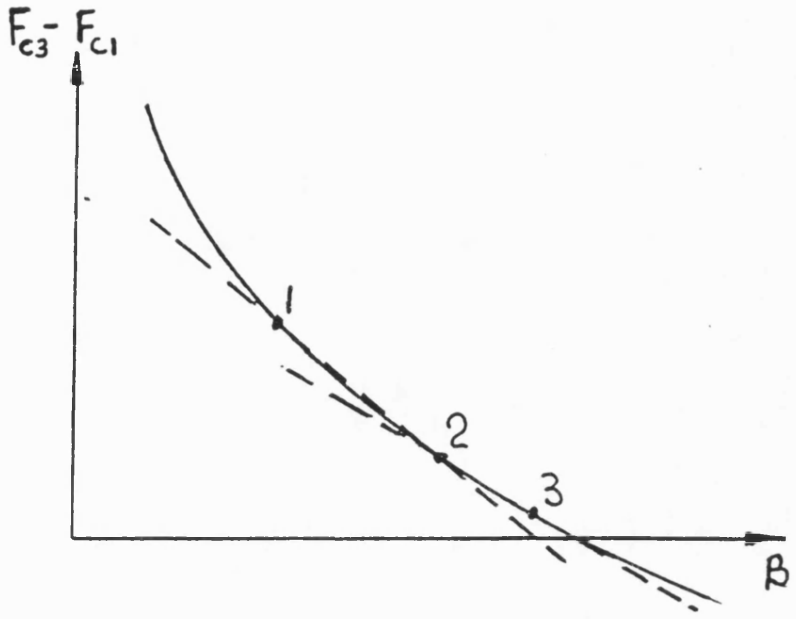

If the actual value of $F_{C3} - F_{C1}$ (point 3) is not zero then its value is used to estimate a further value of β_1 that gives $F_{C3} - F_{C1} = 0$ by taking a straight line from point 2. The procedure, which is a modification of Newtons method, is repeated until $F_{C3} - F_{C1}$ has approached zero within the desired limits of accuracy.

For cases when e_C is less than a certain value, β_1 will lie outside the maximum available range (β_m). The possibility of this situation is tested in the software by initially setting $\beta_1 = \beta_m$. If $F_{C3} - F_{C1}$ is positive then β_1 does not lie in the available range.

The physical interpretation of this situation is that as e_C is reduced the slipper bearing pressure increases as does the bearing pressure force (F_P). At a given value of β_1 this produces a lower value of F_{C1} for radial equilibrium of the forces. The value of F_{C3} does, in fact, increase slightly at a given value of β_1 because of the effect of the increased hydrostatic bearing force acting at the con rod bearing centre. The net result of this is that β_1 has to increase as e_C reduces in order to obtain $F_{C3} - F_{C1} = 0$.

When β_1 does lie outside the available range, the slipper edge will be in contact with the eccentric. The procedure for this situation is to solve the equations of (b) Appendix II using a similar iterative method as that just described.

Having determined the value of β_1 that satisfies the equality of equations 2.17 and 2.23 (ie F_{C3} - F_{C1} = 0) for F_{C1} the values of the remaining variables for the cylinder under consideration can then be calculated.

(b) For $90° \leq \theta \leq 180°$

As θ increases beyond 90° the con rod angle α reduces which reverses the direction of the con rod bearing frictional moment. The slipper contact point now moves to the other side of the cylinder centreline and F_{C1} becomes F_{C2}. This force can be determined by using the same iterative method for the angle β_2 as was used for β_1.

However at θ = 90°, when the con rod changes direction, the effect of clearance between the piston and cylinder needs to be established.

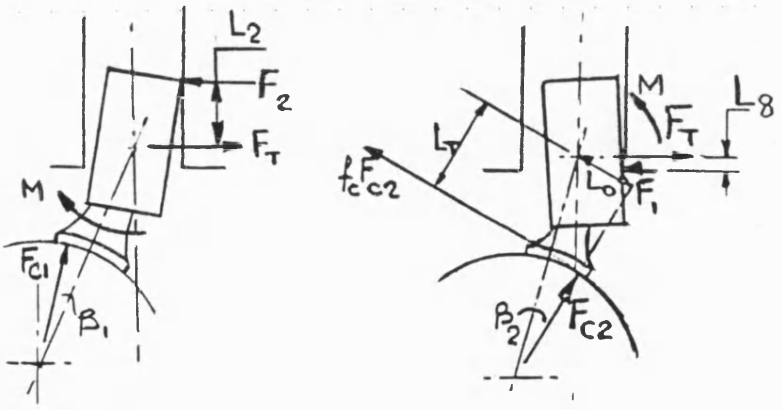

As α is increasing for $\theta < 90°$ the effect of the con rod bearing frictional moment will be to cause the piston to tilt in the bore. Such tilting will happen if the con rod bearing frictional moment $M > F_T L_2$ (see diagram). If $M < F_T L_2$ then the force F_T will be sufficient to maintain the piston against the wall of the cylinder.

At 90°, when M reverses direction, if $M > F_T L_2$, the con rod and the piston will behave as a solid body. The prevailing tilt of the piston will then reduce as α reduces. Here contact is at β_1 with F_{C2} zero. In this situation F_1 will be zero until the piston is flat against the cylinder wall. Now if $M > F_T L_8$, the con rod and piston will

continue to act as a solid body, F_2 becoming zero and the slipper contact moving to β_2 with F_{C1} now zero.

If, following from the condition $M < F_T L_2$, $M < F_T L_8$, the piston will be maintained against the cylinder wall during the whole of the piston stroke.

These changes at 90° were included in the software as a series of IF statements. The presence of this tilting condition and the various combinations of its action are found to be mostly dependent on the value of f_B.

5.9 Motor torque

The torque output at the motor shaft is obtained by summing the torque values for all the cylinders that are under pressure. For a five cylinder machine the torque output is obtained by calculating the respective torques at shaft angles of θ, $\theta + 72°$ and $\theta + 144°$. In the software each set value of θ is incremented by 72° and the individual torques at each angle are added to give the motor shaft torque. When the shaft angle for a given cylinder exceeds 180° relative to its own TDC position, the output torque for that cylinder is set to zero. Thus referring to the diagram below showing con rod angle against θ, the torque from cylinder 3 becomes zero when $\alpha = 0$. Starting the motor shaft angle from zero when cylinder 1 is at TDC, 180° shaft angle in cylinder 3 occurs at a motor shaft angle of 36°.

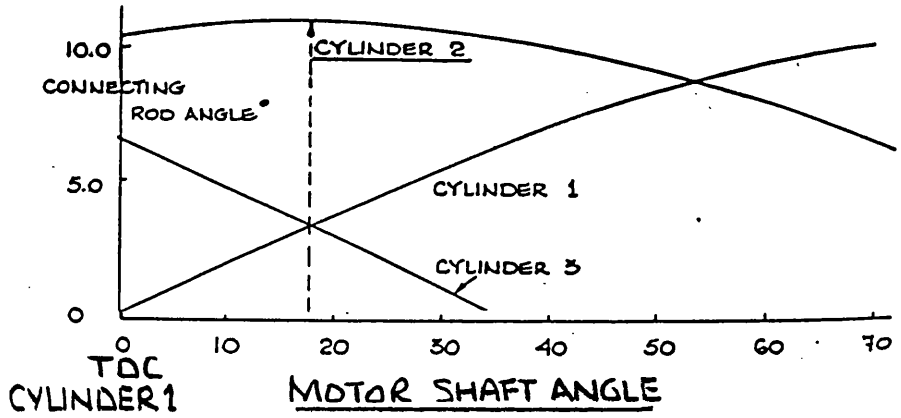

The shaft torque is given by equation 15 Appendix I in which the values of F_{C1} or F_{C2} will be zero depending on the value of θ. Thus, for example, in the range $0 \le \theta \le 90°$, when $F_{C2} = 0$, the non-dimensional shaft torque is:

$$\frac{Q_1}{FR_e} = \frac{F_P}{F}\sin(\theta + \alpha) + \frac{F_{C1}}{F}\sin(\theta + \alpha - \beta_1) - f_C\frac{F_{C1}}{F}\left\{\frac{R_D}{R_e} + \cos(\theta + \alpha - \beta_1)\right\} \quad (2.24)$$

Therefore the motor torque (Q_M) is given by:

$$Q_M = \sum_1^n Q_n \tag{2.25}$$

Now the ideal cylinder torque (Q_I) is given by:

$$\frac{Q_{I1}}{FR_e} = \frac{\sin(\theta + \alpha)}{\cos \alpha} \tag{2.26}$$

$$\therefore \text{ Ideal Motor Torque } (Q_{MI}) = \sum_1^n Q_{In} \tag{2.27}$$

where n denotes the number of cylinders under pressure which is 3 for $0 \leq \theta \leq 36°$ and 2 for $36 \leq \theta \leq 72°$.

$$\text{The mean mechanical efficiency } (\eta_m) = \frac{Q_M}{PD_M} \tag{2.28}$$

where $D_M = \dfrac{5 \times A_P \times 2R_e}{2\pi}$ and $F = PA_P$

so $$PD_M = \frac{5}{\pi} FR_e$$

and $$\eta_m = \frac{\pi}{5} \frac{Q_M}{FR_e} \tag{2.29}$$

$$\text{The instantaneous mechanical efficiency } (\eta_I) = \frac{Q_M}{Q_{MI}} \tag{2.30}$$

$$\text{and the mechanical losses are given by } L_0 = 1 - \eta_I \tag{2.31}$$

A comparison of equations 2.24 with equation 2.26 indicates the way in which the mechanical losses arise. In the ideal motor $F_{C1} = 0$ and $F/F_P = \cos \alpha$. For the motor with friction $F/F_P < \cos \alpha$. The angle of action for F_{C1} is such that the torque component from this force does not make up the torque loss due to the reduction in F_P. As F_{C1} increases so does the frictional loss, but the effect of this reduces with θ because of the reducing radial distance from the shaft centre of the slipper contact point.

6. RESULTS OBTAINED FROM THE MODEL

6.1 Introduction

The motor is designed to operate under a wide range of pressure and speed conditions which result in the frictional mechanisms varying between boundary lubrication to hydrodynamic lubrication together with the effects of squeeze films. The frictional mechanism in the con rod bearing probably contains aspects of all of these effects due to the oscillatory nature of its rotation. As a consequence of this, at any given operating condition the frictional resistance cannot be precisely obtained. As will be shown, when operating at speeds as low as 5 to 10 rev/min hydrodynamic lubrication would seem unlikely to exist. However the bearing shape and the effect of local elastic distortions make it impossible to predict the exact nature of the lubricating mechanism.

In order to gauge the effects of the three main sliding joints and assess the validity of the model, the computational analysis was initially performed using fixed values of the respective coefficients of friction. For the particular motor used in this work the dimensional data is given in Table 1.

6.2 Model results for fixed values of the friction coefficients

As described in 5.9 when one piston is at its top dead centre position (TDC) three pistons are under pressure for the first 36°. At this angle a piston reaches its innermost bottom dead centre position (BDC) and is subsequently connected to the low pressure (return line) connection at the motor. Thus for subsequent rotation of the shaft to 72° only two pistons are under pressure and following on from 72° the cycle repeats itself. Thus there are a total of nine frictional coefficients having effect from 0° to 36° and six coefficients between 36° and 72°.

As discussed in 5.7, the hydrostatic force from the slipper bearing is sensitive to the values of β_1 and e_C. For a value for e_C of 127 micron, the sensitivity of the motor losses to changes in the friction coefficients f_P, f_C and f_B was investigated. The results of this analysis are shown in Fig 3 at a shaft angle of 35.9° from which it can be seen that changes in f_C and f_B have approximately equal effects on the losses. On the other hand changes in f_P affect the losses by around 25% of those arising from either f_C or f_B.

In order to select values of the friction coefficients for assessment with the model values of the mechanical efficiencies obtained from the tests described in Chapter 3 are used for the purposes of comparison. The measured variation of mechanical efficiency with θ is shown in Fig 4 for a motor speed of 3.4 rev/min. Also shown are the model results for values of f_C and f_P of 0.1 and f_B of 0.13. Using the methods described in 5.9 the mechanical losses for both the measured and model data are shown in Fig 5. Clearly there are important differences between the measured and model results which are probably due to variations in the levels of friction during the rotational cycle of the motor.

However, the model loss values do agree with the measured results at a level to suggest that the values selected for the friction coefficients provide a reasonable basis for sensitivity or comparative analysis to be carried out.

6.2.1 The effect of the friction coefficients on motor performance

The sensitivity of the model to changes in the friction coefficients is shown in Fig 3 at $\theta = 35.9^{o}$. From Fig. 3 it can be seen that there are many combinations of the coefficient values that produce the same value of L_o at this angle.

The relationship between f_C and f_B for the values of f_P of 0.10 and 0.15 that give a loss value of 0.114 are shown in Fig. 6. Point A corresponds to the values used for the model results in Fig 5. The model results obtained from the values corresponding to point B on Fig 6 are also shown on Fig 5. It can be seen that the maximum difference in the losses obtained from the two models is 0.005 (or 0.5%). Thus the results from B are approximately a maximum of 5% greater than those from A.

This difference between the results from the fixed coefficient models is small in comparison to the difference between the model and measured results. The way in which the losses vary with θ must therefore be caused by other parameter variations. Whilst not accurately predicting the shape of the loss variation the general accuracy of the fixed coefficient model is sufficiently encouraging to allow its use for sensitivity analysis and an examination of the behaviour of other parameters in the motor.

6.2.2 The effect of e_C on motor performance

As has been described in 5.7, the value of e_C is likely to affect the motor performance. The model results previously described were based on e_C set at 127 micron, a value that experience shows to be not unrealistic.

Fig.5 also shows the results from the model with a value for e_C of 25 micron. The effect of this change can be seen to reduce the losses in the range 0.015 to 0.025 with a much reduced torque step at 18°. This represents a considerable improvement on the motor performance resulting in a 25% reduction in the losses.

However in general terms the change has not significantly altered the shape of the loss variation. The value of e_C is sensitive to the operating pressure due to distortion of the slipper. Although this distortion will cause three dimensional changes in the slipper face curvature, the effect of such distortion will be similar to that obtained by changes in e_C. Under given operating conditions at low speed it is possible that changes in the contact force may also change the distortion of the slipper. This is, however, not likely to be at the level of difference observed between the fixed coefficient model and the measured results in Fig 5.

The predicted effect of e_C on the motor performance is summarised in Fig 7(a) where it can be seen that, over the range considered, at a shaft angle of 35.9° improvements in the mechanical efficiency of nearly 3% can be achieved. The value of the contact force F_{C1}, shown in Fig 7(b), also reduces considerably with a reduction of e_C.

The variation in the contact angle β_1, also shown in Fig 7(b), is seen to reach its maximum possible value of 28° when e_C is 58 micron. For lower values of e_C the slipper contact changes to the mode (b) described in 5.7. It is appropriate at this juncture to examine how conditions in the motor affect the slipper contact angle and the effect that this has on the motor performance.

6.2.3 Slipper contact angle

As described in 5.8 the leakage through the slipper will increase as β increases due to the reduced flow resistance presented in the clearance space. Thus equation 2.17 shows that for equilibrium of the forces F_{C1} must increase with β whereas the force required to overcome the con rod bearing friction obtained from equation 2.23

reduces with β as a result of the increased radius of application about the con rod centre.

The relationship between the values of F_{C1}/F and F_{C3}/F with β from these equations is shown in Fig 8(b) for two different values of e_C. The value of β_1 for equality of the forces is seen to reduce with e_C and the value of F_{C1} to increase. The effect on the ratio of the hydrostatic bearing pocket pressure to supply pressure P_r is shown in Fig 8(a) which indicates the increase in this parameter that is obtained with reduced radial clearance e_C and the reduction in F_{C1}. As described in 5.8 the iterative process used in the software derives the crossover points shown in Fig 8 by using the modified Newton's method.

The value of β will also vary with the friction coefficients and in situations where the predicted value of β exceeds the circumferential length of the slipper (ie when $\beta > \beta_m$) further increases in the slipper flow path area are obtained by the slipper tilting about its edge as described in 5.8. The analytical method used for this condition is described in Appendix II part (b) which is based on the intersection of the two circles formed by the slipper and the eccentric.

As discussed in 6.2.2 the variation of β with e_C as shown in Fig 7 reaches its maximum value for the given condition at e_C = 58 micron. For values of e_C less than 58 micron the equilibrium condition for F_{C1} is obtained using the method just described. Reducing e_C below 58 micron has a relatively small effect on η_m and F_{C1}, because the angle of action of F_{C3} remains unchanged at β_m.

The value of e_C is therefore seen to have an important influence on the motor as a reduction in this parameter increases the efficiency and reduces the slipper contact force. The slipper contact force is an important parameter as it has a strong influence on the life of the slipper face. The temperature rise in the fluid leaking through the slipper will be increased by the friction associated with F_{C1} which, together with the temperature rise associated with the pressure loss in the flow path, could result in the dynamic viscosity being reduced in the slipper space with a resulting reduction in the pocket pressure.

The variation in the contact angle β with θ obtained from the model during the pressure cycle of 180° is shown in Fig 9. The variation in the hydrostatic slipper bearing pressure ratio is also shown in Fig 9 which simply reflects the changes in β.

The associated changes in F_C with θ are shown in Fig 10 which as can be seen, generally increases when θ increases beyond 90°. Following reversal of the con rod at 90°, the contact force changes from F_{C1} to F_{C2} in order to reverse the direction of the moment that it creates about the con rod bearing centre. However, the direction of the moment created by the slipper friction remains in the same direction when θ increases beyond 90°. Thus when $\theta > 90°$ this moment is now additional to that created by the con rod bearing friction which results in F_{C2} being greater than F_{C1}.

At $\theta = 90°$ the variables β, F_C and P_r show discontinuities as the slipper contact position moves from β_1 to β_2. However, as described in 5.8, the presence of clearance between the piston and cylinder can create tilting of the piston in this clearance space during reversal of the con rod at $\theta = 90°$. The effect of this on β_2, F_C and P_r is shown in Figs 9 and 10 for a diametral piston clearance of 75 micron. The conditions which cause tilting of the piston depend to a large extent on the level of friction in the con rod bearing. This will be discussed in the next section.

6.2.4 Piston forces

As described in 5.5, the piston forces derived in Appendix IV are generally affected by the level of friction in the con rod bearing and the position of the inner edge of the piston in relation to the cylinder.

For the values of the friction coefficients used in the model the alignment of the piston in the cylinder varies throughout the pressure cycle. As described in 5.8(b) the piston can be maintained against the cylinder wall if the normal force at the con rod bearing centre $F_T > \frac{M}{L_2}$. This condition was found to occur for shaft angles greater than 60°.

However when $\theta = 90°$ for the piston to be maintained against the cylinder M must be $< F_T L_8$. For the given conditions, $M > F_T L_8$ and as a consequence the con rod and the piston rotate together until the outer edge of the piston contacts the cylinder. During this period $F_2 = 0$. After this point is reached, there is rotation of the con rod bearing under the action of F_{C2} which is resisted by the piston forces F_1 and F_2. For a diametral clearance of 75 micron the angular tilt of the piston is 0.12°. At 90° shaft angle, the shaft has to rotate a further 8° before the con rod has rotated sufficiently to take up the piston diametral clearance.

During rotation of the piston the equations for F_{C1} and F_{C2} developed in appendices IV and V do not apply. The equations for this action are discussed in 6.2.5.

The piston forces obtained from the model for shaft angles either side of the piston clearance region can be seen in Fig 11. The sign convention used here is that forces acting from right to left (see diagrams in 5.8(b)) are taken as positive. Thus as the piston is forced against the cylinder at $\theta = 60^{o}$, the force F_1 changes from negative to positive.

At 62° shaft angle the piston starts to emerge from the cylinder when $X > L_4 - L_1$ as it moves inwards. This does not have an immediate effect as F_2 is providing the resistance to the friction moment in the con rod bearing.

Following the completion of the piston rotation in its clearance with the cylinder, F_1 and F_2 both increase to react against the con rod friction moment which has reversed direction and F_2 has changed sign which reflects this reversal. As the length L_8 is reducing, the consequent reduction in the piston moment arm causes both F_1 and F_2 to increase particularly after L_8 becomes negative at $\theta = 122^{o}$. It can be seen from Fig 11 that the values of F_1/F and F_2/F reach a maximum of 0.34 and 0.25 and at the end of the stroke these are 0.26 and 0.24 respectively.

The model assumes that the friction coefficient f_P has the same value at both points of application of F_1 and F_2. The net friction associated with the piston is therefore dependent on the sum of the magnitudes of F_1 and F_2. Thus, for a value of 0.1 for f_P, and a maximum value of $\frac{F_1 + F_2}{F}$ of 0.56, this represents a loss of the available piston force of 5.6%.

The normal force F_T at the con rod bearing centre increases at $\theta = 90^{o}$ as a result of the shift in the slipper contact force from F_{C1} and F_{C2}. This causes F_1 to increase in the manner shown in Fig 11.

The effect of piston friction is to reduce the force in the con rod. The effect of the increase in the piston forces on the con rod force when $\theta > 90^{o}$ can be seen in Fig 12. This reduction is also reflected in that of F_{C2} in Fig 10.

6.2.5 Equations for the piston rotation region

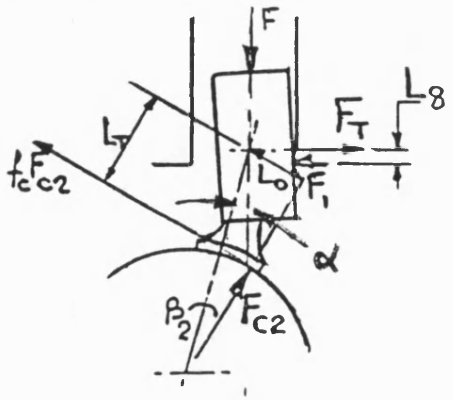

For the situation shown in the diagram during rotation of the piston in its clearance space we have:

$$F_1 = F_T + F_{C2}(\sin(\beta_2 + \alpha) - f_C \cos(\beta_2 + \alpha)) = F_T + A_B F_{C2} \tag{2.32}$$

and $$F_{C2}(L_O - f_C L_T) = F_1 L_8 \tag{2.33}$$

putting $L_O - f_C L_T = A_5$ (as in Appendix V)

Now $$F_T = J_3 F_{C2} + F_P \sin\alpha \text{ from equation 12 Appendix I, because } F_{C1} = 0 \tag{2.34}$$

Thus substitution of F_1 into equation 2.33 gives:

$$F_{C2} = \frac{L_8 F_P \sin\alpha}{A_5 - (J_3 + \sin(\beta_2 + \alpha) - f_C \cos(\beta_2 + \alpha))L_8} \tag{2.35}$$

For equilibrium of the radial forces along the cylinder axis we have:

$$F = F_N + f_P F_1 \tag{2.36}$$

Substituting for F_1 and F_N from equation 9 appendix I into equation 2.36 gives:

$$F = F_P \cos\alpha + J_2 F_{C2} + f_P (J_3 F_{C2} + F_P \sin\alpha + A_B F_{C2})$$

$$\therefore \quad F_{c2} = \frac{F - F_P(\cos\alpha + f_P \sin\alpha)}{J_2 + f_P(J_3 + \sin(\beta_2 + \alpha) - f_C \cos(\beta_2 + \alpha))} \tag{2.37}$$

Now denoting F_{C2} in equation 2.35 by F_{C4} the value of β_2 at which F_{C4} - F_{C2} = 0 can be established by using the modified Newton's method as described in 5.8.

To illustrate the process that arises during rotation of the piston, the way in which F_{C4} and F_{C2} vary with β from equations 2.35 and 2.37 is shown in Fig 13. Also shown are the relationships for F_{C1} and F_{C3} immediately prior to $\theta = 90^{o}$.

Referring to Fig 13, F_{C1} changes from point 1 to F_{C2} at point 2. As the shaft rotates the piston rotates to point 3 when nearly all the piston diametral clearance has been taken up. Because the length L_8 is reducing F_{C2} reduces between 2 and 3. At point 4, F_{C2} has increased to provide the necessary torque on the con rod to rotate the con rod bearing. The changes in F_{C2}, β, and P_r that arise in the piston clearance region are shown in Figs 9 and 10.

In Fig 11 the piston force F_2 is zero during this movement of the piston in its clearance space. F_1 remains relatively constant in this region because the change in F_{C2} is small.

The effect of the piston rotation on the motor mechanical losses is shown in Fig 5 where it is seen to cause a reduction of around 0.011 (1.1%) at a shaft angle of 26° when the piston has ceased to rotate. The reduction in the losses between 18 and 26° generally coincides with that of the measured results.

7.0 THE VARIATION OF THE MOTOR MECHANICAL LOSSES WITH SHAFT ANGLE

7.1 Introduction

The mechanical losses resulting from the piston and slipper friction forces are directly affected by the level of friction in the con rod bearing. The hydrostatic pressure in the slipper bearing varies as a result of changes in β. This provides a level of contact force such that equilibrium of the forces occurs whilst overcoming the frictional moment in the con rod bearing. As was shown in section 4.0 changes in β incur negligible movement of both the eccentric and the con rod.

The way in which the equilibrium value of β arises can be examined by considering what happens if β is, say, less than the equilibrium value. F_{C1} will be less than the value required for rotation of the con rod (F_{C3} in Fig 8). Providing there is sufficient

torque at the motor shaft to allow rotation, the eccentric will rotate a fractional amount without causing rotation of the con rod but allowing it to move inwards a fractional amount. When the eccentric has rotated such that β has increased to the equilibrium value, the con rod will be rotated under the action of F_{C1} (or F_{C2}).

During starting, this process can occur as the shaft and transmission system twist prior to rotation of the load. The influence of transmission stiffness and pressure rise rate on start torque has been examined by various research workers as is discussed in Chapter 3. When the motor is stationary and unpressurised the piston and con rod can be positioned anywhere in the respective clearance bands and the disposition will vary between cylinders. Thus the prevailing value of β will likewise vary prior to start up.

During very slow rotation stick-slip occurs between the sliding components. This can be contributed to by the occurrence of small rotational movements of the eccentric without rotation of the con rod. When the radial clearance e_C is less than 50 micron, the slipper tilts slightly about an edge to generate a sufficient leakage path in order to provide the requisite value of *Pp*. The value of e_C will have a direct effect on the contact conditions between the slipper and the eccentric. As e_C is reduced the contact force will be distributed over a greater length thus reducing the peak stress. It is likely that this situation will be more favourable for lubrication of the contact area which should reduce the onset of the stick-slip process.

For the model conditions Fig 8 shows that β varies between 13° and 17° for one piston work cycle. An examination of slipper faces often shows witness marks at angles of this order. In instances where low mechanical efficiency occurs these marks are often more pronounced at smaller angles from the slipper face centre. Conversely in special tests with con rods having increased thickness of the slipper lands (reported in Chapter 3), no witness marks were present and the mechanical efficiency was high. The improved performance in this case was a result of reduced distortion of the slipper face particularly at the outer four corners and possibly also because the face was manufactured to produce a smaller clearance with the eccentric.

Measurement of slipper curvature, within the levels of tolerance required was found to be virtually impossible because the variations around the arc length with the distance from the centre are less than the accuracy of metrology equipment. For example, the variation in radius over the arc length of 28°, measured from a point

25 micron displaced from the true centre, would be 3 micron. This dimension is of the same order as the limits of roundness. Thus the limit of accuracy for measurement of the radius would be in the region of 100 micron.

7.2 The variation of mechanical losses during the pressure cycle for one cylinder

The way in which the mechanical losses vary with shaft angle reflects all the changes that have been described. Fig 14 shows the ideal and actual torques divided by FR_e and the mechanical losses, being the difference between these two values, are shown in Fig 15 as $\frac{\Delta Q}{FR_e}$. The mean mechanical efficiency η_m from equation 2.29 in 5.9 reflects the changes in the instantaneous displacement of the motor. Thus, for the ideal motor, η_m varies with θ, as shown in Fig 4, with a mean value of unity.

Fig 15 also shows the individual cylinder mechanical losses as a fraction of the ideal torque $\frac{\Delta Q}{Q_I}$ from the cylinder at the given angle and it can be seen that the fractional loss tends to infinity as Q_I tends to zero at low and high shaft angles.

From Appendix I the generalised torque equation gives:

$$\frac{Q}{FR_e} = \frac{F_P}{F}\sin(\theta+\alpha) + \frac{F_{C1}}{F}\sin(\theta+\alpha-\beta) - \frac{f_C F_{C1}}{F}\left(\frac{R_D}{R_e} + \cos(\theta+\alpha-\beta)\right)$$

$$+ \frac{F_{C2}}{F}\sin(\theta+\alpha+\beta) - \frac{f_C F_{C2}}{F}\left(\frac{R_D}{R_e} + \cos(\theta+\alpha+\beta)\right) \quad (2.38)$$

$F_{C1} = 0$ for $\theta > 90°$

$F_{C2} = 0$ for $\theta < 90°$

$$\frac{F_P}{F} = \frac{P_P A_S}{P A_P} = P_R \frac{A_S}{A_P} = f(\beta)$$

Ideal torque given by $\frac{Q_I}{FR_e} = \frac{\sin(\theta+\alpha)}{\cos\alpha}$

The difference between the ideal and actual torque is dependent on the relative values of F_P and F_C, the angle β and the value of the friction coefficient f_C. As has been shown the magnitudes of F_C and β are very dependent on the slipper clearance e_C. However they are also dependent to a lesser degree on the magnitude of f_C which

affects the vector sum of F_P and F_C and, hence, the equilibrium of the forces parallel to the cylinder axis.

The mechanical loss $Q_I - Q$ will therefore depend on the magnitude of F_P and F_C, the angle of action β of F_C and the frictional loss associated with the contact force F_C. These losses are shown separately in Fig 15 as ΔQ_G and ΔQ_F where ΔQ_G will be referred to as a geometric loss component.

At $\theta = 0$ and 180° when $Q_I = 0$ the losses obtained from equation 2.38 are:

$$\theta = 0 \qquad \frac{Q_I - Q}{FR_e} = \frac{F_{C1}}{F}\sin\beta_1 + f_C\frac{F_{C1}}{F}\left(\frac{R_D}{R_e} + \cos\beta_1\right)$$

and $\alpha = 0$.

$$\theta = 180° \qquad \frac{Q_I - Q}{FR_e} = \frac{F_{C2}}{F}\sin\beta_2 + f_C\frac{F_{C2}}{F}\left(\frac{R_D}{R_e} - \cos\beta_2\right)$$

and $\alpha = 0$

For these two shaft positions it is seen from Figs 9 and 10 that F_{C2} and β_2 are both greater than F_{C1} and β_1 which results in the geometric torque loss being greater at 180°. However the reduction in the slipper friction loss between these two positions is such that the overall loss at 180° is slightly less than that at $\theta = 0$. Piston friction acts to reduce the load on the con rod and as the torque is negative at these two positions increased piston friction causes the losses to be reduced.

At $\theta = 90°$ the reversal of the con rod and the bearing frictional moment generally result in increased losses because of the increased piston forces, the increase in β and the reduction in the slipper bearing pressure, as discussed in 6.2.6.

During the period of reverse tilting of the piston, F_{C2} reduces because of the reduced moment on the piston arising from the reducing piston length L_8. This results in the geometric torque loss component remaining approximately constant with a reduction in the friction loss. Once the piston has become fully tilted at $\theta = 98°$ the effect of the con rod bearing frictional moment and the increasing piston forces cause an increase in both loss components. The geometric loss component continues to rise because of the effect of increasing piston friction which affects the slipper bearing by reducing both P_R (and as a consequence F_P) and F_{C2}. The reduction in F_{C2} and the reducing radius of action of $f_C F_{C2}$ about the shaft centre causes the frictional loss to gradually reduce until 180°.

7.3 Motor mechanical losses

The motor mechanical losses, L_O, are the cumulative losses $\sum\Delta Q$, divided by the total ideal motor torque Q_{MI}. The variation of ΔQ with θ, shown in Fig 15, can be used to obtain the value of $\sum\Delta Q$ at any given shaft angle by summing values at 72° intervals (eg at TDC from 0°, 72° and 144°). The total ideal motor torque, Q_{MI}, obtained from equations 2.26 and 2.27, varies with shaft angle in the way shown in Fig.4.

For the particular motor, the maximum torque from one cylinder occurs at 80° (Fig.14) (when the other cylinders are at 8° and 152° respectively). In the region 0° to 18° the variation of $\frac{\sum\Delta Q}{Q_{MI}}$ produces the gradual reduction in the motor mechanical losses shown in Fig.5.

At θ = 18° there is a small increase in loss due to increased piston and slipper losses following reversal of the con rod. However the piston clearance effect limits the loss at this position because there is no rotation in the con rod bearing. As θ increases from 18° the length L_8 is reducing and there is a consequent reduction in the losses because of the reduced moment on the piston about the con rod centre.

From 26° to 36°, the cumulative losses reduce but, because this reduction is slightly less than the reduction in Q_{MI}, the motor mechanical losses increase slightly in this region. At 36°, the motor mechanical loss (corresponding to 36°, 108°, and 180°) reduces due to the depressuriation of the cylinder at 180°. Subsequently, for shaft angles in the region 36° to 72° when only two cylinders are pressurised, despite the variations of ΔQ for these cylinders, the value of L_O remains almost constant.

As a summary, it is seen that the cyclic variations of the cylinder and motor losses are of a totally different nature. Despite this difference, changes in the values of parameters, such as e_c and the friction coefficients, have little effect on the shape of the motor loss variation (Fig.5.)

8.0 THE EFFECT OF CHANGES IN THE FRICTION COEFFICIENTS

8.1 Introduction

As discussed in 6.2, the sensitivity of the motor performance to changes in the friction coefficients was obtained from the model. This analysis produced the relationship in fig.6 between the friction coefficients for a given level of mechanical losses at $\theta = 35.9^{o}$. The two different sets of values for the coefficients from Fig.6 showed a similar variation in the losses with shaft angle (Fig.4).

The coefficient values of 0.1, 0.1 and 0.13 for f_C, f_P and f_B used in the model were selected so as to match the measured results at $\theta = 18^{o}$ and 36^{o}. As can be seen from Fig 5 the divergence between the theoretical and measured results is at a maximum at shaft angles of 0, 36 and 60^{o}. This probably results from variations in the coefficients during the pressure cycle.

At this point it is useful to determine how different combinations of the friction coefficients taken from Fig 6 affect the variation of the motor parameters with shaft angle and, in particular, the effect on the way in which the losses are distributed in the motor.

8.2 Motor losses

Results from the model are shown in Fig 16 for extreme values for f_C, and f_B where it is seen that reducing f_B and increasing f_C, increases the magnitude of the positive torque step at 18^{o} shaft angle. Conversely, reducing f_C, and increasing f_B reduces the magnitude of the torque step which for $f_B > 0.147$, becomes negative. For $f_B \geq 0.147$ it is seen from Fig 16 that shaft angle movements in the piston clearance region are extended from 8^{o} to 12^{o} following $\theta = 18^{o}$. It is also seen that there is an increase in losses at around 26^{o} shaft angle followed by a reduction before finally increasing when rotation of the con rod begins at around 31^{o}. This change has resulted from the increased level of con rod bearing friction which causes the piston to be inclined in its clearance space with the cylinder throughout the piston stroke.

Thus, at 18^{o} shaft angle, for the cylinder at 90^{o}, $M > F_T L_2$ and the piston remains inclined in the cylinder clearance space. When the con rod angle α has reduced sufficiently to bring the piston against the cylinder wall it will tilt about its lower edge when $M > F_T L_8$.

The trends obtained from the model for the higher values of f_B give improved agreement with the measured results for shaft angles in the region of 15° to 30°. A reduction in the diametral clearance from 75 to 50 micron provides a further improvement to this comparison.

9.0 CONCLUDING REMARKS

This chapter has been concerned with an evaluation of the mathematical model in which constant values of the three friction coefficients have been used. In general terms the model provides a reasonable estimate of the mechanical losses in the motor as compared to measured results at 3.2 rev/min. However, approximately the same results can be obtained from the model with different combinations of the coefficients although some combinations seem to provide more realistic results than others in particular ranges of the shaft rotational cycle.

It is clear from the analysis presented in this chapter that because of the motor geometry, the frictional coefficients will not be constant but will vary individually for a number of reasons. The simulation results shown in Fig 5 demonstrate that the deviation from the measured results can be associated with events in the cycle where changing conditions in the sliding faces will produce significant changes in their frictional characteristics.

The nature of the frictional mechanisms needs to be examined in order to gain an understanding of these frictional losses and how they are to be expressed mathematically. As the speed of the motor is increased the sliding faces will experience improved lubrication. For the con rod bearing this is particularly important because hydrodynamic lubrication will cause a reduction in the frictional losses when compared to those under conditions of boundary lubrication. This will have a significant effect on the forces imposed on the piston and slipper, and hence, on the motor performance.

TABLE 1

Eccentric Radius R_D	=79.4 mm
Distance between Eccentric and Shaft Centres R_E	=27.4 mm
Piston Diameter D_P	=79.4 mm
Hydrostatic Slipper Feed Restrictor Length L_P	=12.7 mm
Restrictor Diameter d_o	= 0.533 mm
Piston Area A_P	=4948 mm^2
Projected Mean Effective Slipper Area A_S	=5352 mm^2
Mean Width of Slipper (straight side) L_w	=66.3 mm
Length of Slipper Lands w	=8.31 mm
Maximum subtended Angle between the Con Rod Centre and the Slipper Edge β_m	=28^o
Length between Con Rod Centre and outer edge of Piston L_2	=27.94 mm
Length between Con Rod Centre and inner edge of Piston L_1	=26.7 mm
Length between Con Rod Centre and inner edge of cylinder at TDC (Θ=0) L_4	=43.2 mm
Con Rod Bearing Radius R_B	=29.2 mm
Con Rod to Eccentric Centre distance L	=142.9 mm
Con Rod Centre to Slipper Face Length L_R	= 63.5 *mm*

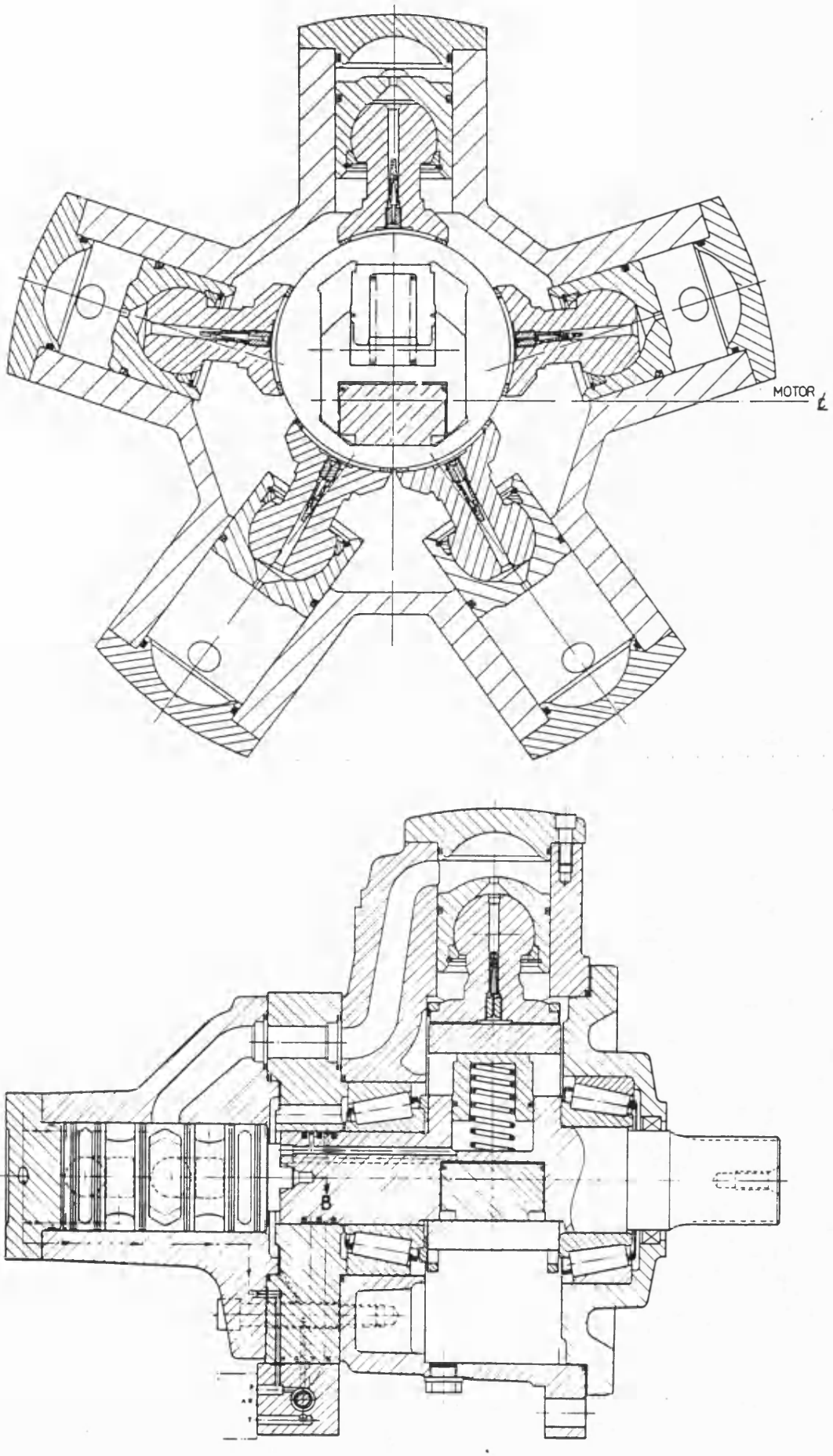

Fig 1 Cross sectional views of the hydraulic motor

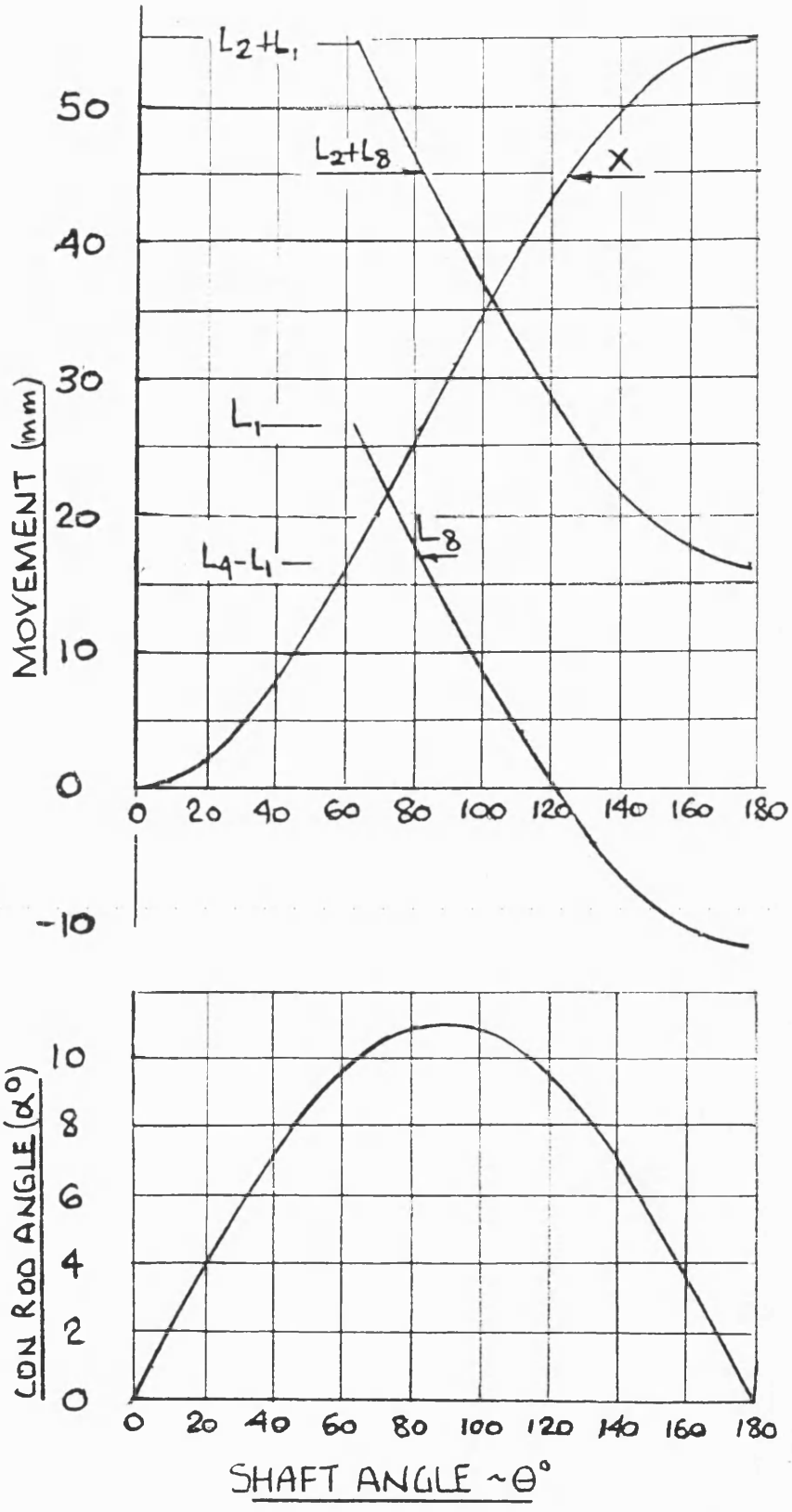

Fig 2 Variation of piston displacement and con rod angle with shaft angle

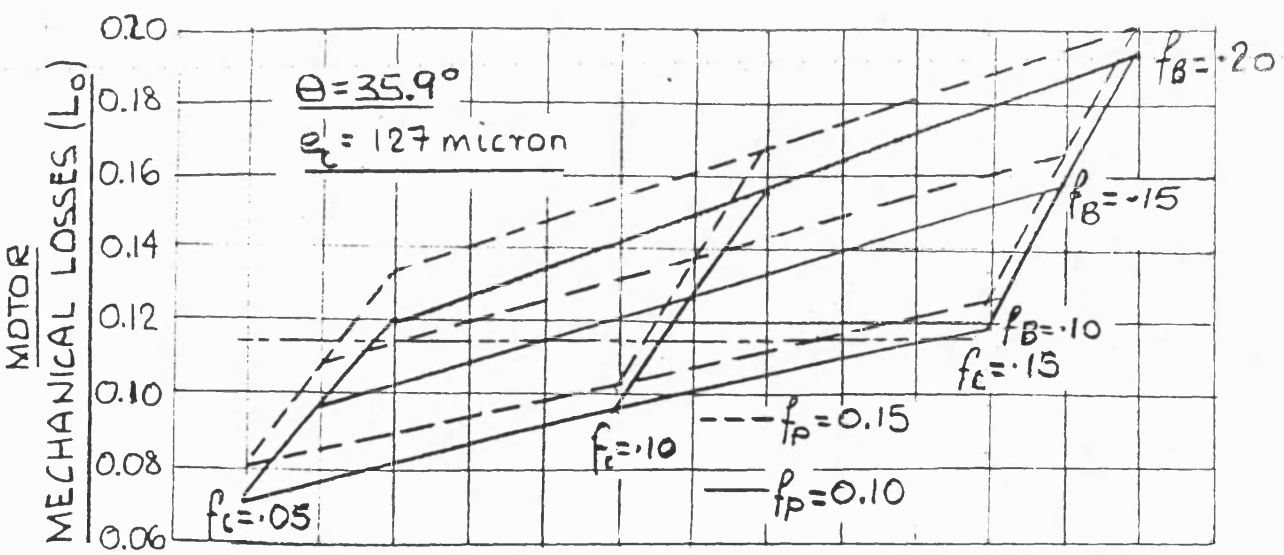

Fig 3 Effect on mechanical losses of changes in the friction coefficients

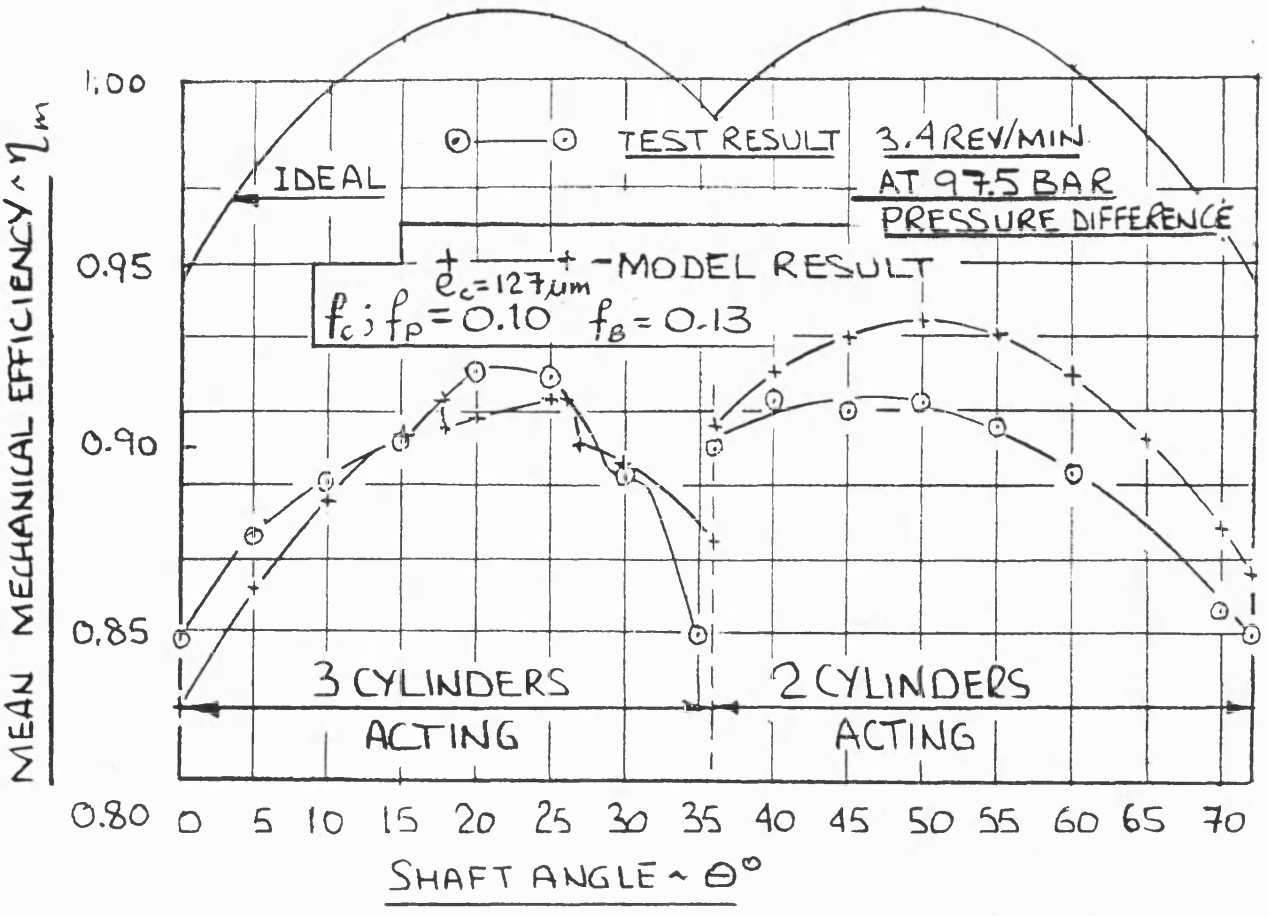

Fig 4 Variation in motor efficiency with shaft angle

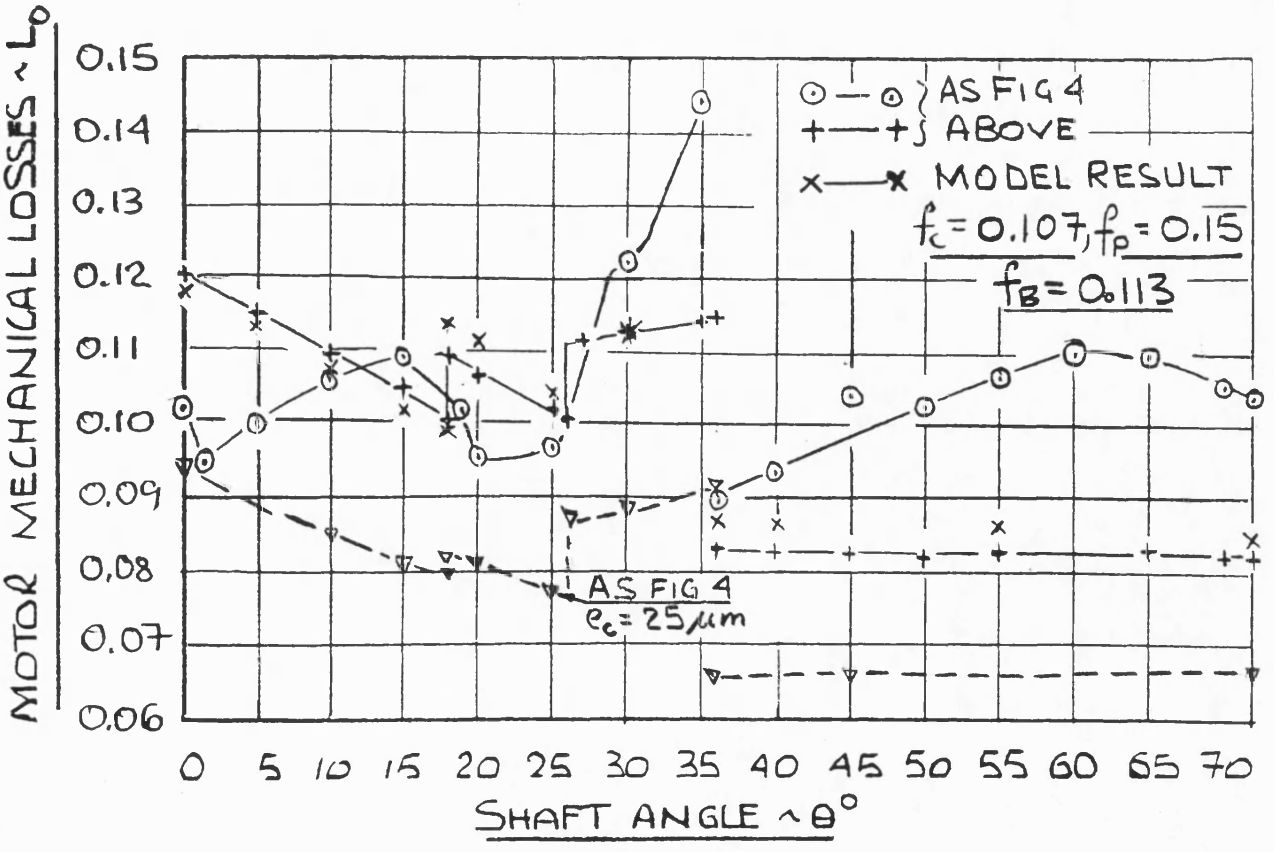

Fig 5 Variation in motor mechanical losses with shaft angle

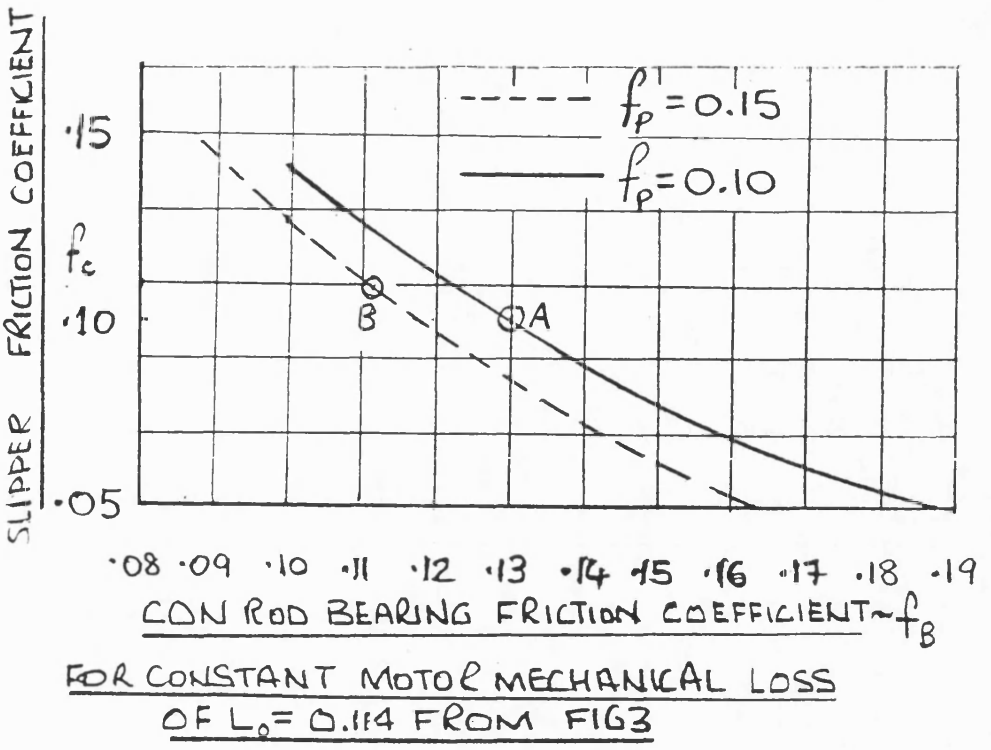

Fig 6 Variation in the friction coefficients for the same level of mechanical losses

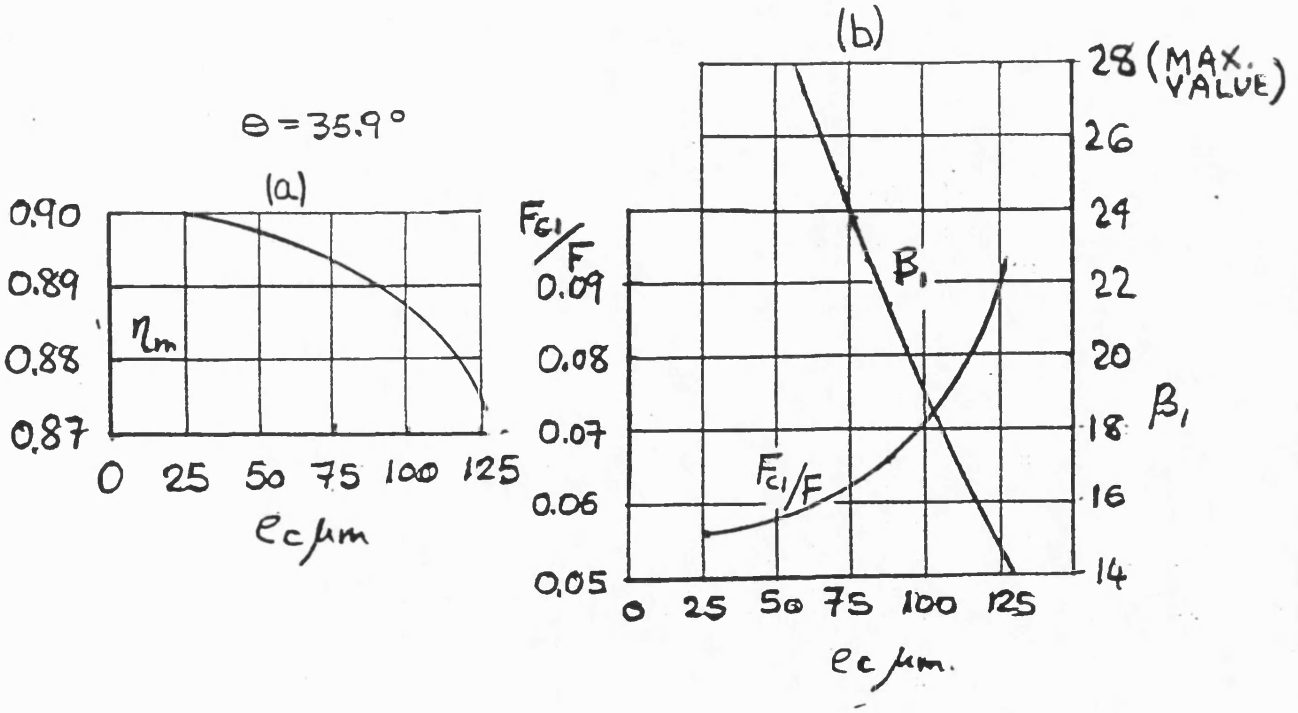

Fig 7 Variation in the motor performance with e_C

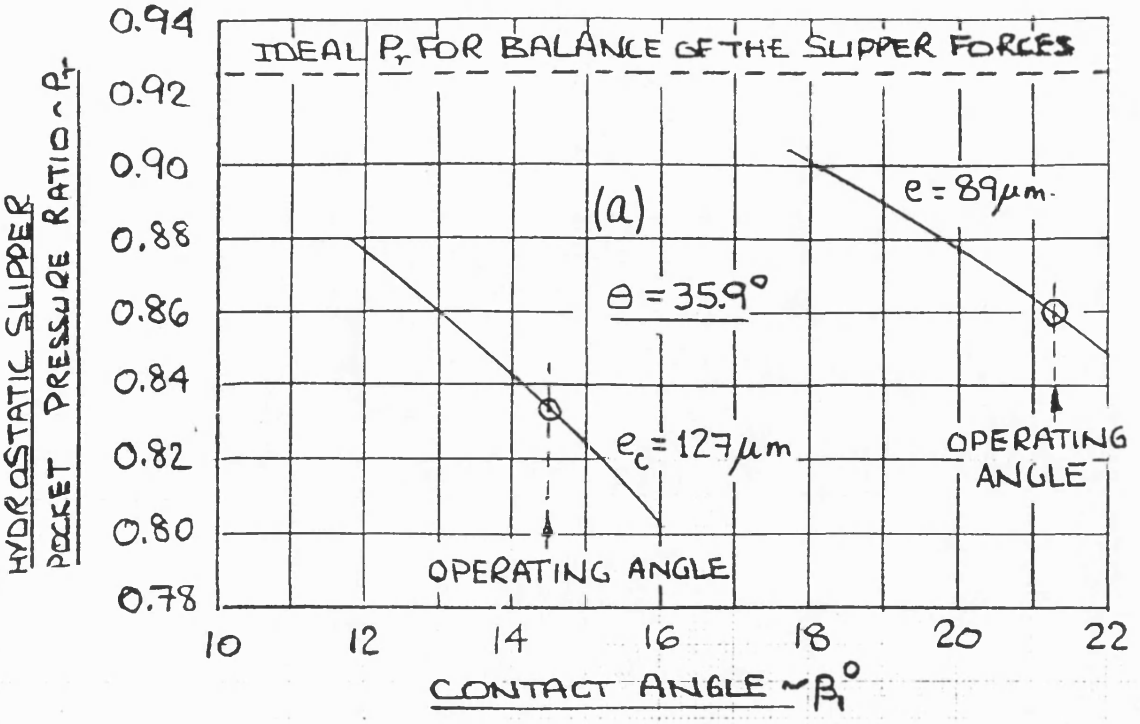

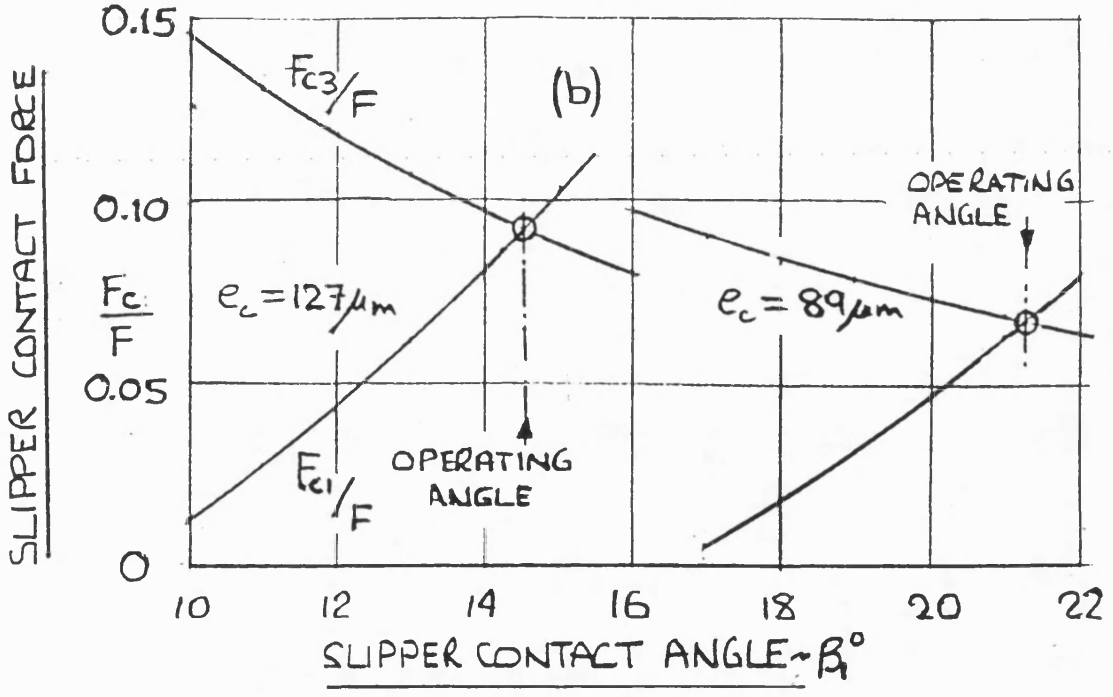

Fig 8 Interaction of the forces to obtain the slipper contact angle

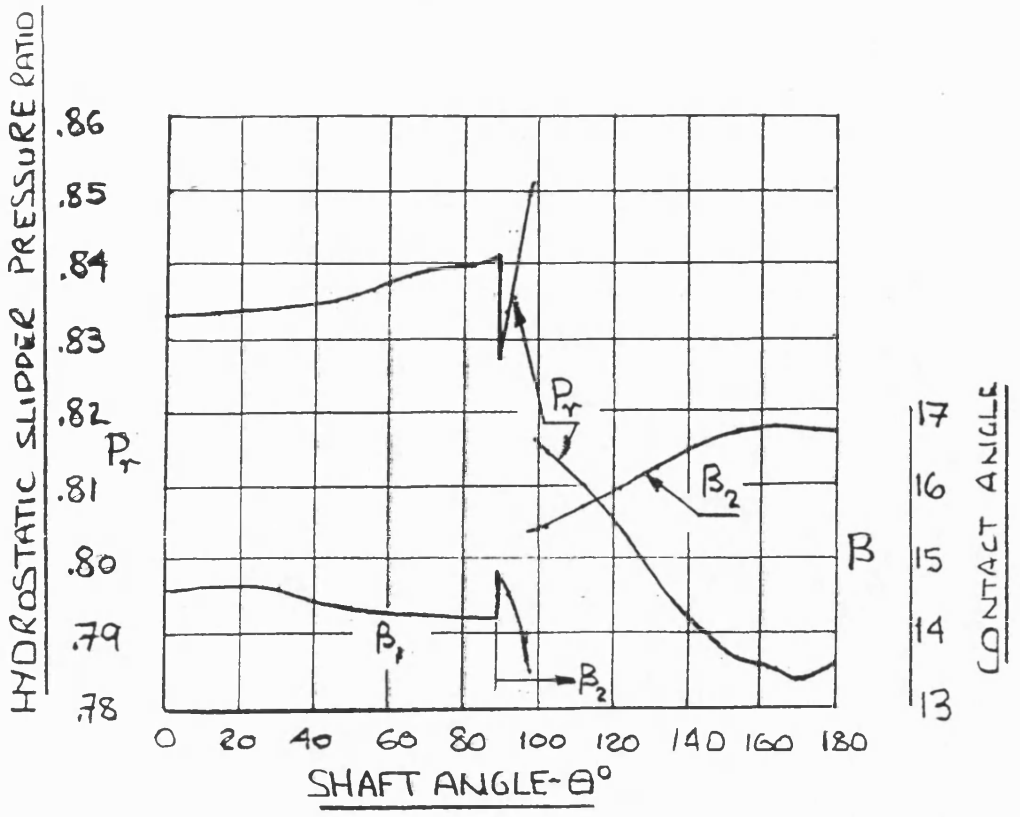

Fig 9 Variation in the contact angle and hydraulic slipper pressure ratio with shaft angle

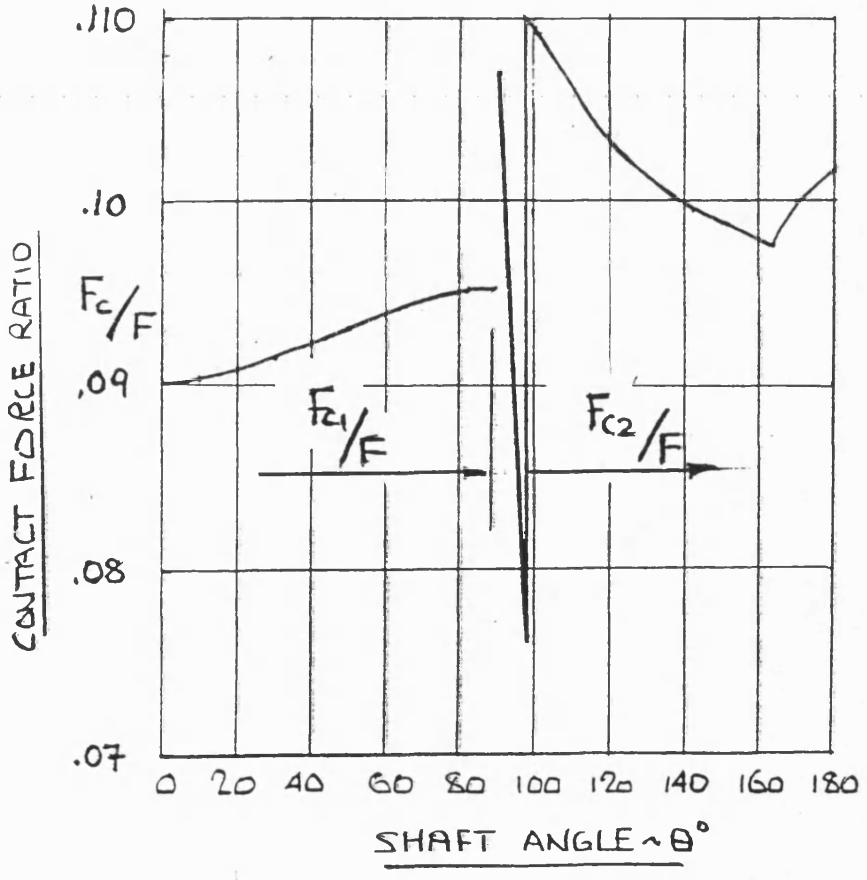

Fig 10 Variation in the slipper contact force with shaft angle

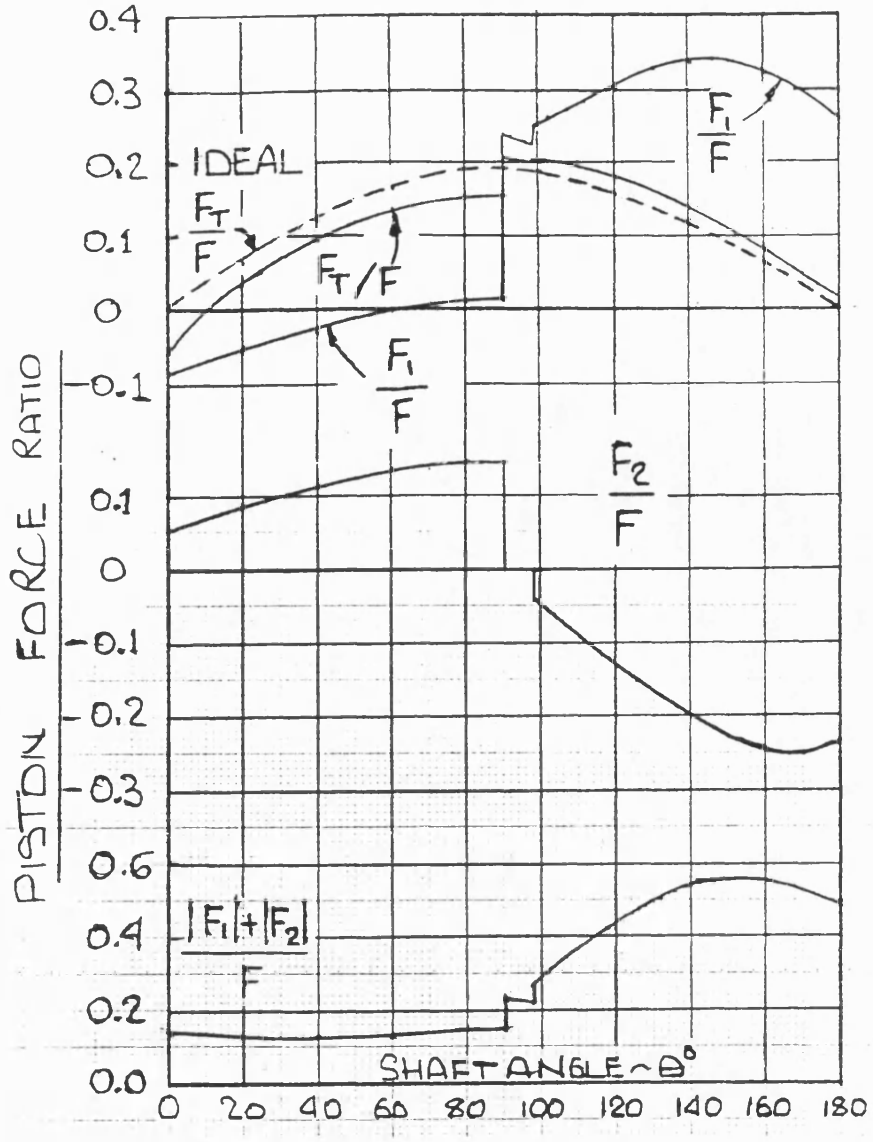

Fig 11 Variation in the piston forces with shaft angle

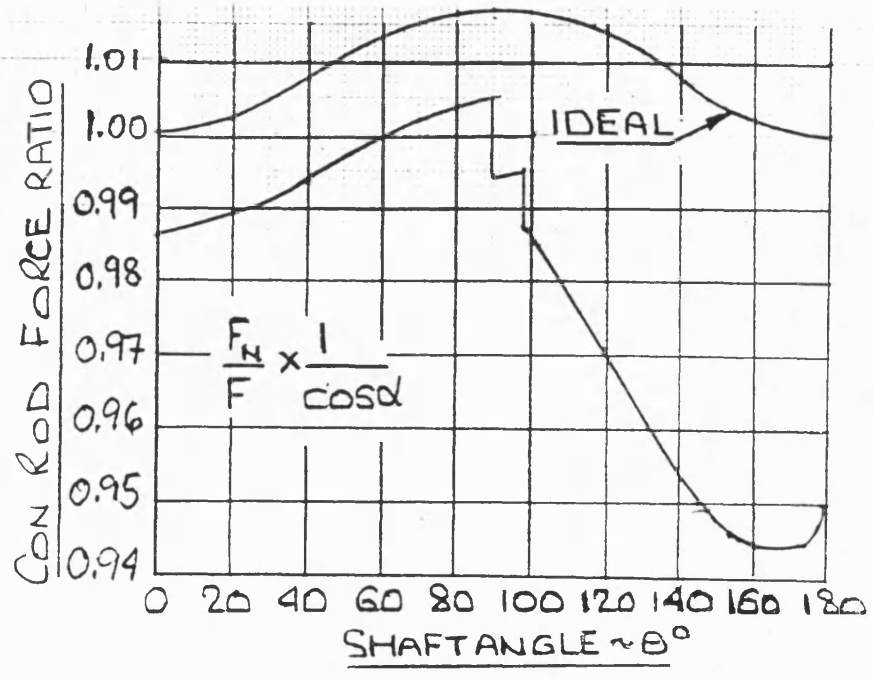

Fig 12 Variation in the force transmitted by the con rod with shaft angle

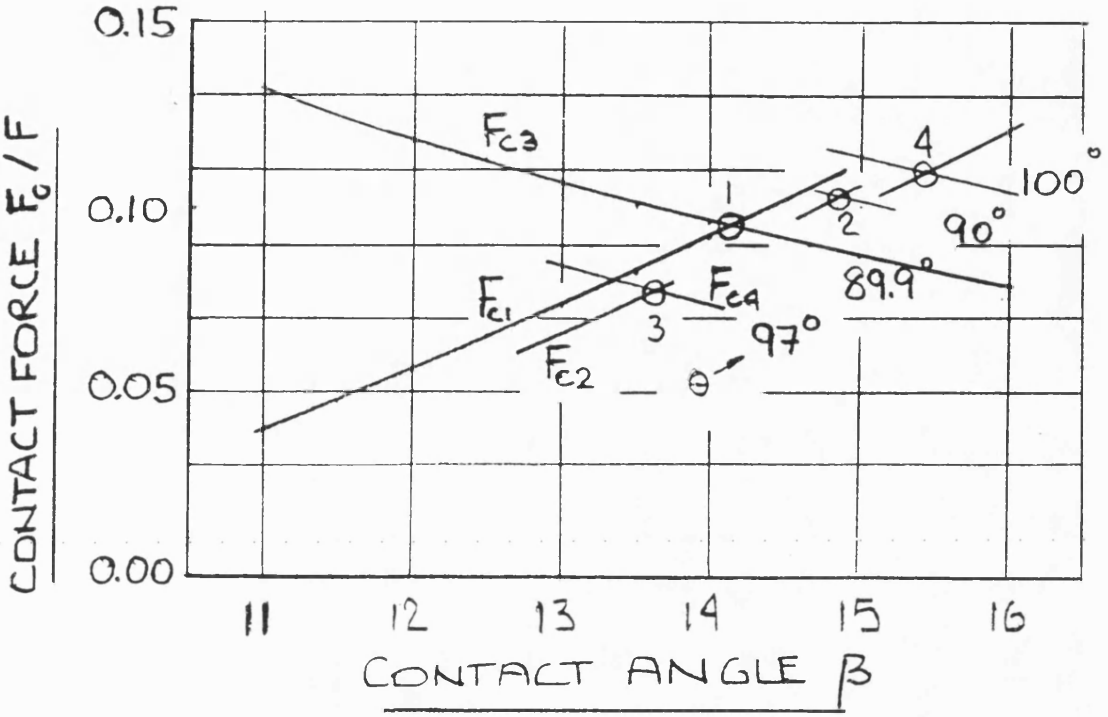

Fig 13 Variation of the contact angle in the region of piston rotation in its clearance space

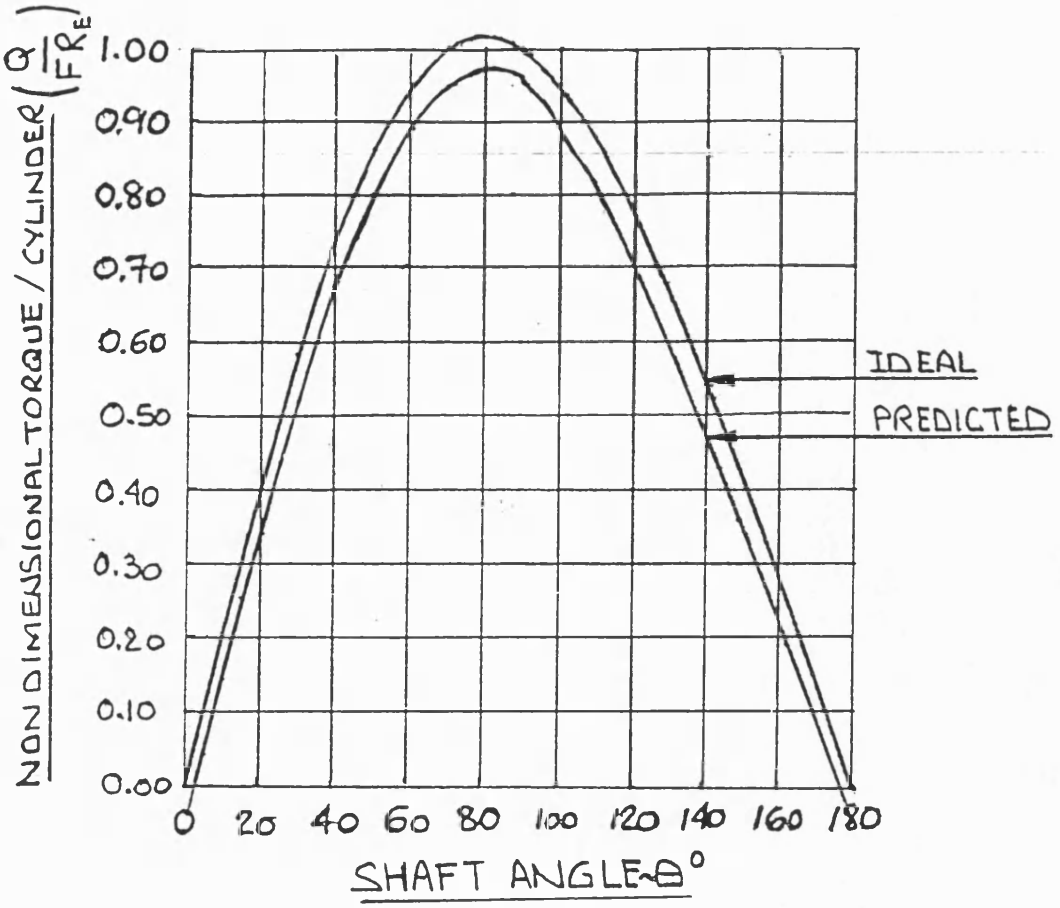

Fig 14 Variation of the ideal and modelled cylinder torque with shaft angle

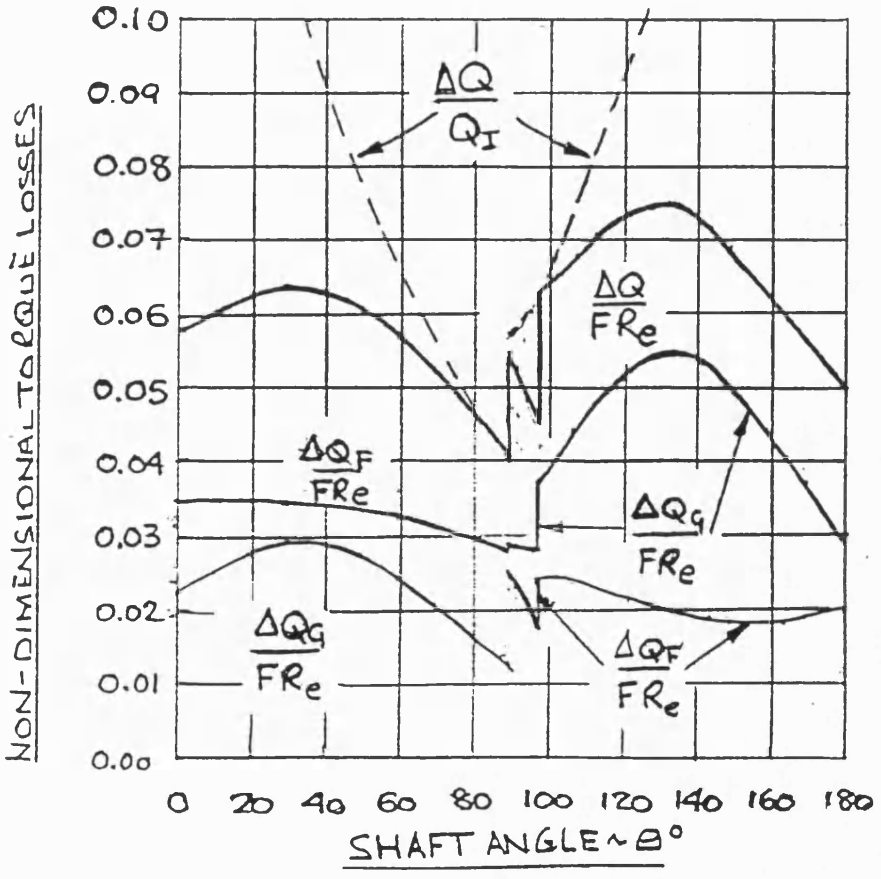

Fig 15 Variation of the cylinder losses with shaft angle

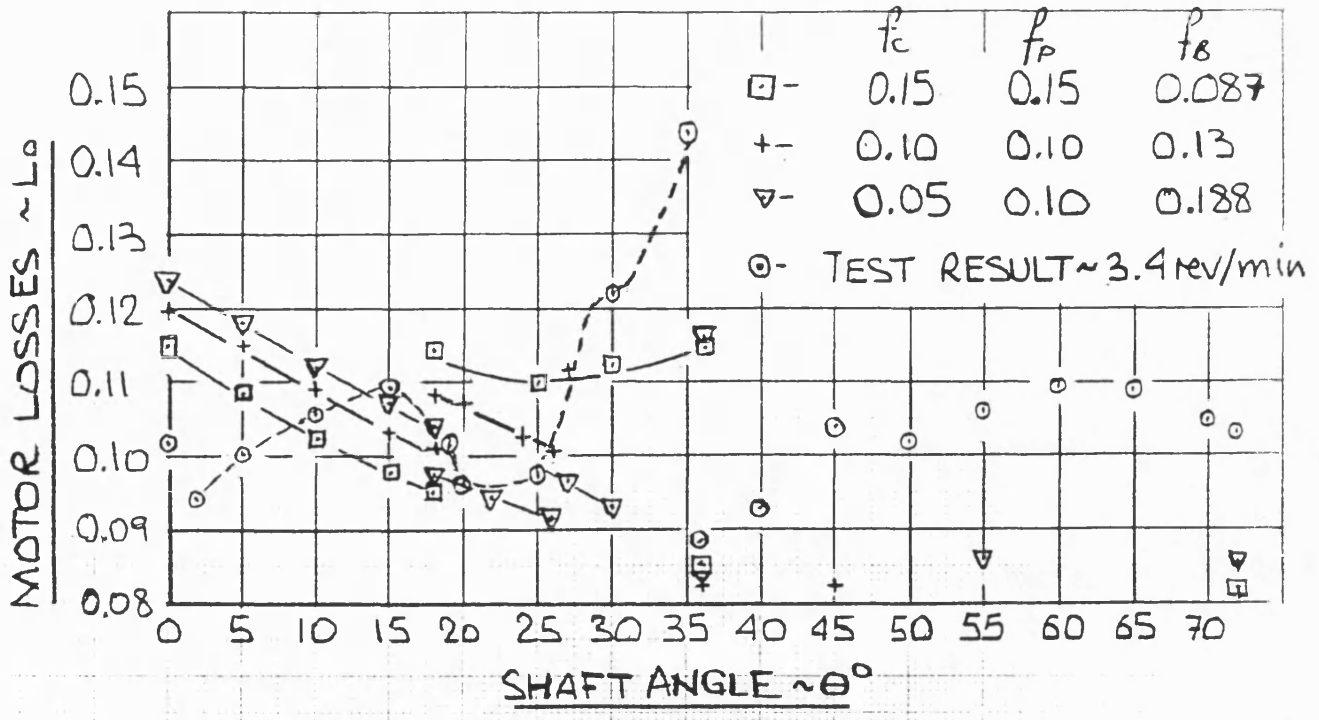

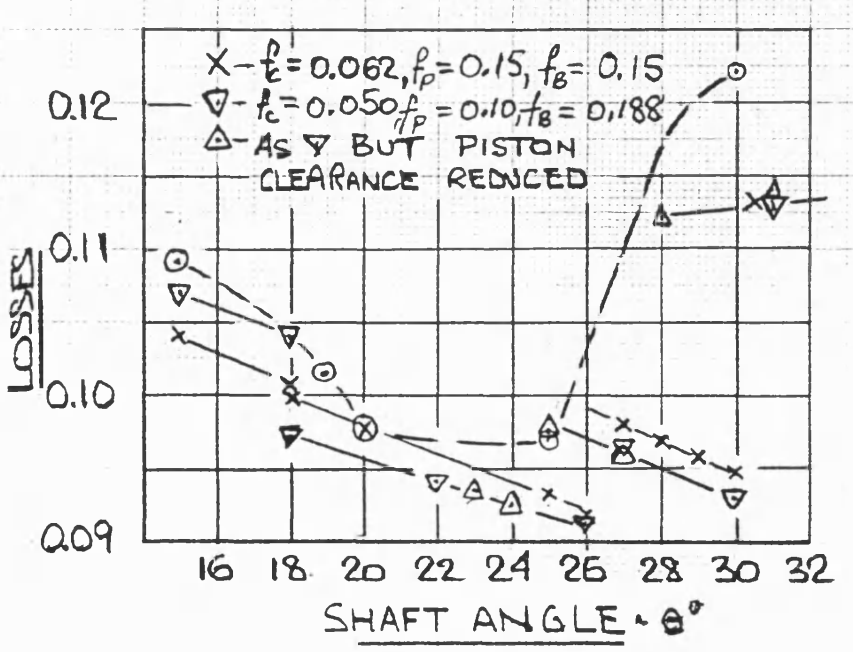

-Fig 16 Effect of the friction coefficients on the motor mechanical losses-

Appendix I

Equations for the slipper and eccentric forces and motor torque

Resolving the forces parallel and perpendicular to the connecting rod axis as shown in Fig 1 produces:

$$F_L = F_P + F_{C1}\cos\beta_1 - f_C F_{C1}\sin\beta_1 + f_C F_{C2}\sin\beta_2 + F_{C2}\cos\beta_2 \quad (1)$$

and $$F_R = F_{C1}\sin\beta_1 + f_C F_{C1}\cos\beta_1 + f_C F_{C2}\cos\beta_2 - F_{C2}\sin\beta_2 \quad (2)$$

Rearranging equations (1) and (2) as follows:

$$F_L = F_P + F_{C1}(\cos\beta_1 - f_C \sin\beta_1) + F_{C2}(\cos\beta_2 + f_C \sin\beta_2)$$

or $$F_L = F_P + AF_{C1} + BF_{C2} \quad (3)$$

where $$A = \cos\beta_1 - f_C \sin\beta_1 \quad (4)$$

$$B = \cos\beta_2 + f_C \sin\beta_2 \quad (5)$$

and $$F_R = F_{C1}(f_C \cos\beta_1 + \sin\beta_1) + F_{C2}(f_C \cos\beta_2 - \sin\beta_2)$$

or $$F_R = CF_{C1} + DF_{C2} \quad (6)$$

where $$C = f_C \cos\beta_1 + \sin\beta_1 \quad (7)$$

$$D = f_C \cos\beta_2 - \sin\beta_2 \quad (8)$$

Finally resolving the forces F_L and F_R parallel and perpendicular to the cylinder axis:

$$F_N = F_L\cos\alpha + F_R\sin\alpha$$

$$= F_P\cos\alpha + F_{C1}(A\cos\alpha + C\sin\alpha) + F_{C2}(B\cos\alpha + D\sin\alpha)$$

$$= F_P\cos\alpha + KF_{C1} + J_2F_{C2} \quad (9)$$

where $$K = A\cos\alpha + C\sin\alpha \quad (10)$$

and $$J_2 = B\cos\alpha + D\sin\alpha \quad (11)$$

also $$F_T = F_L\sin\alpha - F_R\cos\alpha$$

$$= F_P\sin\alpha + F_{C1}(A\sin\alpha - C\cos\alpha) + F_{C2}(B\sin\alpha - D\cos\alpha)$$

$$= F_P\sin\alpha + JF_{C1} + J_3F_{C2} \quad (12)$$

where $$J = A\sin\alpha - C\cos\alpha \quad (13)$$

and $$J_3 = B\sin\alpha - D\cos\alpha \quad (14)$$

The forces acting on the eccentric in relation to the shaft centre which are shown in Fig.2 produce torque from the motor shaft as the following:

$$\text{Torque } Q_1 = F_P R_e \sin(\theta + \alpha) + F_{C1} R_e \sin(\theta + \alpha - \beta_1) + F_{C2} R_e \sin(\theta + \alpha + \beta_2)$$
$$- f_C F_{C1}\{R_D + R_e \cos(\theta + \alpha - \beta_1)\} - f_C F_{C2}\{R_D + R_e \cos(\theta + \alpha + \beta_2)\} \quad (15)$$

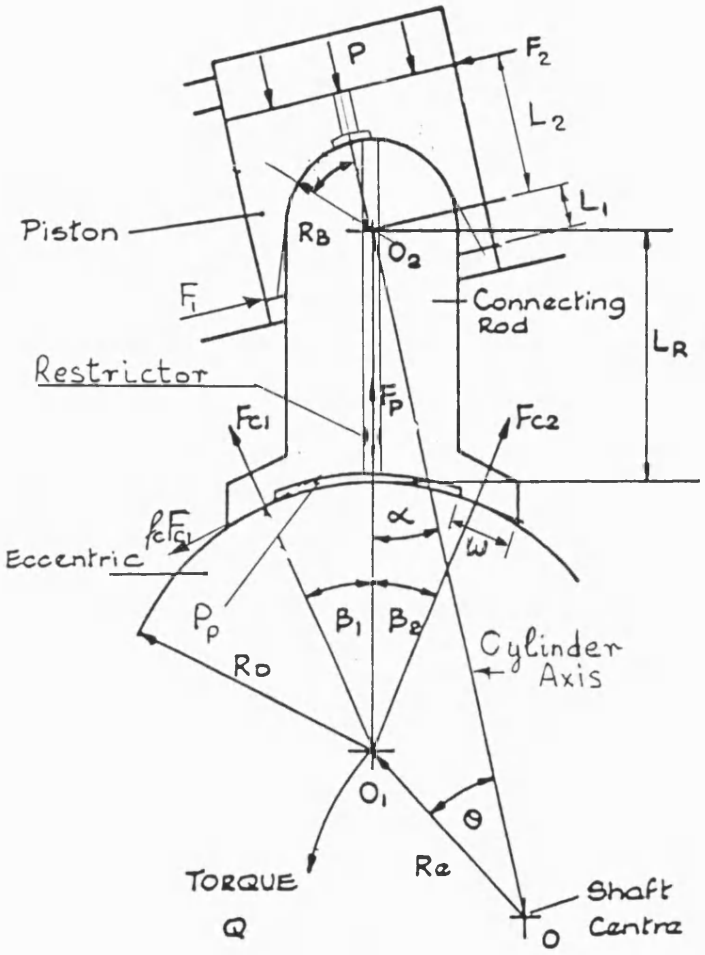

FIG1 CYLINDER CROSS-SECTION

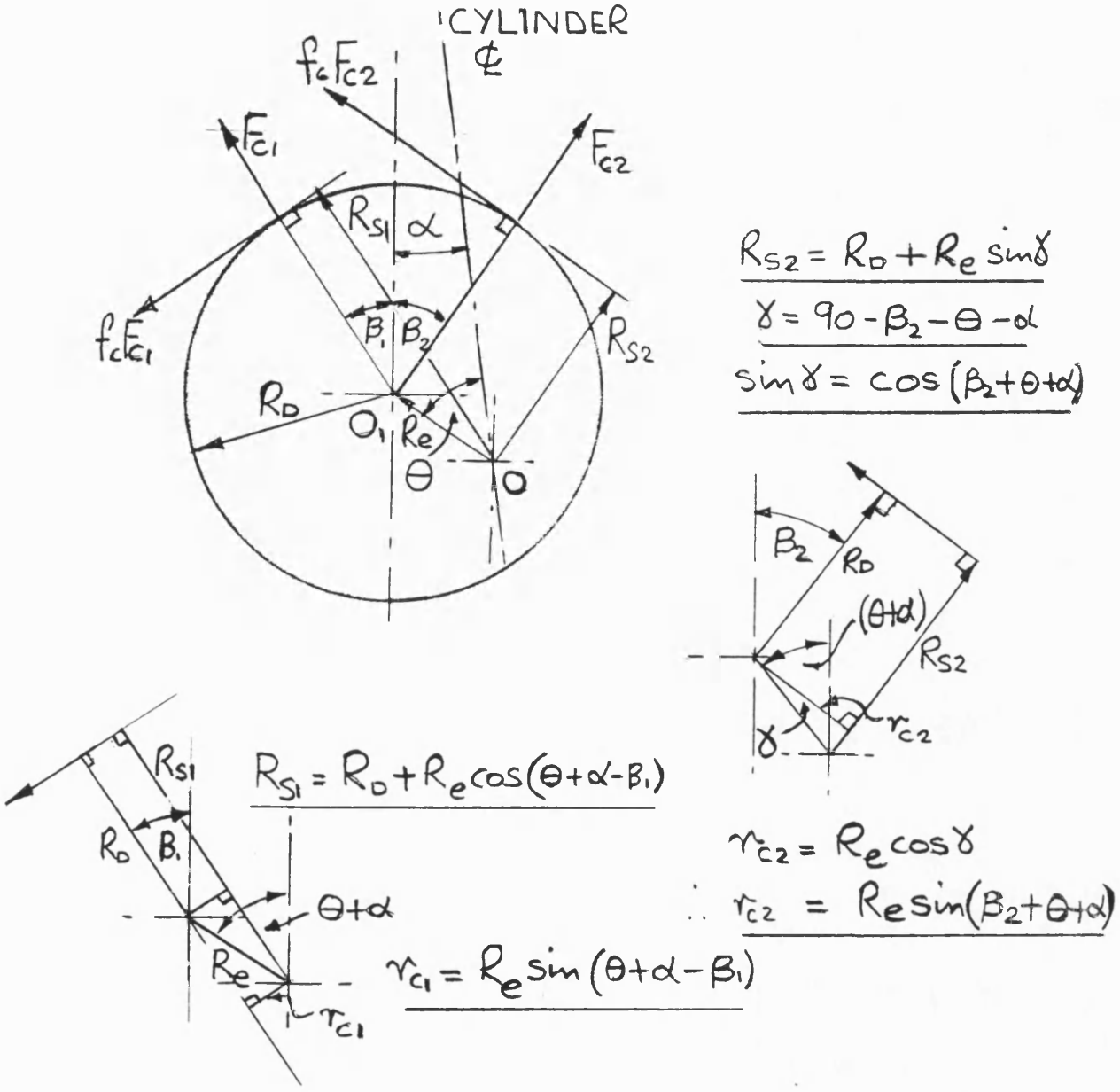

FIG2 MOMENTS ACTING ABOUT THE SHAFT CENTRE

Appendix II

The effect of the slipper contact angle β on the slipper bearing force F_P.

The pressure generated in the hydrostatic slipper is derived from the motor inlet pressure from which flow is supplied to the bearing through a restrictor. This flow then passes to low pressure in the motor casing through the clearance between the slipper face and the surface of the eccentric.

The net leakage area in the clearance space will depend upon the shape of the slipper face in relation to the surface of the eccentric and the angular disposition of the connecting rod centre in relation to the line between the eccentric and connecting rod bearing centres.

Fig.3 depicts this situation for a slipper face that is circular and whose radius is greater than that of the eccentric. Contact between the slipper and the eccentric occurs at the angle β which can be between zero and β_m.

Leakage flow through the slipper clearance

(a) Tangential contact between the slipper and eccentric faces

For small clearances and low values of Reynolds Number the fluid flow (Q_S) across the slipper side lands will be given by:

$$Q_S = \int_0^l \frac{h^3 P_p \, dl}{12 \mu \omega} \tag{16}$$

where $dl = R_D d\beta$, $h = f(\beta)$ and the integration ranges will be between $\beta_1 + \beta_m$ and $\beta_m - \beta_1$ and zero on either side of the contact angle β_1.

Referring to Fig.3 the clearance h is given by:

$$R_S^2 = (R_D + h)^2 + e_C^2 - 2(R_D + h)e_c \cos(180 - \beta)$$

For e_C and h small in relation to R_D and R_S this can be reduced to:

$$R_S^2 = \left(R_D^2 + 2R_D h\right) + 2R_D e_C \cos\beta$$

$$\therefore h = \frac{R_S^2 - R_D^2}{2R_D} - \frac{2R_D e_C \cos\beta}{2R_D}$$

$$= \frac{(R_S + R_D)(R_S - R_D) - 2R_D e_C \cos\beta}{2R_D}$$

$$\approx \frac{2R_D e_C - 2R_D e_C \cos\beta}{2R_D}$$

$$\therefore h = e_C(1 - \cos\beta) \tag{17}$$

Thus the leakage flow of Equation (16) will be given by:-

$$Q_S = \frac{P_P R_D e_C^3}{12 \mu \omega} \int_0^\beta (1 - \cos\beta)^3 d\beta \tag{18}$$

Consider $I = \int_0^{\beta} (1-\cos\beta)^3 d\beta = \int_0^{\beta} (1 - 3\cos\beta + 3\cos^2\beta - \cos^3\beta) d\beta$

where $\cos^3\beta d\beta = \cos\beta(1 - \sin^2\beta)d\beta = \cos\beta d\beta - \sin^2\beta d(\sin\beta)$

$$\therefore \int_o^{\beta} \cos^3\beta d\beta = \sin\beta - \frac{\sin^3\beta}{3}$$

$$\int_o^{\beta} \cos^2\beta d\beta = \left[\tfrac{1}{2}\sin\beta\cos\beta\right] + \frac{\beta}{2}$$

$$\therefore I = \tfrac{5}{2}\beta - 4\sin\beta + \tfrac{3}{2}\sin\beta\cos\beta + \frac{\sin^3\beta}{3} \qquad (19)$$

The values of I for the two integration ranges on the left and right hand sides of the contact line are denoted by:

$$I_R = I \text{ for } (\beta_m + \beta_1)$$

and $$I_L = I \text{ for } (\beta_m - \beta_1)$$

The clearances at each end of the slipper face are given by:

$$h_R = e_c(1 - \cos(\beta_1 + \beta_m))$$

and $$h_L = e_c(1 - \cos(\beta_m - \beta_1))$$

The total slipper leakage will therefore be given by

$$Q_L = \frac{P_P e_c^3}{12\mu\omega}\left\{2R_D(I_R + I_L) + \frac{L_\omega}{e_c^3}(h_R^3 + h_L^3)\right\} \qquad (20)$$

(b) Non-tangential Contact

Non-tangential contact will occur if the clearance has to be increased further when β_1 has increased to β_m. This situation is shown in Fig.4 where the eccentricity e is greater than the difference between the slipper face and eccentric radii.

$\therefore$ For $e = e_C + e_1$

$$h = \frac{R_S^2 - R_D^2 - 2R_D e\cos\beta}{2R_D}$$

$$\approx \frac{2R_D e_C - 2R_D e\cos\beta}{2R_D}$$

$$\therefore h = e_C - (e_C + e_1)\cos\beta$$

$$= e_C\left(1 - \left(1 + \frac{e_1}{e_C}\right)\cos\beta\right)$$

and putting $\alpha = 1 + \frac{e_1}{e_c}$

gives $h = e_c(1 - \alpha\cos\beta)$ (21)

hence $h^3 = {e_C}^3(1 - 3\alpha\cos\beta + 3\alpha^2\cos^2\beta - \alpha^3\cos^3\beta)$ (22)

Referring to Fig.4 β_S is the angle at which $h = 0$ corresponding to the contact point and this is obtained from equation (21) as:

$$\beta_S = \cos^{-1}(1/\alpha) \quad (23)$$

Thus the side leakage will be given by:

$$Q_S = \frac{P_P {e_C}^3 I}{12\mu\omega}$$

where $I = \int_{\beta_s}^{2\beta_m} (1 - 3\alpha\cos\beta + 3\alpha^2\cos^2\beta - \alpha^3\cos^3)d\beta$

and $I = (2\beta_m - \beta_S)\left(1 + \frac{3}{2}\alpha^2\right) - \alpha(\sin 2\beta_m - \sin\beta_S)(3 + \alpha^2)$

$$+ \tfrac{3}{2}\alpha^2(\sin 2\beta_m \cos 2\beta_m - \sin\beta_S\cos\beta_S) - \frac{\alpha^3}{3}(\sin^3\beta_S - \sin^3 2\beta_m) \quad (24)$$

The total leakage flow will be given by:

$$Q_L = \frac{P_P e_C^3}{12\mu\omega}\left\{2R_D I + L_W\{1 - \alpha\cos(2\beta_m + \beta_S)\}^3\right\} \quad (25)$$

(c) <u>The case of $R_S < R_D$</u>

From Fig. 5 the clearance 'h' from $\Delta O_1 B O_e$ is given by

$$R_S^2 = (R_D + h)^2 + e^2 - 2(R_D + h)e\cos\lambda \quad (26)$$

where $\lambda = b + \beta_m - \beta$

$\therefore$ Neglecting small terms gives:-

$$R_S^2 = R_D^2 + 2hR_D - 2R_D e\cos\lambda$$

$$\therefore h = -\frac{(R_D + R_S)(R_D - R_S)}{2R_D} + e\cos\lambda$$

and for $R_D \approx R_S$ $\quad h = e\cos\lambda - e_R$ (27)

where here $e_R = R_D - R_S = -e_c$ as used for case (a) and (b)

Similarly for $\Delta O_1 A O_C$ and $h = 0$

$$e_1 = \frac{e_R}{\cos \beta_m} \tag{28}$$

Also from Fig.5 for triangle $O_C A O_e$ (for $h = 0$) we have:-

$$R_S^2 = R_S^2 + e_D^2 - 2R_S e_D \cos \rho_m$$

$$\therefore e_D = 2R_S \cos \rho_m \tag{29}$$

and for $e_D << R_S$, $\rho_m \approx 90^o$ (30)

Also for $e_1 << R_D$, $\gamma \approx \rho_m - \beta_m$ (31)

$$\therefore \gamma \approx 90 - \beta_m \tag{32}$$

Now for $\Delta O_1 O_C O_e$ we have:-

$$e \sin b = e_D \sin \gamma = e_D \sin(90 - \beta_m)$$

$$\therefore e \sin b = e_D \cos \beta_m \tag{33}$$

Also $e_1 + e_D \cos \gamma = e \cos b$

$$\therefore e_1 + e_D \sin \beta_m = e \cos b \tag{34}$$

Now $\cos \lambda = \cos(b + \beta_m - \beta)$

$$= \cos \beta (\cos b \cos \beta_m - \sin b \sin \beta_m) + \sin \beta (\sin b \cos \beta_m + \cos b \sin \beta_m) \tag{35}$$

$\therefore$ substituting Equation (33) for sin b and Equation (34) for cos b into Equation (35) we have:

$$e \cos \lambda = e \cos \beta \left(\left(\frac{e_1}{e} + \frac{e_D}{e} \sin \beta_m \right) \cos \beta_m - \frac{e_D}{e} \cos \beta_m \sin \beta_m \right)$$

$$+ e \sin \beta \left(\frac{e_D}{e} \cos^2 \beta_m + \left(\frac{e_1}{e} + \frac{e_D}{e} \sin \beta_m \right) \sin \beta_m \right)$$

$$= e_1 \cos \beta \cos \beta_m + \sin \beta (e_D + e_1 \sin \beta_m)$$

And substituting for e_1 from Equation (28) gives:-

$$h = e \cos \lambda - e_R = e_R (\cos \beta - 1 + \sin \beta (\tan \beta_m + \alpha)) \tag{36}$$

where $\alpha = \frac{e_D}{e_R}$

For $\alpha = 0$

when $\beta = 0$

$$h = 0$$

and when $\beta = 2\beta_m$

$$h = e_R\left(\cos 2\beta_m + \sin 2\beta \frac{\sin \beta_m}{\cos \beta_m} - 1\right)$$

Now: $\cos 2\beta_m = \cos^2 \beta_m - \sin^2 \beta_m$

$$\sin 2\beta_m = 2 \sin \beta_m \cos \beta_m$$

$$\therefore h = 0$$

For $\alpha > 1$

when $\beta = 0$

$$h = 0$$

and when $\beta = 2\beta_m$

$$h = e_R(\cos 2\beta_m + \sin 2\beta_m(\tan \beta_m + \alpha) - 1)$$

$$= 2e_R \alpha \sin \beta_m \cos \beta_m$$

The leakage flow will be dependent on the term $R_D \int_0^{2\beta_m} h^3 d\beta$ where h is given by Equation (36). Writing this as:

$$h = e_R(x + ay + b)$$

where

$x = \cos \beta$
$y = \sin \beta$
$a = \tan \beta_m + \alpha$
$b = -1$

h^3 will therefore be given by:-

$$e_R^3\left(x^3 + 2ax^2y + 3bx^2 + 3a^2y^2x + 6abyx + 2b^2x + a^3y^3 + 3a^2by^2 + 3ab^2y + b^3\right) \quad (37)$$

The leakage is obtained from integrating this equation for 'h^3' as a function of β.

Integration

$$\int_0^{2\beta_m} \cos^3 x dx = \sin \beta_m - \frac{\sin^3 \beta_m}{3}$$

$$2a\int_0^{2\beta_m}\cos^2 x\sin x dx = -\frac{2a}{3}(\cos^3 2\beta_m - 1)$$

$$3b\int_0^{2\beta_m}\cos^2 x dx = -\frac{3}{2}\sin 2\beta_m \cos 2\beta_m - 3\beta_m$$

$$3a^2\int_0^{2\beta_m}\sin^2 x\cos x dx = a^2\sin^3 2\beta_m$$

$$6ab\int_0^{2\beta_m}\sin x\cos x dx = -3a\sin^2 2\beta_m$$

$$2b^2\int_0^{2\beta_m}\cos x dx = 2\sin 2\beta_m$$

$$a^3\int_0^{2\beta_m}\sin^3 x dx = -a^3\left(\frac{\cos^3 2\beta_m}{3} - \cos 2\beta_m + \frac{2}{3}\right)$$

$$3a^2b\int_0^{2\beta_m}\sin^2 x dx = -3a^2\left(\beta_m - \frac{\sin 2\beta_m}{4}\right)$$

$$3ab^2\int_0^{2\beta_m}\sin x dx = 3a(\cos 2\beta_m - 1)$$

$$b^3\int_0^{2\beta_m} dx = -2\beta_m$$

Denoting the integral $\int_0^{2\beta}(x + ay + b)^3 d\beta$ as the above terms by I, the total leakage flow will be:

$$Q_L = \frac{P_P e_R^3}{12\mu\omega}\left(2R_D I + 8L_W(\alpha\sin\beta_m\cos\beta_m)^3\right) \qquad (38)$$

(d) The hydrostatic bearing pressure

The value of the bearing pressure (P_P) is determined by a restrictor that is placed in the bearing supply drilling in the connecting rod. The size of the restrictor (d_O) in relation to the magnitude of the leakage flow (Q_L) is such that the flow through the restrictor will be laminar.

Consequently the relationship between the restrictor pressure drop and the leakage flow will be given by:

$$Q_L = \frac{\pi d_O^4(P - P_P)}{128\mu L_P} \qquad (39)$$

where Q_L is given by equations (20), (25) or (38) depending upon the conditions between the slipper and the eccentric surfaces.

Denoting these equations by $Q_L = \dfrac{f(g)P_P e_C^3}{12\mu\omega}$

where *f(g)* is a function of either β or α depending upon whether the contact mode is that of the type in case (a) or cases (b) and (c) above. Equation (39) then gives:

$$\frac{\pi d_0^4 (P - P_P)}{128\mu L_P} = \frac{P_P e_C^3 f(g)}{12\mu\omega}$$

Thus $$\frac{128 e_C^3 L_P f(g)}{12\pi\omega d_o^4} = K_6 f(g) = \frac{P}{P_P} - 1$$

or $$\frac{P_P}{P} = \frac{1}{1 + K_6 f(g)} \qquad (40)$$

Here it is assumed that the dynamic viscosity (μ) has the same value in the restrictor and in the leakage space between the slipper and eccentric.

(d) The hydrostatic bearing force

For the rectangular type of slipper used in the motor, if the clearance space between the slipper and the eccentric is assumed to be parallel and equal everywhere, the pressure varies proportionally with distance across the slipper lands.

Thus taking the mean projected area of the slipper as A_S the pressure force(F_P) on the slipper acting in the direction along the connecting rod centre line will be given by:

$$F_P = P_P A_S$$

Taking a force balance ratio K_1 based on the piston force F which is given by PA_P, where A_P is the piston area one obtains:

$$F_P = K_1 F = K_1 P A_P$$

Thus $$K_1 = \frac{P_P A_S}{P A_P} \qquad (41)$$

Hence using the value of P_P/P from equation (40) the value of F_P and K_1 can be obtained for different values of the contact angle β.

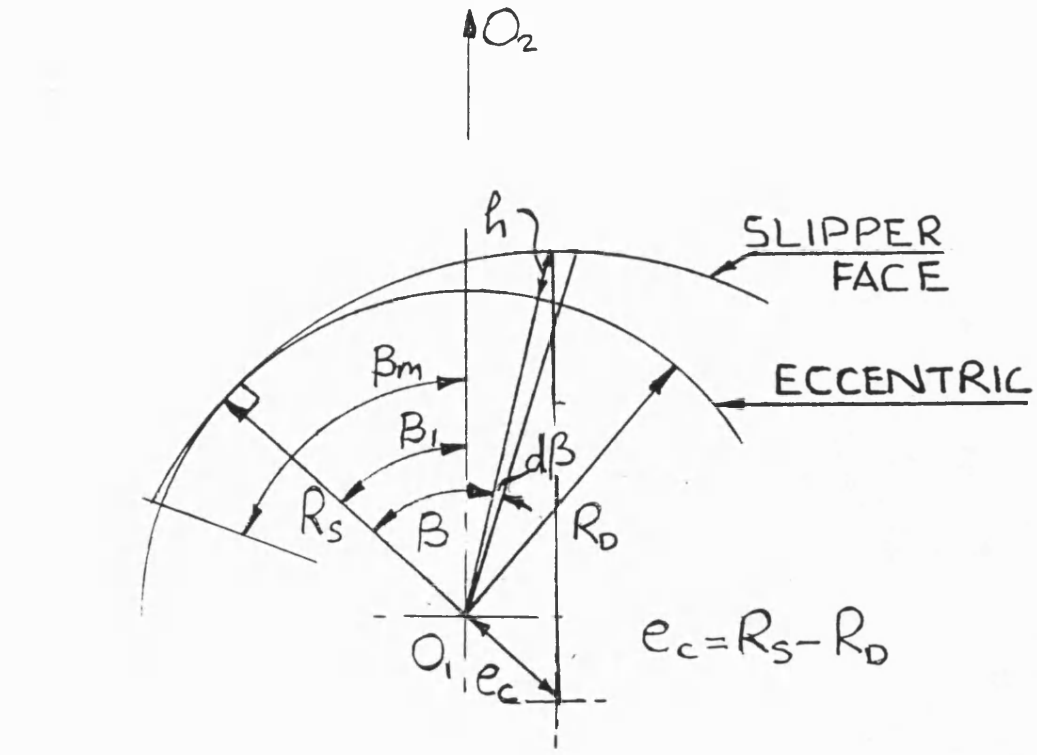

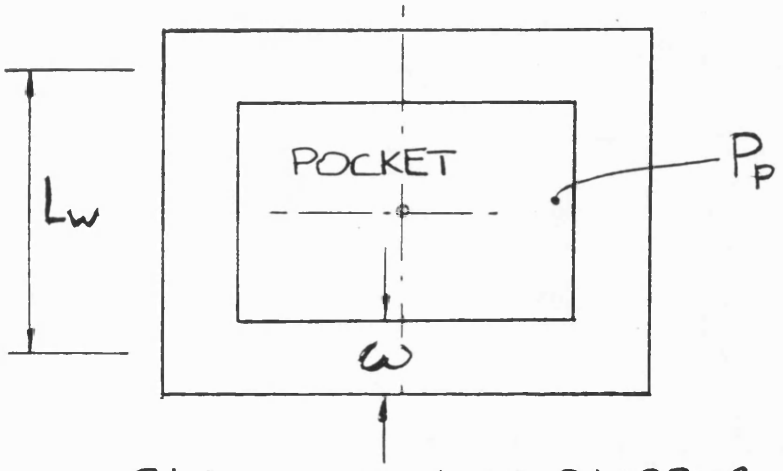

PLAN VIEW OF SLIPPER

FIG 3. SLIPPER CLEARANCE FOR $R_S > R_D$ AND TANGENTIAL CONTACT

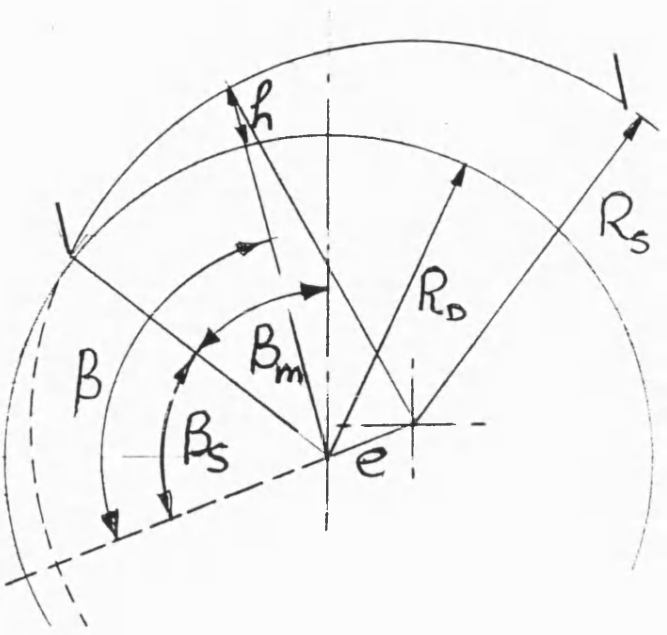

FIG4. NON TANGENTIAL CONTACT OF THE SLIPPER FOR $R_S > R_D$

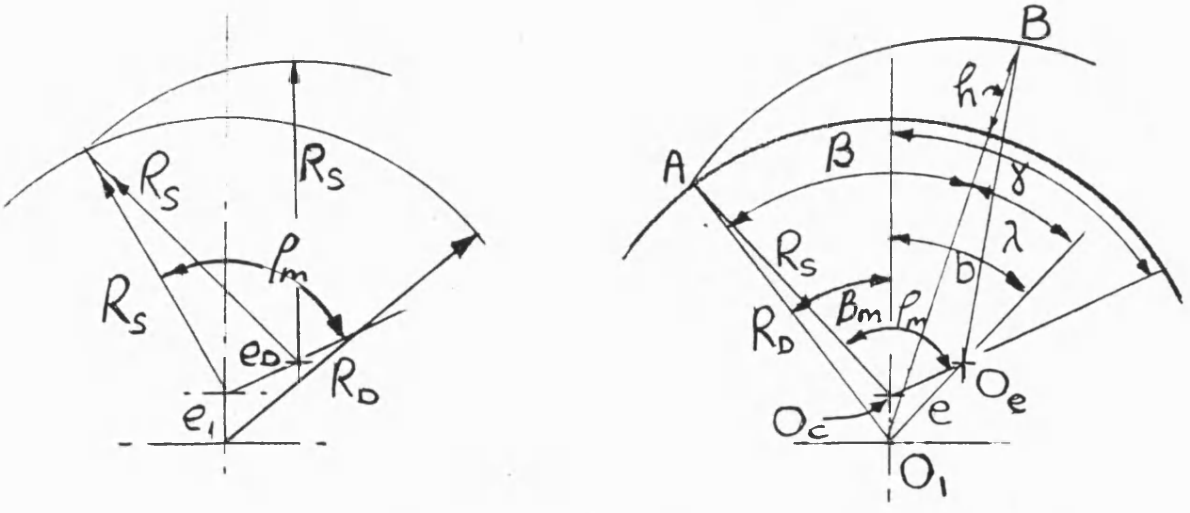

FIG5. SLIPPER CONTACT AND GEOMETRY FOR $R_S < R_D$

Appendix III

Forces acting at the connecting rod bearing

In the particular hydraulic motor under investigation the connecting rod bearing is spherical but in this analysis it is taken as cylindrical. The effect of sphericity will be to modify the frictional forces which will be discussed elsewhere. Here the coefficient of friction is taken as a mean value acting at the full radius of the bearing as shown in Fig.6. The forces F_N and F_T acting at the bearing centre are parallel and perpendicular to the cylinder axis as derived in Appendix I.

(a) For $0 \leq \theta \leq 90^0$ when the connecting rod angle α is increasing.

Resolving Horizontally

Resolving the forces horizontally one obtains:-

$$(F_{B1} - F_{B2})\sin\theta_C - f_B \cos\theta_C(F_{B1} + F_{B2}) = -F_T$$

$$\therefore F_{B1} = \frac{F_{B2}(\sin\theta_C + f_B\cos\theta_C) - F_T}{(\sin\theta_C - f_B\cos\theta_C)} \qquad (42)$$

Resolving Vertically

$$(F_{B1} + F_{B2})\cos\theta_C + f_B \sin\theta_C(F_{B1} - F_{B2}) = F_M$$

Here F_M is given by F_N - F_H

where F_H = Hydrostatic Force = $\pi(R_B \sin\theta_C)^2 P$

$$\therefore F_{B1}(\cos\theta_C + f_B\sin\theta_C) = F_M + F_{B2}(f_B\sin\theta_C - \cos\theta_C)$$

Substituting for F_{B1} from equation (42) gives:

$$(F_{B2}(\sin\theta_C + f_B\cos\theta_C) - F_T)(\cos\theta_C + f_B\sin\theta_C)$$

$$= (F_M + F_{B2}(f_B\sin\theta_C - \cos\theta_C)(\sin\theta_C - f_B\cos\theta_C))$$

$$\therefore F_{B2} = \frac{F_M(\sin\theta_C - f_B\cos\theta_C) + F_T(\cos\theta_C + f_B\sin\theta_C)}{2\left(1 + f_B^2\right)\sin\theta_C\cos\theta_C} \qquad (43)$$

Substituting F_{B2} into equation (42) gives

$$F_{B1} = \frac{F_M\left(\sin^2\theta_C - f_B^2\cos^2\theta_C\right) + F_T\left(f_B - \cos\theta_C\sin\theta_C\left(1 + f_B^2\right)\right)}{2\left(1 + f_B^2\right)\sin\theta_C\cos\theta_C(\sin\theta_C - f_B\cos\theta_C)} \qquad (44)$$

The coefficients in Equations 43 and 44 are replaced by the following:

$$B_2 = \sin\theta_C - f_B\cos\theta_C$$

$$B_3 = \cos\theta_C + f_B\sin\theta_C$$

$$B_4 = 2\left(1 + f_B^2\right)\sin\theta_C\cos\theta_C$$

$$B_5 = \sin^2\theta_C - f_B^2\cos^2\theta_C$$

$$B_6 = f_B - \cos\theta_C \sin\theta_C\left(1 + f_B^2\right)$$

$$B_7 = (B_4 B_2)$$

$$\therefore F_{B1} + F_{B2} = \frac{(B_2B_7 + B_5B_4)F_M + (B_3B_7 + B_6B_4)F_T}{B_4B_7}$$

$$= B_8F_M + B_9F_T \qquad (45)$$

where $B_8 = \dfrac{B_2B_7 + B_5B_4}{B_4B_7}$

and $B_9 = \dfrac{B_3B_7 + B_6B_4}{B_4B_7}$

(b) For $90^0 \le \theta \le 180^0$ when the connecting rod angle α is decreasing as shown in Fig.6.

Resolving horizontally

$$(F_{B2} - F_{B1})\sin\theta_C - f_B\cos\theta_C(F_{B1} + F_{B2}) = F_T$$

$$\therefore F_{B1} = \frac{F_{B2}(\sin\theta_C - f_B\cos\theta_C) - F_T}{(\sin\theta_C + f_B\cos\theta_C)} \qquad (46)$$

Resolving vertically

$$(F_{B1} + F_{B2})\cos\theta_C + f_B\sin\theta_C(F_{B2} - F_{B1}) = F_M$$

$$\therefore F_{B1}(\cos\theta_C - f_B\sin\theta_C) = F_M - F_{B2}(\cos\theta_C f_B \sin\theta_C)$$

Substituting for F_{B1} from Equation (46) gives:

$$(F_{B2}(\sin\theta_C - f_B\cos\theta_C) - F_T)(\cos\theta_C - f_B\sin\theta_C) = (F_M - F_{B2}(\cos\theta_C + f_B\sin\theta_C))(\sin\theta_C + f_B\cos\theta_C)$$

Thus $F_{B2} = \dfrac{F_T(\cos\theta_C - f_B\sin\theta_C) + F_M(\sin\theta_C + f_B\cos\theta_C)}{2\sin\theta_C\cos\theta_C\left(1 + f_B^2\right)}$ (47)

and $F_{B1} = \dfrac{F_M\left(\sin^2\theta_C - f_B^2\cos^2\theta_C\right) - F_T\left(f_B + \cos\theta_C\sin\theta_C\left(1 + f_B^2\right)\right)}{2\sin\theta_C\cos\theta_C(\sin\theta_C f_B + \cos\theta_C)\left(1 + f_B^2\right)}$ (48)

The coefficients in Equations (34) and (35) are replaced by the following:-

$$E_2 = \sin\theta_C + f_B\cos\theta_C$$

$$E_3 = \cos\theta_C - f_B\sin\theta_C$$

$$E_4 = 2\left(1 + f_B^2\right)\sin\theta_C\cos\theta_C$$

$$E_5 = \sin^2\theta_C - f_B^2\cos\theta_C$$

$$E_6 = f_B + \cos\theta_c \sin\theta_c\left(1 + f_B^2\right)$$

$$E_7 = 2\left(1 + f_B^2\right)\sin\theta_C \cos\theta_C E_2$$

$$\therefore F_{B1} + F_{B2} = \frac{(E_2E_7 + E_5E_4)F_M + (E_3E_4 + E_6E_4)F_T}{E_4E_7}$$

$$= E_8F_M + E_9F_T \qquad (49)$$

where $E_8 = \dfrac{E_2E_7 + E_5E_4}{E_4E_7}$

and $E_9 = \dfrac{E_3E_7 - E_6E_4}{E_4E_7}$

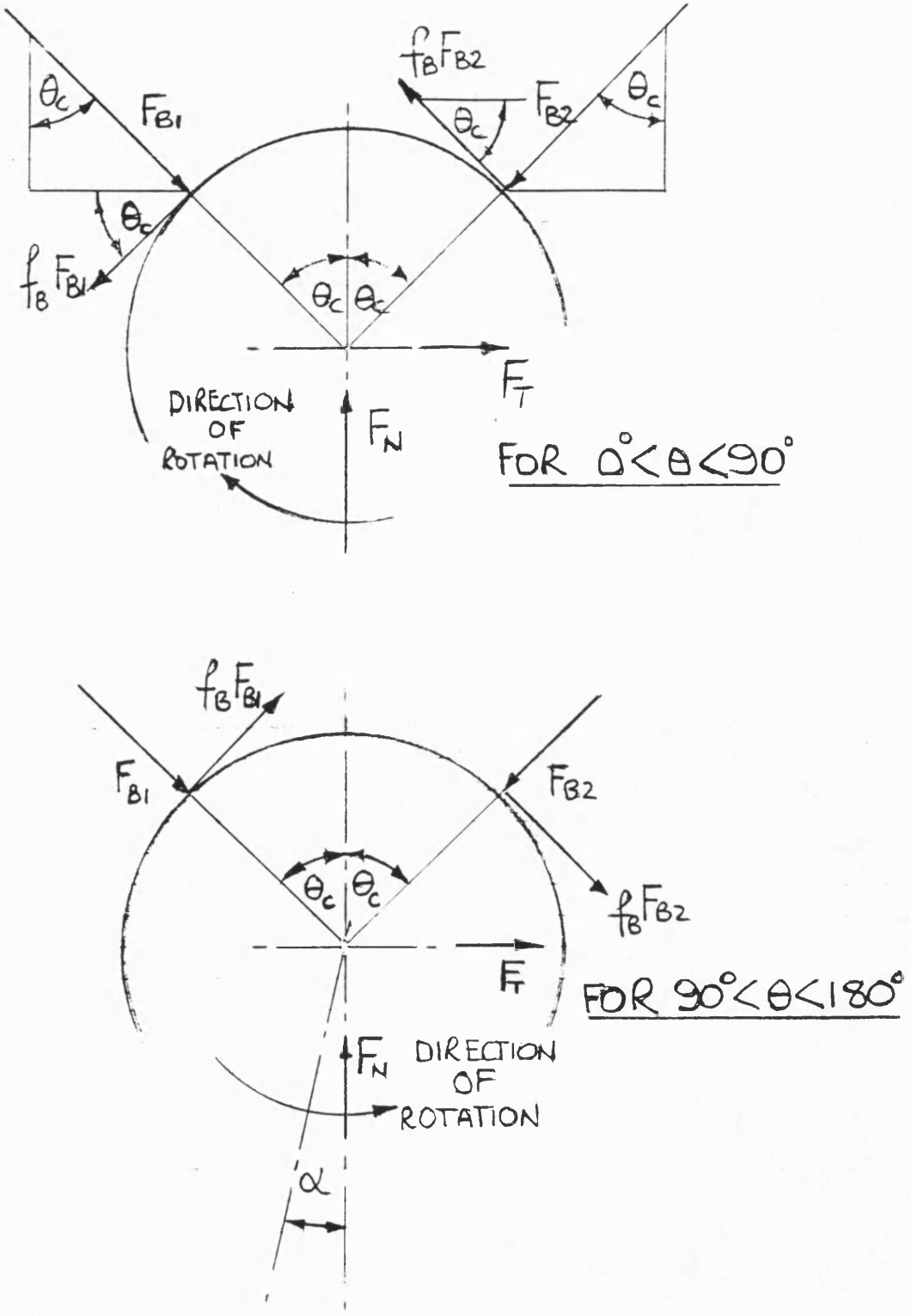

FIG 6 FORCES ON THE CON ROD BEARING

Appendix IV

Forces acting on the piston

The piston transfers the pressure force to the connecting rod and also has to resist the frictional torque from the connecting rod bearing. As shown in Fig.7, the resultant side forces between the piston and cylinder are assumed to act at the top and bottom of the piston and the sum of these forces produce friction between the piston and the cylinder.

(a) For the case of $0 \leq \theta \leq 90^0$

Bearing friction torque

$$\therefore \quad F_1 L_1 + F_2 L_2 = f_B R_B (F_{B1} + F_{B2}) \tag{50}$$

Horizontal forces

$$F_2 - F_1 = F_T$$

Combining these two equations and substituting for $(F_{B1} + F_{B2})$ from Equation (45) yields:

$$F_1(L_1 + L_2) + F_T L_2 = f_B R_B (F_{B1} + F_{B2}) = f_B R_B (B_8 F_M + B_9 F_T)$$

$$\therefore F_1 = \frac{f_B R_B B_8 F_M}{(L_1 + L_2)} + F_T \frac{(f_B R_B B_9 - L_2)}{(L_1 + L_2)} \tag{51}$$

$$\therefore F_1 = D_1 F_M + D_2 F_T \tag{52}$$

$$\text{and } F_2 = F_1 + F_T \tag{53}$$

where $D_1 = \dfrac{f_B R_B B_8}{(L_1 + L_2)}$

and $D_2 = \dfrac{f_B R_B B_9 - L_2}{(L_1 + L_2)}$

Vertical Forces

$$F = F_N + f_P(F_1 + F_2)$$

$$= F_N + f_P(2F_1 + F_T) = F_N + f_P(2D_1 F_M + (2D_2 + 1)F_T)$$

Now $F_M = F_N - F_H$ where F_H = Hydrostatic force on the piston.

$$\therefore F = F_N(1 + 2D_1 f_P) + F_T f_P(2D_2 + 1) - 2D_1 f_P F_H$$

Expressions for F_N and F_T have been derived in Appendix I, Equations (9) and (12). For this analysis F_{C2} is taken as zero for $0 \leq \theta \leq 90^0$ and F_{C1} as zero for $90^0 \leq \theta \leq 180^0$.

Thus substituting equations (9) and (12) into the above equation for F gives:

$$F = (F_P \cos\alpha + KF_{C1})(1 + 2D_1 f_P) + (F_P \sin\alpha + JF_{C1}) f_P (2D_2 + 1) - 2D_1 f_P F_H$$

This, after rearrangement, results in:

$$F_{C1} = \frac{F - F_P(\cos\alpha(1+2D_1f_P) + \sin\alpha f_P(2D_2+1)) + 2D_1f_PF_H}{K(1+2D_1f_P) + Jf_P(2D_2+1)}$$

or $$F_{C1} = \frac{F - F_PD_3 + 2D_1f_PF_H}{D_4} \qquad (54)$$

where $D_3 = \cos\alpha(1 + 2D_1f_P) + \sin\alpha f_P(2D_2 + 1)$

and $D_4 = K(1+2D_1f_P) + Jf_P(2D_2+1)$

As the piston moves down the cylinder from the top dead centre position it eventually emerges from the cylinder so that the position of the force F_1 is at a distance less than L_1 from the bearing centre. Referring to this distance as L_8 equation (50) for the bearing friction torque becomes:

$$F_1L_8 + F_2L_2 = f_BR_B(F_{B1} + F_{B2})$$

and now $$F_1 = \frac{f_BR_BB_8F_M + F_T(f_BR_BB_9 - L_2)}{(L_2 + L_8)}$$

$$\therefore F_1 = D_1F_M + D_2F_T \qquad (55)$$

where: $D_1 = \frac{f_BR_BB_8}{(L_2 + L_8)}$

and $D_2 = \frac{f_BR_BB_9 - L_2}{(L_2 + L_8)}$

This condition will occur when $X > L_4 - L_1$ and $L_8 = L_4 - X$

(b) <u>For the case of $90^0 \le \theta \le 180^0$</u>

At 90°shaft angle the bearing friction torque changes direction (see Fig.8.) and so the horizontal forces give:

$$F_1 - F_2 = F_T$$

<u>Bearing Friction Torque</u>

$$F_1L_8 + F_2L_2 = f_BR_B(F_{B1} + F_{B2}) \qquad (56)$$

Substituting for F_1 from the above and $(F_{B1} + F_{B2})$ from Equation (49) into Equation (56) produces:

$$F_2 = \frac{F_ME_8f_BR_B}{(L_8 + L_2)} + \frac{F_T(f_BR_BE_9 - L_8)}{(L_8 + L_2)}$$

$$= G_1F_M + G_2F_T \qquad (57)$$

where: $G_1 = \frac{f_BR_BE_8}{(L_8 + L_2)}$

and $$G_2 = \frac{f_B R_B E_9 - L_8}{(L_8 + L_2)}$$

For the case when $L_8 < 0$ as in Fig.8 put $L_8 = X - L_4$

$$F_2 L_2 - F_1 L_8 = f_B R_B (F_{B1} + F_{B2})$$

Substituting, as before, for F_1 and $(F_{B1} + F_{B2})$ gives

$$F_2 = \frac{f_B R_B E_8 F_M}{(L_2 - L_8)} + \frac{(f_B R_B E_9 + L_8) F_T}{(L_2 - L_8)}$$

$$\therefore F_2 = G_1 F_M + G_2 F_T \qquad (58)$$

where $$G_1 = \frac{f_B R_B E_8}{(L_2 - L_8)}$$

$$G_2 = \frac{f_B R_B E_9 + L_8}{(L_2 - L_8)}$$

Vertical Forces

$$F = F_N + f_P (F_1 + F_2) = F_N + f_P (2F_2 + F_T)$$

$$= F_N + f_P (2G_1 F_M + 2G_2 F_T + F_T)$$

Now $F_M = F_N - F_H$ as before

and $$\therefore F = F_N (1 + 2G_1 f_P) + F_T f_P (1 + 2G_2) - 2G_1 f_P F_H \qquad (59)$$

Assuming for this case $F_{C1} = 0$, F_N and F_T are obtained from Equations (9) and (12) which substituting into Equation (59) produces:

$$F = (F_P \cos\alpha + J_2 F_{C2})(1 + 2G_1 f_P) + (F_P \sin\alpha + J_3 F_{C2})(1 + 2G_2) f_P - 2G_1 f_P F_H$$

After rearrangement this results in:-

$$F_{C2} = \frac{F - F_P (\cos\alpha (1 + 2G_1 f_P) + \sin\alpha f_P (1 + 2G_2)) + 2G_1 f_P F_H}{J_2 (1 + 2G_1 f_P) + J_3 (1 + 2G_2) f_P}$$

or $$F_{C2} = \frac{F - F_P H_3 + 2G_1 f_P F_H}{H_4} \qquad (60)$$

where $$H_3 = \cos\alpha (1 + 2G_1 f_P) + \sin f_P (1 + 2G_2)$$

$$H_4 = J_2 (1 + 2G_1 f_P) + J_3 (1 + 2G_2) f_P$$

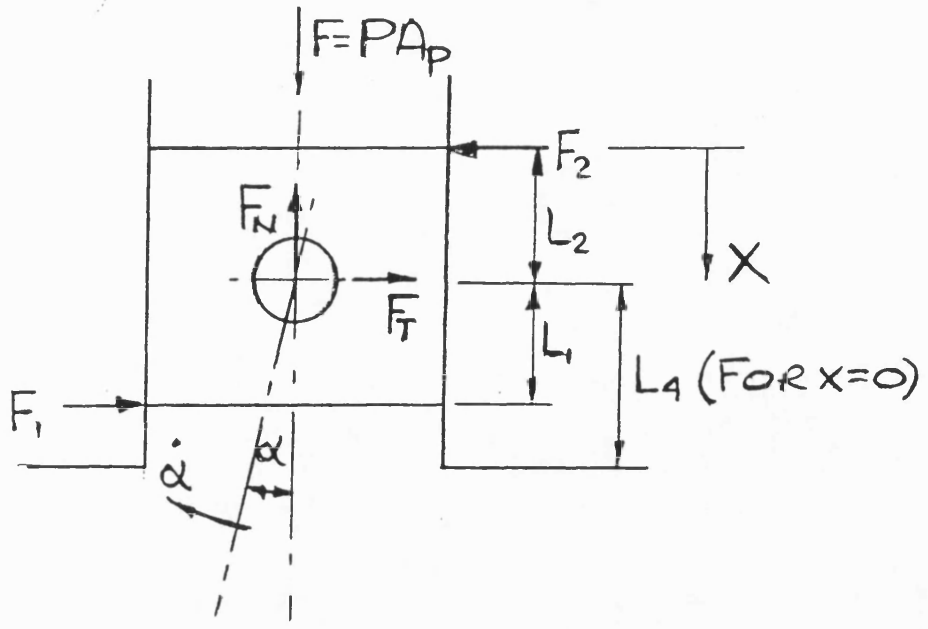

FIG 7. PISTON FORCES FOR $\theta < 90°$

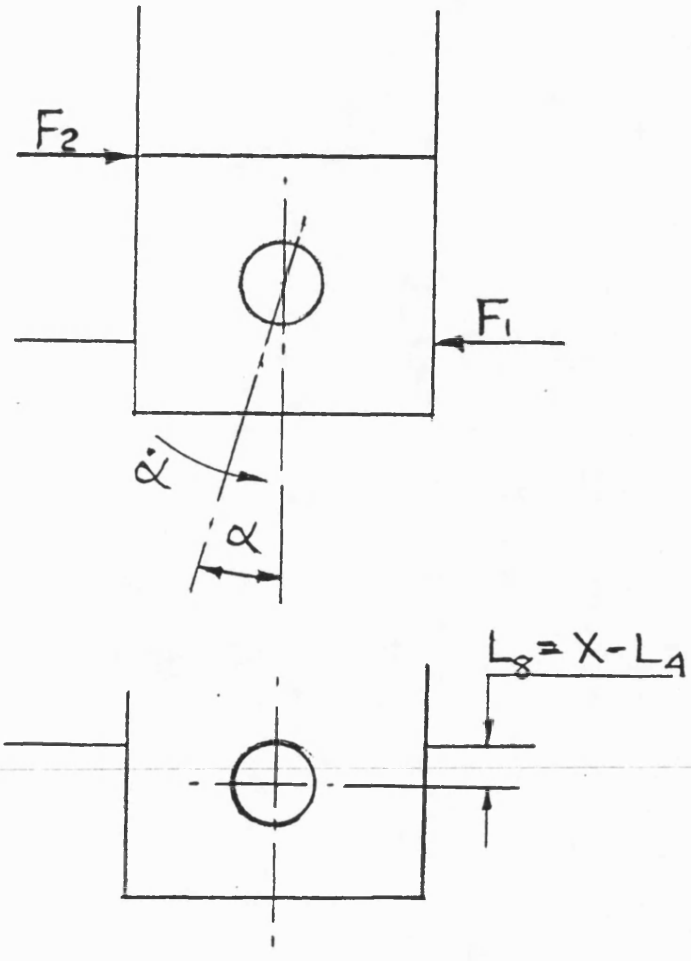

FIG 8. PISTON FORCES FOR $\theta > 90°$

Appendix V

The effect of bearing friction on the slipper forces

Referring to Fig.9. the effect of $\dot{\alpha}$ changing direction can be seen to change the contact force from F_{C1} to F_{C2}.

(a) For $0 \leq \theta \leq 90^0$ (referring to Fig.10)

The length $L_O = L \sin \beta$

and $L_T = L \cos \beta - R_D$

Here it is assumed that for small differences between the slipper face and eccentric radii movement of the contact point through the angle β will not alter the centre distance L.

Taking moments about the bearing centre gives:-

$$F_{C1}(L_O + f_C L_T) = f_B R_B (F_{B1} + F_{B2}) \tag{61}$$

Putting $A_4 = L_O + f_C L_T$ and substituting for $(F_{B1} + F_{B2})$ from Equation (45) and F_N and F_T from Equations (9) and (12) for $F_{C2} = 0$ gives:

$$F_{C1} A_4 = f_B R_B (B_8 (F_P \cos \alpha + K F_{C1}) + B_9 (F_P \sin \alpha + J F_{C1}) - B_8 F_H)$$

$$\therefore F_{C1} = \frac{f_B R_B (B_8 \cos \alpha + B_9 \sin \alpha) F_P - B_8 f_B R_B F_H}{(A_4 - f_B R_B (B_8 K + B_9 J))}$$

or $$F_{C1} = \frac{D_5}{D_6} F_P - \frac{B_8 f_B R_B F_H}{D_6} \tag{62}$$

where $D_5 = f_B R_B (B_8 \cos \alpha + B_9 \sin \alpha)$

and $D_6 = A_4 - f_B R_B (B_8 K + B_9 J)$

(b) For $90^0 \leq \theta \leq 180^0$

Taking moments about the bearing centre (see Fig.10)

$$F_{C2}(L_O - f_C L_T) = F_{C2} A_5 = f_B R_B (F_{B1} + F_{B2})$$

where $A_5 = (L_O - f_C L_T)$

Substituting for $(F_{B1} + F_{B2})$ from Equation (49) and F_N and F_T from Equations (9) and (12) with $F_{C1} = 0$ gives:-

$$F_{C2} A_5 = f_B R_B (E_8 (F_P \cos \alpha + J_2 F_{C2}) + E_9 (F_P \sin \alpha + J_3 F_{C2}) - E_8 F_H)$$

$$\therefore F_{C2} = \frac{f_B R_B (E_8 \cos \alpha + E_9 \sin \alpha) F_P - E_8 f_B R_B F_H}{A_5 - f_B R_B (E_8 J_2 + E_9 J_3)}$$

$$= \frac{H_5}{H_6} F_P - \frac{E_8 f_B R_B F_H}{H_6} \qquad (63)$$

where $H_5 = f_B R_B (E_8 \cos \alpha + E_9 \sin \alpha)$

and $H_6 = A_5 - f_B R_B (E_8 J_2 + E_9 J_3)$

FRICTIONAL MOMENT

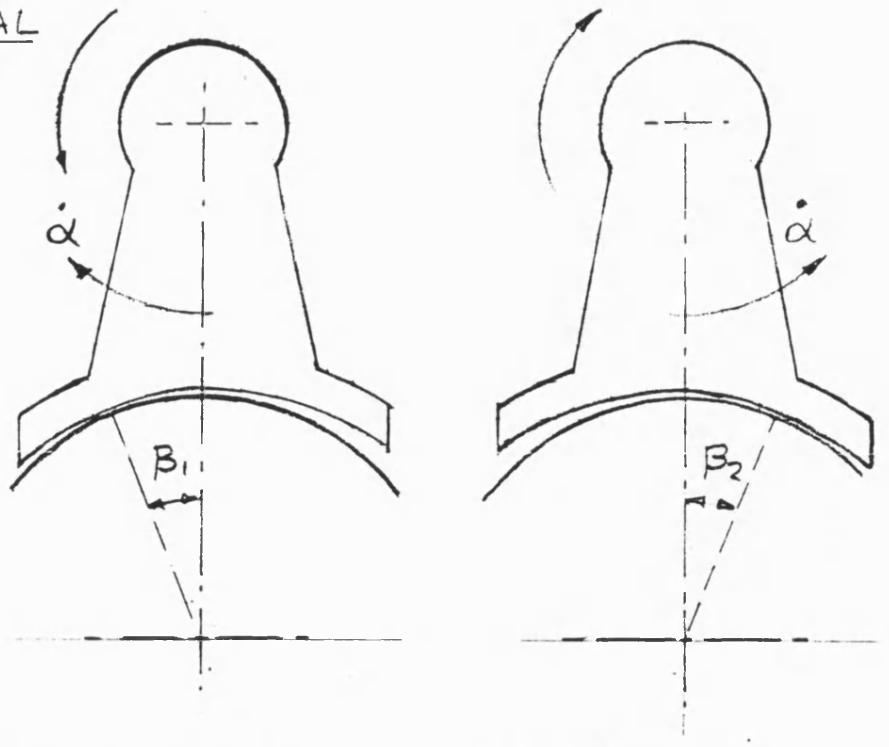

FIG9 THE EFFECT OF CHANGES IN THE DIRECTION OF THE CON ROD ANGLE

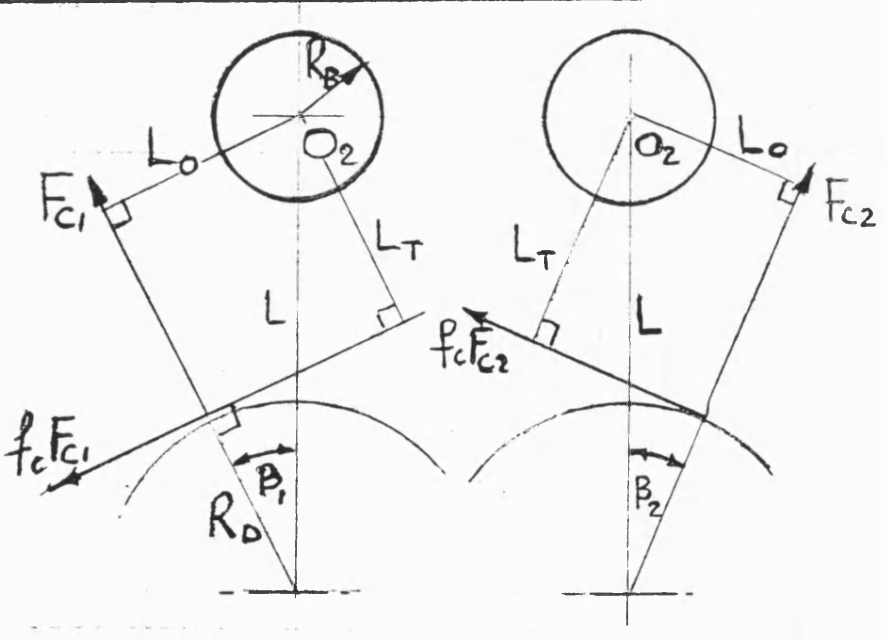

FIG10 FRICTIONAL MOMENT OF THE CON ROD BEARING

CHAPTER 3

PRACTICAL TESTS

1.0 BACKGROUND

In 1975 the author was requested by Chamberlain Industries Ltd, manufacturers of the Staffa radial piston eccentric hydraulic motor, to evaluate the possibility of testing a new variable displacement motor in the laboratories at Bath University.

At that particular time there was considerable research activity into the starting characteristics of hydraulic motors and their performance at low speeds. A programme of work at Bath University under Bowns was concerned with the factors that affect the starting torque of hydraulic motors. This was reported in a paper[9] at the 5th BHRA International Symposium and in the PhD thesis by Rolfe[10]. A major feature of this work was to demonstrate the importance of pressure rise rate and transmission stiffness. These were shown to have a significant influence on the values of mechanical efficiency obtained from a particular type of radial piston motor when tested with a locked shaft.

Other research workers[11,12] were also concerned with the most effective methods of testing motors for starting torque and appropriate test configurations for operating motors at low speed. The results of these activities have recently been incorporated into International standards (ISO 4392-1 and -2) which are still under active consideration by the respective ISO committee of which the author is a member.

The current standards are based on:

* A startability test which employs a force loaded beam, slight movement of which is used to indicate when starting has taken place.

* A low speed test in which the motor shaft is constrained to rotate at constant speed when under constant inlet pressure.

* A third method, proposed by CETIM of France and now accepted by the *ISO* committee, involves operating the motor under conditions of constant inlet flow with the torque being maintained at a constant level. This would be as an alternative to ISO 4392-2 for low speed testing.

In order to fulfill the original test requirements a rig frame was built to facilitate "back to back" testing of a Staffa VB80 dual displacement type motor (maximum displacement 1.34 *L/rev*, minimum displacement 0.44 *L/rev*) wherein the motor was used to drive a similar unit acting as a pump. The two units were rigidly connected together by an inductive type of torquemeter of 20,000 *Nm* capacity and the speed of rotation controlled by means of either a variable restrictor or a pressure relief valve in the outlet flow from the pump unit. The test rig is shown in the photograph of Fig 1 and the circuit in Fig 2.

2.0 MOTOR TESTS AT MAXIMUM DISPLACEMENT AND LOW SPEED

The ISO test standards are based on maintaining two parameters constant these being either pressure and speed or flow and torque with the static test designed to give the mechanical efficiency and leakage as a function of shaft angle. These tests require specialised control systems for maintaining constant speed or torque for the low speed test. In the test rig used for this work it was found that the motor speed could be maintained at a sufficiently steady level by controlling the flow from the pump unit. A minimum speed of around 1 *rev/min* at 100 *bar* could be obtained by shutting off the outlet flow completely when the pump unit displaced all of its flow through internal leakage.

The movements between the sliding faces in the motor vary with shaft angle in an almost sinusoidal manner and as the purpose of these tests was to provide information for the modelling of the motor small variations in speed were not considered of significant importance.

3.0 LOW SPEED TEST RESULTS

The results of the low speed test in Figs 3 and 4 are photographs taken from a storage oscilloscope which show the motor torque against time at mean speeds of 3.4 and 9.2 *rev/min* for an inlet pressure of 97.5 *bar*. The mean torque was 1850 *Nm* and 1960 *Nm* at these two speeds and the variation in the torque about these values reflects the changes in the instantaneous displacement and friction with shaft angle.

The results in Figs 3 and 4 demonstrate a significant increase in mechanical efficiency at the higher speed and a noticeable difference in the shape of the torque ripple, particularly at 36^0 shaft angle when the cylinder at *BDC* is depressurised. At the lower speed stick slip motion occurred which can be seen as a ripple at a frequency of around 30 Hz. This frequency was the approximate value of the natural frequency associated with the transmission inertia and the pump unit displacement. At 9.2 *rev/min* the sudden changes in torque at 0^0 and particularly at 36^0 produce a torque ripple which is also associated with the natural frequency of the load system.

Stick slip could have occurred in both or either of the motor and pump units but it is interesting to see that the oscillations disappear between 18 and 36^0 which coincides with the shaft angle of a cylinder passing through 90^0. As was discussed in Chapter 2 the condition of the piston tilting at 90^0 shaft angle when reversal of the con rod occurs causes a considerable change in the frictional forces and a consequent reduction in the losses at this position.

There is no rotation in the con rod bearing during this condition and the elimination of the effects of reversal of the con rod particularly at the position where maximum torque is obtained may provide sufficient relaxation to prevent from stick slip occurring. The recommended minimum operating speed for this motor is 5 *rev/min* and, consequently in practice, the stick slip condition is normally avoided.

Because the rotational speed was found to be substantially constant during the tests the time scale was sufficiently accurate to provide direct indication of the shaft angle. One piston cycle takes 72^0 of shaft rotation and the reduced scale photographs of Figs 5 and 6 show how the torque fluctuations are repeated every 72^0 Deg. The pressure in a cylinder is also shown in these figures and its relation with the cyclic position can be clearly seen.

For this size of motor at a pressure drop of 97.5 *bar* the mean theoretical torque, Q_{MT}, is 2080 *Nm* which provides the mean mechanical efficiency from the results of Figs 3 and 4.

Thus

$$\eta_m = Q_M / Q_{MT}$$

where Q_M is the motor torque.

The instantaneous mechanical efficiency is given by:

$$\eta_I = Q_M / Q_{MI}$$

where Q_{MI} is the theoretical instantaneous torque at the given angle θ.

Thus $\eta_I = \eta_m Q_{MT} / Q_{MI}$

where Q_{MT} / Q_{MI} is obtained from the ideal values of Fig 1 Chapter 2.

The mechanical losses are therefore given by:

$$L_o = 1 - \eta_I = 1 - \eta_m Q_{MT} / Q_{MI}$$

The values of η_m and L_o for the two speed conditions obtained in this way are shown in Figs 7 and 8 where the torque is the mean value from the recordings in Figs 3 and 4 at a given shaft angle.

4.0 PRESSURE RISE RATE TESTS

As was mentioned in section 1.0 work by Rolfe[9] at Bath University was carried out on aspects of testing and modelling of hydraulic motors which had shown that for static tests with a locked shaft the rate at which pressure was admitted to the motor had a considerable effect on mechanical efficiency.

A similar test was performed on the Staffa motor with a locked shaft by controlling the rate of opening of the inlet valve, the results from which are shown in Fig 9. The results obtained by Rolfe for a different type of radial piston motor, which are shown in Fig 10, covered a much wider range of pressure rise rates, η_m reaching its maximum value for rates above 200 *bar/s*. Although not shown in Fig 9, η_m did not increase for rates above a value of 11 *bar/s*.

These results show that motor torque during starting is extremely sensitive to the way in which pressure is initially introduced to the motor. The effect of pressure rise rate is also influenced by the stiffness of the transmission system that is connected to the motor shaft. The combination of these two parameters determines the amount of twist in the motor shaft and, consequently the movement of the motor components.

Both of these figures originally appeared in the paper[9]. There will be further discussion on the results of this and the previous section in section 7.0.

5.0 TESTS AT LOW SPEED AND MINIMUM DISPLACEMENT

The motor unit was tested at low speed with its displacement set to the minimum value (0.44 *L/rad*) which corresponds to one third of the maximum displacement. The results are shown in Fig 11 for a pressure difference of 147 *bar*.

With the restrictor on the pump unit outlet closed off completely the motor speed was very low (< 0.3 rev/min) and at the minimum efficiency the motor appeared to stop rotating momentarily as the shaft angle approached 36^0.. The large increase in efficiency after 36^0 shaft angle indicates that the low value of efficiency at 36^0 is caused by the cylinder that reaches its *BDC* position at this angle.

At this low speed the cylinder had been pressurised for several minutes with the consequence that the friction had risen to a level such that the motor had ceased to operate. This situation does not normally apply during starting because, during starting, squeeze film effects will maintain the clearances between the sliding components unless the pressure had been admitted very slowly in the manner described in section 4.0.

The mechanical efficiency for the larger displacement at a pressure of 147 *bar* is also shown for comparison. Thus at approximately similar speeds, the effect of reducing the displacement is to reduce η_m by around 10 to 12%.

6.0 INDUSTRIAL TESTING

6.1 Background

During 1977 the author became responsible for engineering of the Staffa motor at Chamberlain Industries when he was appointed Technical Director. Despite their position of world market leader for low speed motors the company did not have a product development programme and as a consequence was involved in a minimal level of engineering testing of any kind.

A programme was instituted to investigate the possibility of developing an automatic control to provide constant power from the dual displacement motor, so that for a fixed input flow the motor speed would vary with changes in the load conditions. The results of this work were presented in a paper[13] by the author at the 5th BHRA International Fluid Power Symposium in 1981.

At this time the company was concerned with a major change to the product that involved replacing the white metal facing to the slipper with a bronze material which could be brazed in the company's manufacturing plant. This material change had the benefit of higher pressure capability and reduced cost but a disadvantage in not having the good bearing properties of white metal.

To avoid the problem of reduced bearing capability the motor had to be run in very carefully after assembly and to improve this a thin layer of tin was applied to the slipper face. The bronze was less tolerant than white metal to the surface finish of the eccentric and to the effects of distortion of the slipper component.

There was considerable pressure on the company to increase the pressure and power rating of its motors and allow their use with different fluids. This, coupled with the slipper face problem, generated a need to develop a more fundemental understanding of the parameters that affect the performance of the slipper bearing. This required a combination of analytical and test work to establish the important parameters involved which led to an initial examination of the problem using the approach described in Chapter 2. The work was not fully completed at the time but sufficient insight was gained to identify some of the problems.

The engineering development laboratory had a single "back to back" test rig of 50 *kW* maximum power capability. Using a particular method of power regeneration allowed the test power to be increased by around 2.5:1. Eventually a second test rig, hydraulic power pack and control consul were installed which can be seen in the photograph of Fig 12 which shows the general layout of the laboratory test facility.

A proper evaluation of the motor components demanded specialised test rigs for investigating the performance of individual components. At the time no references in the English language were found that related to such work. Any available referenced work usually concerned axial piston swash or bent axis type machines and that of Turnbull[4] on plate valves gave some insight for analysing the likely performance of slippers at high rotational speeds.

The work of Causemann[14] and more recently that of Ezato[6] on piston friction are examples of special purpose test rigs which, in these instances, were used to measure piston friction. Kobayashi[15] also used a special purpose test rig to measure the friction in the spherical joint of an axial piston swash type pump. Boinghoff[16] has examined theoretically the effect of friction in the spherical joint of a bent axis pump.

As was shown in Chapter 2, the motor performance is very sensitive to the radius of the slipper in relation to that of the eccentric. As described in Chapter 2, there is a difficulty in obtaining an accurate measurement of the slipper face. Being machined from a forging the thickness of the slipper had, at that time, a wide tolerance limit. As a consequence of such component variations, the level of distortion of the slipper face would vary considerably, particularly at the four outer corners.

There was, therefore, a considerable area of uncertainty as to the proportion of the mechanical losses attributable to each of the three sliding faces, the extent to which these could be influenced by the materials, manufacturing process and the range of variability that was likely to occur.

Real development work was hindered by lack of resources and pressure from both within and outside the company on matters which were often of some urgency. The test work that was done was carried out in a piecemeal fashion, as time allowed, on the basis of the prognostications that resulted from analytical work. This was a good example of the British industrial problem; insufficient resources causing a lack of knowledge of a product that had been manufactured for years.

The remainder of this chapter is therefore concerned with a description of the various tests and the results obtained which will be used in subsequent chapters to provide information for the improvement of the model and a discussion of how the design itself could be modified.

6.2 Average Running Torque

A typical performance test result for the motor having bronze faced slippers is shown in Fig 13 where the effect of speed on mechanical efficiency can be seen for the two motor displacements. The mechanical efficiency is also affected by motor inlet pressure; the results for the minimum displacement in Fig 13 showing this to be reduced by 6.8% at 40 rev/min for the pressure increased from 207 *bar* to 276 *bar*.

Following the change to the bronze slipper facing material it was found that operation of the motor at full rating in the first few minutes could result in a serious loss of torque to the extent that the motor would sometimes stop rotating. Examination of the slipper faces showed little, if any, signs of wear or pick up and following reassembly and 20 minutes running in the motor would operate normally. This problem was difficult to quantify but, according to information contained in a research report[17] on bronze bearings, this phenomena can occur and if found early enough would not result in any consequential damage.

The problem highlighted doubts about the method of machining the slipper faces and the accuracy of this radius. There were also problems at the time in achieving the desired surface finish on the eccentric of dual displacement motors. This type of motor operates at much higher speeds than the version having fixed displacement which increases the probability of seizure. These difficulties brought into sharp focus the lack of knowledge of the parameters that affect the performance of slippers.

To obviate this problem the running in procedure for production motors was changed and the time extended but, despite these measures, occasional problems persisted. White metal is a very tolerant material and in many circumstances had been able to accommodate production variances without serious loss of performance or reliability. However, as a result of the lack of fundamental knowledge, this fact had not been fully appreciated.

Extensive tests on a motor having a thicker edge to the slipper demonstrated the important effect of distortion in this component as it showed none of the usual visual signs of contact on the slipper face. The motor design did not allow this increased thickness at maximum displacement and consequently such a modification could not be effected on production units.

The tin coating applied to the slipper face allows its shape to conform to that of the eccentric and thus accommodates differences in their radii. The amount of tin removed during running in would therefore depend on the level of this difference in the radii. Differences in the amount of tin removed reflected the variation in the manufacturing tolerances. White metal is a softer substrate and it was felt that this was a major factor for the more consistent performance obtained with this material because of its ability to accommodate manufacturing tolerances and distortion.

An additional test on four motors was performed by restricting the outlet flow. This creates a back pressure such that, in the absence of torque loading on the motor shaft, those pistons that are acting as a motor drive those that are acting as a pump.

Two of the motors tested in this way had slippers of the bronze material and the other two of white metal. Assuming that the mechanical efficiency for those cylinders acting as a motor was the same as for those acting as a pump enables the mean mechanical efficiency to be calculated as follows:

Thus $\eta_m P_m D = P_p D / \eta_m$ or $\eta_m = (P_p / P_m)^{1/2}$

This is not the true mean mechanical efficiency for normal operation because the frictional losses from the shaft bearings and the distributor valve will be almost zero for the test condition. The results thus obtained in Fig 14 show the white metal slippers to have an efficiency that is about 1-2% greater than those with bronze slippers. The model results in Chapter 2 indicate that an increase in f_C of 0.1 to 0.12 would result in a 1% reduction in η_m. Fig 14 also shows the variation of mechanical efficiency with oil viscosity for a speed of 25 rev/min.

6.3 Tests with High Water Based Fluids

The Staffa motor had originally been developed in conjunction with the National Coal Board in the late 50's and, since that time, used extensively with 60/40 water in oil emulsion fluid for mining applications. However, on making the change to the bronze slipper material, it was necessary to submit the modified motor for the standard life test at MRDE Bretby. This was not completed due to the unexpected failure of the con rod bearing in the piston.

The Coal Board was also asked to consider using the motors with 95/5 oil in water emulsion and consequently carried out tests using a standard motor which had bronze slippers. The motor type was of dual displacement having maximum and minimum displacements of 3.08 and 1.48 L/rev respectively. The results obtained for the mechanical efficiency with both fluids were as follows:

Test conditions - 138 bar pressure drop; 10.4 bar outlet pressure

	Displacement (*L/rev*)			
	1.48		3.08	
Fluid	60/40	95/5	60/40	95/5
Efficiency variation at 1 rev/min	67-85%	57-75%	76-89%	63-82%
Efficiency at 80 rev/min			86%	75%
Efficiency at 150rev/min	86%	70%		
Lowest obtainable efficiency		33%		60%

The use of the 95/5 fluid reduces the mechanical efficiency obtained with 60/40 fluid by up to 17% at 1 rev/min. In the worst case the mechanical efficiency fell to 33% at minimum displacement with the 95/5 fluid.

95/5 fluid has a viscocity of 1cSt as compared to 60 cSt for 60/40 fluid which will considerably increase the leakage and could cause the flow in the hydrostatic slipper supply restrictor to become turbulent thus reducing the available bearing pressure. However increasing the size of the restrictor had no discernible effect and thus it was felt that the reduced mechanical efficiency (for both fluids in relation to oil) resulted mainly from higher levels of friction in the sliding contacts. Certainly for the 95/5 fluid squeeze film effects would be negligible which coupled with an increase in the static coefficient of friction would be expected to cause a reduction in efficiency. The life problem of the con rod bearing even with 60/40 fluid gives a lie to what is already expected - that the con rod bearing is the major cause of poor efficiency.

It is of interest to note that, at the time, a series of tests using a phospor bronze cup insert in the con rod bearing were performed by running a motor continuously with 60/40 fluid against back pressure at low speed (3-5 rev/min). The use of this material in the bearing eliminated the failure problem with water based fluids.

6.4 Static Tests on a Piston and Con Rod Assembly

A number of con rod and piston assemblies were tested on a special rig having two cylinders in opposition that were both pressurised onto an eccentric. The purpose of this test was to measure the slipper hydrostatic bearing pressure and the leakage flow from the slipper. Rotation of the eccentric was not possible and because of the arrangement there was zero eccentricity and hence zero torque. The con rod axes were therefore in line with that of the cylinder.

Because there was no rotation of the con rod, there would have been no frictional torque from the con rod bearing. Thus the slipper contact force, F_C, would, as a result, have been zero. This allowed the slipper to lift off from the eccentric surface, the leakage through the bearing supply restrictor reducing the bearing pressure until the bearing force was equal to the net force from the piston.

For the particular type of slipper used the area of the face was such that for balance the ideal ratio between the pocket and supply pressures is 0.9.

Two different shapes of hydrostatic slipper pocket were used as shown in Fig 15 and the variation of pocket pressure ratio with the supply pressure is shown in Fig 16 at two different oil supply temperatures. The temperature of the eccentric was also measured and found to be substantially the same as that of the supplied fluid during steady state operation. The temperature has the effect of reducing the operating pocket pressure ratio by around 0.02. The slippers having square corners show a reduction in the pressure ratio as the supply pressure increases beyond 150 *bar* which was considered to be due to increased leakage from the corners as a result of distortion which increased with pressure. This is confirmed by the leakage flows shown in Fig 17 where the flow for the square cornered pocket increases at a greater rate at higher pressures.

7.0 DISCUSSION OF RESULTS

7.1 Low Speed Performance at Maximum Displacement

The variation in the losses with shaft angle at the two speeds in Fig 8 show marked differences which reflect the changing friction conditions as the speed is increased. These have resulted in increasing the mechanical efficiency and a noticeable change in the shape of the ripple.

The application of the mathematical model in Chapter 2 made a comparison between the model incorporating constant values of the friction coefficients and the practical results shown in Fig 8. This demonstrated that variations in the friction coefficients at low speed were related to the cyclic events in the motor geometry.

The stick slip observed at 3.4 *rev/min* does not occur at the 9.2 *rev/min* condition. This is considered to be an indication that the conditions in the con rod bearing have changed from almost dry contact to those of boundary lubrication.

For the lower speed condition the increase in the losses (Fig 8) beyond 0^0 (TDC) is possibly due to the reduction in film thickness in the sliding components in that particular cylinder. As was discussed in Chapter 2 there is an indication of the con rod bearing reversal causing the piston to reverse its tilt in the clearance region with the cylinder. This could explain the reduction in losses after 18^0 shaft angle. The con rod angle will remain unaltered during this period of tilting resulting in the con rod bearing oil film being squeezed to a level such that the frictional conditions approach those for dry surfaces.

The slight ripple at 27.5^0 following the piston tilt reversal is considered to be a result of stiction in the con rod bearing when the losses momentarily reduce at 28^0 shaft angle. The friction losses increase further beyond 28^0 due, possibly, to further reductions in the film thickness because even at this angle the con rod angle has only changed a small amount from that at the 90^0 position.

As the con rod bearing reversal progresses the interface will become wetted from fresh fluid which would result in the friction eventually reducing. Fig 18, gives the relationship between the ratio of the angular velocity of the con rod to its maximum value and shaft angle. This shows that, as the velocity of the bearing for the No.2 cylinder increases from zero at 18^0 shaft angle, that for the No.1 cylinder is reducing; the two velocities being equal at an angle of around 54^0. Now at 3.4 *rev/min*, the maximum value of the angular velocity, $(d\alpha/dt)_m$, is only 0.05 *rad/s*. Around the dwell point at 90^0, the oil film will become extremely thin with the potential of becoming almost dry. It is likely, therefore, that a considerable amount of shaft rotation is required before lubrication of the bearing creates conditions for the friction level to fall. As this is happening, however, the velocity in the No. 1 cylinder is reducing to a low value. This could explain why the losses tend to increase following the sharp reduction at 36^0 when cylinder No.3 is depressurised.

From Fig 8 it is seen that the losses for the 9.2 rev/min speed condition show a much more gradual increase from the 0^0 to 36^0 shaft positions. The higher velocities in the con rod bearings have caused a sufficient reduction in their friction coefficient, f_B, such that tilting of the piston in the cylinder does not occur. The higher velocities, and the effect of squeeze films, have resulted in lower friction and, as a consequence, a reduced level of the losses. As is shown in Chapter 4, the rate of collapse of a squeeze film is strongly dependent on the degree of taper in the bearing clearance. For the con rod bearing the distortion of the piston cup is likely to be sufficient to eliminate some of the taper that prevails in the clearance either side of the contact point when the components are unloaded. The friction in the con rod bearing will thus be affected by the squeeze film effect and the lubricity of the fluid.

7.2 Pressure Rise Rate Effect

The effect of pressure rise rate in Fig 9 shows that for 100 *bar* at 0^0 shaft angle the mechanical efficiency varies between 80% and 87% for pressure rise rates between 2 and 11 *bar/s*. Thus at the highest rise rate the pressure took 9.1*s* to reach 100 *bar*. For the motor at 0^0 *(TDC)*, when operating at 3.4 *rev/min*, the mechanical efficiency was 85%. For the Nos.2 and 3 cylinders the pistons had been under pressure for a time of 3.5 and 7.1 *s* respectively. It is interesting to see that, even though these times were less than that required for the locked shaft test to reach 100 *bar*, with a pressure rise rate of 11 *bar/s*, a lower efficiency was obtained.

The torques obtained from the locked shaft test apply only to those values that were measured as the pressure was being increased. Following the cessation of the pressure increase, when twisting of the shaft had ceased, it is possible that this was followed by a reduction in motor torque as the squeeze film process was completed.

However, this would not be associated by a reversal of the shaft because, with the motor then acting as a pump, the torque in the shaft would be insufficient to cause this. Thus the torque in the locked shaft does not represent the value under which the motor could start rotation.

The stiffness of the motor shaft together with that of the transmission is important in terms of the amount of shaft rotation thus created. If the rotation angle is greater than a certain amount the slipper contact angle, β, will reach the value required for causing rotation of the con rod. The motor torque can then be determined using the method described in Chapter 2. However if the rotation angle is less than this value, thus giving a lower value of β, the torque output obtained from the motor shaft will be greater than that which is obtained when the con rod is being rotated.

This effect can be obtained from the theoretical model using values of β that are less than those required for the equilibrium condition described in Chapter 2. In other words, there can be equilibrium of the radial forces but insufficient slipper contact force to cause rotation of the con rod. This situation will produce a torque on the motor shaft but will not allow it to rotate. For the given set of frictional conditions the variation in η_m with β is shown in Fig 19.

Thus, Fig 19 shows that, for values of β less than 15.0^0, there is more torque available at the shaft than in normal operation.

The amount of shaft rotation that is required to achieve a given value of β is given by equation 2.5 of section 4.0, Chapter 2.

Thus $\phi = L_R e_C \beta / R_D (R_D + L_R)$

where for $e_C = 75$ μm; $\beta = 10^0$; $\phi = 0.0042^0$

The stiffness of the motor shaft and the torque transducer was approximately 10^6 *Nm/*^{0}. Thus for a nominal torque of 1900 *Nm* the shaft rotates through an angle of 0.0019^0.

Now 1900 *Nm* represents a motor mechanical efficiency of 0.914 and the twist in the shaft for this torque will create a change in the contact angle of:

$$0.0017 \times 10 / 0.0042 = 4.05^0$$

The equilibrium value of β of 15.2^0 is larger than that caused by the amount of twist in the shaft. Thus, during the locked shaft tests there has been insufficient shaft rotation to create an equilibrium condition in the motor. The test therefore produces more torque than the motor is capable of sustaining which explains why the measured rotating efficiency was less than that obtained from the locked shaft test.

It can be seen from Fig 19 that for β changing from 6^0 to the value of 15.1^0 the indicated change in efficiency is - 11%.

7.3 Low Speed Performance at Minimum Displacement

The low speed test results in Fig 11 demonstrate the extreme sensitivity of the motor mechanical efficiency at minimum displacement when operating at different speeds. Even at the relatively high speed of 20 *rev/min* there is a reduction in efficiency of around 10% when compared to operating at 17 *rev/min* with the motor at maximum displacement. As the speed was reduced the frictional losses increased to a point where rotation eventually stopped. Predictions from the model indicates that the value of the con rod and slipper bearing friction coefficients would need to rise to around 0.4 to 0.5 for such low values of efficiency at 36^0 shaft angle.

7.4 Average Running Efficiencies

The results in Fig 13 show the effect of operating speed at different motor displacements and pressures for a motor in which the slippers were bronzed faced. It can be seen that the efficiency reaches its maximum value, for the motor at minimum displacement, at a speed of 140 rev/min. The reduction in efficiency at speeds greater than this value is considered to be largely the result of flow pressure losses which vary with N^2. At the maximum displacement, which is 3.6 times greater than the minimum value, the corresponding speed would be 39 *rev/min*. From Fig 13 at maximum displacement the efficiency is seen to level off and remain approximately constant for speeds above 45 *rev/min*.

The data for 200 bar is used in Fig 20 to show the variation of the actual torque loss with speed for the two displacements. It can be seen that, for both displacements, these are the same at a speed of 30 rev/min. This is interesting because individually the torque losses from each of the three interfaces could be expected to be different as the maximum velocities of the piston and the con rod bearing will reduce as displacement is reduced. The effect of the reduced velocity in the con rod bearing is likely to have caused an increase in its friction. The effect of this will be to increase both the piston and slipper contact forces and their frictional losses.

Fig 13 also shows the effect of increasing the pressure to 276 *bar* which reduces the efficiency by between 3 and 8% over the speed range of 20 to 200 *rev/min*. As was shown in Fig 16 the slipper pressure ratio is subject to variations as a result of distortion and possibly temperature changes in the leakage path which will be affected by the motor speed. These serve to increase the contact force and hence the slipper frictional loss.

8.0 CONCLUDING REMARKS

The results from the tests have shown that the motor mechanical efficiency is sensitive to the operating pressure due to the effects of:

(a) Distortion of the slipper which causes a loss of hydrostatic pressure

(b) Changes in the frictional conditions in the con rod bearing. This is particularly noticeable when operating at speeds lower than 9 *rev/min*.

These effects have a strong influence on the efficiency when operating the motor at reduced displacement. The frictional mechanisms are also seriously affected by the use of water based fluids. It is considered that improvements to the existing design could reduce these problems.

These aspects are discussed in the next Chapter together with an examination of methods to incorporate the effect of the varying frictional conditions in the model developed in Chapter 2.

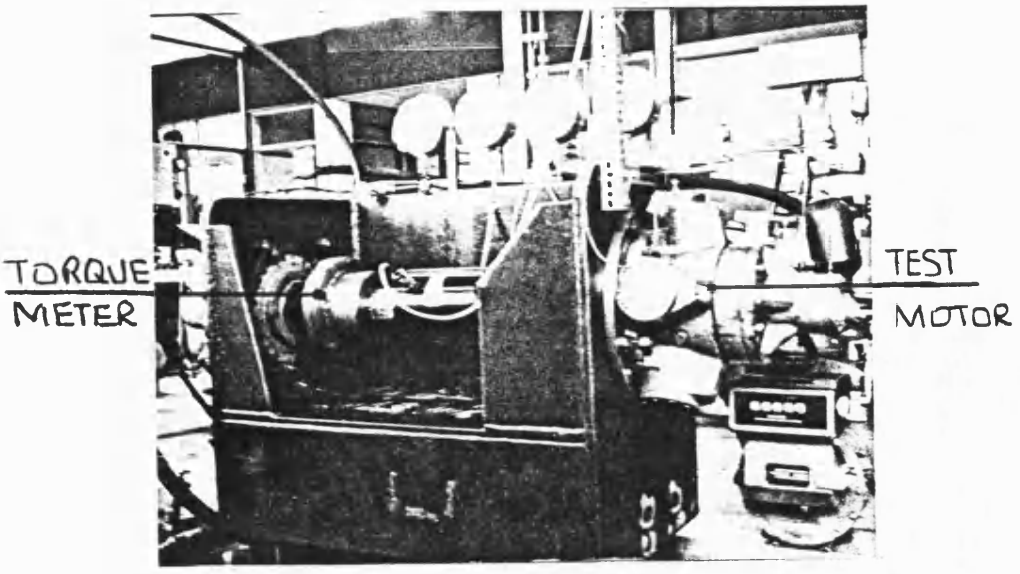

Fig 1 Low speed test rig

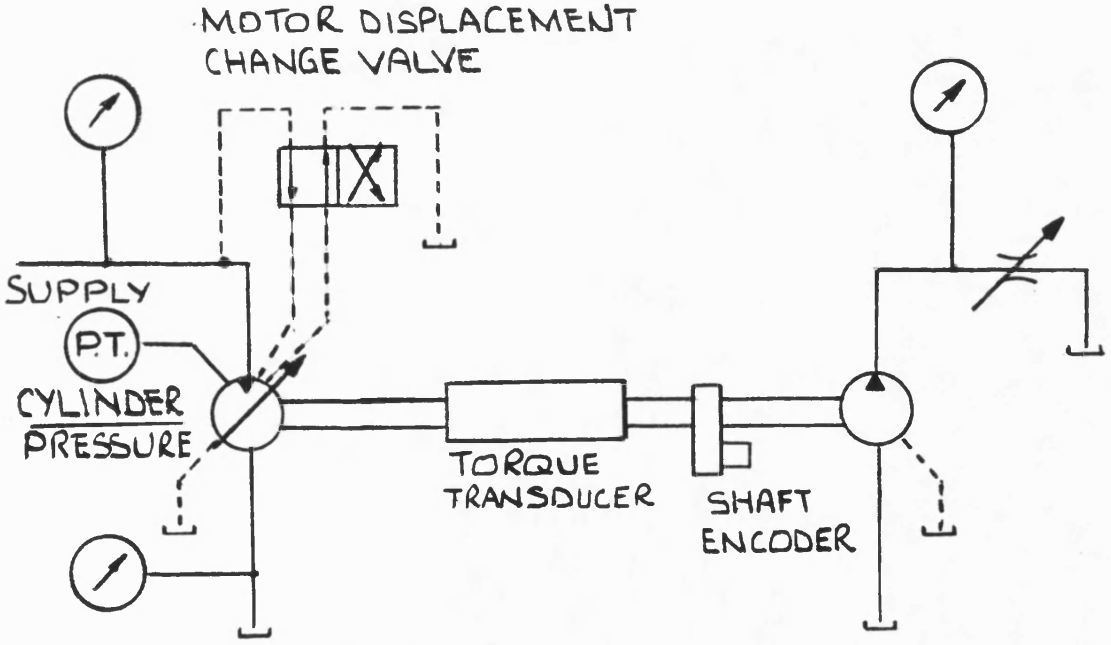

Fig 2 Circuit for low speed test rig

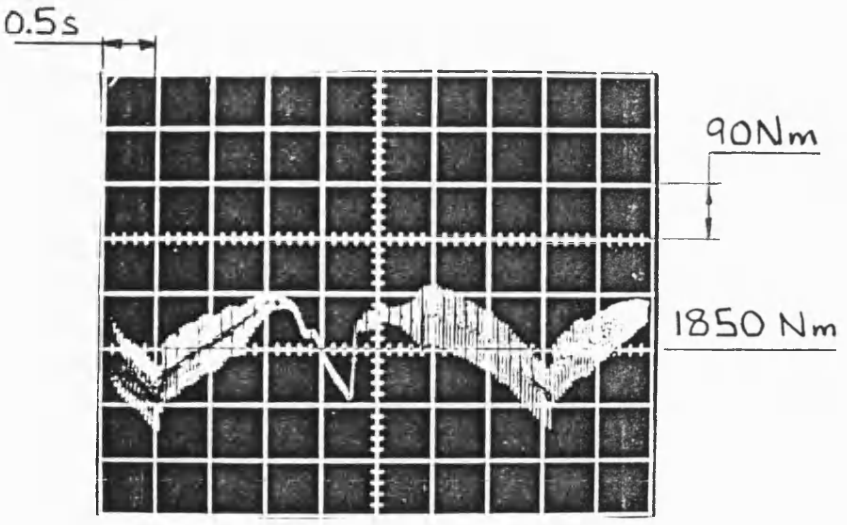

Fig 3 Measured torque at 3.4 *rev/min* for one cycle

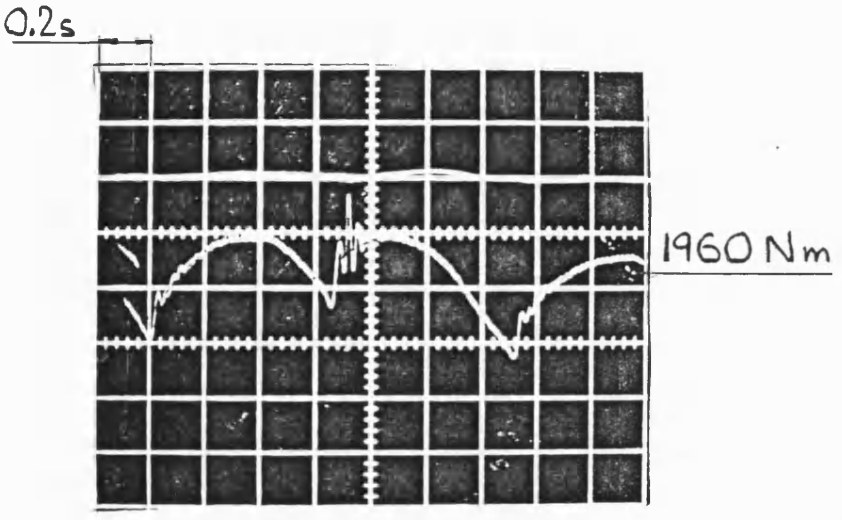

Fig 4 Measured torque at 9.2 *rev/min* for one cycle

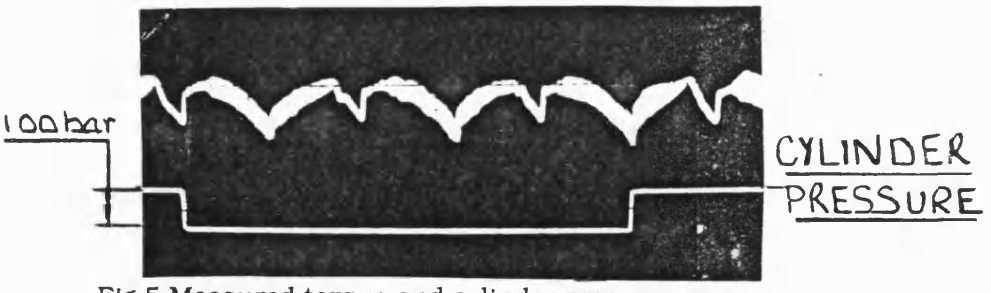

Fig 5 Measured torque and cylinder pressure
at 3.4 *rev/min* for one half of a shaft revolution

Fig 6 Measured torque and cylinder pressure
at 9.2 *rev/min* for one half of a shaft revolution

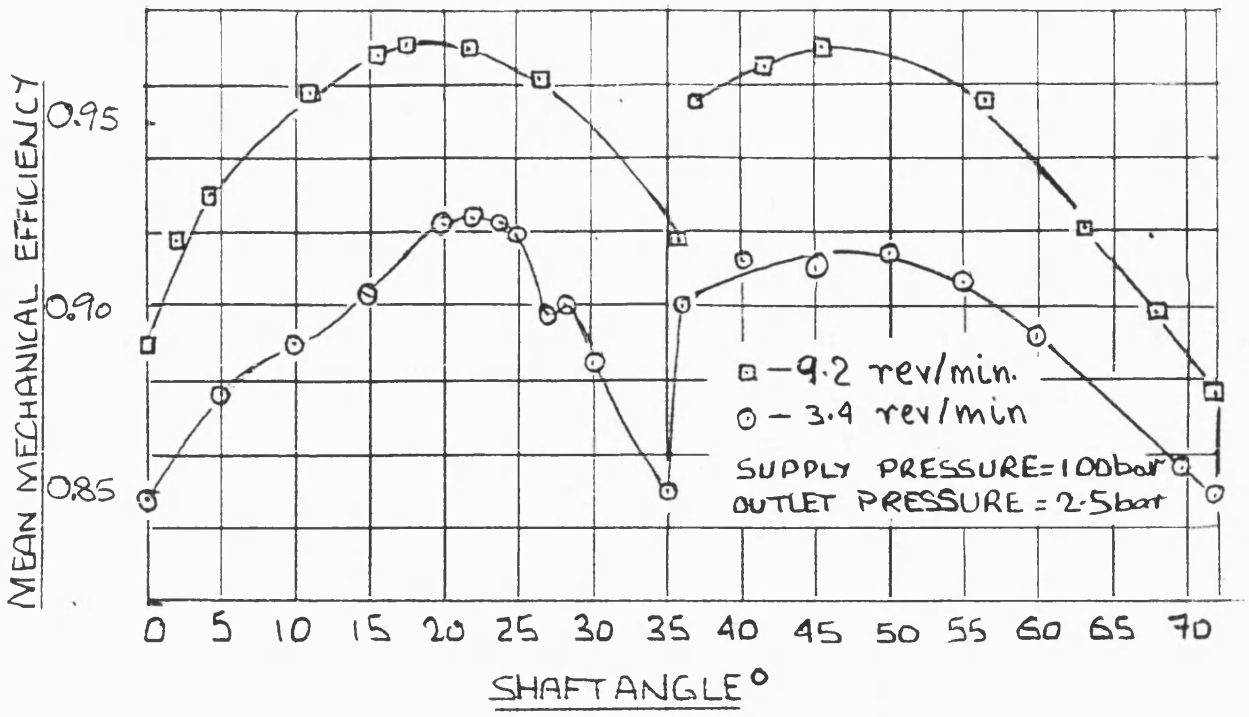

Fig 7 Mean mechanical efficiency at 3.4 and 9.2 *rev/min*

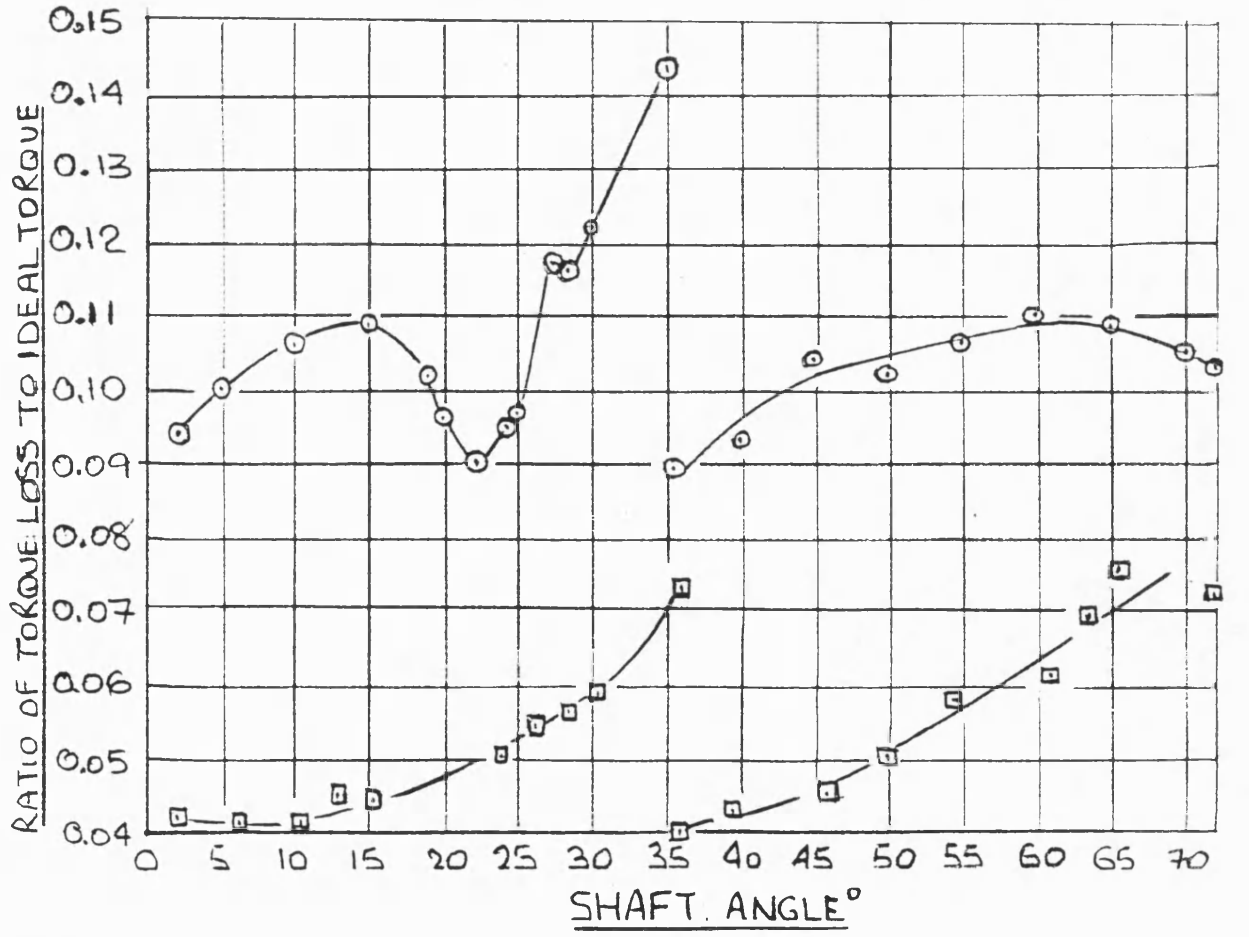

Fig 8 Mechanical losses at 3.4 and 9.2 *rev/min*

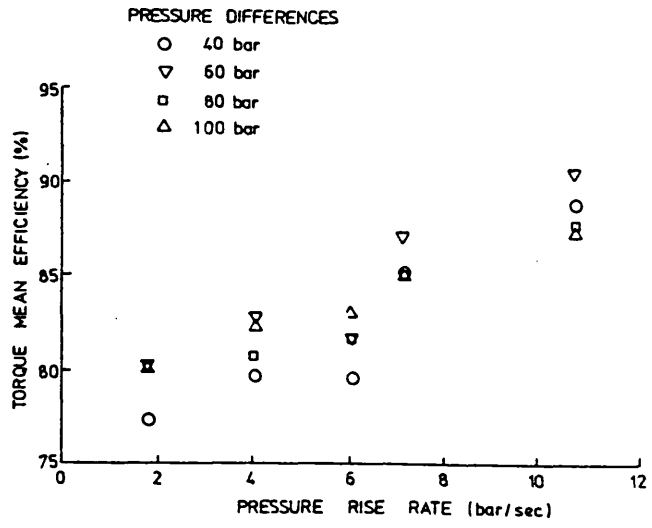

Fig 9 Effect of pressure rise rate on the motor measured torque

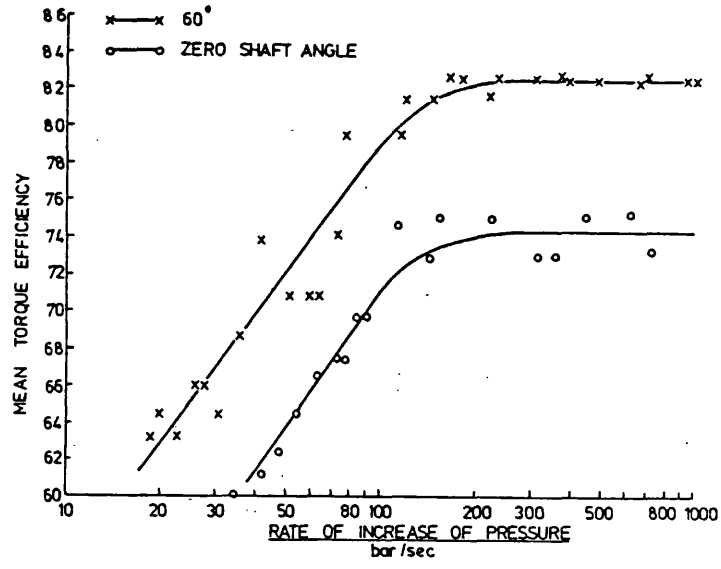

Fig 10 Effect of pressure rise rate on the measured torque for a motor of a different type

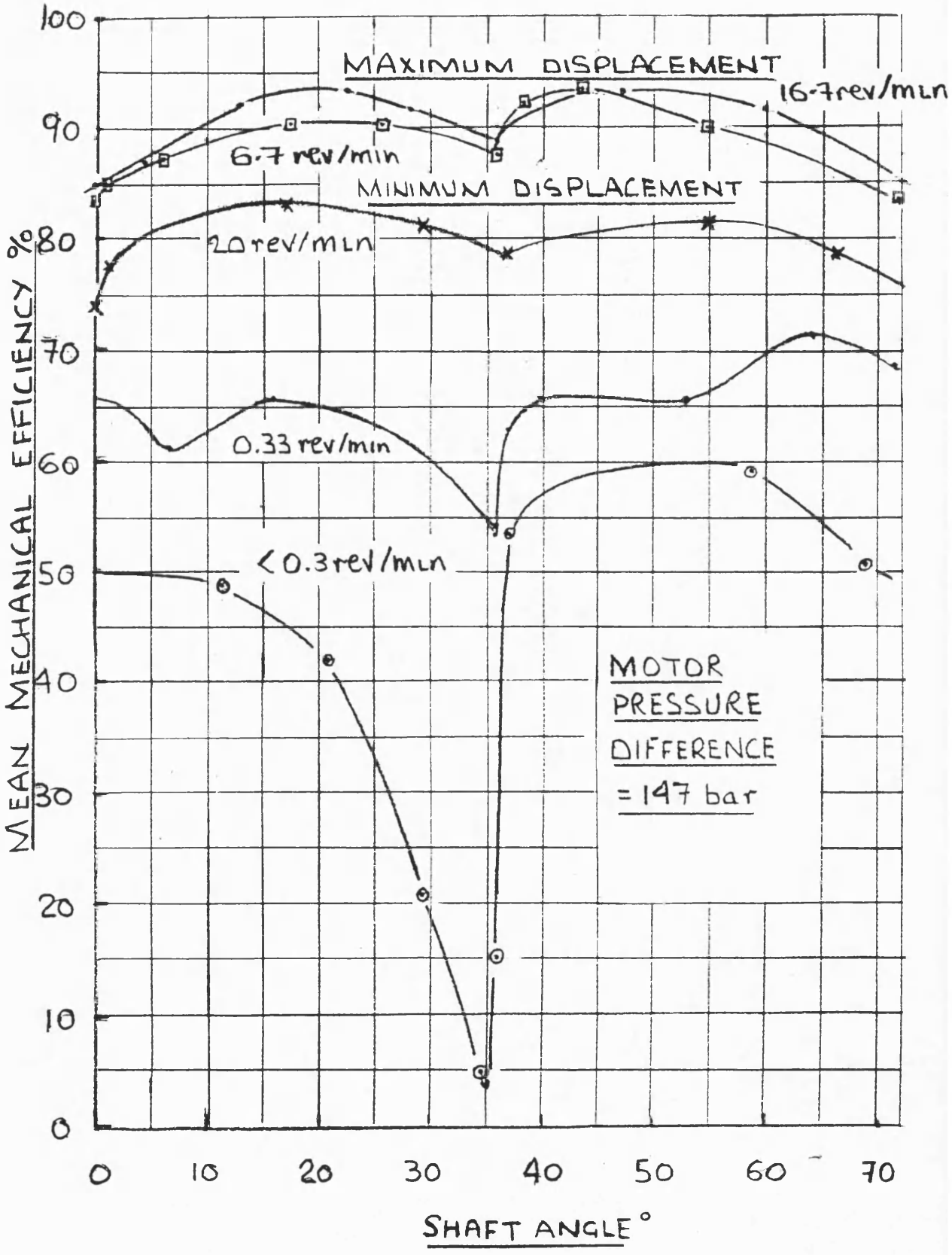

Fig 11 Measured mechanical efficiency at maximum and minimum displacement for speeds up to 20 *rev/min*

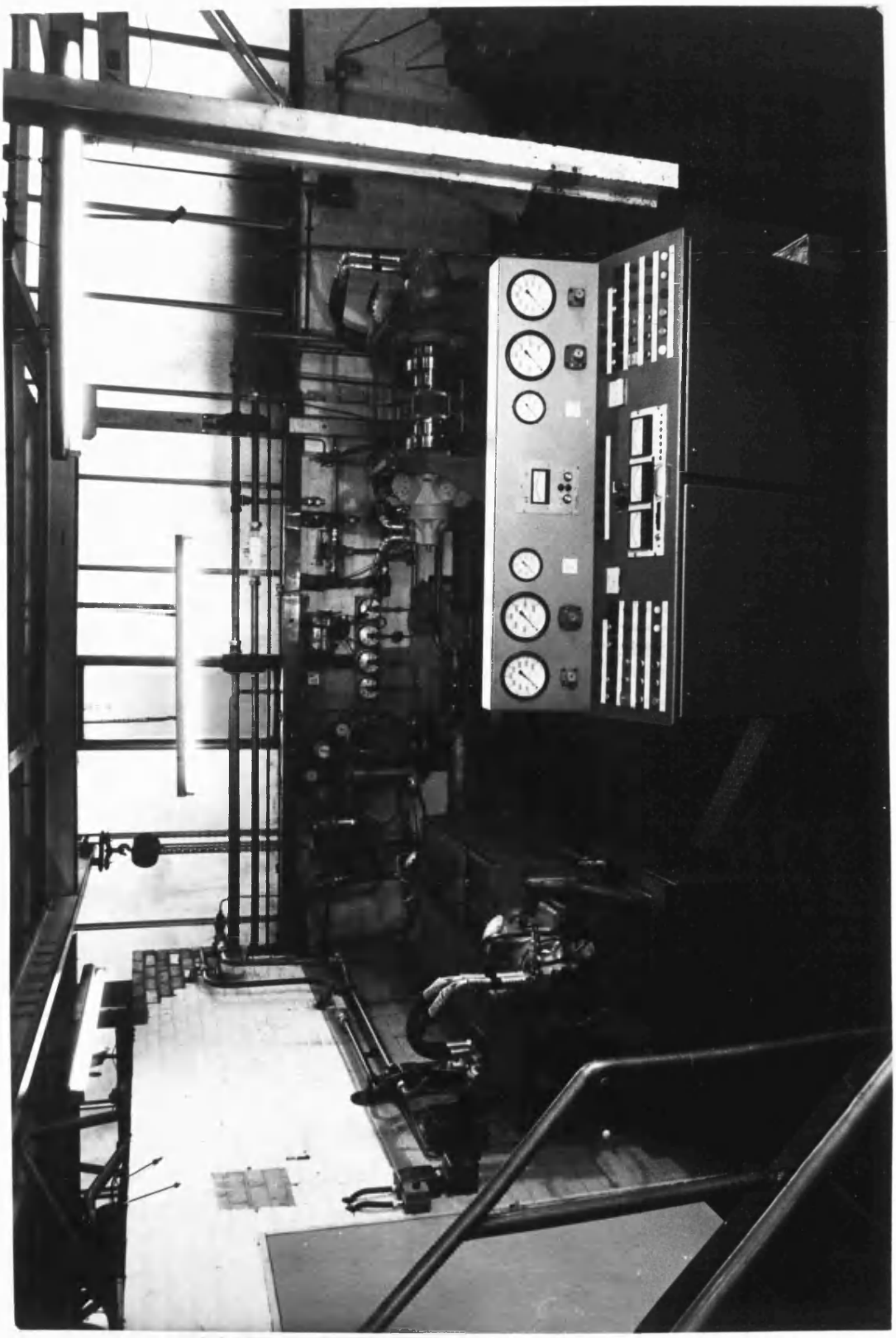

FIG 12 LAYOUT OF THE LABORATORY TEST FACILITY

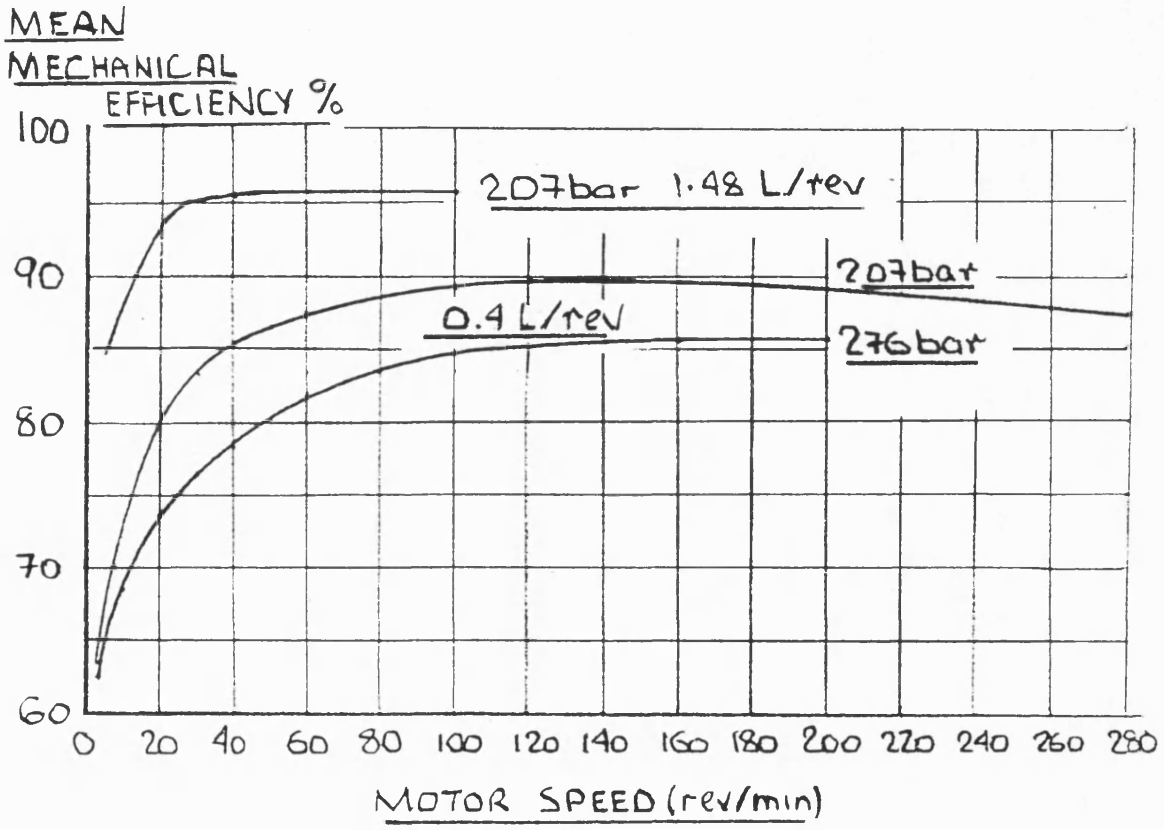

Fig 13 Measured mechanical efficiency at maximum and minimum displacement for speeds up to 280 *rev/min*

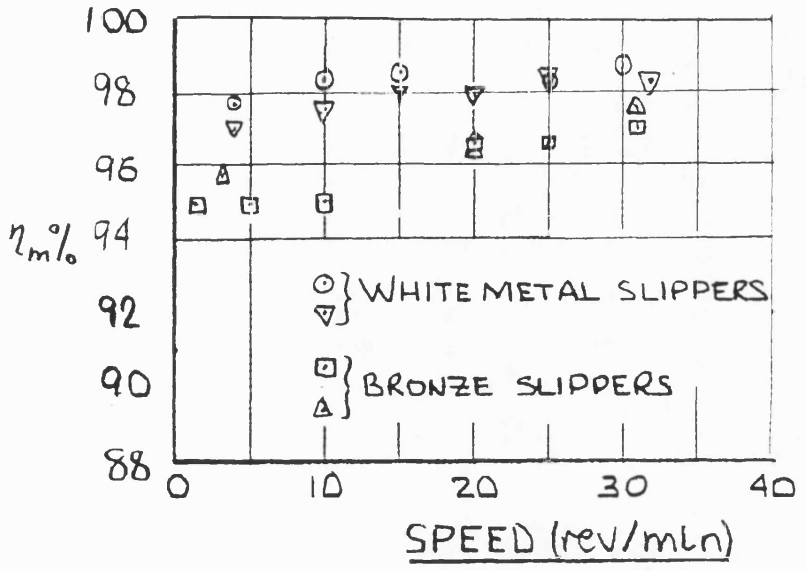

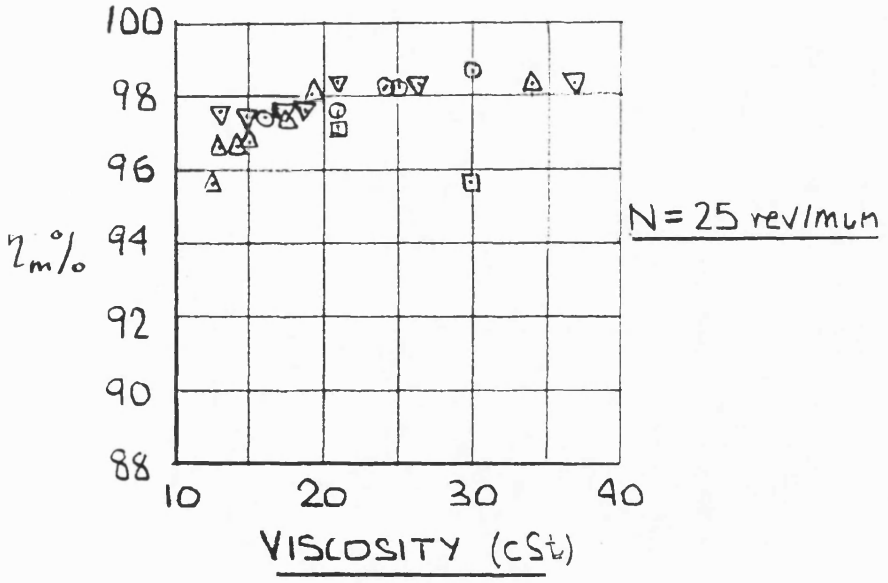

Fig 14 Low speed test with back pressure for different material slippers

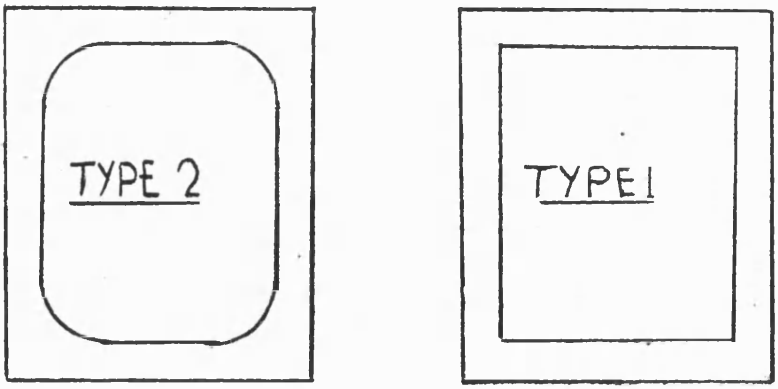

Fig 15 Shape of the slipper pockets

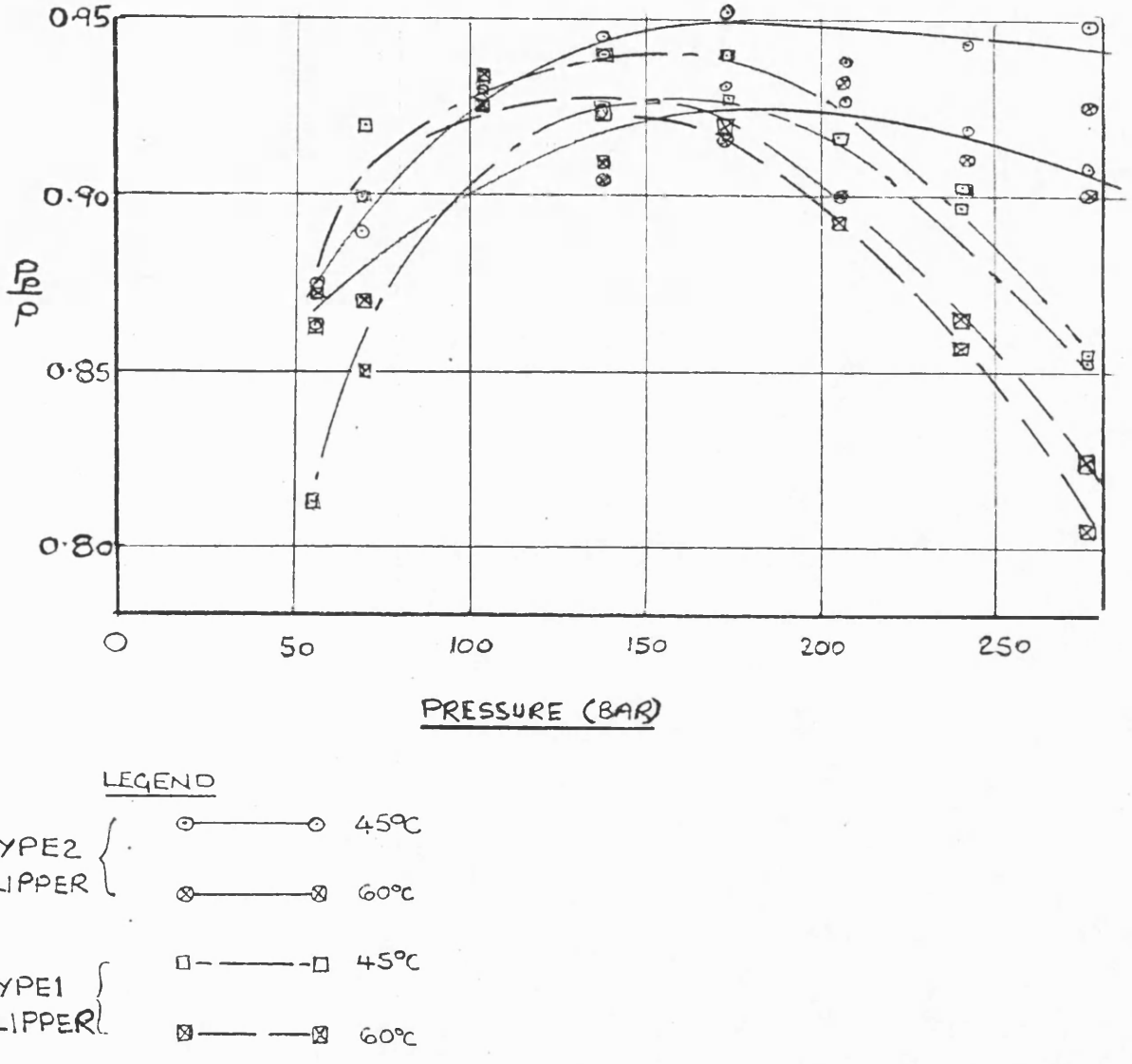

Fig 16 Variation of the slipper pocket pressure with supply pressure and temperature under static conditions

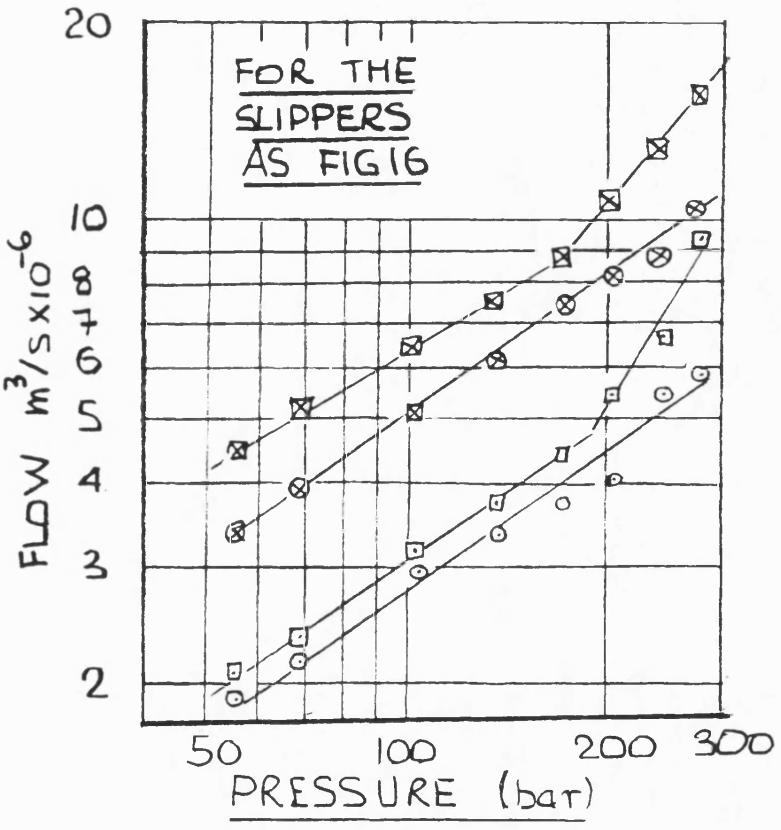

Fig 17 Slipper leakage flow

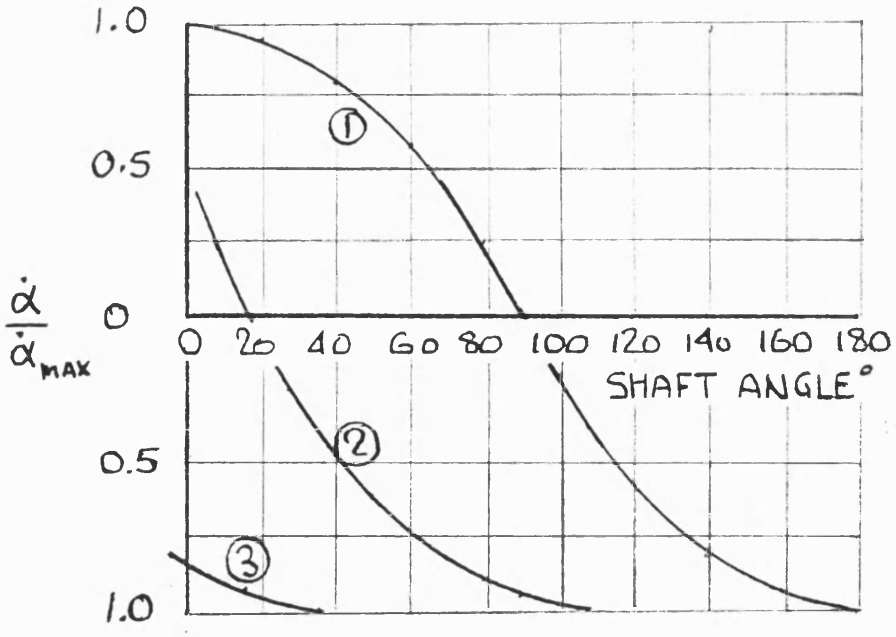

Fig 18 Con rod velocity variation with shaft angle

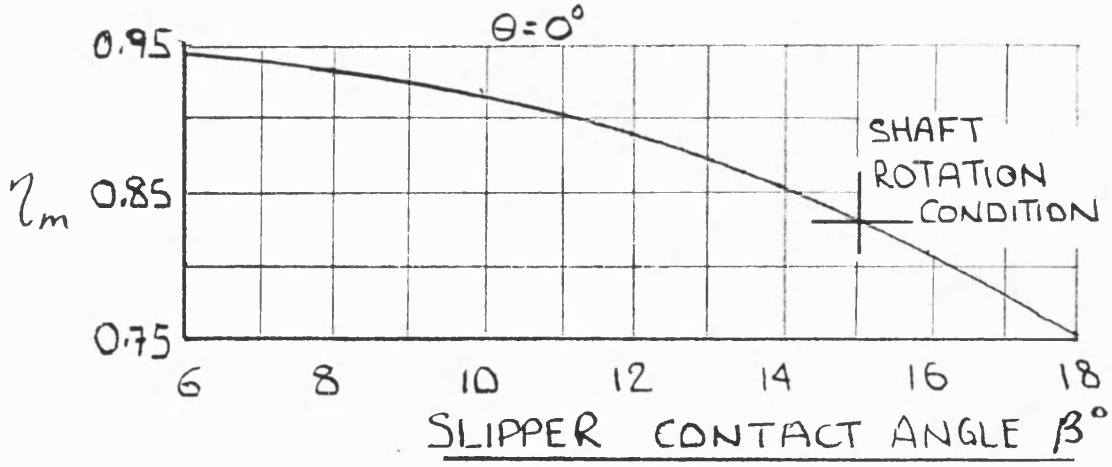

Fig 19 Theoretical variation of η_m with the slipper contact angle β

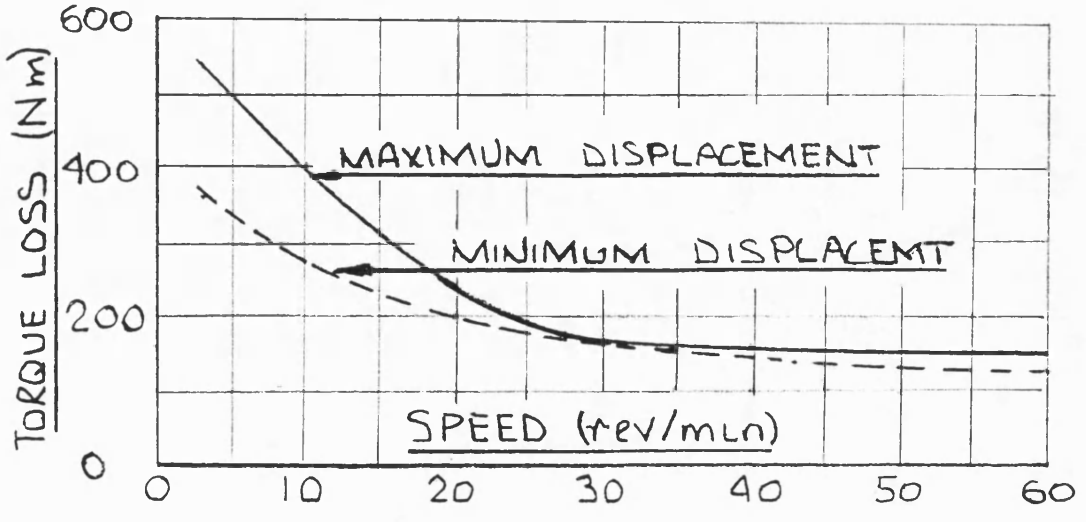

Fig 20 Measured torque loss variation with speed

CHAPTER 4

REGIMES OF LUBRICATION AND THEIR EFFECT ON FRICTION

1.0 INTRODUCTION

The mathematical analysis developed in Chapter 2 for the motor used fixed values for the three coefficients of friction. However comparisions with the measured motor performance showed that these coefficients are likely to vary during the pressure cycle. The test results at the higher speed indicate that, as might be expected, the coefficients would need to vary in a somewhat different manner than those at the lower speed.

The basis of a friction coefficient relates to operation of the sliding surfaces under dry conditions or those of boundary lubrication. These conditions may exist at low speeds but clearly, it is necessary to examine the various load carrying bearings in order to establish the likely lubricating processes and how these might change over the operating envelope of the motor.

The three bearing surfaces experience sliding velocities that vary during the pressure cycle. That of the slipper varies about a mean value but for the con rod bearing and the piston to cylinder interface the velocity fluctuates about zero. In particular the surface velocity of the con rod bearing is zero when the shaft is at 90^{0} whilst that for the piston is zero at the outer and innermost positions .

The performance of the bearings will therefore, to a greater or lesser extent, depend upon;

a) The effects of squeeze films on the rate at which the bearing clearance closes following the commencement of the pressure cycle. For the con rod bearing the squeeze process may also have an effect when the rotational velocity is zero.

b) The level of distortion in the joint

c) Hydrodynamic effects which reduce with reducing speed

2.0 SQUEEZE FILM EFFECTS

When two adjacent surfaces are put under compressive load, the surfaces will approach each other at a rate dependent on the oil leakage from the clearance space. The mass of the components in question is small in relation to the applied pressure force. Consequently the oil pressure that arises will be that which creates sufficient separating force in opposition to that which is applied. This means that, because of the small mass of the moving parts, for instantaneous changes in the applied force there will be instantaneous changes in the separating pressure.

Thus for a given applied force the larger the area of the separating faces, the lower will be the required separating pressure and hence the rate of closure of the faces. In the motor, the con rod bearing has the largest ratio of applied force to bearing area of the three sliding faces. Consequently the level of friction during conditions of boundary lubrication is likely to be critically dependent on the clearance in the bearing. This bearing is spherical (Fig 1) except that the cup is formed by machining the spherical surface about a point that is to one side of the centreline, the appropriate choice of which distance determines the angle of contact.

An analysis of the pressure generated in the squeeze film between these two surfaces is given in Appendix I. The solution of this problem requires the numerical integration of equation 7 in Appendix I for the radially inward flow in the inner region where $r<r_m$. The radius r_m is that at which the maximum film pressure P_m occurs. Thus (dh_1/dt) can be obtained in terms of the maximum pressure P_m at the given radius r_m and the clearance h_1.

Similar integration for flow in the outer region for $r>r_m$ enables P_m to be obtained as a function of h_1 and dh_1/dt. By equating the equations for P_m thus obtained, the variation of (dh_1/dt) with r_m and h_1 can be determined. This analysis only applies to the ideal situation of perfect sphericity of the components. There will be, in fact, considerable distortion of the surfaces and the solution of this problem would require Finite Element and Computational Fluid Dynamics Programs in which interactive capabilities are available.

The components are in contact on a line at 45^0 to the bearing axis and when pressurised the contact zone will produce surfaces which are parallel. On either side of this zone the film thickness will be divergent and to simplify the analysis of this situation the effect of squeeze films is considered for:

a) A flat annular ring and a flat face

b) An annular ring that has a convex surface and a flat face

2.1.0 Flat Annular Ring

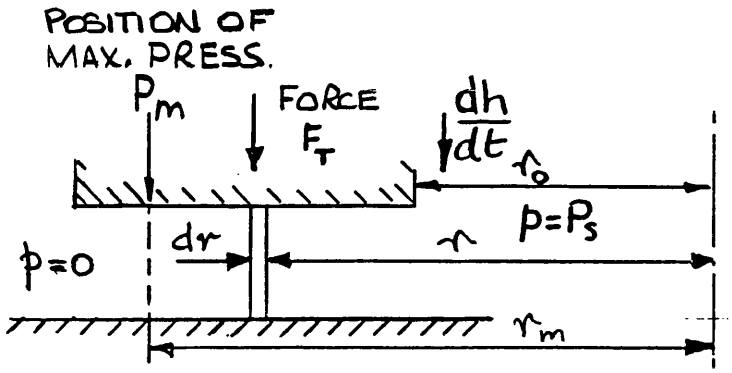

The squeeze film effect for the annular ring is analysed initially in Appendix II for the general case of convergent clearance in the outward radial direction which is then simplified for the special case of parallel clearance.

Using the dimensions for the spherical bearing (ref Fig 1) where r_0=14.26*mm*, r_c=20.16*mm* and r_1=24.7*mm*, it is useful to first consider the case of parallel clearance for plates having these inner and outer radii. Here it is a question of selecting a value for r_m in order to obtain a value of $(3\mu/h^3)dh/dt$ (hereafter referred to by S_P) from equation 12 Appendix II that produces a force that is equal to the applied force. Taking the applied force, F_T, as that acting on the piston for a supply pressure (P_s) of 200 bar produces the following values:

r_m = 18.99 mm

$(3\mu/h^3)dh/dt$ = - 1.91x10^{12} Nm^{-4}

P_m = 1130 bar

F_T=99000 N

The pressure distribution for this constant viscosity situation, shown by graph (a) in Fig 2, would be sustained for all values of the clearance h as it diminishes. The change of clearance with time can be established by integration of $(1/h^3)dh/dt$

Thus $dh/h^3 = - 1.91\times10^{12}t/3\mu$

$$(1/h^2 - 1/h_1^2) = 2x1.91x10^{12}t/3\mu$$

Taking a value of μ=0.05 Nsm^{-2} and for h_1=10^{-5}m, we obtain:

$$t = 3.9x10^{-14}x(10^{12}/h_2^2 - 10^{12}/100)$$

$$t = 3.93x10^{-2}x(1/h_2^2 - 1/100)$$

Here h_2 is in micron. Typical values for the time t for the clearance to reduce are given in the following table:

h_2(μm)	t(s)
5	0.0012
1	0.039
0.5	0.1560
0.10	3.90
0.05	16.00

It is of interest to determine how the value of the radius r_m affects the value of the parameter S_P. Examination of equation 12 Appendix II shows that S_P is negative (ie h decreases with time) for r_m less than the critical value of:

$$((r_1^2-r_o^2)/2\log(r_1/r_o))^{1/2}$$

For r_m greater than the critical value, the value of S_P that satisfies the flow equations becomes positive. For this zone P_m is negative, which represents a physically unrealisable situation. There are therefore two flow zones either side of the critical radius at which the magnitude of the values of S_P and P_m tend to infinity.
For the given conditions the critical radius occurs at r_m = 19.24 *mm*. The variation of P_m with r_m is shown in Fig 3 from which can be seen the value that corresponds to that of the pressure distribution of graph (a) in Fig 2. Fig 3 also shows the variation of the squeeze force with S_P which gives the value of S_P when the squeeze force is equal to the available piston force.

2.1.1 The effect of Pressure on Viscosity

At the high levels of pressure that are generated between the faces of the bearing it is pertinent to examine the influence of pressure dependent viscosity (piezo viscous fluid) on the squeeze film effect. As shown by Cameron[18], the viscosity variation can be modelled quite accurately for pressures in the range up to 1500 *bar* by:

$$\mu=\mu_0 exp(K_0 p) \qquad (1)$$

where μ_0 is the datum viscosity for the fluid at the supply temperature. Equation 1 can be included in the flow equations in Appendix II from which P_m can be obtained as follows:

$$exp(-K_0 P_m) = exp(-K_0 P_s) - K_0(S_P) I_I \qquad (2)$$

$$\text{and } exp(-K_0 P_m) = 1 - K_0(S_P) I_o \qquad (3)$$

Here $I_0 = r_m^2(2l_n(r_1/r_m) - (r_1/r_m)^2 + 1)$

and $I_I = r_m^2(2l_n(r_o/r_m) - (r_o/r_m)^2 + 1)$

Equations 2 and 3 give:

$$S_P = (1 - exp(-K_0 P_s))/K_0(I_0 - I_I) \qquad (4)$$

where $I_0 - I_I = 2r_m^2 l_n(r_1/r_0) - (r_1^2 - r_0^2)$

Now for constant viscosity, when $K_o = 0$, we have from equation 12 Appendix II:

$$S_{P0} = P_s/(I_0 - I_I)$$

For a given value of r_m, the ratio of the S_P values for the constant and variable viscosity cases are:

$$S_P/S_{P0} = (1 - exp(-K_0 P_s))/K_0 P_s \qquad (5)$$

From the BP literature for their range of oils a typical value of K_o is $2x10^{-8}\ N^{-1}m^2$. This causes the viscosity to increase by a factor of 7.38 for a change in pressure from 1 to 1000 bar. This value will depend on the type of oil used and takes no account of temperature changes in the fluid resulting from the energy dissipated in the viscous flow.

For this value of K_0 the ratio of S_P values obtained from equation 5 is 0.83. Taking a value of r_m = 18.72 *mm* the value of P_m is 2422 bar compared with 600 bar for $K_0 = 0$. Thus a given value of P_m will occur at a smaller value of r_m than that for $K_0 = 0$.

The pressure distribution obtained from the boundary conditions and a given value of r_m is given by:

$$exp(-K_0 p) = exp(-K_0 P_m) + S_P K_0 r_m^2 (2 l_n(r/r_m) - (r/r_m)^2 + 1) \quad (6)$$

For $K_0 = 2x10^{-8}$, the value of r_m was chosen that gave the same value of P_m as that which provided balance with the piston force when $K_0 = 0$ (ie 1130 *bar*). This produces the pressure distribution shown by graph (b) in Fig 2 which will give a very similar separating force as that obtained for K_0=0 but with r_m = 18.6 *mm* rather than 18.99 *mm*. However the value of S_P has reduced to $-6.7x10^{11}$ which increases the time for the clearance to close by a factor of 2.85.

2.1.2 The Effect of Viscous Heating on Viscosity

In the paper by Thoma[19] on sealing gaps which included the effect of viscous heating of the fluid, the separating force was shown to be less than that obtained for a constant viscosity fluid. The amount of the reduction was shown to be dependent on the pressure level. The analysis was for the fluid flow across a clearance which took no account of heat transfer between the fluid and the surfaces of the components.

This approach can be applied to the squeeze film effect by assuming that the fluid viscosity varies exponentially with temperature.

Thus $\mu = \mu_1 exp(-B\,(T-T_0))$ (7)

where T_0 is the supply temperature and T the temperature at any point in the flow. If it is assumed that the value of B does not vary with pressure then μ_1 can be represented as a function of pressure as in equation 1.

Thus $\mu = \mu_0 exp(K_0 p) exp(-B\,(T-T_0))$ (8)

where μ_0 is the viscosity at the inlet temperature and atmospheric pressure.
The increase in fluid temperature is caused by the dissipation of pressure due to viscous effects.

Thus $\rho C_P (T - T_0) = (P_m - p)$

so $T - T_0 = (P_m - p)/\rho C_P = C(P_m - p)$ (9)

Equation 9 into equation 8 gives:

$$\mu = \mu_0 exp(K_0 p) exp(-BC\,(P_m - p)) \quad \text{where } C = 1 / (\rho C_p)$$

$$\mu = \mu_0 exp((K_0 + BC)p) exp(-BCP_m) \qquad (10)$$

Substitution for μ into the flow equations in Appendix II yields two equations for P_m which are given by:

$$exp(-K_1 P_m) = exp(-K_1 P_s) - S_P I_I K_1 exp(-BCP_m) \qquad (11)$$

where $K_1 = K_0 + BC$

and

$$exp(-K_1 P_m) = 1 - S_P K_1 I_0 exp(-BCP_m) \qquad (12)$$

These equations then give:

$$exp(-K_1 P_m) = (I_I - I_0 exp(-K_1 P_s))/(I_I - I_0) \qquad (13)$$

and

$$S_P = (exp(-K_1 P_s) - exp(-K_1 P_m))/K_1 I_I exp(-BCP_m) \qquad (14)$$

Thus at a given value of r_m values for I_I and I_0 can be obtained which then allow values for P_m and S_P to be determined from equations 13 and 14. Taking B as 1/36 which represents a 67% reduction in viscosity between 40 and 80°C the value of P_m of 1130 bar occurs at r_m =18.3 *mm*, but S_P has increased in magnitude to 2.2×10^{12} (cf 6.7×10^{11}). More importantly the resulting pressure distribution will not produce sufficient resisting force. Even with P_m as high as 1666 bar the pressure distribution, shown by graph (c) in Fig 2, still produces less force than that required, as can be seen by comparison with that of graph (a). At this condition the magnitude of S_P has increased to 5.37×10^{12} (2.81 times greater than for the case of constant viscosity). The effect of temperature on viscosity due to viscous heating is thus seen to have a significant effect on the rate at which the film closes during the squeeze film process.

3.0 SUMMARY FOR THE PARALLEL CLEARANCE CASE

To summarise this examination of squeeze film effects for a parallel clearance the process probably falls between those obtained for isothermal (ie B=0) and adiabatic conditions. The value of S_P for the constant viscosity case falls roughly between these two extremes. Fuller[20] refers to experimental work carried out using optically flat plates which produced times to close the gap that were significantly greater than those predicted by the theoretical constant viscosity model, particularly when the film thickness was less than about 1 micron.

Because of the squeeze film effect, surfaces can therefore remain separated for quite considerable periods of time. Thus, for example, closure of the film to the level of 0.1 micron would take, for conditions of constant viscosity of 0.05 Nsm^{-2}, approximately 4s. For the motor operating at 3.4 rev/min the time for one half revolution is 8.8s. A shaft movement of 5^0 either side of 90^0, when the con rod is at its maximum angle, creates a displacement in the bearing of $8.6 \times 10^{-4} m$ during a period of 0.25s. Thus for the bearing surfaces that are parallel, the squeeze film effect can play an important role in minimising possible surface contact.

For the con rod bearing dimensions given in Fig 1, contact between the two spheres occurs at the radius r_c at an angle to the centre line of 45^0. The clearance between the two components varies with angular position about the contact point as shown in Fig 4. This clearance is, however, extremely sensitive to the effect of distortion of the piston cup. For a constant pressure of 1000 bar applied to the cup the resulting distortion, obtained by finite element methods, is also shown in Fig 4. This produces an upward bulge in the cup and causes the sphere to contact the cup at a slightly smaller radius shown by point A in Fig 4. This creates inward and outward flows that pass through clearances that are varying divergently with a critical radius r_m that will be less than the radius corresponding to the new contact point at A (see Fig 4).

The effect of tapered films between the two surfaces can be examined using the analysis of Appendix II with particular reference to a determination of the influence that this has on the time for reducing the film thickness.

4.0 TAPERED CLEARANCES

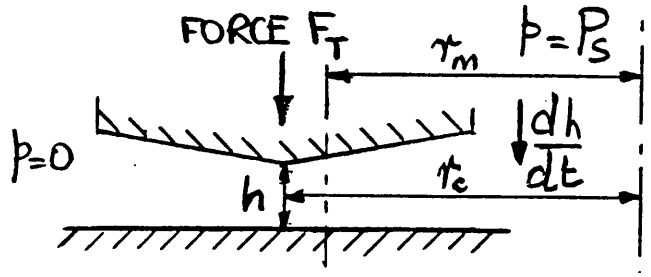

In the analysis of Appendix II, for a given change in clearance with radius the integrals I_D, I_0 and I_1 can be obtained for a given value of r_m. Here I_D is the integral that is obtained from considering the flow in the radially divergent region for $r>r_c$.

Using equation 21 of Appendix II produces a value for $6\mu dh/dt$ (referred to as D_T) which enables values for P_m and P_c and the pressure distribution to be calculated.

The problem here is that D_T is a function of the level of clearance. Consequently the value of D_T needs to be determined at different clearances, the closure time being the area under the graph of dt/dh against h.

The clearance variation in Appendix II is defined by the slope of the surface which is denoted by the dimensionless parameter a. Some resulting pressure distributions for values of a of 0.0002 and 0.0004 are shown in Fig 5 for two different clearances.

Referring to Fig 4, the clearance variation for a slope of 0.0004 is shown in relation to that for the bearing cup. The bearing pressure distributions, as can be seen from Fig 5, have a much more pronounced peak than that obtained for a parallel clearance. For a given peak pressure the closing rate between the two faces is greater than that of the parallel clearance resulting in the closing time being reduced. The variation in clearance represented by the chosen values of a are:

a	.0004	.0002	.00004
H_0-H_1 (μm)	4.18	2.0	.418

These variations in clearance are small but they become significant when the minimum thickness (H_1) falls to less than 1μm. The calculated rate at which the film thickness reduces becomes smaller as H_1 reduces.

The variation of dt/dh with H_1 is shown in Fig 6 for a peak pressure of 1130 bar, giving a time for the clearances to close from 0.6 to 0.1 micron that is approximately 1/50th of that for the parallel clearance. For a peak pressure of 3000 bar this time would reduce to 1/100th of that for the parallel plate.

The minimum possible clearance will depend on the surface finish of the components, the actual shape of the surfaces and the properties of the fluid. If hydrodynamic lubrication is possible this will determine the final level of clearance after the squeeze film effect has ceased. The next sections will examine these aspects in order to establish the lubrication mechanisms that are likely to prevail under the range of operating conditions.

5.0 COMPONENT DISTORTION

5.1 Con Rod Bearing

It was shown in section 3 that the levels of distortion generated by a pressure of 1000 bar are of the same order of magnitude as the shape of the clearance path between the sphere and the cup in the con rod bearing.

The degree of distortion that is obtained when the piston force is impressed on the bearing can be determined approximately by using the equations for the contact between two discs whose length is that of the contact path. Here the piston cup is a disc the surface of which has negative curvature. The Hertzian equations for this situation, represented in the following diagram and summarised by Cameron[18], produce the following relationships:

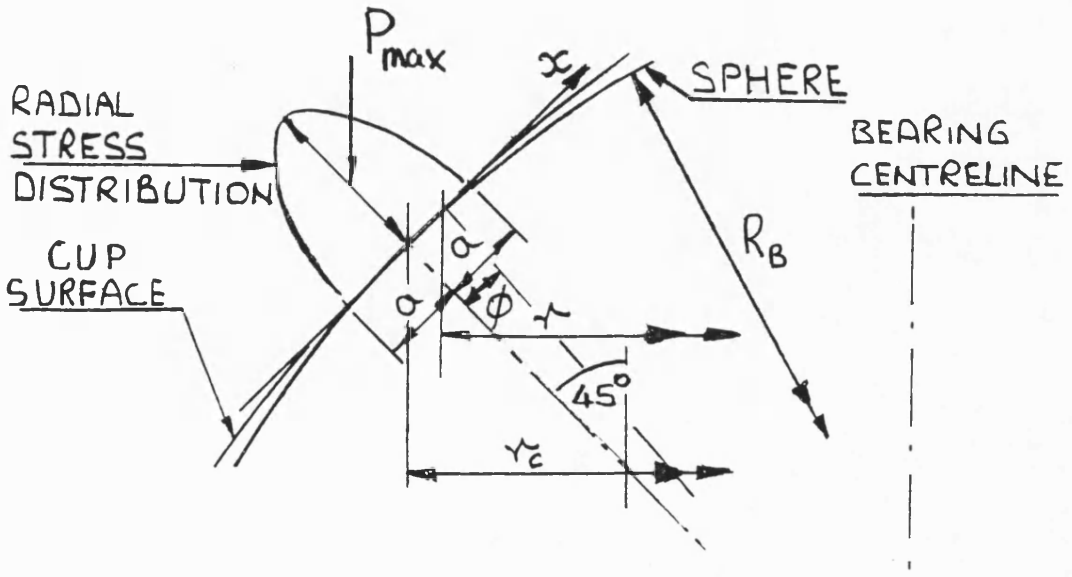

$$P_{max}=0.418(EW/RL)^{1/2}$$

and $a = 1.52(WR/LE)^{1/2}$ (semi width of the contact zone)

where Poisson's Ratio =0.3

For the ball joint the radius of curvature $R = R_c^2/c$

where c= difference in the two radii

From Fig1 we have R_c=29.2 *mm*

For a contact angle of 45^0 and a radius of the sphere of 28.51 *mm*

we get:

$$c = 0.69\ mm$$

$$R=1.24\ m$$

$$L=130\ mm$$

For $E=2.1x10^{11}$ Nm^{-2} and W=96000x1.414 *N* (piston force resolved normal to the contacting surface for P_s =200 bar) gives.

$$P_{max}=1758 \text{ bar}$$

and $a= 3.77\ mm$

The pressure distribution for the contact conditions is given by:

$$p=P_{max}(1-(x/a)2)^{1/2}$$

From the diagram the radius $r = R_B\sin(45 - \phi)$ or $R_B\sin(45 + \phi)$

and $\phi = x/R_B$

where the circumference of the circle is assumed to be a straight line over the angle ϕ.

For the dimensions of the bearing, this pressure distribution is shown by graph (a) in Fig 7. Fig 7 graph (b) shows the pressure distribution for the squeeze film for the parallel plate as derived in section 2.1.0 and shown in Fig 2 (a). Applying the squeeze film analysis to the Hertz contact width produces the pressure distribution shown by graph (c) in Fig 7. This produces a squeeze rate which is 7 times greater than that for the larger area. The corresponding times to squeeze down to 0.1 and 0.05 μm would be 0.57s and 2.26s respectively.

The pressure on either side of the contact zone will depend on the amount of hydrodynamic effect that is present. The presence of such pressure will reduce the force across the contact zone and hence the level of distortion thus created. The presence of supply pressure (P_s) will also reduce the contact force and alter the level of distortion.

5.2 Slipper Bearing

The clearance between the slipper bearing face and the eccentric will vary either side of the line of contact by an amount that is dependent on the value of e_c. There will be distortion around the rectangular periphery of the slipper which will create increases in the clearance. It will also cause the clearance to be tapered in the outward direction by varying amounts around the periphery. This will result in increased leakage and reduced pressure force on the slipper lands which will increase the magnitude of the contact force (F_c). The effect of this will be similar to that caused by increasing the slipper radius in relation to that of the eccentric. The effect of changing this parameter was demonstrated in Chapter 2 to have a considerable influence on motor efficiency.

Kobayashi and Ikeya[7] have carried out a structural analysis of the piston to slipper pad ball joint for an axial piston swash plate pump using finite element methods. This configuration is axisymmetric and the flow through the slipper clearance was obtained by integration of the variation in clearance with radius. The film clearance between the slipper pad and the swash plate was then adjusted to give a hydrostatic pressure force which balanced that of the piston by considering the pressure drop across the hydrostatic feed restrictor.

The work showed how the film thickness and leakage flow varied with the thickness of the slipper pad. This analysis for static conditions did not include the condition where the slipper comes into contact with the swashplate in order to overcome friction in the ball joint.

The con rod and slipper component in the radial piston motor has a complex shape which is not axisymmetrical and involves a complex distribution of the various forces. The evaluation of this situation using finite element methods would be considerably more complex than that for the axial piston machine described. Such techniques are not generally available at the current time.

5.3 Piston and Cylinder Distortion

The results obtained by Ezato and Ikeya[6] showed that the friction coefficient between the piston and cylinder of an axial piston machine varied with the pressure, speed and the angular position of the shaft. For a given shaft position and speed there were no significant differences in the values of the friction coefficient with changes in pressure. This tends to indicate that distortion of the components at the point of contact has little effect on the conditions at the contact. As with the ball joint the shapes of the components and the force distribution are complex for which computational techniques are not available at the present time to solve this type of problem.

5.4 Summary

There are varying degrees of distortion in the sliding faces of the motor which cannot be determined accurately. As a result it is difficult to define, with any precision, the lubricating mechanism in the bearings. However it is worthwhile, despite the difficulties introduced by the effect of distortion, to investigate the possibility of hydrodynamic lubrication.

6.0 Hydrodynamic Lubrication

The existence of hydrodynamic lubrication largely depends on the film thickness which can be estimated using well known methods. For this section the methods described by Fuller[20] are used for examining the con rod and slipper bearings. Fuller presents the results of numerical methods developed separately by Karelitz[21] and Needs[22] for the solution of Sommerfeld's theory for journal bearings.

The contact force between the slipper and the eccentric arises when there is insufficient force from the hydrostatic pressure. This force has to be carried by the rectangular edges of the hydrostatic slipper bearing pocket. For this situation the numerical method produces a film thickness of less than 0.3 micron at a speed of 50 rev/min for a

value of e_c of 25 micron. This would be considered too small to support hydrodynamic lubrication and at the test speeds of 3.4 and 9.2 rev/min the bearing must therefore be operating under boundary lubrication conditions.

Assuming that the con rod bearing has retained its circular shape but that the distortion has reduced the difference in radii of the components to 2.5 micron, film thicknesses of less than 0.2 micron at speeds less than 50 rev/min are obtained. The distorted shape of the bearing will be far from circular (at the level of elastic displacements less than 10 micron) but it may be that wedge shapes are created which could conceivably generate hydrodynamic effects.

The surface finish of the components is of great importance and it is the experience of the author that when this is greater than around 0.3 micron, poor performance and failure will result. It is interesting to note that after initial operation of motors for a few tens of hours the surface of the sphere becomes smooth to a level of less than 0.03 micron.

The operation of motors with high back pressure for even relatively short periods of time can cause failure of the con rod bearing. When operating under these conditions the sliding surfaces are continuously loaded. Under conditions of low backpressure these surfaces are unloaded for one half of the cycle during which time the film thickness between these surfaces can increase. The fact that the presence of backpressure causes failure indicates the importance of the squeeze film effect on the lubricating mechanism.

The wear problem reported in Chapter 3 when operating with water based fluids is likely to be due to poor lubricity but this may also be associated with a reduction in squeeze film effects due to reduced viscosity.

It is interesting to note that some earlier types of radial piston motors did not have hydrostatic bearings in the slippers. During stall conditions squeeze film effects in the slipper bearing caused the mechanical efficiency to reduce to around 25% after a period of 40 to 50 seconds. This would have required the slipper coefficient of friction to rise to a level of about 0.45.

In this context the loss of torque during the very low speed test at low motor displacement, described in Chapter 3, must have been due to squeeze film effects eventually resulting in a breakdown of the boundary lubrication conditions.

7.0 EVALUATION OF THE MODEL USING VARIABLE FRICTION COEFFICIENTS

7.1 Introduction

The difference between the mechanical losses obtained from the model for constant values of the friction coefficients and the measured results, as described in Chapter 2, can be ascribed to:

a) The conditions of lubrication between the contact surfaces.

b) The solid body assumption used to describe the forces acting at the contact interfaces.

In section 6.0 it was shown that the possibility of hydrodynamic lubrication in the slipper bearing at speeds lower than 50 rev/min is unlikely. In the the con rod bearing the possibility of hydrodynamic lubrication is dependent on the level of distortion of the components. However, even when severe distortion is assumed, it was shown in section 6.0 that hydrodynamic lubrication is unlikely.

In this section the model is used to show how variations in the friction coefficients can produce a similar variation of the losses as those obtained from the tests. As there are three different coefficients to consider the analysis is far from exact, particular in view of the limiting assumptions that are implicit in the model.

7.2 The Effect of Velocity and Lubrication on Friction

In the work by Ezato and Ikeya[6] the friction force between the piston and cylinder of an axial piston swashplate pump was measured using a special purpose test rig. Their results obtained friction coefficients that varied between 0.3 and 0.1 over a speed range of 0.3 to 6 rev/min. At the low speed condition the friction coefficient increased from 0.09 to 0.3 as the piston moved out of the cylinder bore with increasing shaft angle.

The paper by Causemann[14] gave results for the piston friction in a radial piston motor using a special purpose test rig. This indicated values of the friction coefficient that were in the region of 0.09 at 6.5 rev/min falling to 0.06 at 50 rev/min. In the axial piston units the piston is in bending due to the side load from the action of the slipper against the swashplate. This increases as the piston moves out of the cylinder.

In the radial piston motor there is a bending moment only when the con rod bearing centre moves out of the cylinder bore and in some designs this situation never arises thus minimising the forces on the piston. However the length to diameter ratio of the piston is smaller by a factor of around 3 or 4:1 in the radial units. The use of piston seals in radial motors also allows the piston to cylinder clearance to be increased. Both of these factors would, in general, create an increase in the friction in this sliding joint.

The experimental work by Kobayashi[7] et al obtained values for the static friction coefficient for the piston to slipper ball joint in an axial piston machine. These ranged between 0.65 and 0.3 for inlet pressures of 20 bar to 130 bar. The materials used were a high strength steel ball with a slipper cup bearing of high strength brass.

At 3.4 rev/min the velocities of the contacting surfaces are extremely small. For the con rod bearing the velocity ranges from $1.6 \times 10^{-3} ms^{-1}$ at TDC to zero at 90^0 shaft angle whilst for the slipper these velocities are 0.037 and 0.02 ms^{-1}. If the con rod bearing becomes dry the friction coefficient can increase to around 0.7. For the slipper, completely dry conditions would not be expected and the maximum values of the friction coefficients would be likely to be of the order of 0.3 to 0.4.

The work by Rabinowicz[23] on the dependence of the kinetic friction coefficient on previous sliding history, showed wide variations in its value at very low speeds of contact. The values are also strongly dependent on the degree of prevailing lubrication. For steel on steel the coefficients range between 0.05 for perfect lubrication and 0.7 for unlubricated surfaces at a velocity of $10^{-5} ms^{-1}$. At $10^{-3} ms^{-1}$ these values change to 0.1 and 0.6 respectively.

An important feature was the dependence of the coefficient on the previous history of velocity with time particularly with reference to the distance travelled. Rabinowicz showed that the coefficient changes gradually and only after a sliding distance of the order of $10^{-5} m$. The static coefficient can, in fact, maintain its initial value unchanged for the first $2 \times 10^{-6} m$.

This effect is demonstrated by the stick slip motion that was shown by the tests at 3.4 rev/min (Chapter 3) but which was not apparent at 9.2 rev/min. The effect of pressure rise rate during the locked shaft test (Chapter 3) also demonstrates this phenomena by causing larger rotational movements as the pressure rise rate is increased.

7.3 Variable Friction Coefficients

7.3.1 The Model Results for the 3.4 rev/min condition

The results from the model using constant values of the friction coefficients for the 3.4 rev/min case shown in Fig 5 Chapter 2 were principally at variance with the measured results in particular ranges of the shaft rotation.

For the analysis discussed in 5.1, with direct contact between the con rod bearing components at 100 bar supply pressure, the peak radial stress would be 880 bar in the centre for the contact zone. The resulting pressure distribution would be impressed on any fluid present in the bearing film. The bearing takes 1s to rotate through the shaft angle range of 80^0 to 100^0 when the con rod angle changes by only +- 0.2^0. It is likely that the film in this region is extremely thin. The amount of fluid that is both retained in the film and brought in during small movements of the bearing will, to a large extent, depend on the lubricity of the fluid. The process will also be influenced by any squeeze film effects.

The variation in the friction coefficients shown in Fig 8 was based on a general increase over the one half revolution cycle with $f_B > 0.147$ in the cylinder at 90^0. This causes the piston to be tilted in the cylinder bore as described in 8.2 Chapter 2. The piston then experiences full rotation in the two regions of $F_1 = 0$ followed by $F_2 = 0$. This also causes the reduction in the losses at 18^0 motor shaft angle, shown in Fig 9, when piston rotation commences with $F_1 = 0$.

The reduction in the frictional coefficients between 130^0 and 180^0 was found to be necessary to establish the magnitude of the torque step at 36^0 motor shaft angle. This depends entirely on the values of the friction coefficients that relate to the cylinder for which the shaft angle is 180^0 when the motor shaft angle is 36^0. A reduction in the value of f_B is felt to be realistic if it can be accepted that the introduction of fresh fluid into the con rod bearing will sufficiently improve the conditions between the surfaces.

The results from the model, shown in Fig 9, provide particularly good agreement in the range of 15^0 to 30^0 shaft angle. The model shows that, in this region, rotation of the piston in its clearance with the cylinder occurs which causes the reduction in the losses between 18^0 and 25^0.

The results displayed in Figs 5 Chapter 3 show small variations in the measured cyclic fluctuations in motor torque. These variations will be caused by differences in component dimensions, clearances, surface roughness and so on. In particular the torque loss would be expected to increase when a piston is pressurised at each cyclic interval of 72^0 as predicted by the model. The measured results do not show this which is probably due to overlap in the distributor valve.

At the TDC position, the initial film thickness would have been relatively large as the piston had been under only 2 to 3 bar pressure immediately prior to this position. The rotational movement to 10^0, which takes 0.5s, will be associated with a squeeze film effect in all three of the bearing surfaces. The model was altered slightly, as shown by the dotted lines in Fig 8, to reflect this situation which has caused a reduction in the mechanical loss of 0.007 (0.7%) at 0^0 shaft angle as shown in Fig 9.

The purpose of the analysis has been to obtain a model that is a realistic representation of the motor under given conditions. This can then be used for design purposes in order to examine the effect of changes to various parameters or improvements in the design principles used in the motor. The values of the friction coefficients shown in Fig 8 are probably higher than might have been presumed in the absence of a suitable model. These are shown in section 7.3.3 to have a significant effect on the forces acting in the motor components.

7.3.2 The Model Result for the 9.2 rev/min condition

The measured losses at 9.2 rev/min shown in Fig 9 are generally similar in shape to those of 3.4 rev/min for shaft angles above 36^0. However in the range 0^0 to 36^0 the increase is smoother and the magnitude of the step at 36^0 is reduced. Here the general level of the frictional losses has obviously reduced but this has been accompanied by the absence of piston rotational movements after 18^0 shaft angle.

Fig 8 shows the reduced level of the friction coefficients and the overall shape assumed for the analysis. The maximum value for f_B at 0.19 is considered realistic. Here the shaft takes 0.18s to rotate through 10^0. For 10^0 either side of the stationary point at 90^0 the elapsed time is probably still significant in terms of the squeeze film effect. However, the value of f_B at 90^0 is such that the piston is kept against the cylinder wall and piston rotation does not occur.

Torque variations from cycle to cycle are noticeable in the test results of Fig 6 Chapter 3. For the single cycle recording in Fig 4, Chapter 3, the torque at 72^0 shaft angle is lower than it is at 0^0 shaft angle. The measured difference represents a higher mechanical loss of 0.014 (1.4%). This level of variation is significant representing, for example, the effect of a change in the coefficients f_B or f_C of around 0.05.

7.3.3 Motor Parameters

The variation of the piston forces for an individual cylinder during the pressure cycle of one half of a shaft revolution is shown in Fig 10 together with the values for the original constant coefficient model shown for comparison.

The increasing values of the friction coefficients which, as seen from Fig 8, are lower at the start of the cycle than in the constant coefficient model, cause the piston forces to gradually increase with rotation of the shaft. These forces eventually reach significantly higher values in the region 90^0 to 180^0.

In particular, the changes in the range of 90^0 to 100^0 shaft angle reflect the rotational movement of the piston. As described in Chapter 2, the value of f_B is such that the piston is always tilted in the cylinder bore which creates the fluctuations in torque and mechanical losses in this region. Thus at 90^0 shaft angle, F_1 falls to zero as the piston rotates in the reverse direction. When the piston becomes flat against the cylinder wall at 96^0 shaft angle, F_2 becomes zero and the piston pivots about its lower edge when F_1 increases. On the completion of the piston rotation both F_1 and F_2 increase to maximum values that are 33% and 44% greater than the values predicted by the constant coefficient model.

The sum of the piston forces has a maximum value of 0.77 which creates a mechanical loss of 7.7%. These large changes in the piston forces are partly responsible for the changes in the hydraulic slipper pressure ratio P_r which ranges from 0.73 to 0.875 as shown in Fig 13.

The effect of the higher values of the friction coefficients has caused a 43% increase in the slipper contact force (see Fig 14) at 130^0 shaft angle. The variation of the contact force is associated with the changes in the slipper contact angle and the slipper pocket pressure ratio shown in Figs 12 and 13.

A comparison of Fig 9 with Fig 16 of Chapter 2 shows that the motor mechanical losses predicted by the two models are the same in the shaft angle range $0 < \theta < 90^0$. However the individual losses in each of the three cylinders that are operating in this region are substantially different as is shown in Fig 11. These reflect the effect of the changing frictional conditions in the sliding surfaces which are mainly a result of those that occur in the con rod bearing.

8.0 CONCLUSION

This Chapter has attempted to show that, even for speeds up to 50 rev/min or more, the sliding components in the motor are probably under conditions of boundary lubrication. These surfaces experience velocities that vary cyclically. In particular, the velocity in the con rod bearing falls to zero half way through the cycle.

Static friction coefficients vary considerably with velocity and the level of lubrication. In the motor, squeeze film effects are shown to be capable of having an influence on the lubricating mechanism even at speeds down to 3 rev/min. For speeds lower than this, as was described in Chapter 3, the mechanical efficiency of the motor was shown momentarily to fall almost to zero. This was considered to be the result of the bearings being statically loaded for periods of time that were appreciably greater than that of the squeeze film process, thus creating excessively high values of the friction coefficients.

As was shown in section 4.0, the rate at which component surfaces approach each other during the squeeze film process is very sensitive to the presence of non parallelism between the surfaces. In the con rod bearing, the high unit loading creates relatively large distortions which cause the surfaces to be conformal in the region of contact. This ensures that the surfaces are absolutely parallel and the area of contact, although relatively small, is still sufficient to create a significant squeeze film effect between the components.

The thickness of the film can be of the same order as that of the component surface finishes, in which case, it is possible for the squeeze film process to last for periods of time that are significant, even at low speeds.

The effectiveness of the squeeze film process will be considerably influenced by the properties of the fluid. For fluids of low lubricity that also have no piezo viscous properties, the squeeze film process will last for much shorter periods of time. These times may be smaller than those required even for operation at the speeds of 50 to 100 *rev/min* that are typical of the levels used for endurance testing by the coal industry for 60/40 water based fluids. It is in this type of application that the con rod bearing experiences problems of insufficient life which, as was described in Chapter 3, was improved considerably by the use of a phosphor bronze bearing in the piston.

For the slipper and piston bearing faces, the much lower unit loadings will not create such high levels of surface parallelism as in the con rod bearing. As a consequence, therefore, these are not likely to experience the same benefit from squeeze films.

The values of the friction coefficients in the model generally fall in the range of those obtained by the various researchers cited. As described in 7.3.1, the variation of f_B at 3.4 *rev/min* was based on that which caused the piston to be tilted in the cylinder bore when its shaft angle had reached 90^0. The agreement with the measured results could have been improved if f_B had been assumed to increase to higher values in the shaft angle range of 100^0 to 130^0.

However, the variations of all three coefficients were chosen in order to obtain the best overall fit with the measured losses for the particular motor under the given operating conditions. More detailed test methods would be required in order to establish these changes more accurately.

Despite these limitations the results from the model are considered to be accurate at a level that would enable it to be applied to examine methods for improving the design and performance of the motor. It can also be used to determine how the performance is affected by variations in component dimensions, surface finish, clearances and so on. Chapter 5 will be concerned with such applications and the use of the model for forming the basis of an alternative operating principle in a radial piston motor.

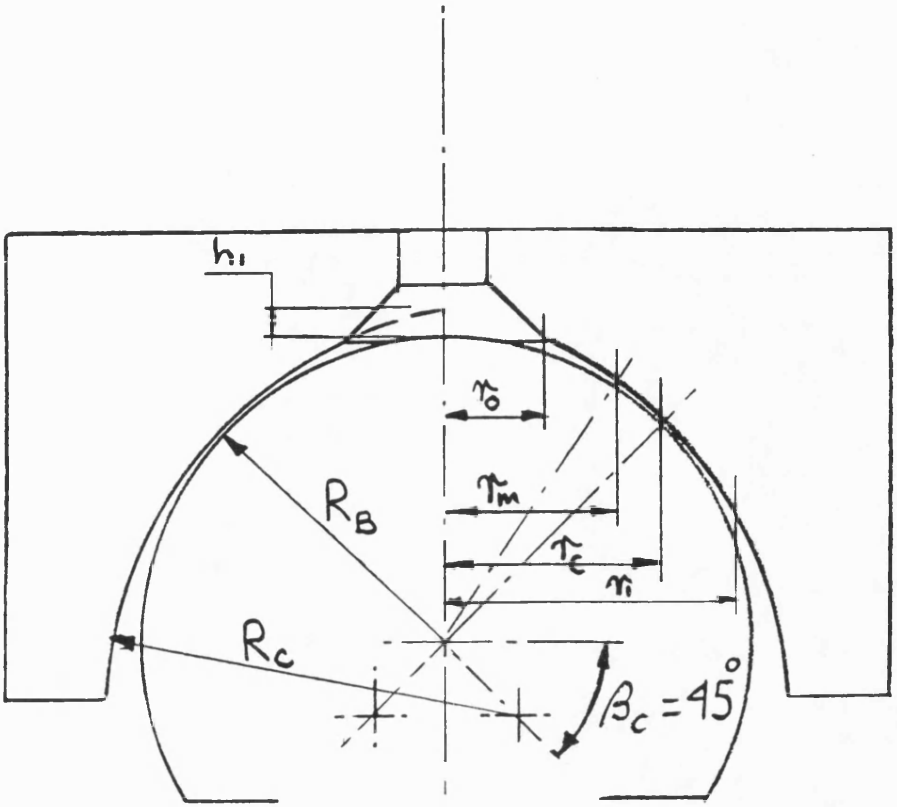

$r_o = 14.26$ mm
$r_c = 20.16$ mm
$r_i = 24.70$ mm
$R_c = 29.20$ mm
$R_B = 28.51$ mm

Fig 1 Cross section of the con rod bearing

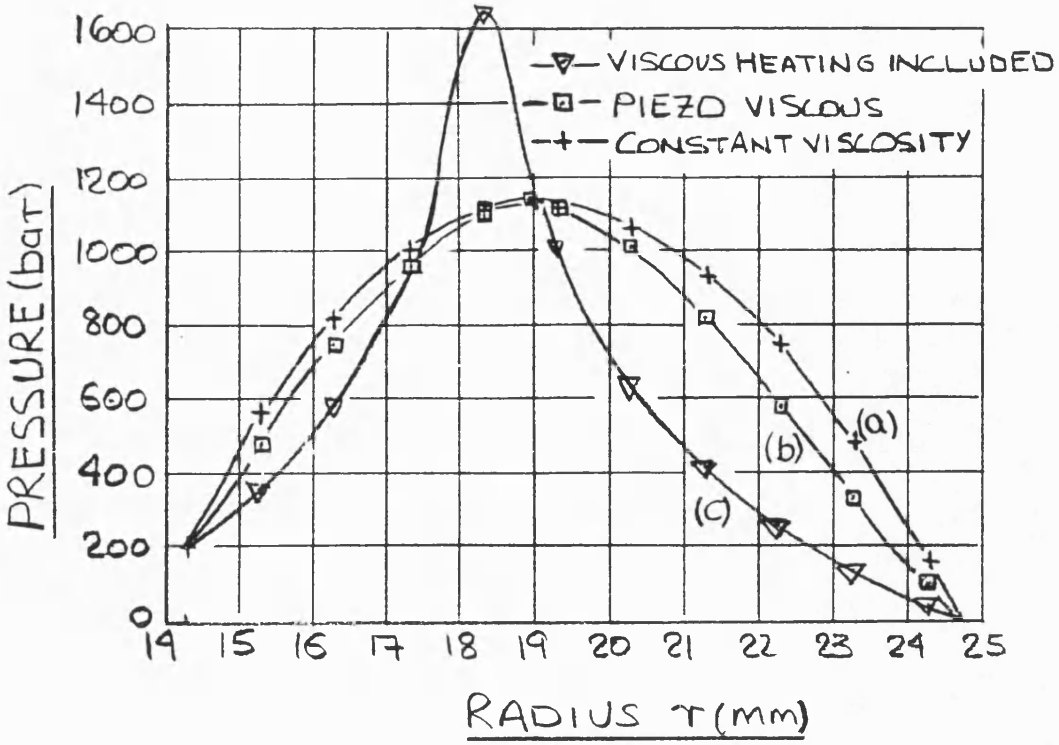

Fig 2 Squeeze film pressure distribution for parallel plate

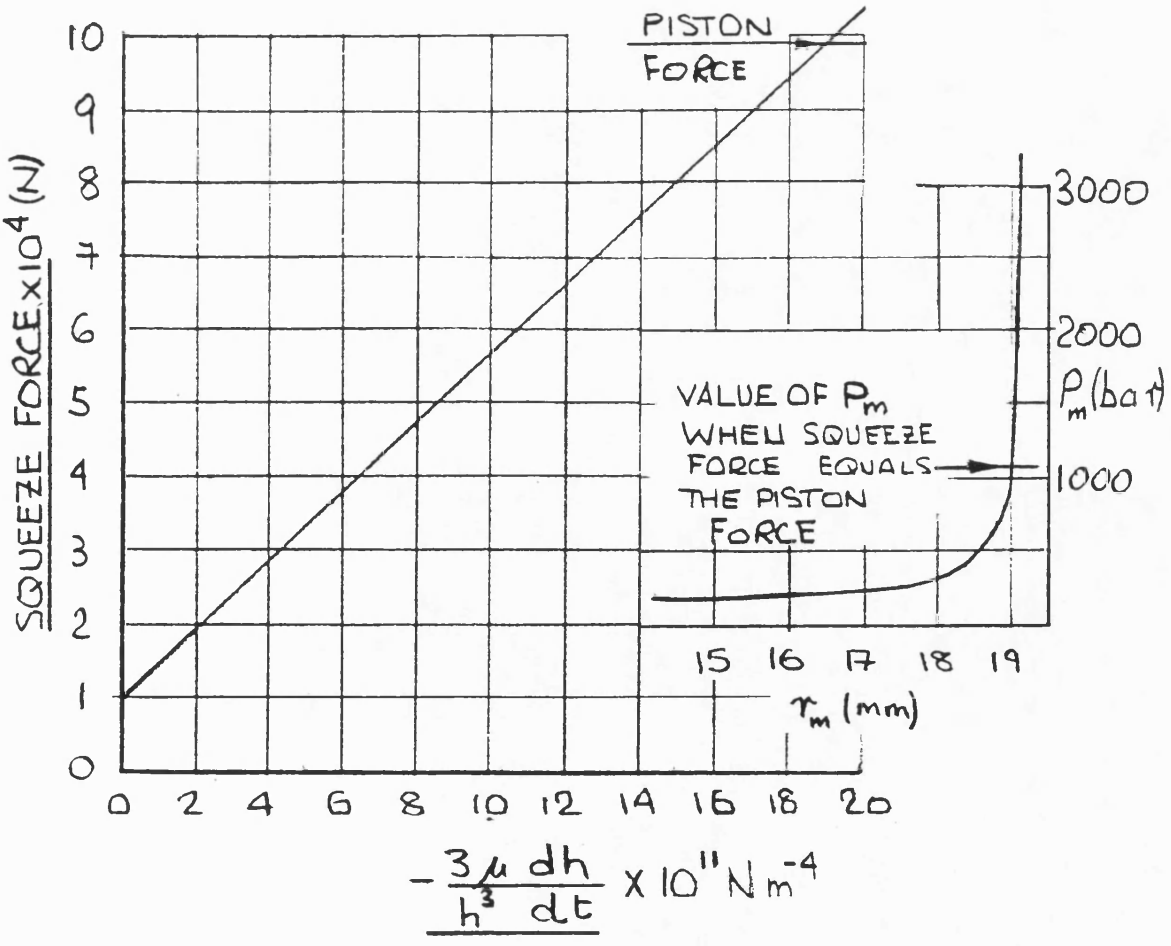

Fig 3 Squeeze film force, rate and maximum pressure for parallel plate

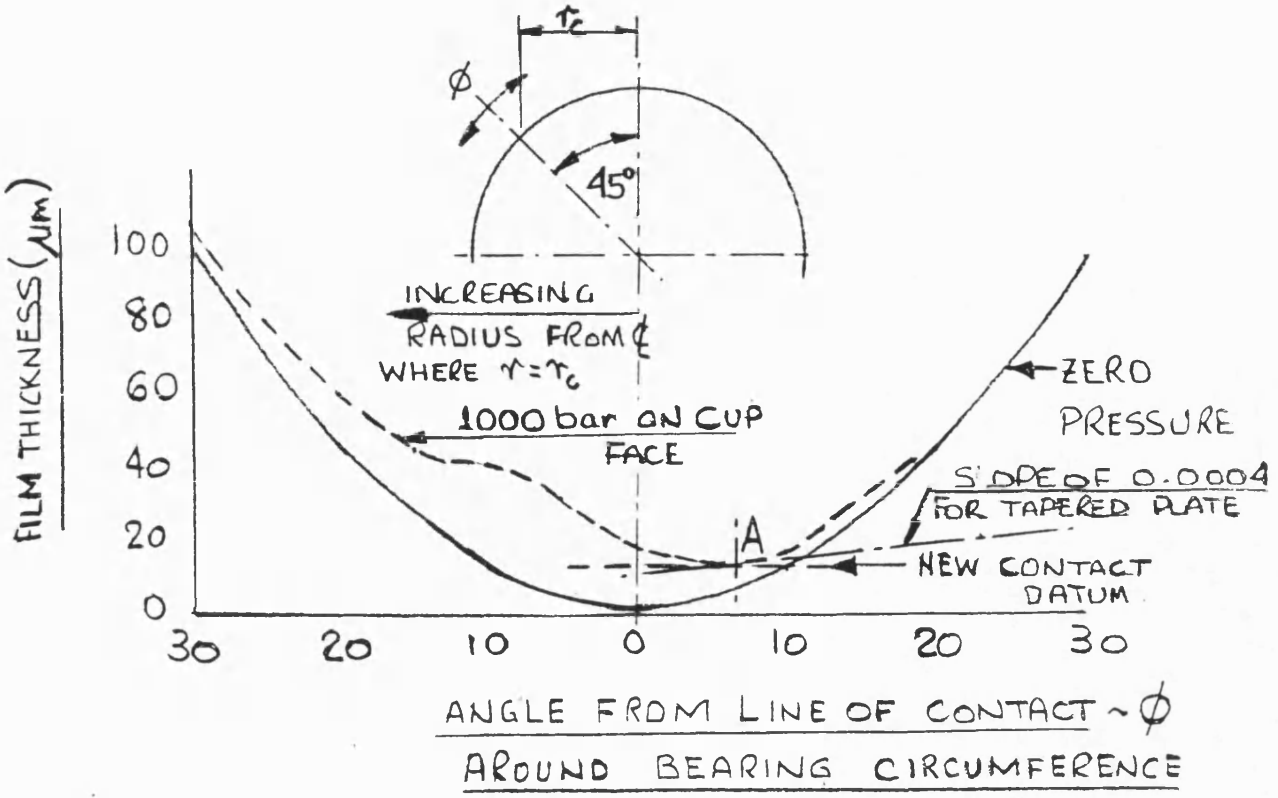

Fig 4 Con rod bearing film thickness

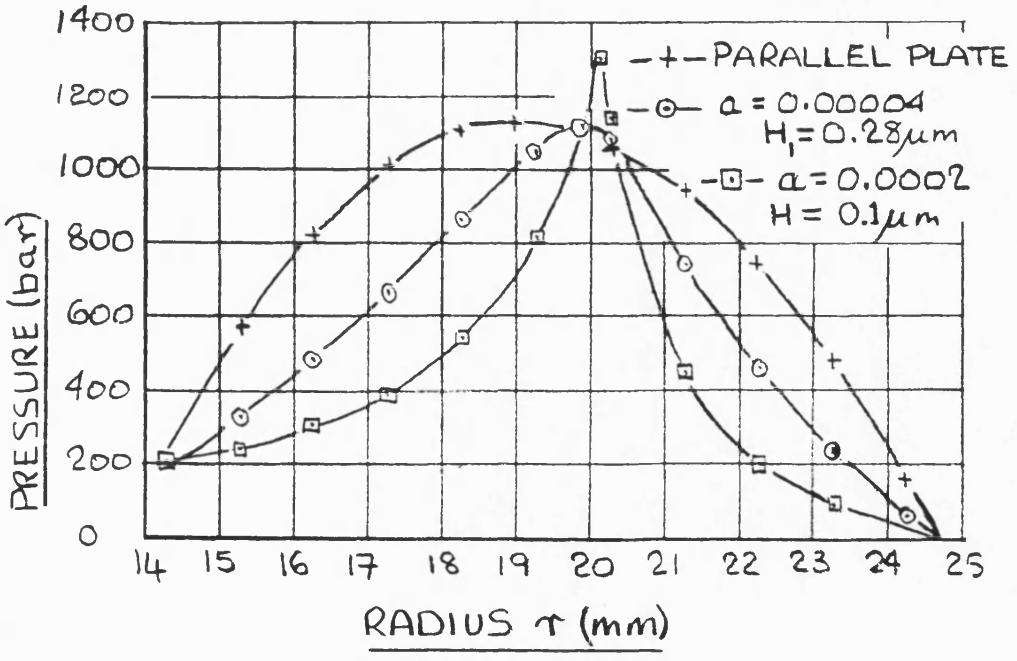

Fig 5 Effect of surface shape on pressure distribution

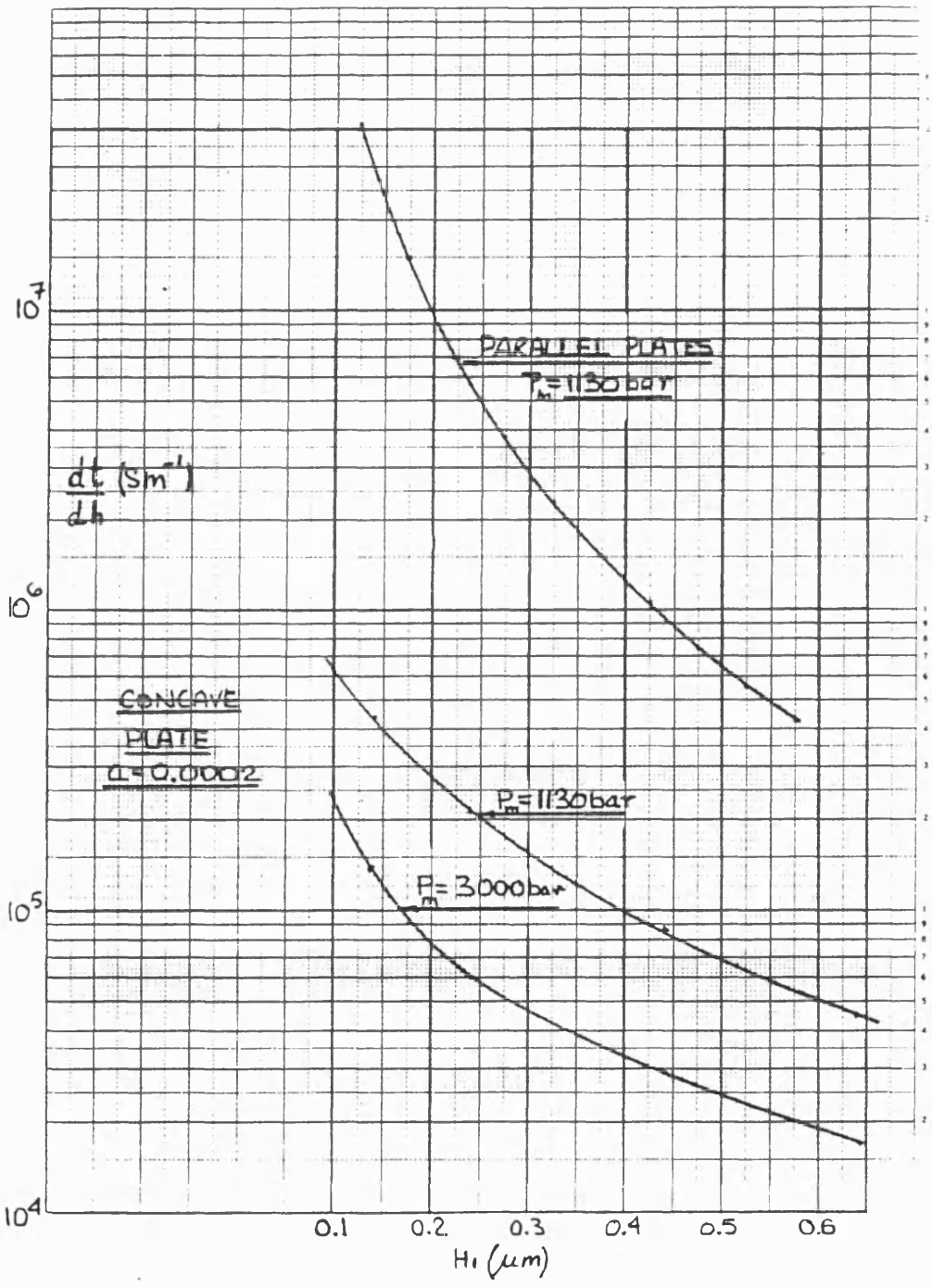

Fig 6 Effect of surface shape on squeeze rate

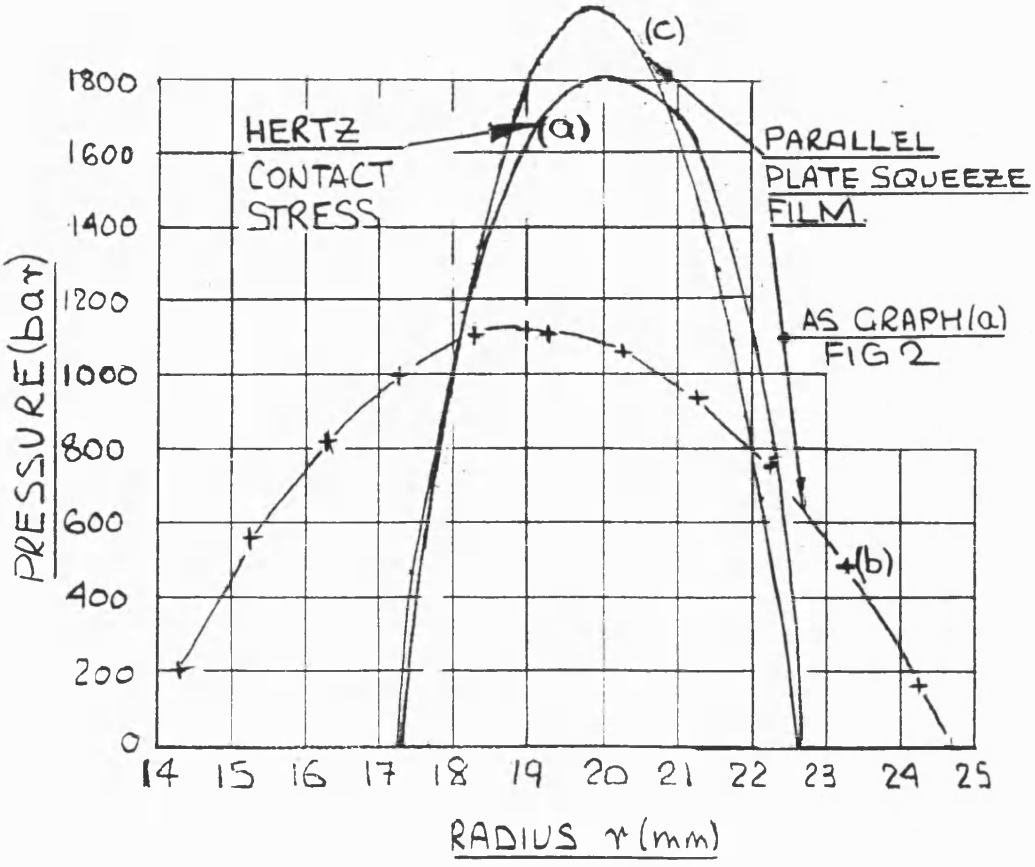

Fig 7 Film pressure distribution for contact conditions

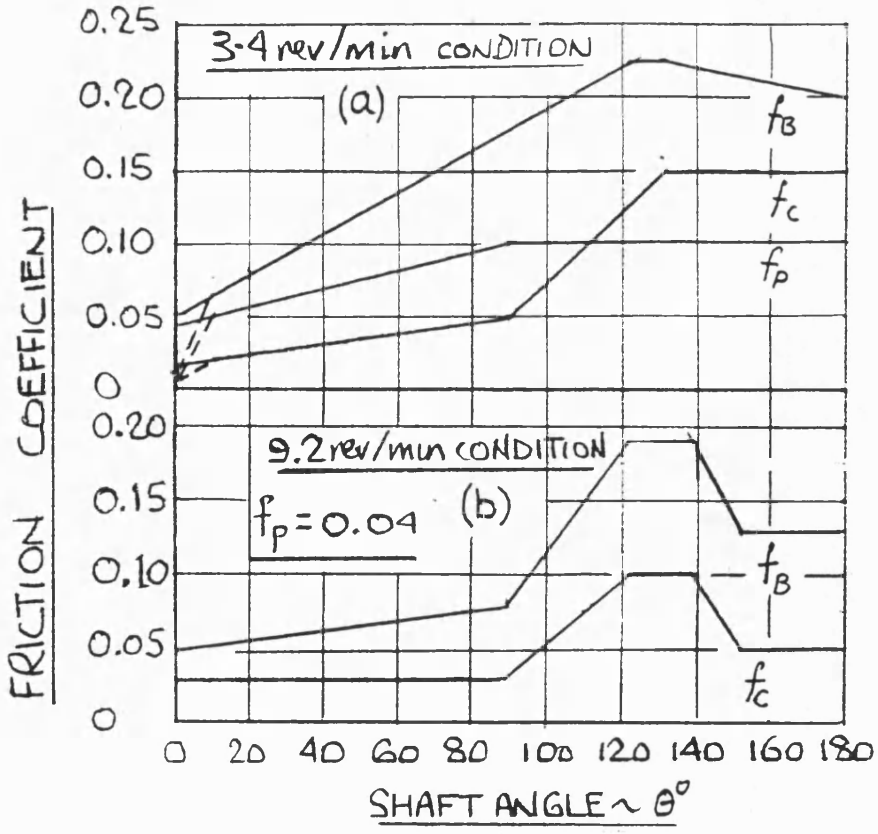

Fig 8 Friction coefficient variations used in the model

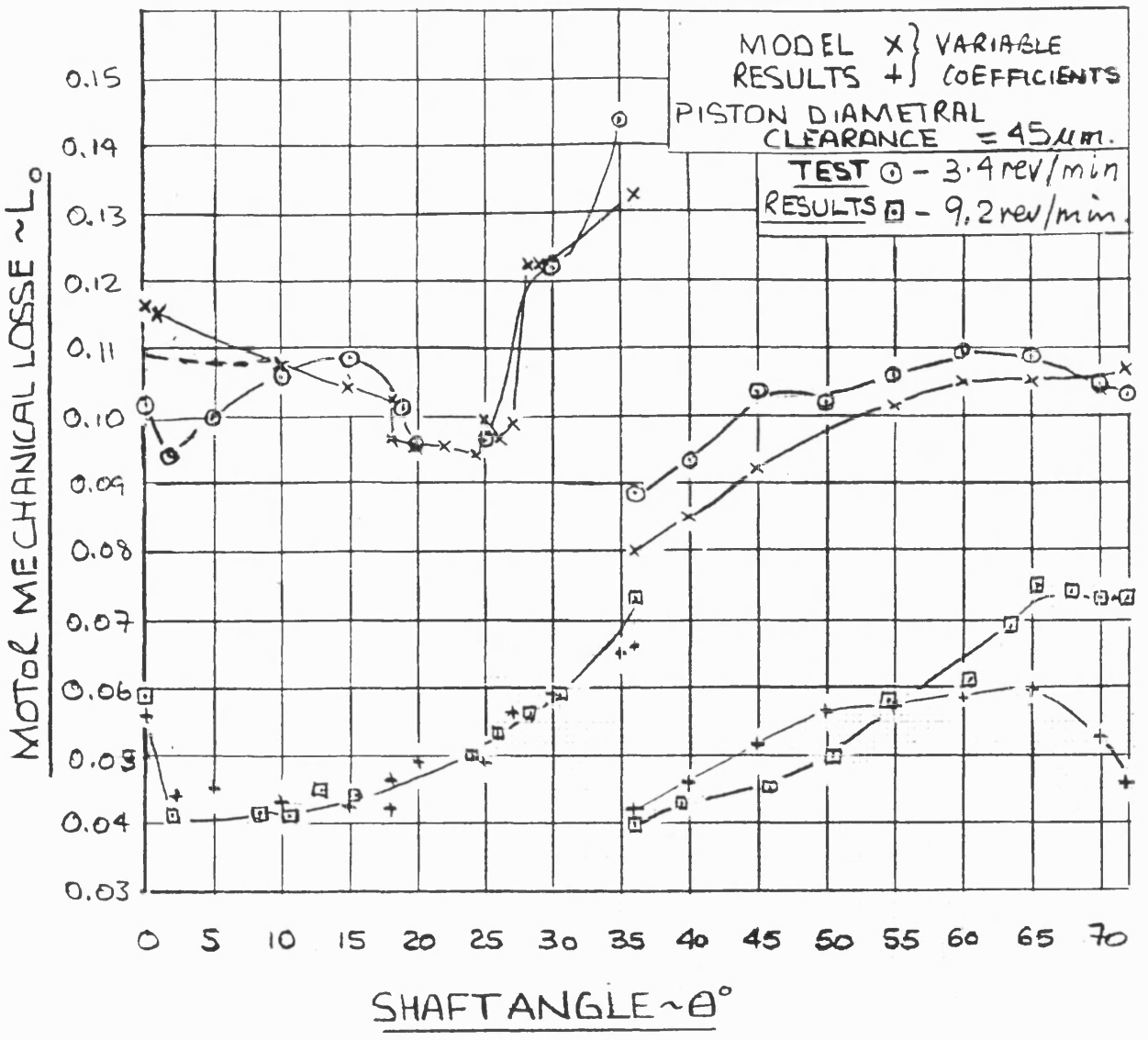

Fig 9 Predicted motor mechanical losses with variable friction coefficients

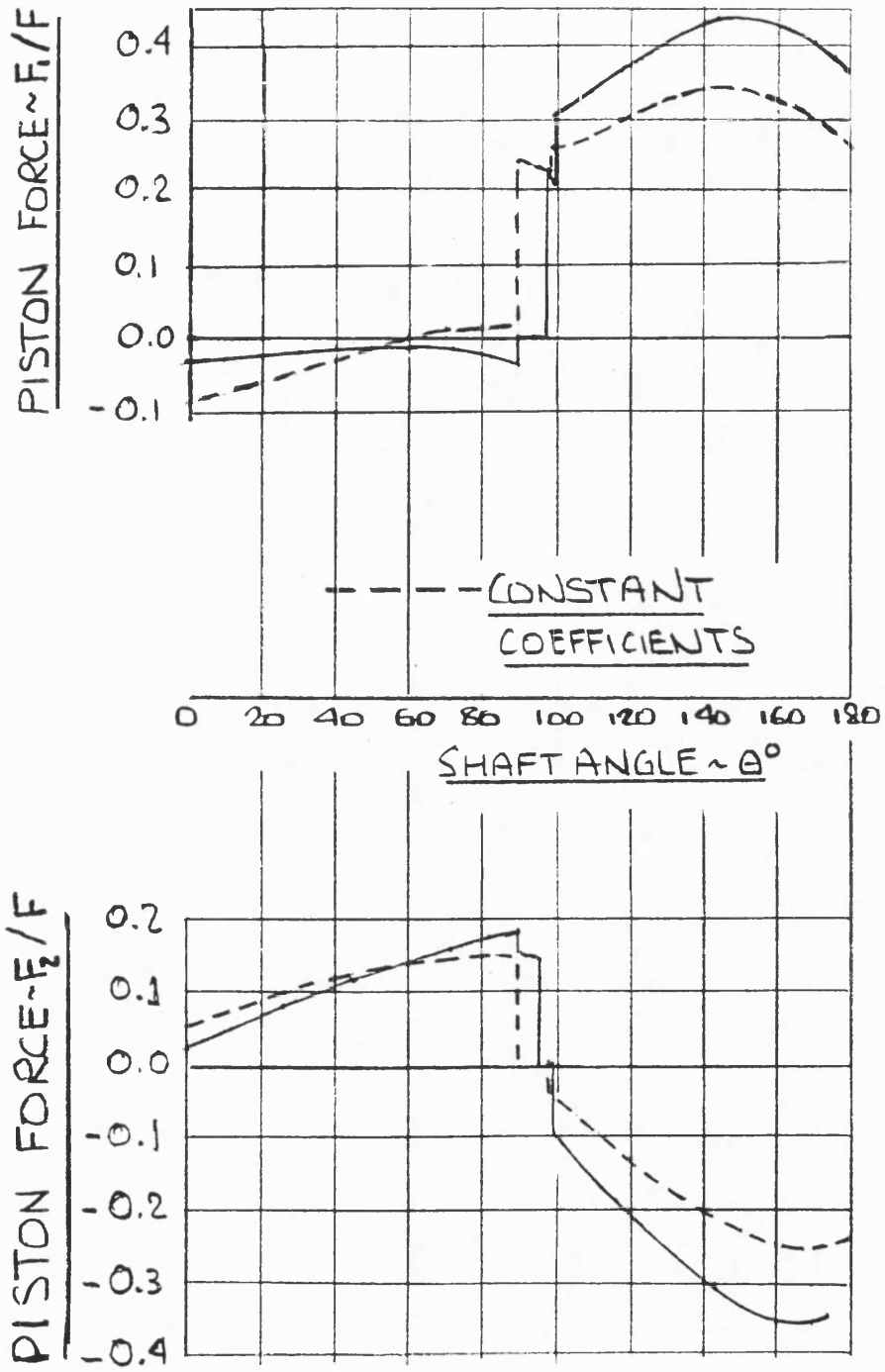

Fig 10 Predicted piston forces with variable friction coefficients (3.4 rev/min condition)

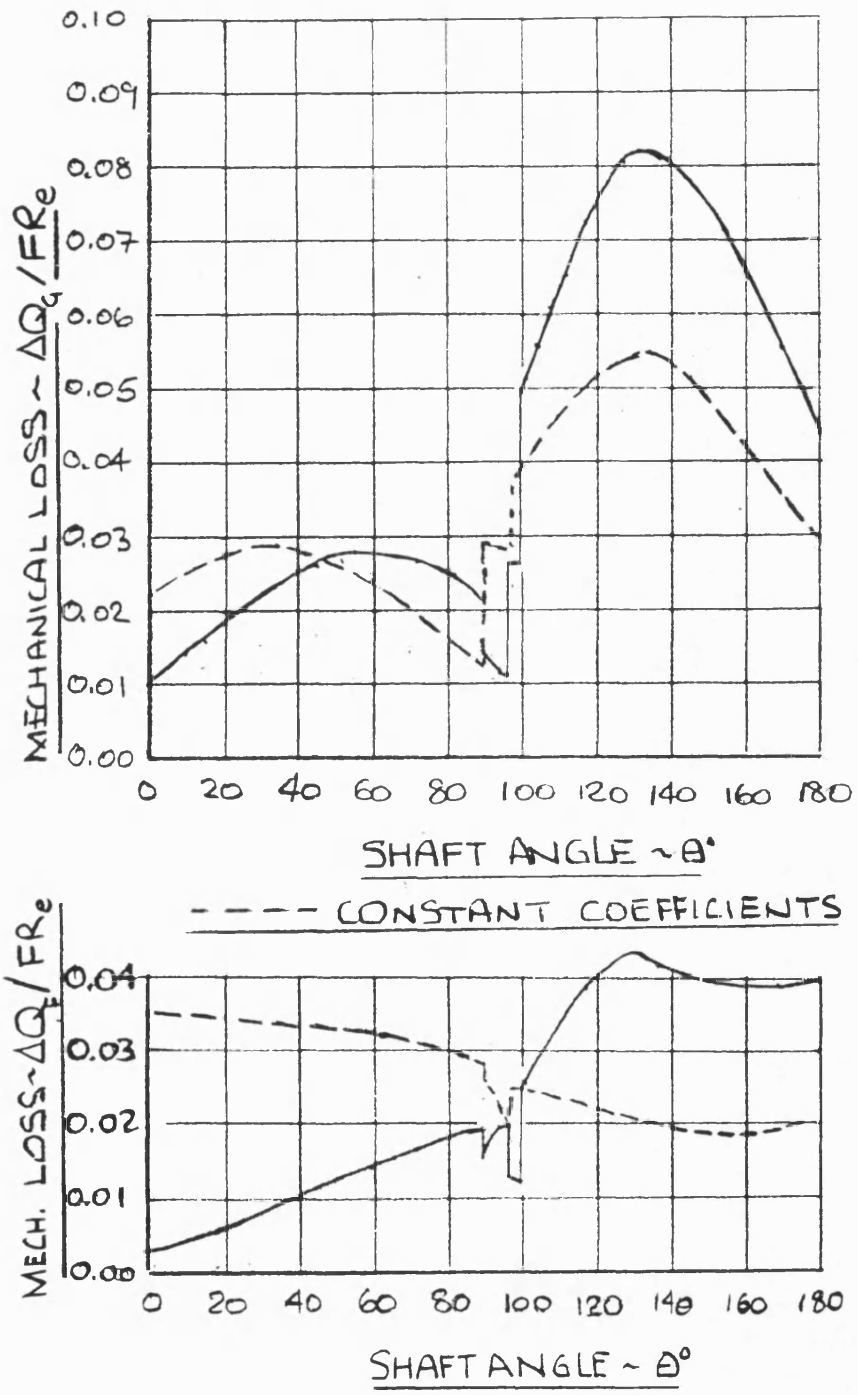

Fig 11 Predicted mechanical losses for each cylinder with variable friction coefficients

(3.4 rev/min condition)

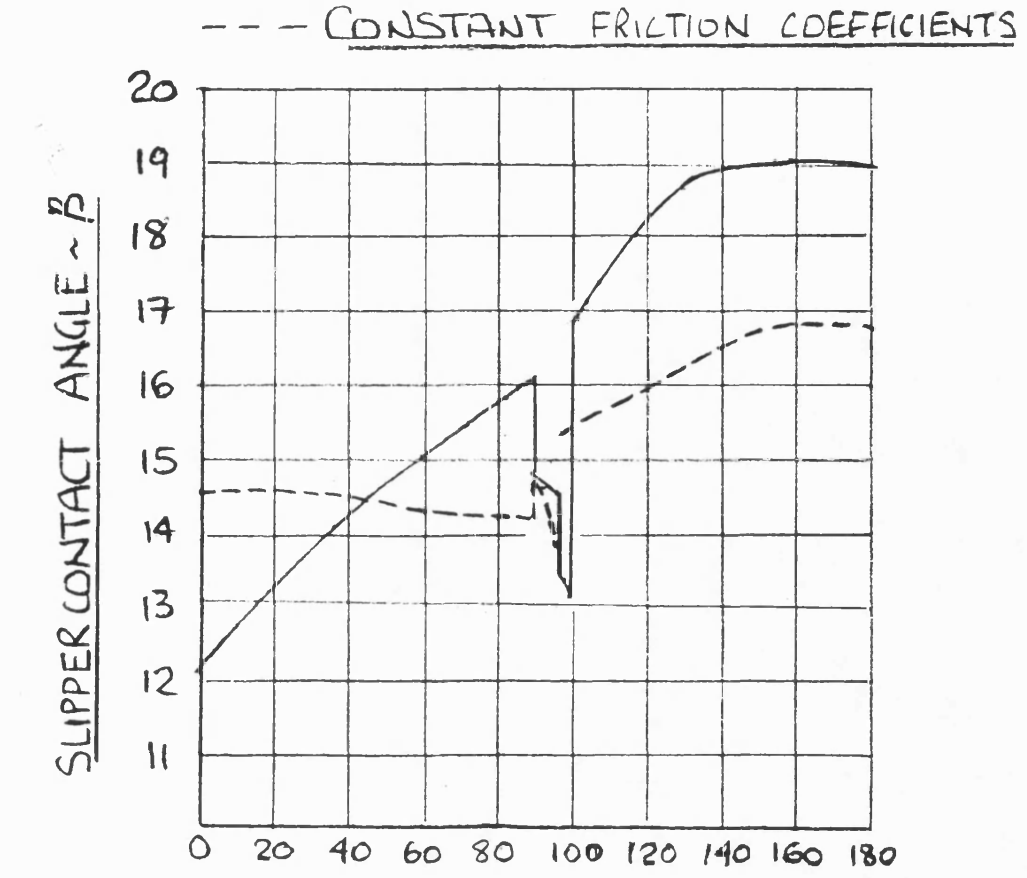

Fig 12 Slipper contact angle with variable friction coefficients (3.4 rev/min condition)

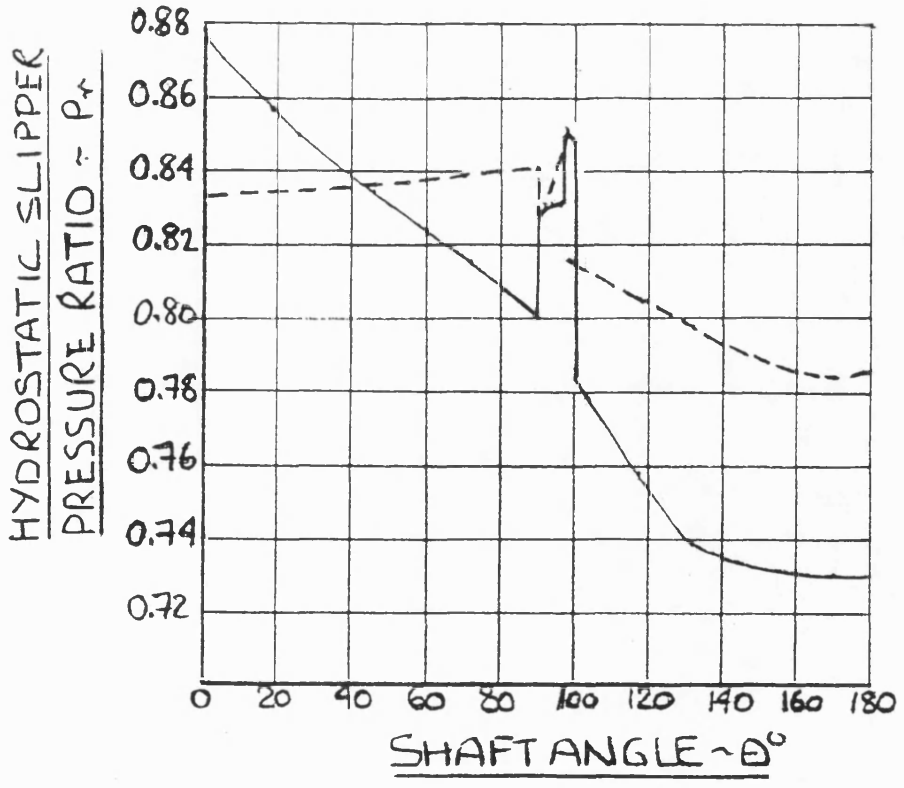

Fig 13 Hydrostatic slipper pressure ratio with variable friction coefficients

(3.4 rev/min condition)

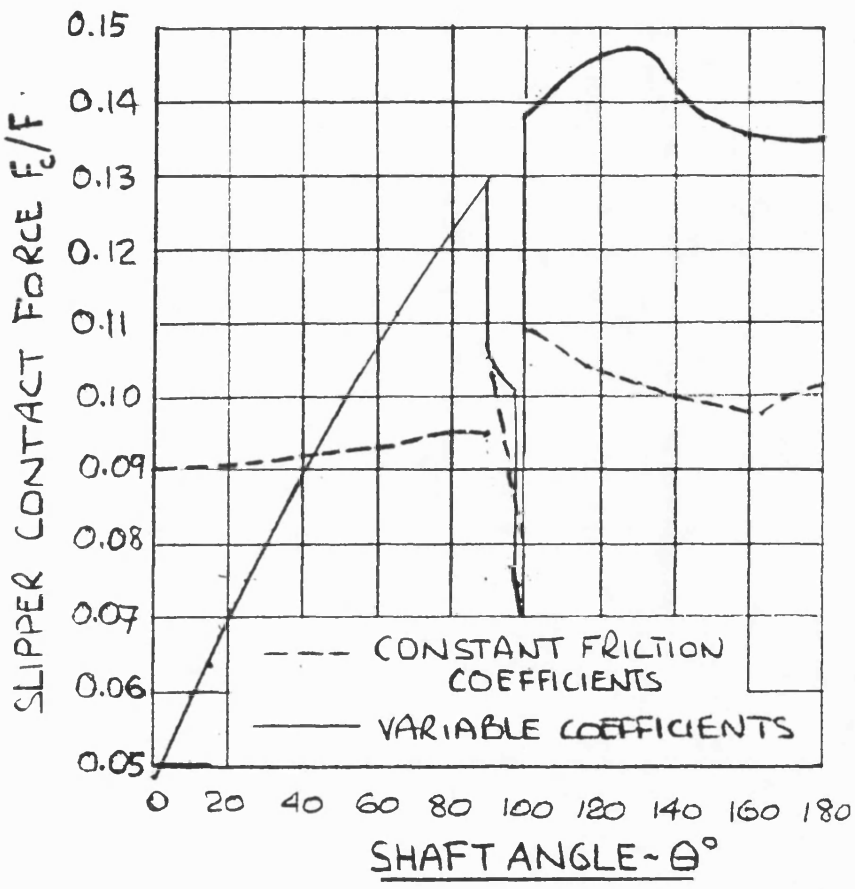

Fig 14 Slipper contact force with variable friction coefficients (3.4 rev/min condition)

APPENDIX I

Squeeze film effects of a spherical bearing

This analysis considers the effect of the squeeze film between a sphere and a spherical cup whose radius is slightly greater than that of the sphere. The diagram shows the centre of the cup (O_2) to be offset to one side of the sphere centreline. Contact therefore occurs at an angle β_c to the vertical which is determined by the amount of offset and the difference in the sphere and cup radii. With the cup displaced vertically a distance h_1 above the sphere it is necessary to establish the variation in h with the angle β from the contact line.

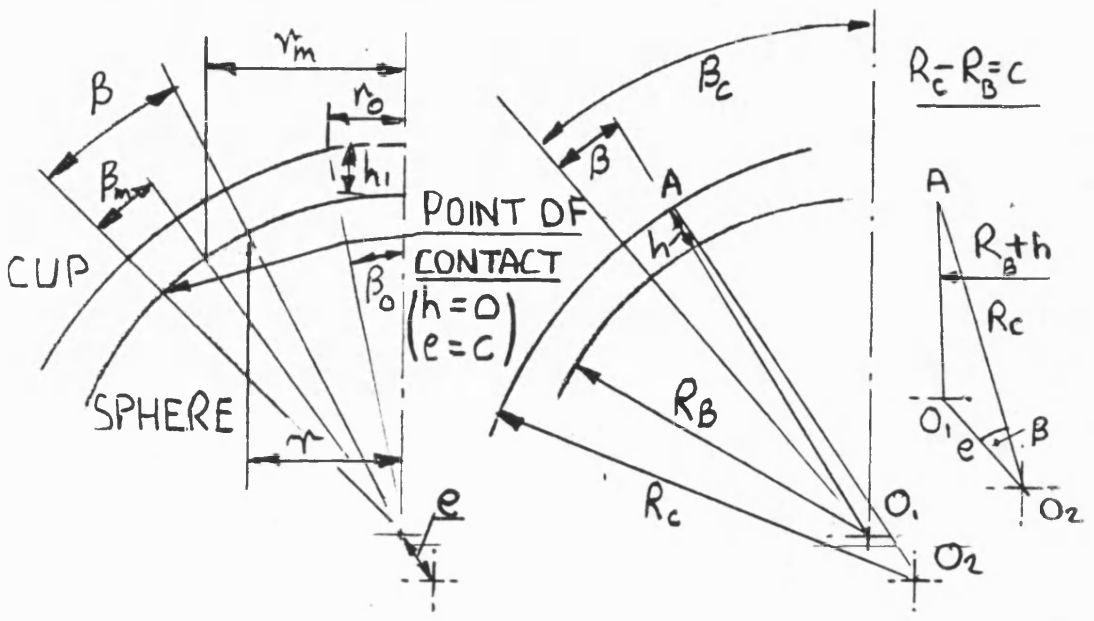

From the cosine rule:

$$(R_B + h)^2 = R_B^2 + 2R_B h + h^2 = e^2 + R_c^2 \cos\beta$$

for h^2 and $e^2 \approx 0$

$$\therefore \left(R_c^2 - R_B^2\right) = (R_c - R_B)(R_c + R_B) = 2CR = 2Rh + 2eR\cos\beta$$

$$\therefore h = c - e\cos\beta \qquad (1)$$

Consider the cup to be displaced a distance 'h_1' vertically up from the ball along the vertical centreline.

Now $h_1 = c - e\cos\beta_c$

$$\therefore e = \frac{c - h_1}{\cos\beta_c}$$

and from equation (1)

$$h = c - \left(\frac{e - h_1}{\cos\beta_c}\right)\cos\beta$$

$$\therefore h = \frac{c\left(\cos\beta_c - \cos\beta\right) + h_1\cos\beta}{\cos\beta_c} \qquad (2)$$

Now consider the cup to be moving towards the ball with velocity $-\frac{dh_1}{dt}$. For the conditions where the pressure at r_o is the supply pressure P_s, the pressure in the clearance will increase to a maximum of P_m at $r = r_m$ and in his region the squeeze flow will be radially inwards.

Neglecting compressibility effects, the flow displaced radially inwards at radius 'r' will be given by:

$$-2\pi(r_m^2 - r^2)\frac{dh_1}{dt} \tag{3}$$

This flow will be equal to the viscous flow through the incremental distance $R_B d\beta$ at clearance 'h' which is given by:-

$$\frac{-2\pi h^3 r dp}{12\mu R_B d\beta} \tag{4}$$

where $\frac{dp}{d\beta}$ is negative.

Putting equation (3) equal to equation (4) yields:

$$(r_m^2 - r^2)\frac{dh_1}{dt} = \frac{h^3 r}{12\mu R_B}\frac{dp}{d\beta} \tag{5}$$

Now $$r = R_B \sin(\beta_c - \beta)$$

and so $$r_m^2 - r^2 = R_B^2(\sin^2(\beta_c - \beta_m) - \sin^2(\beta_c - \beta)) \tag{6}$$

We have from equation (2) h as a function of β and consequently substituting this and equation (6) into equation (5) and rearranging terms gives:

$$\frac{R_B^2(\sin^2(\beta_c - \beta_m) - \sin^2(\beta_c - \beta))12\mu\cos^3\beta_c}{\sin(\beta_c - \beta)(c(\cos\beta_c - \cos\beta) + h_1\cos\beta)^3}\frac{dh_1}{dt}d\beta = dp \tag{7}$$

The solution of this equation, for a given value of $\frac{dh_1}{dt}$, requires the integration of the LHS between the limits of β_m and β_o and the RHS between the limits of P_m and P_s.

The complete solution of the problem can be achieved by obtaining a similar equation for the outward flow $r > r_m$. Expressing both of these equations in terms of the maximum pressure P_m will give $\frac{dh_1}{dt}$ as a function of r_m. Equating the separating force, which is $\int 2\pi p r dr$, with that acting on the piston cup, will then determine the value of r_m that applies to the situation and the closing rate $\frac{dh_1}{dt}$.

APPENDIX II

Squeeze film effect between an annular ring and a flat surface

1.0 Case of radially reducing clearance

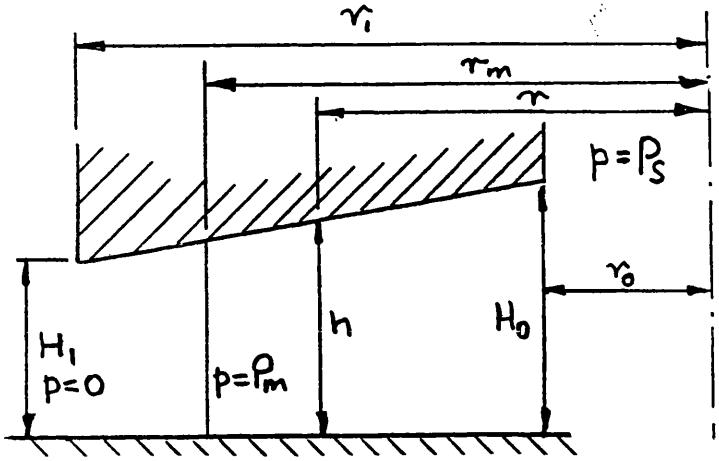

Clearance $h = H_0 + a(r_0 - r)$ and $a = \dfrac{H_0 - H_1}{r_1 - r_0}$

$\therefore h = H_c - ar$

where $H_c = H_0 + ar_0$

For this situation for the maximum pressure $P_m > P_s$ which occurs at radius r_m where $\dfrac{dp}{dr} = 0$, the flow will be radially inward from r_m to r_0.

Thus for this inner ring:

$$-\pi(r_m^2 - r^2)\frac{dh}{dt} = \frac{h^3}{12\mu} 2\pi r \frac{dp}{dr}$$

where $\dfrac{dp}{dr}$ is positive and $\dfrac{dh}{dt}$

$$\therefore \frac{dp}{dr} = -6\mu \frac{dh}{dt}\frac{(r_m^2 - r^2)}{rh^3} = -6\mu \frac{dh}{dt}\frac{(r_m^2 - r^2)}{r(H_c - ar)^3}$$

For $p = P_m$ at $r = r_m$

and $p = P_s$ at $r = r_0$

$$\therefore p - P_m = -6\mu \frac{dh}{dt}\int_{r_m}^{r} \frac{(r_m^2 - r^2)dr}{r(H_c - ar)^3} \qquad (1)$$

For the outer ring, the flow is radially outward when $\dfrac{dp}{dr}$ is negative.

$$\therefore -\pi(r^2 - r_m^2)\frac{dh}{dt} = -\frac{h^3}{12\mu}2\pi r\frac{dp}{dr}$$

hence $p = 0$ at $r = r_1$

and $p = P_m$ at $r = r_m$

$$\therefore p - P_m = -6\mu\frac{dh}{dt}\int_{r_m}^{r}\frac{(r_m^2 - r^2)dr}{r(H_c - ar)^3} \tag{2}$$

We need to solve for P_m and r_m which can be done by integrating equations (1) and (2) between the limits r_0 and r_m and r_1 and r_m respectively.

Thus $$P_m = 6\mu\frac{dh}{dt}\int_{r_m}^{r_0}\frac{(r_m^2 - r^2)dr}{r(H_c - ar)^3} + P_s \tag{3}$$

$$= 6\mu\frac{dh}{dt}I_I + P_s \tag{4}$$

Also $$P_m = 6\mu\frac{dh}{dt}\int_{r_m}^{r_1}\frac{(r_m^2 - r^2)dr}{r(H_c - ar)^3} \tag{5}$$

$$= 6\mu\frac{dh}{dt}I_O \tag{6}$$

Equations (4) and (6) give:

$$I_O - I_I = \frac{P_s}{6\mu\frac{dh}{dt}} \tag{7}$$

Thus a given value of $\frac{dh}{dt}$ will determine the value of r_m from equation (7) which can then be used in either equation (4) or (6) to obtain the value of P_m and the pressure distribution from equations (1) and (2).

The integral $$\int_{r_m}^{r}\frac{(r_m^2 - r^2)dr}{r(H_c - ar)^3}$$

$$= \int_{r_m}^{r}\frac{r_m^2 dr}{r(H_c - ar)^3} - \int_{r_m}^{r}\frac{r dr}{(H_c - ar)^3}$$

$$= \quad I_1 \quad - \quad I_2$$

put $y = H_c - ar$

$$\therefore dy = -a dr \text{ and } r = \frac{H_c - y}{a}$$

$\therefore$ <u>For I_1</u> using the Heavyside expansion method gives:

$$\frac{1}{r\,(H_c - ar)^3} = \frac{a}{(H_c - y)y^3} = \left(\frac{1}{H_c^3(H_c - y)} + \frac{1}{H_c y^3} + \frac{1}{H_c^2 y^2} + \frac{1}{H_c^3 y}\right)a$$

and $$I_1 = -r_m^2 \int \frac{a\,dy}{(H_c - y)y^3 a} = -r_m^2\left\{-\frac{l_n(H_c - y)}{H_c^3} - \frac{1}{2H_c y^2} - \frac{1}{H_c^2 y} + \frac{l_n y}{H_c^3}\right\}$$

$$= r_m^2\left\{\frac{l_n ar}{H_c^3} + \frac{1}{2(H_c - ar)^2 H_c} + \frac{1}{H_c^2(H_c - ar)} - \frac{l_n(H_c - ar)}{H_c^3}\right\} \qquad (8)$$

and for I_2

$$\int \frac{r\,dr}{(H_c - ar)^3} = -\int \frac{(H_c - y)}{a^2 y^3}\,dy$$

$$= \frac{1}{a^2}\left[\frac{H_c}{2y^2} - \frac{1}{y}\right]$$

$$= \frac{1}{a^2}\left[\frac{H_c}{2(H_c - ar)^2} - \frac{1}{(H_c - ar)}\right]$$

$$= \frac{1}{a^2}\left[\frac{2ar - H_c}{2(H_c - ar)^2}\right] \qquad (9)$$

Inserting the limits into equations (8) and (9) gives:

$$\int_{r_m}^{r} \frac{(r_m^2 - r^2)dr}{(H_c - ar)^3 r} = \frac{r_m^2}{H_c^3} l_n \frac{r}{r_m}\left(\frac{H_c - ar_m}{H_c - ar}\right) + \frac{r_m^2}{2H_c}\left\{\frac{1}{(H_c - ar)^2} - \frac{1}{(H_c - ar_m)^2}\right\}$$

$$+ \frac{r_m^2}{H_c^2}\left\{\frac{1}{(H_c - ar)} - \frac{1}{(H_c - ar_m)}\right\}$$

$$-\left\{\frac{2a(r_m^2 r - r_m r^2) + H_c(r^2 - r_m^2)}{2(H_c - ar)^2(H_c - ar_m)^2}\right\} \qquad (10)$$

Using equation (7) to obtain r_m as a $f(dh/dt)$ it is necessary to obtain the integrals I_O and I_I from equation 10 where r is replaced by r_0 for I_I and r_1 for I_O.

Thus $I_O - I_I$ is given by:-

$$\frac{r_m^2}{H_c^3} l_n \frac{r_1}{r_0}\left(\frac{H_c - ar_0}{H_c - ar_1}\right) + \frac{r_m^2}{2H_c}\left(\frac{1}{(H_c - ar_1)^2} - \frac{1}{(H_c - ar_0)^2}\right) + \frac{r_m^2}{H_c^2}\left\{\frac{1}{(H_c - ar_1)} - \frac{1}{(H_c - ar_0)}\right\}$$

$$-\left\{\frac{2a(r_m^2 r_1 - r_m r_1^2) + H_c(r_1^2 - r_m^2)}{2(H_c - ar_m)^2(H_c - ar_1)^2} - \frac{2a(r_m^2 r_0 - r_m r_0^2) + H_c(r_0^2 - r_m^2)}{2(H_c - ar_m)^2(H_c - ar_0)^2}\right\} \qquad (11)$$

which is equal to $\dfrac{P_s}{6\mu\dfrac{dh}{dt}}$

2.0 Parallel Gap

For a parallel gap the value of 'a' is zero.

Therefore $H_c = H_0 = h$

and equations (7) and (11) give:

$$\frac{3\mu}{h^3}\frac{dh}{dt} = \frac{P_s}{\left\{2r_m^2 l_n\left(\frac{r_1}{r_0}\right) - \left(r_1^2 - r_0^2\right)\right\}} \tag{12}$$

Thus for a parallel gap and a given value of P_S, the value of $\dfrac{1}{h^3}\dfrac{dh}{dt}$ is associated with a unique value of r_m regardless of the value of the clearance h. For the tapered clearance this is not so because the value of the clearance is not explicit in equation (11).

Thus with $a = 0$, we get from equation (4).

$$P_m = \frac{3\mu}{h^3}\frac{dh}{dt}r_m^2\left\{2l_n\left(\frac{r_0}{r_m}\right) - \left(\frac{r_0}{r_m}\right)^2 + 1\right\} + P_s \tag{13}$$

and from equation (6)

$$P_m = \frac{3\mu}{h^3}\frac{dh}{dt}r_m^2\left\{2l_n\left(\frac{r_1}{r_m}\right) - \left(\frac{r_1}{r_m}\right)^2 + 1\right\} \tag{14}$$

3.0 Force on the plate for parallel gap

3.1 For $r_m \geq r \geq r_0$

From equations (1) and (13) we have:

$$p = P_s + \frac{3\mu}{h^3}\frac{dh}{dt}r_m^2\left\{2l_n\frac{r_0}{r_m} - \left(\frac{r_0}{r_m}\right)^2 + 1 - 2l_n\frac{r}{r_m} + \left(\frac{r}{r_m}\right)^2 - 1\right\}$$

$$= P_s + \frac{3\mu}{h^3}\frac{dh}{dt}r_m^2\left\{2l_n\left(\frac{r_0}{r}\right) + \left(\frac{r}{r_m}\right)^2 - \left(\frac{r_0}{r_m}\right)^2\right\} \tag{15}$$

Force $F_l = 2\pi\int_{r_0}^{r_m} pr\,dr$

now $\int r l_n r\,dr = \dfrac{r^2}{2}l_n r - \int\dfrac{r^2}{2}\dfrac{1}{r}dr = \dfrac{r^2}{2}l_n r - \dfrac{r^2}{4}$

$$\therefore F_I = \pi P_s\left(r_m^2 - r_0^2\right) - \frac{6\pi\mu}{h^3}\frac{dh}{dt}\left(r_m^4 l_n\left(\frac{r_m}{r_o}\right) - \frac{r_0^4}{4} - \frac{3r_m^4}{4} + r_0^2 r_m^2\right) \tag{16}$$

3.2 For $r_1 \geq r \geq r_m$

From equation (2) and (14) we have:

$$p = \frac{3\mu}{h^3}\frac{dh}{dt}r_m^2\left\{2l_n\left(\frac{r_1}{r_m}\right) - \left(\frac{r_1}{r_m}\right)^2 + 1 + \left(\frac{r}{r_m}\right)^2 - 1 - 2l_n\left(\frac{r}{r_m}\right)\right\}$$

$$\therefore p = \frac{3\mu}{h^3}\frac{dh}{dt}r_m^2\left\{2l_n\left(\frac{r_1}{r}\right) + \left(\frac{r}{r_m}\right)^2 - \left(\frac{r_1}{r_m}\right)^2\right\} \tag{17}$$

Now $F_O = 2\pi\int_{r_m}^{r_1} prdr$

which from (17) gives:

$$F_O = \frac{6\pi\mu}{h^3}\frac{dh}{dt}\left(r_m^4 l_n\frac{r_m}{r_1} - \frac{r_1^4}{4} - \frac{3}{4}r_m^4 + r_1^2 r_m^2\right) \tag{18}$$

$\therefore$ Total separating force is:

$$F_T = F_I + F_O$$

4.0 Case 1 with radially increasing clearance

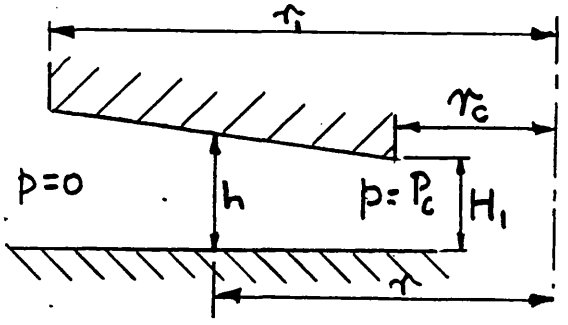

$h = H_0 + ar$

$H_0 = H_1 - ar_0$

Here the radially increasing gap is immediately outside the radially reducing gap described in 1.0 where $r_c = r_1$ and $p = P_c$ at $r = r_c$.

For the boundary conditions, equations (2) and (5) give:

$$P_m = 6\mu\frac{dh}{dt}I_I + P_s = P_c + 6\mu\frac{dh}{dt}I_O \tag{19}$$

Here I_O is obtained by replacing 'r' with 'r_C' in equation (10)

The outward flow from radius r_C for $p = 0$ at $r = r_1$ gives from equation 2:

$$P_c = 6\mu\frac{dh}{dt}\int_{r_c}^{r_1}\frac{\left(r_m^2 - r^2\right)dr}{r\left(H_D + ar\right)^3}$$

or $$P_c = 6\mu\frac{dh}{dt}I_D \qquad (20)$$

Thus equations (19) and (20) give:

$$6\mu\frac{dh}{dt} = \frac{P_s}{(I_D + I_O - I_I)} \qquad (21)$$

Thus for given values of r_m and H_1 the corresponding value of $\mu\frac{dh}{dt}$ can be obtained from equation (21).

Here $$I_D = \frac{r_m^2}{H_D^3} l_n\left[\frac{r_1}{r_c}\left(\frac{H_D + ar_c}{H_D + ar_1}\right)\right] + \frac{r_m^2}{2H_D}\left\{\frac{1}{(H_D + ar_1)^2} - \frac{1}{(H_D + ar_c)^2}\right\}$$

$$+ \frac{r_m^2}{H_D^2}\left\{\frac{1}{(H_D + ar_1)} - \frac{1}{(H_D + ar_c)}\right\}$$

$$+ \frac{2a(r_c^2 r_1 - r_c r_1^2) + H_D(r_c^2 - r_1^2)}{2(H_D + ar_1)^2(H_D + ar_c)^2} \qquad (22)$$

CHAPTER 5

THE INFLUENCE OF THE MOTOR DESIGN ON PERFORMANCE

1.0 INTRODUCTION

It has been shown in Chapter 4 that the model of the motor generally provides a good prediction of the motor performance on the basis of assumed variations in the friction coefficients. In this chapter the model is used to explore the effect of changes to various design parameters and, particularly, those that result in improvements to the performance. Following a discussion on some developments in HTLS motors the model is then extended to evaluate an alternative design proposed by the author.

2.0 SENSITIVITY OF THE DESIGN TO PARAMETER VARIATIONS

In Chapter 2 it was demonstrated that the efficiency of the motor was strongly affected by the value of e_c. From a design point of view distortion of the slipper should be minimised and the face radius machined to within 25μm of that of the eccentric. For the motor in question there is, unfortunately, no scope to reduce the distortion of the slipper without increasing the overall size of the motor.

Other parameters that can be varied include:

a) The con rod bearing contact angle.

b) The slipper feed orifice diameter.

c) The effective slipper area.

d) The con rod bearing friction coefficient.

2.1 Con rod bearing contact angle

The force normal to the con rod bearing surface will be dependent on the contact angle in the bearing, the force reducing as the angle is reduced. However, the hydrostatic force on the piston above the bearing also reduces with the angle.

The simulated effect of this angle on losses is shown in Fig 1; there is a reduction in the losses of around 0.5% for 5^0 either side of 45^0. From the wear and distortion viewpoint 45^0 was probably chosen as an optimum angle. These changes in angle lie within the band of manufacturing tolerances for the two components of the bearing.

2.2 Slipper feed orifice diameter

The size of the slipper feed orifice was normally standardised at 0.57 *mm* although in special situations it was altered in order to obtain improvements in motor starting torque. As was described in Chapter 3 this was not always a success, particularly when using water based fluids.

The simulated results in Fig 2 show the effect of the feed restrictor on motor performance at a shaft angle of 10^0. The trend is to reduce the mechanical losses with increasing size of the restrictor, although this reduction does appear to depend on the values of the friction coefficients.

As can also be seen from Fig 2 the effect on leakage, which is an important operational factor, is quite marked. For this reason, the standard size of the restrictor was increased in dual displacement motors to provide improved cooling of the slipper at increased operating speeds.

2.3 Slipper effective area

The design philosophy originally adopted in the Staffa motor was based on using a slipper effective area greater than that of the piston. This would be expected to minimise the contact force between the slipper and the eccentric and thus maximise the mechanical efficiency.

In most other motors of the eccentric type, the effective area of the slipper is , as far as is known to the author, smaller than that of the piston. Reducing the slipper area in the model has the effect on the losses shown in Fig 3(a). For both the standard and reduced areas the mechanical loss varies strongly with the value of e_c but, at low values of e_c, the effect of changing the area is small. The major advantage is the reduction in leakage that is obtained as shown in Fig 3(b) which is due to the compensating effect of the feed restrictor.

The reduced effect of the area on the loss arises because, for low values of e_c, the slipper contact angle moves to the value limited to that of the maximum slipper arc when $\beta = \beta_m$. The slipper pressure is then adjusted by the action of the slipper tilting slightly about the outer edge in contact with the eccentric in the manner discussed in Chapter 2.

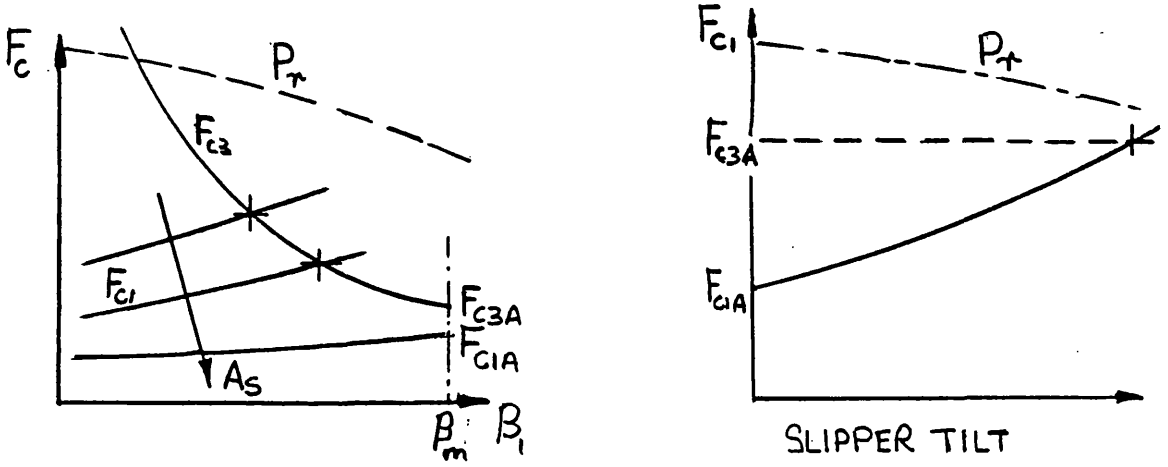

As shown in the diagram, this will occur if the contact force (F_{C1}) required for radial equilibrium at β_m is less than that required for rotation of the con rod (F_{C3}). If the slipper area is too small the contact force that satisfies both requirements will occur at angles less than β_m (as indicated in the diagram).

As the area is reduced, the required slipper pressure is increased but, for the situations where $\beta = \beta_m$, the hydrostatic pressure force will be unchanged. This is because the contact force (F_{C3}) needs to be the same, as depicted by F_{C3A} on the previous diagram; the action of the slipper tilting causing F_{C1} to increase to the level of F_{C3A}.

The variation of F_{C1} with e_C is shown in Fig 3(c) for two of the cylinders at a motor shaft angle of 10^0 where it can be seen that for the cylinder at 10^0, F_{C1} is less than that for the reduced area. This is because for this cylinder $\beta < \beta_m$. At 82^0 shaft angle however, $\beta = \beta_m$ when $e_C = 25\mu m$, and the values of F_{C1} for the two areas are the same.

The variation in the forces F_{C1}, and F_{C3} with β_1 are shown in Fig 4(a) for e_C values of 25 and $127\mu m$. For $127\mu m$ the higher value of F_{C1} is caused by the low slipper pressure ratio, P_r, as shown in Fig 4(b). For $25\mu m$ the slipper pressure is almost equal to the motor supply pressure which results in F_{C1} being less than F_{C3} when $\beta = \beta_m$ as in Fig 4(a). The effect on P_r and F_{C1} when the slipper is tilting is shown in Fig 4(c).

The reduced slipper area of 4700 mm^2 represents a nominal net clamping force on the slipper of around 5% of that of the piston. However a nominal clamping force of 5% has resulted in a contact force of 7.8%

In some designs the nominal clamping force can be as high as 10% or 15% of that of the piston. From the foregoing it is evident that care has to be taken to determine the force at the contact condition as this could increase to unacceptable levels. It is also important that e_C is maintained at less than the maximum value that is consistent with minimising the contact force.

2.4 Con rod bearing friction coefficient

The simulated results of Chapter 4 show that the con rod bearing experiences the highest frictional coefficient. As was explained this would be expected because of the high unit loading at the bearing contact.

From a design viewpoint, any changes that could improve the situation of this bearing would result in a worthwhile improvement in the motor performance. The significance of this coefficient is demonstrated in Fig 5 which shows the reduction in the mechanical loss when compared with the standard variable coefficient model developed in Chapter 4. Thus modifications to the con rod bearing that effectively reduce the level of friction have the potential of providing considerable improvements to the motor efficiency.

2.5 Modified con rod

The effect of friction in the con rod bearing on the motor performance can be reduced if the bearing diameter is reduced. The materials used in the current motor for the piston and the con rod do not provide an ideal combination for this bearing. This was demonstrated by the improved life obtained from the phosphor bronze piston cup insert reported in Chapter 3. Some limited tests were carried out with con rods of aluminium bronze which gave favourable results. In the motor manufactured by the German company, Jahns, shown in Fig 6, this bearing is of aluminium bronze against steel and has a relatively smaller diameter than that of the Staffa motor.

An additional advantage obtained from reducing the bearing diameter is the possibility of relocating the bearing centre radially outwards. This will result in reduced piston forces at extended piston positions. This modification, shown in Fig 7, also avoids the condition that occurs in the standard motor of the bearing centre extending from the cylinder (i.e. length L_B is always positive).

2.5.1 Mechanical losses

The modified con rod has a significant effect on the mechanical losses obtained from the model, shown in Fig 8 (a), which are reduced by between 2 and 3% (an improvement of 20 to 30%) over the major part of the cycle for operation at maximum displacement.

The region of the piston rotating in its clearance space, following 18^0 shaft angle, is reduced because of the increased piston length. This also causes the piston to be forced against the cylinder wall because of the increased moment created by the side force F_T about the inner cylinder opening.

As was seen from the measured results, operation at reduced motor displacement is associated with reduced mechanical efficiency. The magnitude of this reduction is strongly dependent on the speed of rotation. The losses obtained from the model at the low displacement with the same frictional coefficients as were used for the maximum displacement, are shown in Fig 8 (b). As can be seen, on comparison with Fig 8(a), this change of displacement has caused the losses to increase by between 0.10 and 0.15.

This change is similar to that of the measured results although the frictional conditions at the low displacement, particularly in the con rod bearing and the piston to cylinder interface, may well be different. At the lower displacement the con rod bearing rotates through a smaller angle and at lower rotational velocities. Also the piston moves through a smaller distance and the associated lower velocity could well increase the frictional resistance.

The position of the piston midway in its stroke, which occurs at 90^0 shaft angle, is virtually unaffected by the motor displacement. Thus, as the displacement is reduced, the radial distance of the piston from the eccentric centre for $\theta > 90^0$ increases. This results in the piston emerging a smaller distance from the cylinder bore at 180^0 shaft angle with a consequent reduction in the piston forces and the associated frictional losses. The losses obtained from the modified con rod at the low motor displacement condition are 4 to 5% less than for the standard design (representing an improvement of around 25%). This would provide a considerable benefit in the application of motors of this type.

In Chapter 3 the measured variation in mechanical efficiency with speed at two different motor displacements showed that at 30 rev/min the mechanical losses had the same value. The mean value of the actual motor torque occurs at a shaft angle of approximately 10^0. The values of the friction coefficients that predict the same efficiencies as the measured values at 30 rev/min are shown as follows:

f_C	f_B	Maximum Displacement(measured-95.5%)
0.03	0.09	95.4%
0.05	0.07	95.6%
	Minimum	Displacement(measured-83.5%)
0.07	0.13	83.5%
0.09	0.10	83.7%

For the modified motor the predicted efficiencies with these coefficients would be 96.8% and 88% respectively. For the low displacement this represents an improvement of 5.4% but more importantly, operation at increased speed may be possible because of reduced frictional heating of the slipper.

2.5.2 Piston and slipper forces

The modification to the con rod has a significant effect on the piston forces for shaft angles greater than 90^0. This is due to the increasing moment arm created by the increased length between the con rod bearing centre and the point of application of the inner piston force F_1. As the difference between F_1 and F_2 is equal to the side force F_T acting at the con rod centre, the outer piston force F_2 is also reduced. The maximum reduction of these forces, shown in Fig 9, is in the region of 50% which, aside from the benefit of reducing the losses, will result in a reduction in wear to the piston and the cylinder bore.

The slipper contact force, shown in Fig 10, is also reduced but not in the same proportion as the piston forces. This is because the contact force required for radial equilibrium is unaffected by the change.

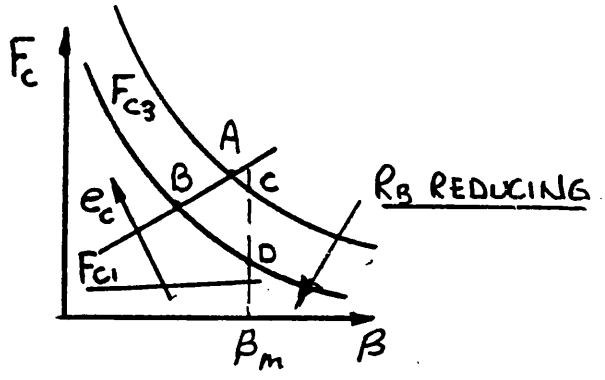

As shown in the preceding diagram, the reduced force required for rotation of the con rod causes the angle β to reduce from points *A* to *B*. If the value of e_c is small enough then β would be equal to β_m and as a consequence F_{C1} would reduce proportionally with the radius, R_B, of the con rod bearing (ie from points *C* to *D*). However the reduction in this force, which ranges between 10 and 25%, would, as for the piston, result in reduced wear and reduced frictional heating of the slipper.

Providing the change in materials of the piston and con rod is such that the smaller diameter bearing can be utilised without increasing the friction (and wear in this joint), the reduced levels of the piston and slipper forces could allow the operating pressure of the motor to be increased by between 10 and 15% and more if e_C can be kept at a sufficiently small value.

3.0 SOME ALTERNATIVE MOTOR DESIGN CONCEPTS

Radial piston eccentric motors that employ different types of oscillating joint mechanisms were discussed in Chapter 1. Each of these concepts have specific advantages from a combination of parameters that include; size, cost, weight, maximum pressure, maximum speed, efficiency, the capability of operating with water based and synthetic fluids and other parameters of lesser importance.

In the UK, the low priority given to R and D investment, has put constraints on the scope for improvements that the engineer can pursue. With high speed pumps and motors, R and D has, in general, been able to lead and, to some extent, create its market. As a result, in recent years, the high speed motor and gearbox unit has, except in specific areas, replaced low speed high torque (LSHT) units in many applications for which they had been traditionally the automatic choice.

A consequence of this has been for some LSHT motor manufacturers to search for methods to reduce the cost of the product. This aim can be in direct conflict with that of developing the product to obtain increased performance. To pursue higher performance from the Staffa motor, the scheme shown in Fig 11 was developed. The intention was to obtain a higher pressure capability by increasing the thickness of the slipper, the length of the con rod and the thickness of the motor casing. This design increased the size, weight and cost of the product.

The German company Dusterloh produces a motor in which the con rod bearing is of the gudgeon pin type. This requires very accurate line boring of the motor case to obtain the necessary alignment of the shaft bearings. Work by Klie[24], in his PhD thesis, describes how the slipper was designed to obtain minimal distortion of the slipper face. As a result this motor has a much higher power rating than the Staffa product, as it is able to operate at maximum pressure at higher speeds. However it has a much higher cost and therefore tends to find a limited application range.

In contrast to the approach of Fig 11 an alternative scheme, shown in Fig 12 was developed. Here the emphasis was on reduced cost by the elimination of the cylinder machining operation in the motor case and the use of cylinder end caps. There is also a technical advantage in this inverted piston design in that it eliminates the side force component between the piston and the cylinder. The reduction in friction obtained by this change would increase the efficiency by around 2 or 3%.

Kawasaki of Japan, licencees of Staffa, in the pusuit of reduced cost, carried out extended testing of the design shown in Fig 13. This method is used in the bent axis pump, manufactured by the Swedish company Volvo, where the piston centre line moves 2^0 out of line with the cylinder. In this radial piston motor, the con rod rotates through an angle of 10^0 which changes the sealing gap by an amount that would be considered unacceptable, as shown in the diagram with Fig 13.

Kawasaki obtained a reasonable life of 2000 to 3000 hours at 175 bar with their initial testing but subsequent tests were unsatisfactory due to apparent small differences in the sealing material. The author, when with the Staffa organisation, had neither the finance to manufacture components nor the personnel to perform the necessary project work. The ability of Kawasaki to test this design is demonstrative of their attitude to R and D.

The organisation evaluates prototypes on a regular basis which often involves quite significant changes in approach and accepts that only a percentage will provide the basis for manufacture. The design offers a 15% saving in overall cost for a 7 cylinder machine. From a technical viewpoint friction in the con rod bearing is eliminated. Providing that the side force at the piston to cylinder contact can be satisfactorily accommodated, there would be a considerable gain in mechanical efficiency.

If the full cylinder pressure acts around the seal periphery, there will be no side force on the piston. The side force component will therefore be a result of the pressure area shown hatched in the diagram with Fig 13. In the event that there is a pressure gradient below the line *AA* (see Fig13) parallel to the cylinder axis through the centre of the sphere some of the side force will be carried by contact of the piston with the cylinder. The theoretical solution of this problem and its successful development would enable the motor to have a competitive edge in terms of price and reduced overall diameter.

4.0 ALTERNATIVE CON ROD BEARING DESIGN

As was shown in 2.4, significant improvements in efficiency are obtained by reducing the con rod bearing friction coefficient. The mechanical losses obtained from the standard model with a value of f_B = 0.04 are shown in Fig 5 compared with those for the variable coefficient model. In addition to the benefit of reduced losses at maximum motor displacement (giving an improvement of up to 70%), it is seen that the losses at the lower displacement are also lower than those for the standard model at maximum displacement. Commensurate with this improvement is the reduced torque step at 36^0 which can cause speed oscillations in some applications when operating at low speeds.

Thus the key to improving the design of this type of motor lies in the utilisation of an oscillating joint having a reduced unit loading.

4.1 Motors with pressure balanced oscillating bearings

4.1.1 Calzoni motor

In the radial piston motor, because the spherical bearing is inside the piston, there is insufficient area to obtain any significant hydrostatic force to separate the components. In the axial piston machine, the ball joint is outside of the cylinder and consequently it can be of greater area than the piston.

In the motor manufactured by the Italian company Calzoni (shown in Fig 9 Chapter 1 and here in Fig 14a), a telescopic cylinder arrangement is used to transmit the pressure force onto the eccentric. Both the outer bearing and the eccentric have spherical surfaces and the magnitude of the contact forces can be set by appropriate choice of the relevant tube diameters (this aspect will be discussed in Section 5).

The spring is used to retain the components when the motor is unpressurised or, possibly during overrunning when the cylinder pressure is lower than that in the motor casing. It can be seen that there is a central rod and bush to improve the location of the two cylinders when they are fully extended.

Calzoni have recently redesigned this motor, shown in Fig 14b, which incorporates the following changes:

a) Elimination of the central rod.

b) Reversal of the cylinders by moving the larger diameter component from the outer to the inner position.

c) Elimination of the cylinder end caps by splitting the motor case across the radial section shown in Fig 14b.

Comparision of the Calzoni design with that of Staffa show that there is no piston side force component. This, together with the significant reduction of the friction in the oscillating joint, provides a considerable reduction in the mechanical losses. Tests carried out by Staffa show that the starting and low speed mechanical efficiency are at least 5% higher than that in the Staffa unit.

The spherical surface on the eccentric allows the slipper to be circular which reduces manufacturing cost. More importantly, any distortion of the slipper face will be axisymmetric which could well maintain parallelism of the clearance space. The consequence of this would be a negligible loss of pressure support giving improved performance when operating at high speeds and pressures.

4.1.2 Design proposed by the author

In 1982 the author proposed the design shown in Fig 15 which is of a similar concept to that of Calzoni except that the outer bearing cup is concave instead of convex. The reasons for using this approach are threefold these being as follows:

a) The upper cylinder can be located at its centre of rotation by a spring loaded pivot. In contrast to the Calzoni design this spring is not required to flex with every piston stroke thus reducing the likelihood of fatigue failure.

b) This arrangement simplifies assembly of the motor, it being possible to push the complete cylinder and cup assembly radially outwards from the centre of the motor casing.

c) The convex shape allows the inlet port to the cylinder to be accommodated within a smaller overall diameter of the motor.

It is an important consideration to maintain the overall diameter and the mounting bolt pitch circle diameter within the dimensions that pertain to those of other manufacturers. These dimensions for four different types of motors are shown plotted against the motor displacement in Fig 16. The dimensions obtained for two displacements of the proposed design are also shown in this figure and are seen to follow the general trend.

Fig 16 also has a scale line relating the linear dimension as a function of the one third power of displacement ($D^{1/3}$). It is interesting to note that at small displacements the size of existing motors increases at a lower rate with displacement but above 1250 cm^3/rev they fall onto a line varying with $D^{1/3}$.

The Calzoni motor uses the smallest possible eccentric diameter consistent with obtaining separation of adjacent slippers around its periphery at their position of nearest approach.

Motor displacement is obtained from the product of the piston area and the eccentricity. There are many combinations of these two parameters. To achieve a given displacement within the constraints of a given overall diameter and peripheral length around the eccentric requires various design alternatives to be considered.

For the proposed motor, the minimum diameter of the eccentric was limited in order to allow variable displacement. This limitation is caused by the space required for the displacement change pistons in the shaft as used, for example, in the Staffa design (see Fig 11). This constraint produces a piston diameter that is relatively larger and an eccentricity that is relatively smaller than in the Calzoni design.

There is also a choice of whether to place the larger diameter cylinder component against the eccentric or the outer bearing cup. Designs were carried out for both of these alternative arrangements.

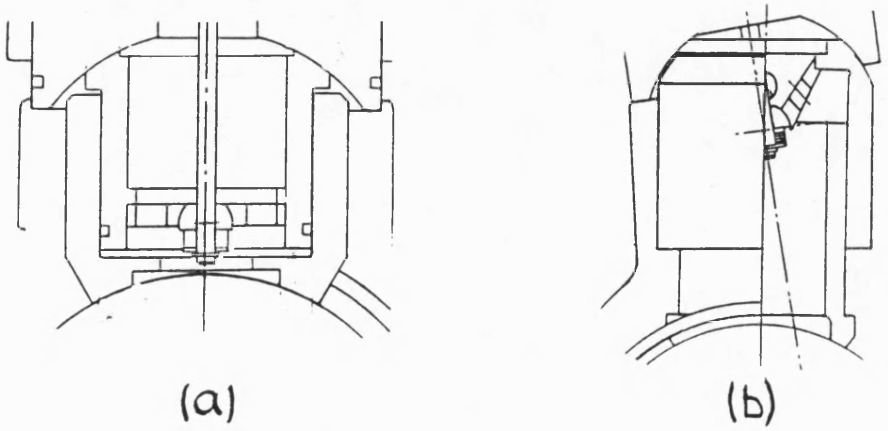

From these arrangements, shown in the diagram, the author found, for all the various considerations, the alternative (b) to be the most suitable. This is the type used in Fig 15 from it which it can be seen that an acceptable spacing of the slippers around the eccentric is obtained. It can also be seen that, at the point of maximum extension of the cylinders, sufficient insertion of the inner cylinder is obtained.

An indication of the way in which the design was originally refined in order to reduce the overall size is shown in Fig 17 which compares two earlier designs having the same displacement. This design is virtually identical to that proposed in Fig 15 except that the outer cup is located in a different manner and has a larger spherical radius. The reduction in size shown has been obtained by reducing the size of the components and a reduced insertion length for the two cylinders.

A comparision is shown in Fig 18 of the proposed design with that of a Staffa motor piston and con rod assembly of similar displacement. The mass of the reciprocating components for the Staffa design is several times greater than that of the proposed design. In the Staffa motor the piston force has to be transferred through the con rod bearing and the con rod in order to apply the hydrostatic slipper pressure force onto the eccentric. In the dual cylinder method this force transference is avoided by applying a large proportion of the pressure force directly onto the eccentric.

The German company Pleiger who produce the motor type shown in Fig 6 of Chapter 1 have, in the last two years, launched the new design as shown in Fig 19. This is seen to use the same outer cup arrangement as in the design proposed by the author, but interestingly, with the cylinders arranged in reverse order as in the new Calzoni motor and shown in the arrangement (a) above. This motor uses individual spool valves to distribute the flow to the cylinders. These valves, located in the cylinder end caps, are operated by the oscillating motion of the cylinders.

To assess the proposed design an analysis, similar to that developed in Chapter 2, was used which is described in section 5.0

5.0 ANALYSIS USED FOR THE PROPOSED DESIGN

The design as proposed in Fig 15 does not have a feed restrictor in the supply to the hydrostatic slipper. This results in the hydrostatic pressure force, to a large extent, being unaffected by the contact angle β. The contact force required for radial equilibrium is therefore only affected by the geometrical relationship of those forces which are dependent on β. It is assumed that the pressure distribution across the slipper lands is unaffected by the value of e_c, this only affecting the leakage flow.

The method used for obtaining the slipper force, F_{C1}, is identical to that developed in Chapter 2 Thus, as β_1 is varied, the value of F_{C1} for equilibrium of the radial forces is compared with that which is required, F_{C3}, to overcome the frictional torque for rotation of the outer cylinder in the outer cup bearing. The equilibrium (or operating) value of β_1 is thus that at which these two forces are equal. The analysis for this situation is developed in the Appendix which, for $0 < \theta < 90^0$, gives the following equation for the force F_{C1} (as shown in the diagram):

$$F_{C1} = (P A_p - F_u - F_s) / f_p(2 E /((L_2 - L_2) - C) + A)$$

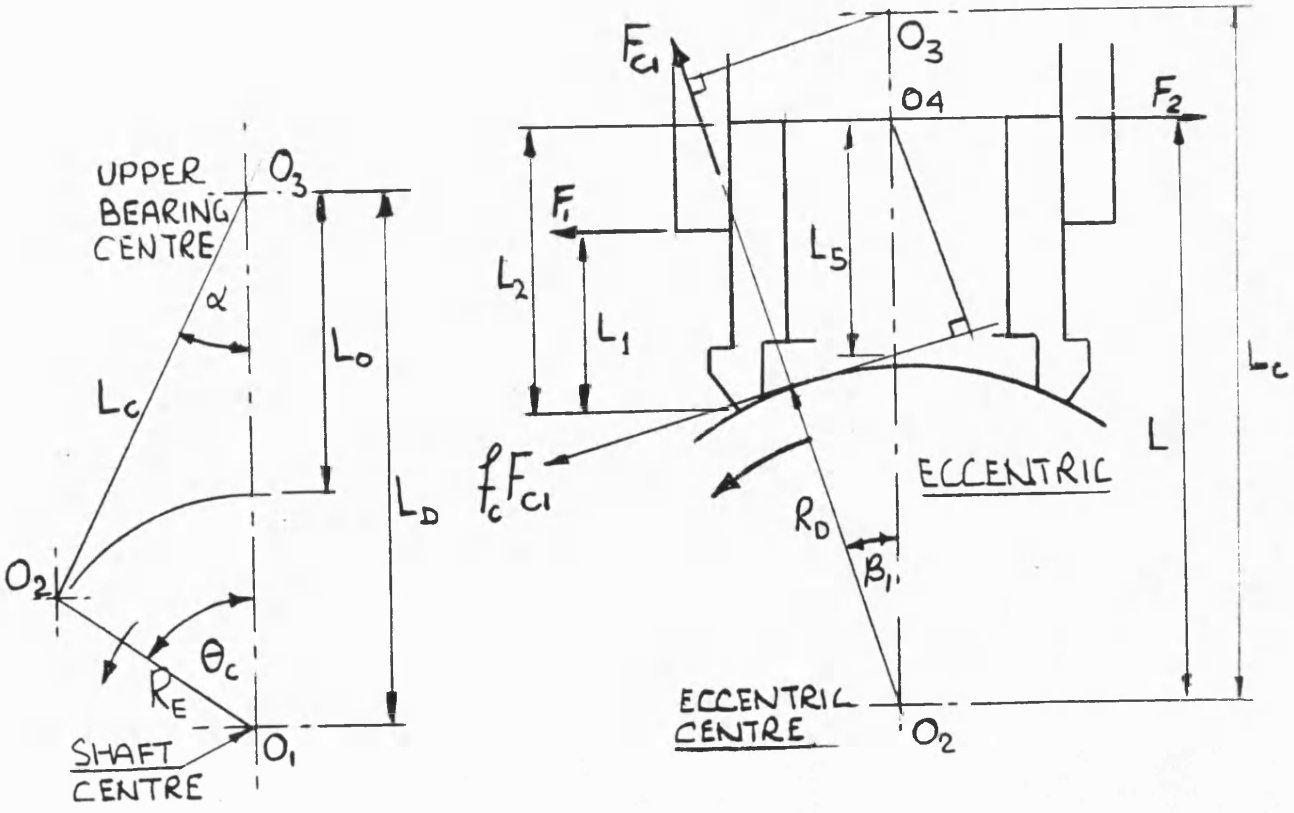

Here the piston area, A_p, is determined by the piston diameter (d_c) and that of the recess in the slipper (d_1). The separating force, F_u, is then determined by the diameter, d_s. F_s is the frictional force created by the piston seal and f_P the friction coefficient between the cylinders. The values of the coefficients A, E and C are all dependent on the angle β_1.

The force required to rotate the cylinder in the bearing cup, F_{C3}, is given by:

$$F_{C3} = f_B R_B S_1 / (f_c (L_c \cos \beta_1 - R_D) + L_c \sin \beta_1)$$

The geometry of the bearing cup is shown in the following diagram.

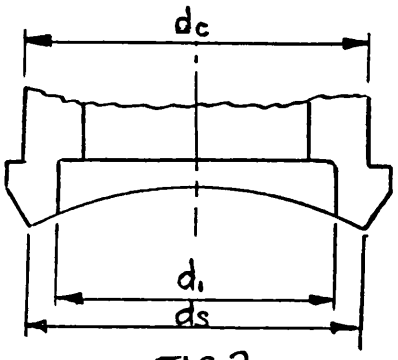

FIG3

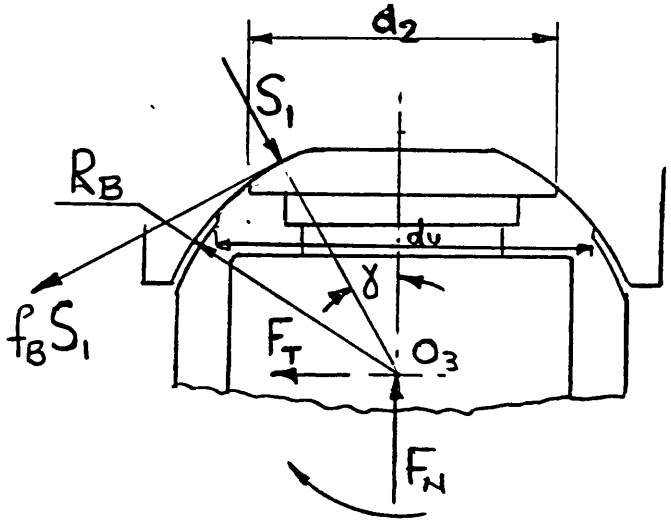

The area, A_B, resulting from the diameter, d_2, and the piston diameter, d_c, determines the pressure force on the upper bearing less the frictional forces from the cylinders and the piston seal. As in the slipper, the hydrostatic force will depend on the diameter, d_u. These, together with the spring force,F_K, determine the value of the force F_N . The side force, F_T, is obtained from the effects of the components of F_{C1} and f_c F_{C1} resolved normal to the cylinder axis.

As shown in the Appendix, these can be used to determine the values of the angle, γ, the bearing reaction force, S_1, and hence the value of F_{C3}.

The major difference between the design principle used in the Staffa type of motor and that proposed here lies in the ability to select the areas A_p and A_B, which can be much smaller than that of the piston itself. The areas of the lands of the slipper and the outer bearing, which are determined by appropriate choice of the diameters, d_s and d_u, can be selected to give a level of clamping force that is necessary to maintain contact between the components.

For shaft angles in the range 90^0 to 180^0 the forces are obtained in a similar manner to those obtained above except that the outer bearing frictional torque has changed direction as the angle α is reducing.

5.1 Dimensional data for the proposed design

Dimensional data for the proposed motor is given as follows:

Cylinder diameter d_c = 64 *mm*

Eccentricity R_E = 25*mm*

Eccentric to cup bearing centre distance L_D = 147 *mm*

Eccentric radius R_D = 66.5 *mm*

Slipper

Hydrostatic pocket diameter d_1 = 53.2 *mm*

Slipper outer diameter d_s = 72 *mm*

Datum length of lower cylinder L_2 = 86.5 *mm*

Outer cup bearing

Bearing cup radius R_B = 45.5 *mm*

Bearing pocket diameter d_2 = 53.2 *mm*

Bearing outer diameter d_u =72 *mm*

For the hydrostatic bearings the path lengths are a small proportion of the spherical circumference. It is therefore assumed that the contact areas are cones having a constant film thickness. Using the equation for a flat circular plate gives for the pressure distribution and separating force:

$p = P(1 - log(r/r_i) / log(r_o/r_i))$

and $F_s = \pi P((r_o^2 - r_i^2) / (2\, log(r_o / r_i) - r_i^2)$

The same dimensions have been used for both bearings hence: r_1, $r_2 = r_i$ and r_s, $r_u = r_o$

These give A_p and $A_B = 0.001\ m^2$

For operation at a pressure of 100 bar the following forces are obtained:

Forces acting on the bearings, F_p and $F_B = 10000\ N$

The separating forces, F_u and F_D from the equation above are therefore = 8320 N

The net clamping force is therefore = 1680 N This represents 16.8% of the available force but only 0.52% of the total pressure force on the full piston area (32000 N).

5.2 Model analysis

Using the equations from the Appendix, together with the software methods developed in Chapter 2, predicted values were obtained for the motor performance. These are presented in Fig 20 which show the variation of the mechanical efficiency with motor shaft angle for the pressure force areas (A_p and A_B) of 0.001 m^2 for an operating pressure of 100 bar.

A significant feature of Fig 20 is the very high efficiency that is obtained which gives an almost constant mechanical loss over the cycle. The torque discontinuity at 36^0 is almost imperceptible which is, as has been seen, a notable feature of the Staffa design.

This improvement in mechanical efficiency over that of the Staffa design is, to a great extent, due to the reduction of the frictional torque in the outer cup bearing in relation to that created in the spherical con rod bearing.

In the Staffa con rod bearing, the effect of the hydrostatic area between the piston and the con rod bearing reduces the contact force to approximately 75% of the force from the piston. In the proposed design the pressure area of 0.001 m^2 in the two bearings is 31% of that of the piston (0.0032 m^2). The nominal clamping force at 15% of the applied pressure force, represents only 5% of the total piston force. The net force transferred across the contact face is therefore only 6.7% of that transferred in the Staffa type of spherical con rod bearing. The apparent reduction in the frictional torque thus created has to be offset against the increase in the cup radius in relation to that of the con rod type (about 2:1).

However, the level of clamping force at 100 bar operating pressure, represents a mean pressure of 8.7 bar in the contact area. The level of this pressure in the con rod bearing, as was shown in Chapter 4, is of the order of 400 bar at the same operating pressure.

The effect of this reduction in the mean pressure on the contact conditions would be expected to result in lower values of the friction coefficient, particularly at low speeds. In general terms, the frictional torque should, therefore, be reduced by around 90% in relation to that generated in the con rod spherical bearing.

For a 50% increase in the pressurised areas (A_p and A_B), which represents a considerable increase in the clamping forces, it can be seen from Fig 20 that the efficiency reduces only by a maximum of 1.2%.

Fig 20 also shows the predicted mechanical efficiency for the motor displacement reduced in the ratio of 3.6 : 1. This has caused the efficiency to be reduced by 7.0% compared to a predicted change in the Staffa unit of up to 15%.

5.3 The levels of the piston and the contact forces

The contact forces, nominally designed to be 15% of the applied force, are slightly less than this level due to the effect of the friction between the cylinders and in the piston seal. Thus at 100 bar, when the applied force is 10000 N, the contact force is in the region of 1350 N which varies by less than 4% over the pressure cycle.

The piston forces (F_1 and F_2) vary considerably over the cycle because of the changing depth of insertion of the cylinders, as is seen in Fig 21. However, the maximum values of F_1 and F_2 only represent 2% of the full piston force. For the Staffa motor these forces were predicted to reach a maximum of around 45% of that from the piston .

It is also seen from Fig 21 that for $\theta < 90^0$ the force F_1 is considerably greater than F_2. However for $\theta > 90^0$, when the cylinder angle α begins to reduce, F_2 increases to a value that is slightly greater than that of F_1. This is because, for $\theta < 90^0$, the frictional force between the eccentric and the slipper is in the direction to assist rotation of the cylinders when α increasing. When $\theta > 90^0$, the torque created by this friction force about the outer cup bearing centre is now acting in the same direction as that caused by the friction in the outer bearing.

Now the side force $F_T = F_1 - F_2 = F_{C2} (\sin \beta_2 - f_C \cos \beta_2)$

The slipper contact angle necessary to obtain the required torque from the contact force is such that when $\theta > 90^0$, $F_{C2} f_C \cos \beta_2$ is slightly greater than $F_{C2} \sin \beta_2$. Hence F_T is negative which results in F_2 being greater than F_1.

For $\theta < 90^0$, the side force $F_T = F_{C1} (\sin \beta_1 + f_C \cos \beta_1)$ which results in F_1 being greater than F_2. If β_1 is negative, this situation still prevails providing $\tan \beta_1 < f_C$.

The minimum depth of engagement of the cylinders when they are fully extended is critically important. Comparing Figs 15 and 7 shows that the ratio of the engaged length to the diameter in the proposed design is at least 3 times greater than that in the Staffa design. The distance of the cup centre from the point of contact between the cylinders is relatively greater in the proposed design. This, together with the much reduced level of the bearing frictional torque and the low side force, should avoid problems of wear in these components.

5.4 OPERATION AT LOW PRESSURE

For operation at low pressure it is necessary to ensure that there is sufficient available force to overcome friction in the cylinders. The locating spring for the outer cylinder is selected to provide a force of 150 *N* but, for the inner cylinder, the only restraint maintaining contact is obtained by the loose fitting retaining ring (see Fig 15). This could only be expected to hold the component to within a minimum of 1 *mm* of the surface of the eccentric.

The leakage flow through this clearance could be such that insufficient pressure is generated in the supply. In this event the slipper may not move into contact with the slipper. At a pressure of 2 bar it is found from the model that there is a net closing force of 20 *N* which may be insufficient when operating at high speed. To avoid loss of contact a feed restrictor could be used as in the Staffa motor which is also used in the new motor by Pleiger (see Fig 19). The size of this restrictor could be such that it is only required when this condition arises, with the pressure drop created under normal conditions being minimal.

The design needs to be evaluated in order to ensure that the levels of distortion do not create values of e_C that result in problems of leakage from the slipper. In this connection, it is interesting to note that the motor of Jahns (see Fig 6), is designed to produce zero leakage and, as a consequence, is very successfully used for flow dividing applications.

The problem of leakage is that, in addition to causing rotational creep when loaded with blocked ports, the flow varies with the shaft angle. This causes variations in speed which increase as the speed is reduced. These speed fluctuations can become particularly noticeable when the motor speed is such that the pulse frequency, which is related to the number of pistons, is close to the natural frequency of the hydraulic system.

This aspect was the subject of a paper by the author[1] which demonstrated the use of simulation techniques for a study of the problem. The work also showed that predictions using linear techniques provided a reasonably accurate assessment of the situation. The speed fluctuations caused by torque ripple and changes in instantaneous displacement were shown to be of lesser importance. However the torque discontinuity, as measured in the radial piston motor, can create problems particularly as most hydraulic systems have low levels of damping.

High speed low torque motors (*HSLT*) with speed reducers have a particular advantage in this situation because of the increased motor speed in relation to the hydraulic natural frequency. This advantage has to be set against the lower mechanical efficiency obtained from such drives at low operating speeds when compared with *LSHT* motors. In the paper by Clifford[25], which compared the efficiency obtained from both these types of motors, it was shown that, under starting conditions, high speed units with gear reducers have a mechanical efficiency that is between 10 and 25% less than that of some low speed motors. At higher speeds this difference reduces to around 10 to 15%.

In order to take advantage of their higher mechanical efficiency at low speed it is therefore essential that the design of *LSHT* motors should be aimed at reducing the level of leakage and its variation with shaft angle, together with any discontinuities in the generated torque.

6.0 OTHER DESIGN APPROACHES

As discussed in Chapter 1 (see Fig 10) the cam type of radial piston motor provides the lowest torque to weight ratio of all the various types of motors. Of the two types of cam motors shown in Fig 10 Chapter 1, that which incorporates a single roller between the piston and the cam track provides a unit that is exceptionally compact.

A cam motor of this type designed by the author, is shown in Fig 22, for which a patent application was submitted in 1980. It can be seen from Fig 22 that it has a much smaller diameter that an eccentric type of the same displacement. Motors of this type are currently being manufactured by Rexroth of Germany and Poclain of France. The maximum speed of these motors is limited because of the high rotational speed of the roller. Also, because of the side load conditions on the pistons, the maximum mechanical efficiency is generally in the range of 85 to 90%.

These motors are usually limited to operating with a single displacement whereas in the eccentric motors, as shown in Fig 11, variable displacement is possible by changing the eccentricity.

Displacement control is a useful feature as it allows the motor speed to be increased without increasing the size of the pump thus reducing the overall system cost.

In axial piston swash plate motors the swash plate is not a rotating component and, as a consequence, the control of its position can be facilitated. In eccentric motors, because the eccentric rotates, control of its position is difficult to achieve. However closed loop control of either the supply pressure (at constant flow - which gives a constant power characteristic), or the speed can be performed. These are a desirable features in some applications.

The author developed a pressure control, a dynamic analysis of which was presented in a paper[13] in 1981. The incorporation of the hydromechanical control onto the motor is shown in Fig 23 which responded to changes in load as shown in the figure. The application in this case was a ship winch that required a low loop gain in order to provide an adequate stability margin for the control system.

The limits imposed by the performance of the slipper placed a restriction on the speed range that could be used for this control and, consequently, the maximum power rating. Developments to improve this situation would thus increase the available power and improve the versatility of the controller and its range of application.

The stability aspect appears generally to require a low value of the gain. The valve shown in Fig 23 was thus designed to suit as wide a range of applications as possible. With the introduction of integrated electronics it is now possible to incorporate proportional type valves that also allow speed governing to be performed by controlling the motor displacement.

7.0 CONCLUSION

This Chapter has been concerned with applying the analytical method for assessing the affects of various parameter changes on the motor performance. In particular it is noted that the benefit of reduced leakage can be obtained from reducing the slipper area providing that a small value of e_C is maintained. To achieve this, account has to be taken of both the method of manufacturing the components, and their structural rigidity.

The analysis has also shown that modifying the piston and con rod can reduce the mechanical losses by up to 20% and 25% respectively at maximum and minimum displacement. The general reduction in the level of the forces experienced by the components could enable the rating of the motor to be increased by up to 15% and possibly more if the value of e_C can be kept to a minimal level.

The incorporation of a slipper having reduced area with the modified con rod provides benefit of reduced leakage without any loss of motor efficiency.

A design proposed by the author shows a predicted mechanical efficiency that is up to 9% greater than that of the Staffa design for the same frictional conditions. When the displacement is reduced by a factor of 3.6 : 1 the mechanical efficiency reduces by 7.0%. In the Staffa motor this change was of the order of 15%. In applications where smooth operation at low speeds is required this approach would provide a motor that could compete effectively with *HSLT* drives. If the motor speed can be increased above current levels *LSHT* motors with single ratio gear reducers would be able to compete in some applications that are now dominated by *HSLT* drive systems.

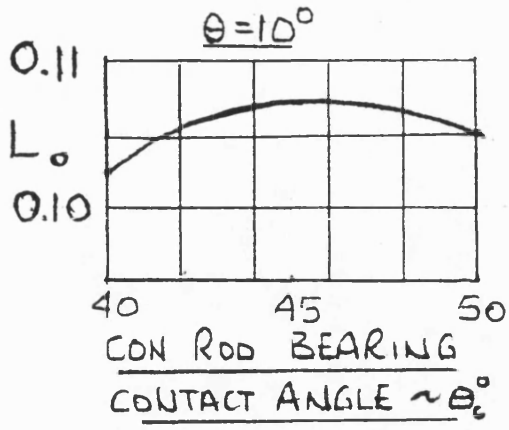

Fig 1 Variation of the losses with the con rod contact angle

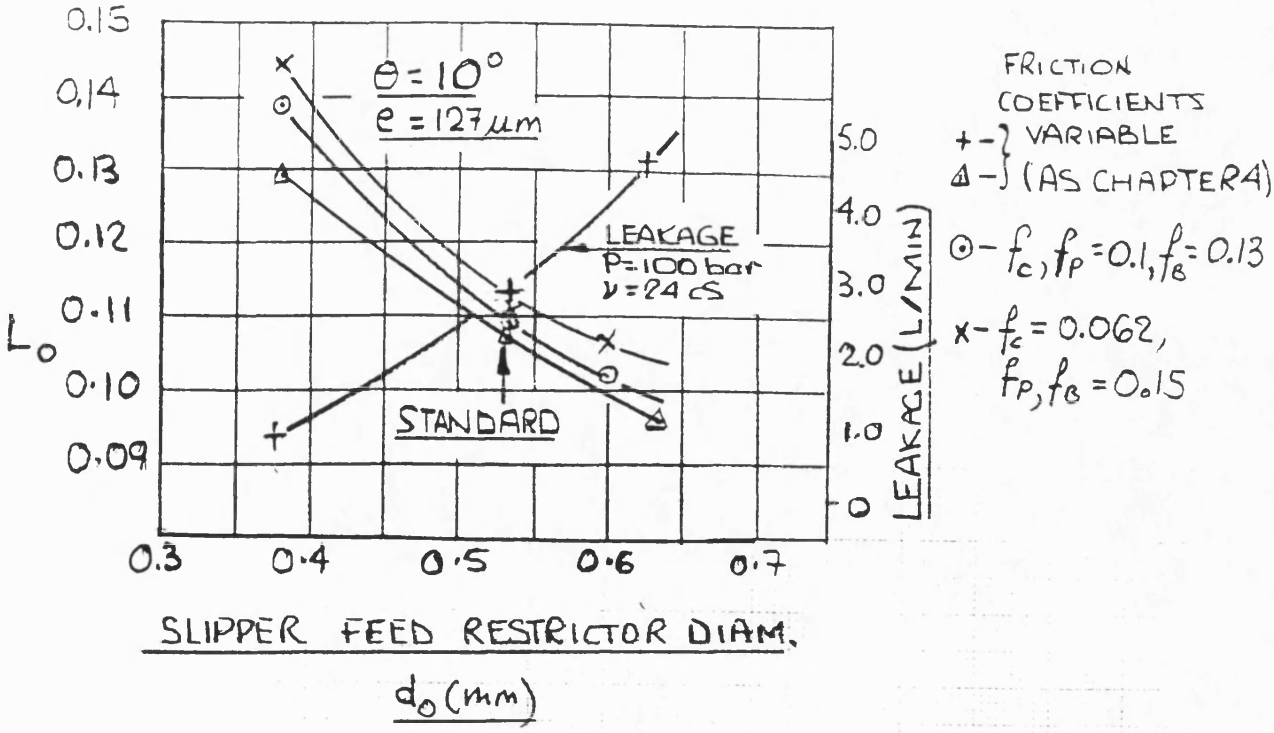

Fig 2 Variation of the losses with the feed restrictor size

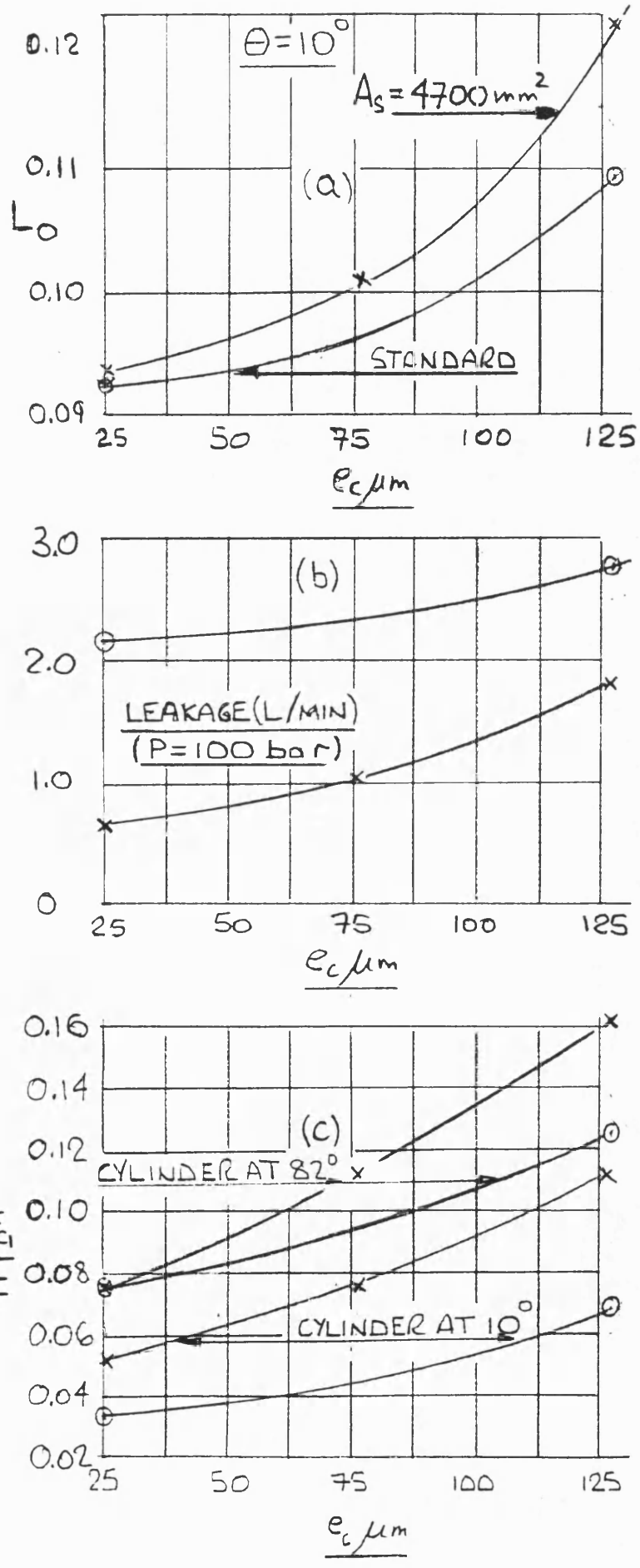

Fig 3 The effect of reduced slipper area

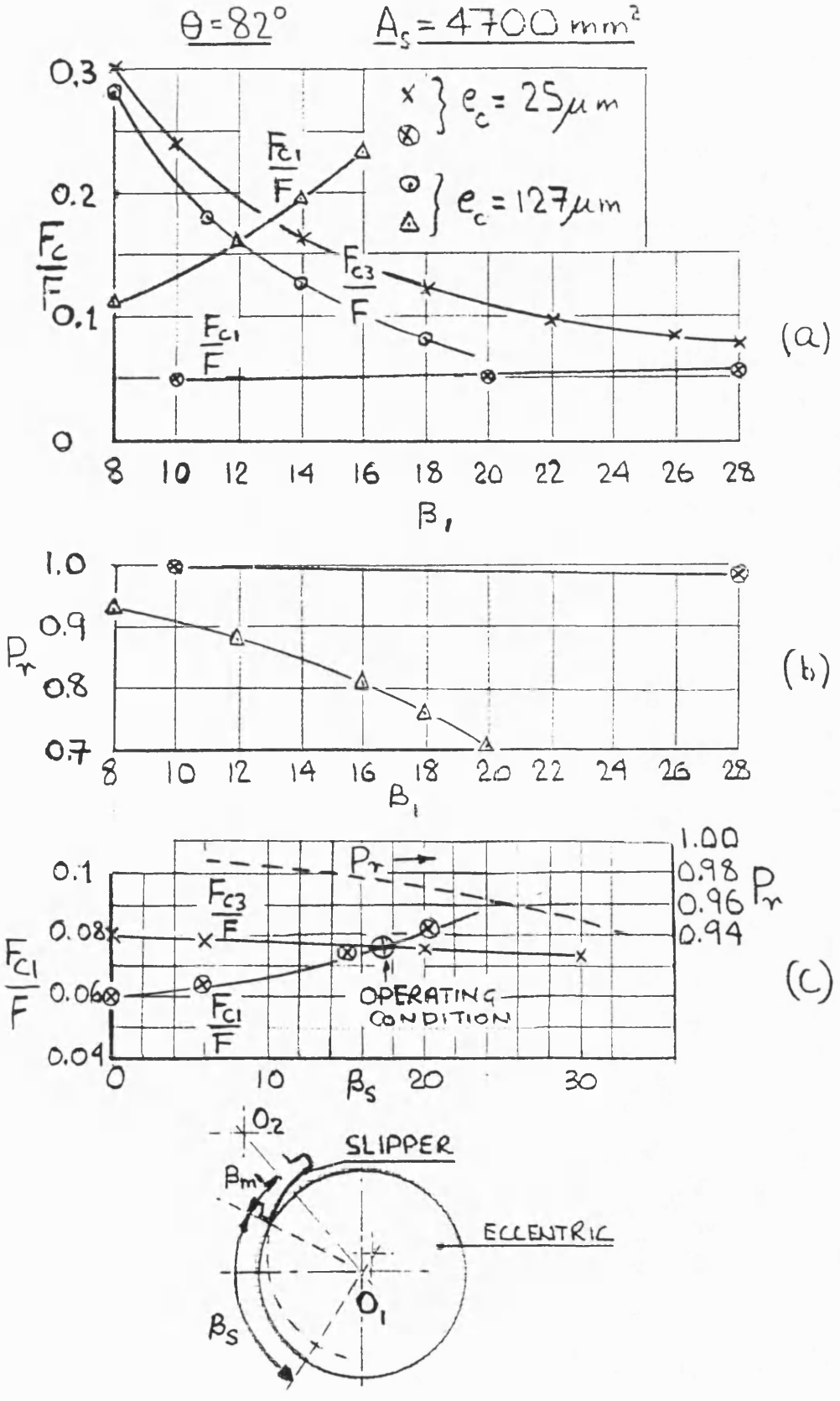

Fig 4 The effect of reduced slipper area on the slipper geometry

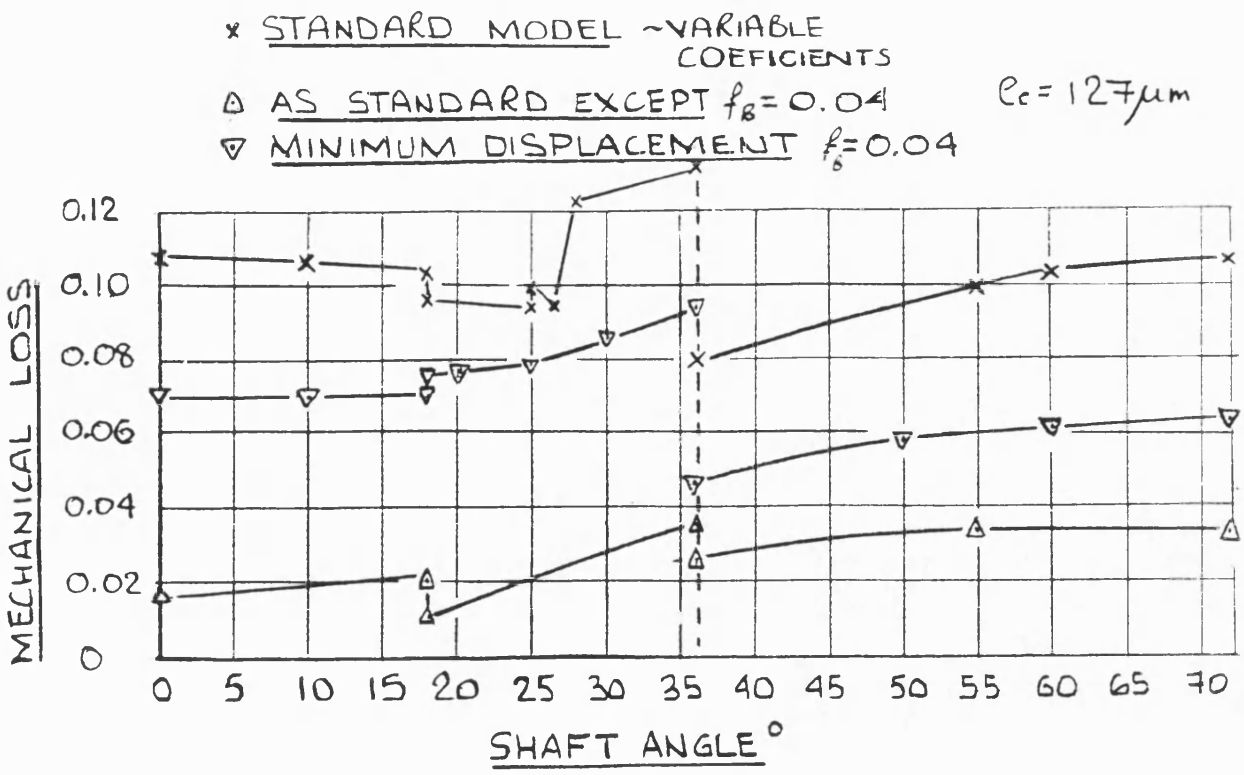

Fig 5 The effect of the con rod bearing friction coefficient on the losses

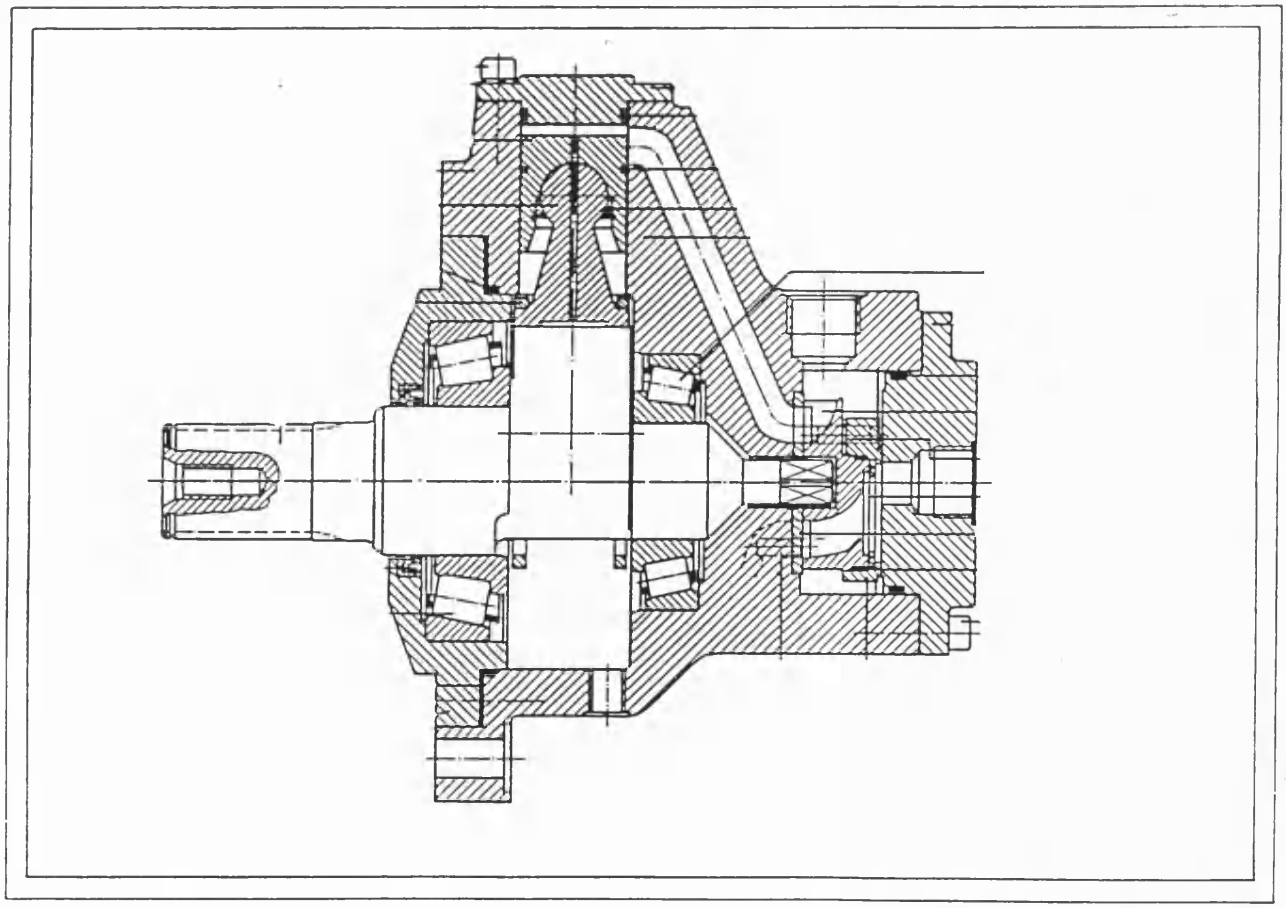

Fig 6 Fig The Jahns motor

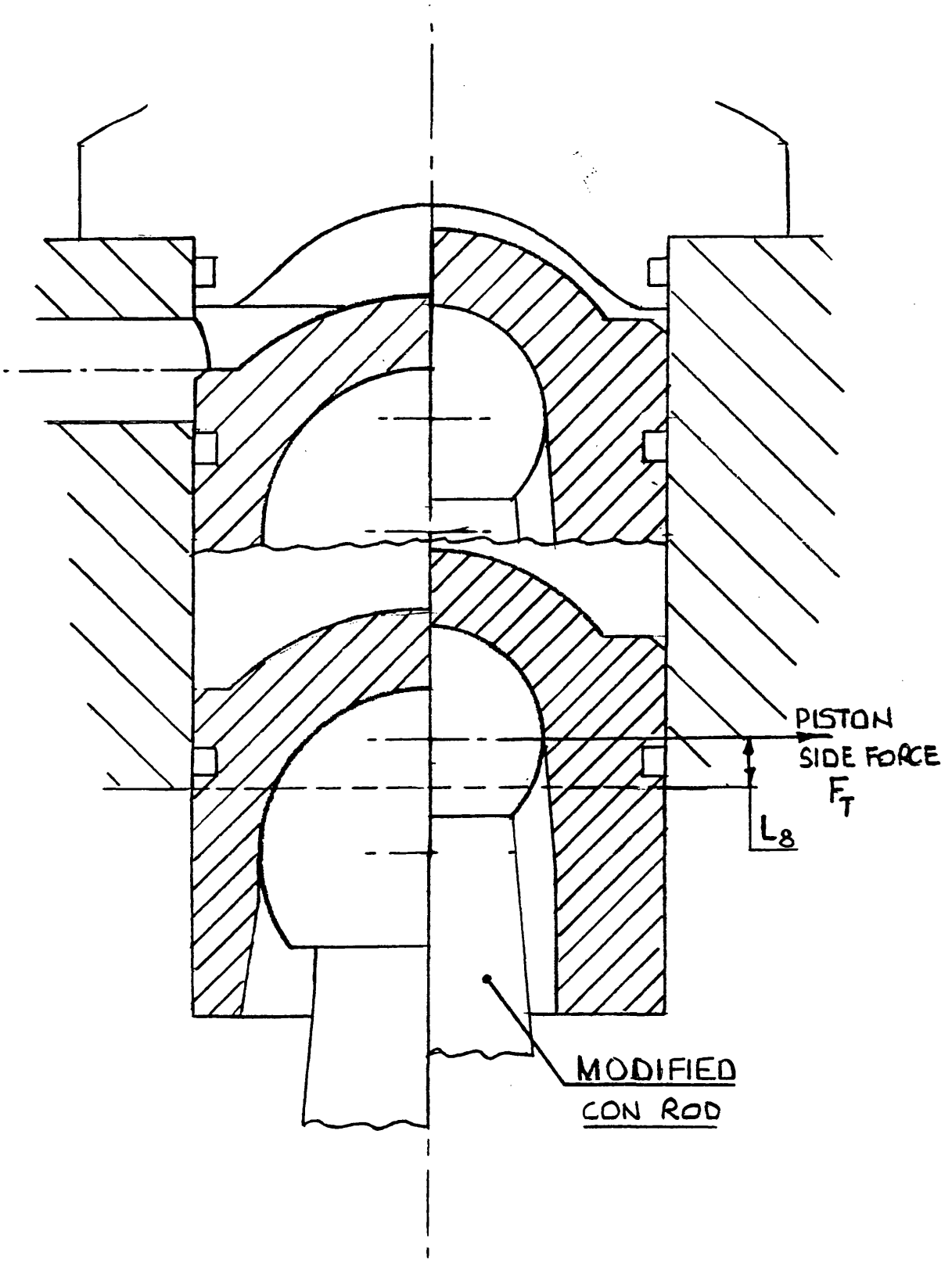

Fig 7 Modified con rod

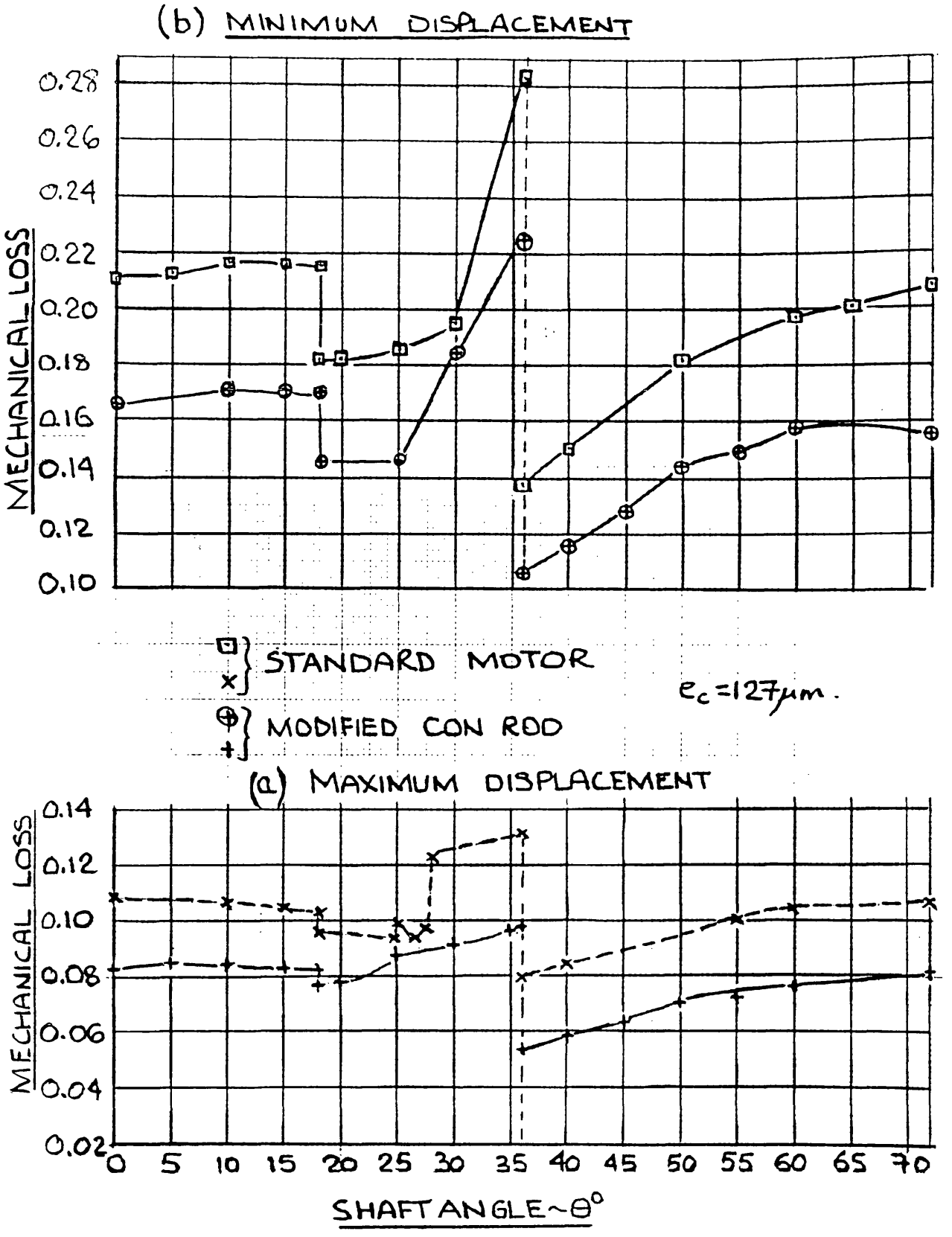

Fig 8 Motor mechanical losses with the modified con rod

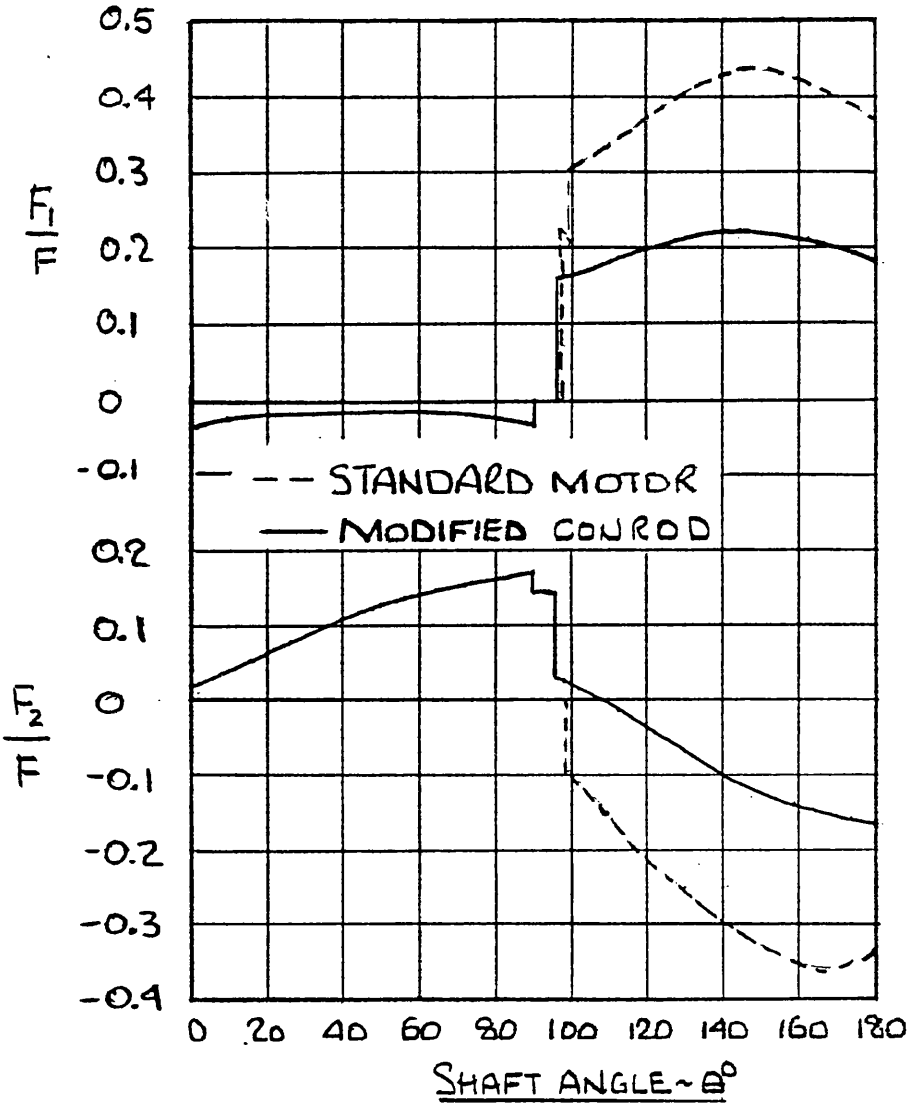

Fig 9 Piston force variation with shaft angle

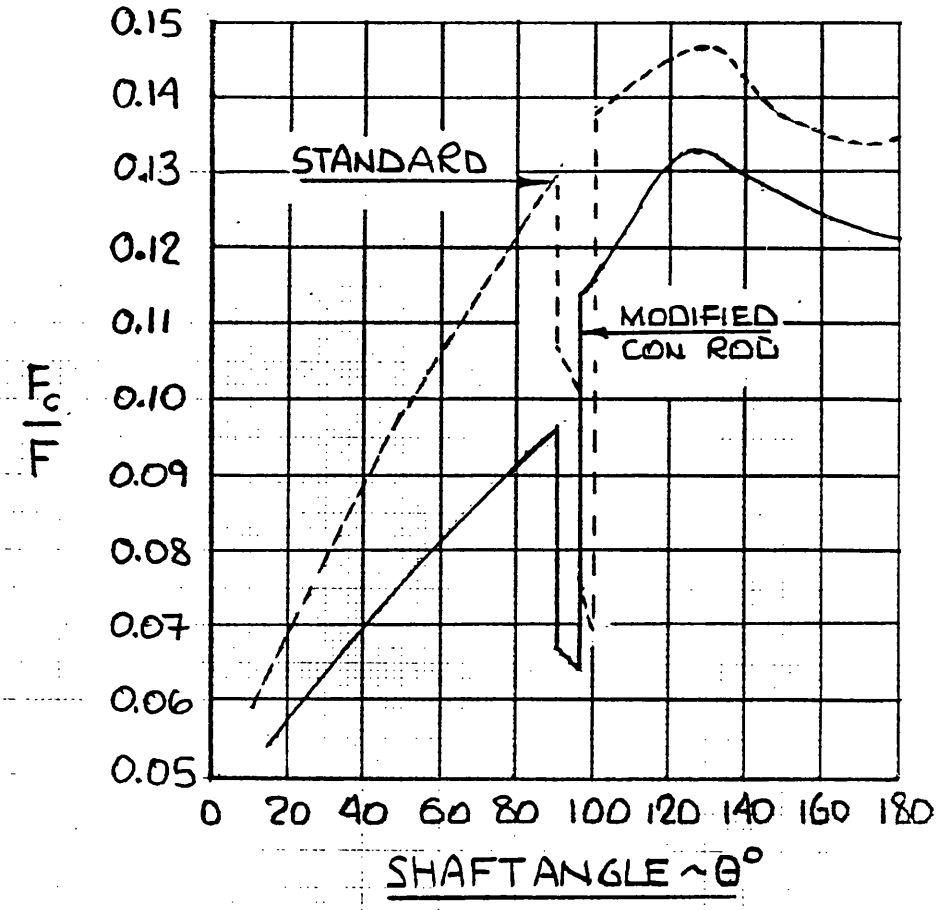

Fig 10 Slipper contact force variation with shaft angle

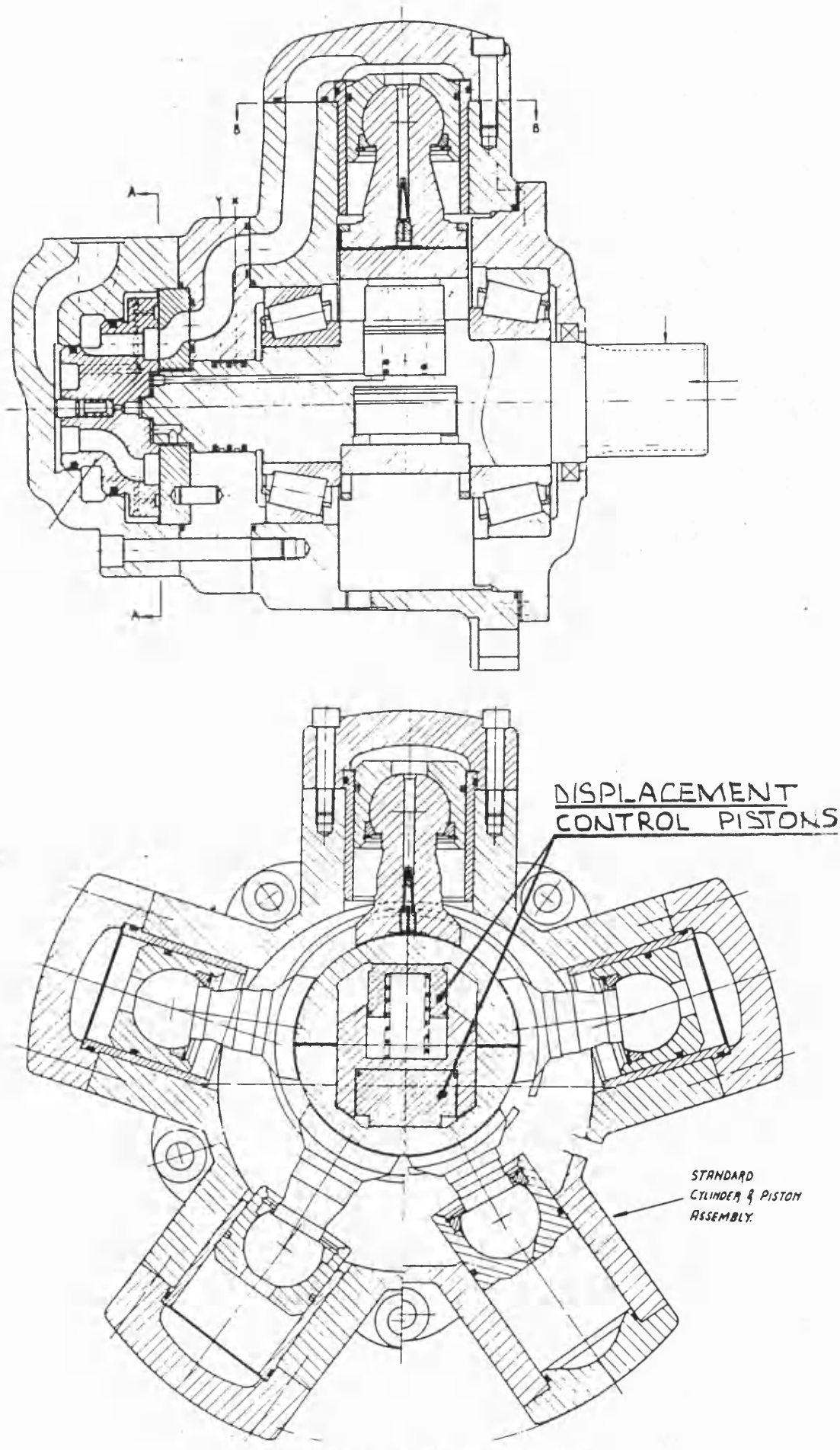

Fig 11 Motor design for increased power

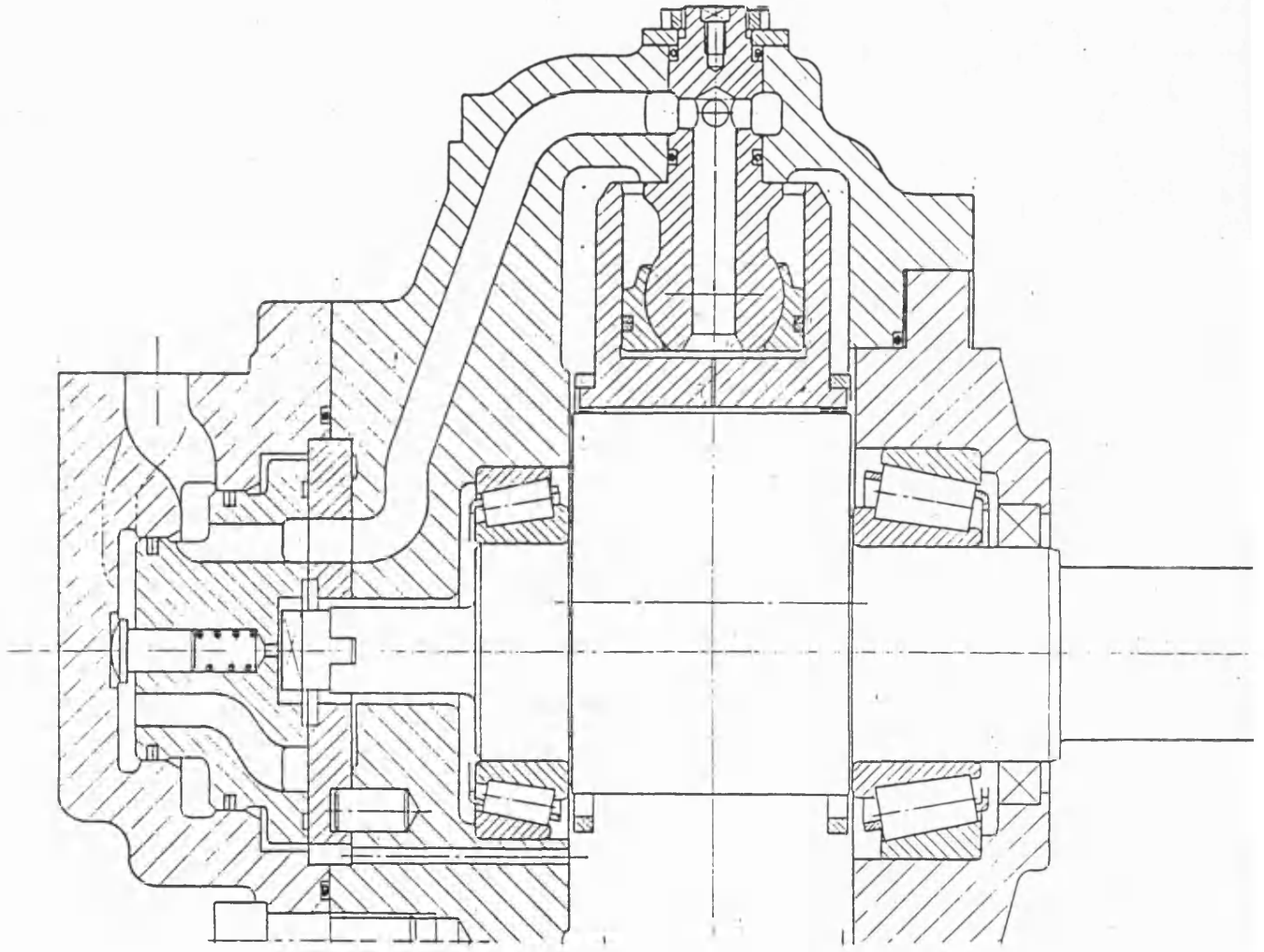

Fig 12 Motor design for reduced cost

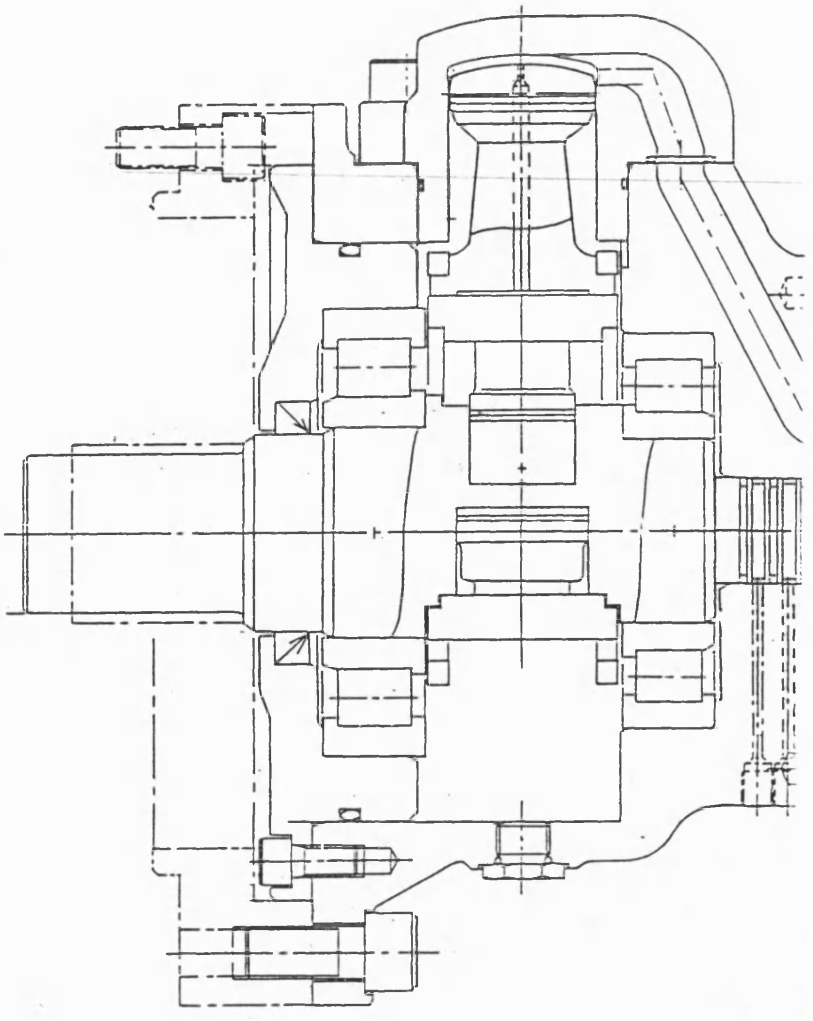

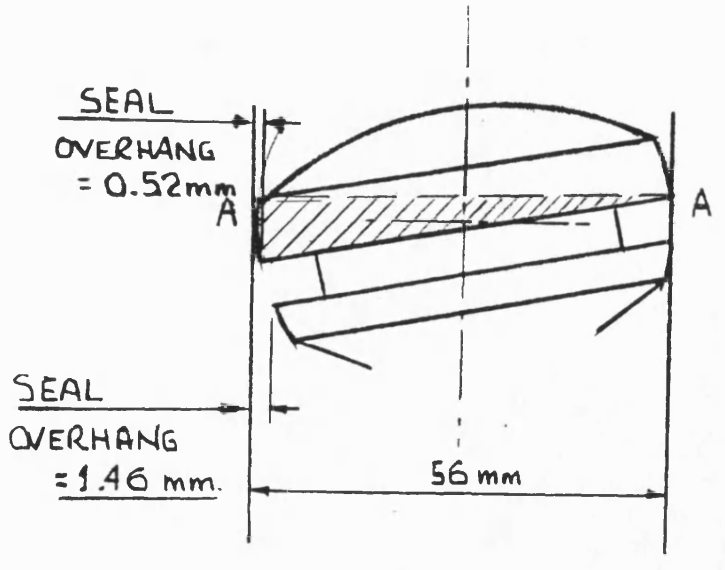

Fig 13 Kawasaki motor development

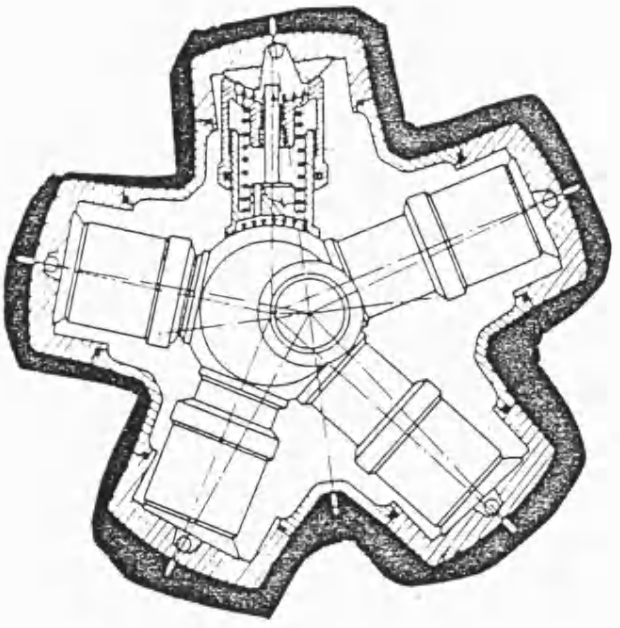

(a) CALZONI ORIGINAL DESIGN

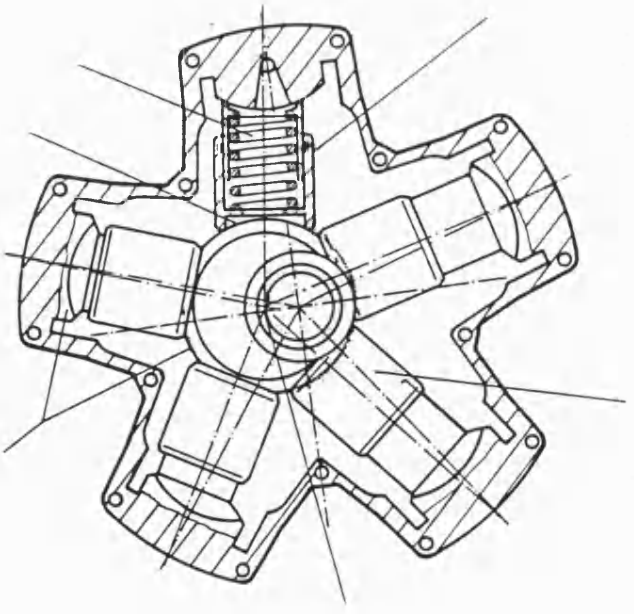

(b) NEW CALZONI DESIGN

Fig 14 Calzoni motor

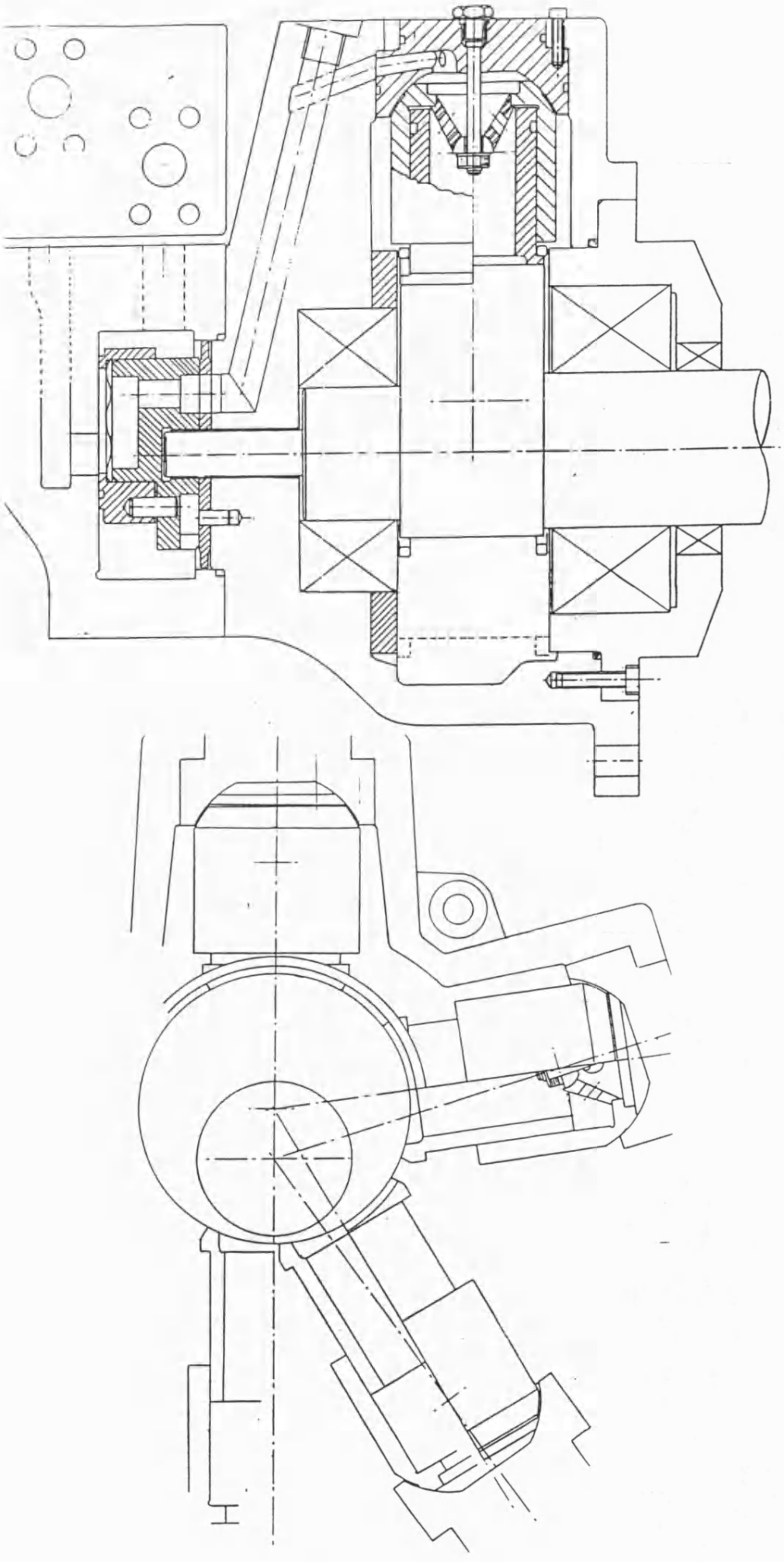

Fig 15 Proposed motor design

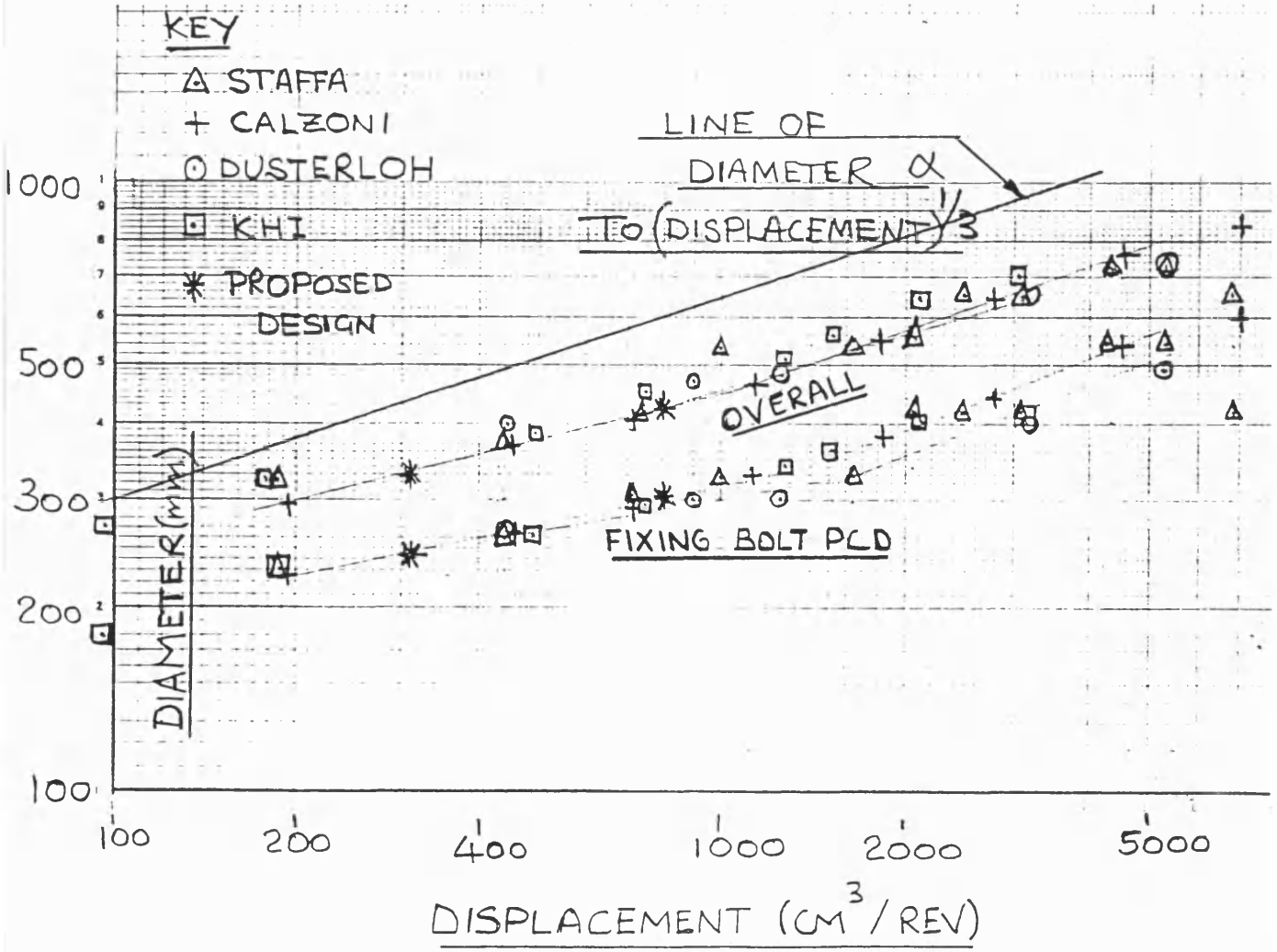

Fig 16 Sizes of available motors

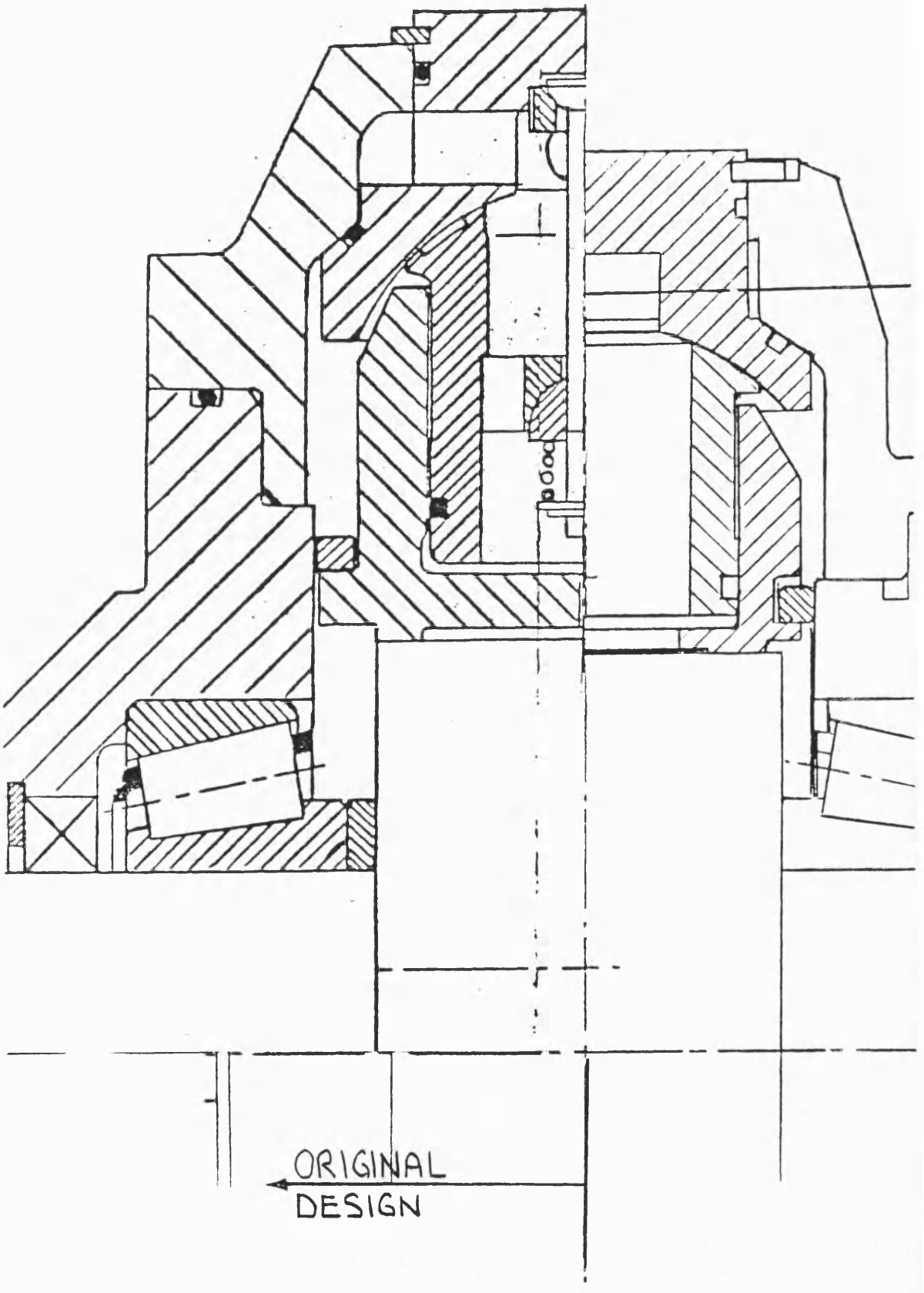

Fig 17 Design evolution

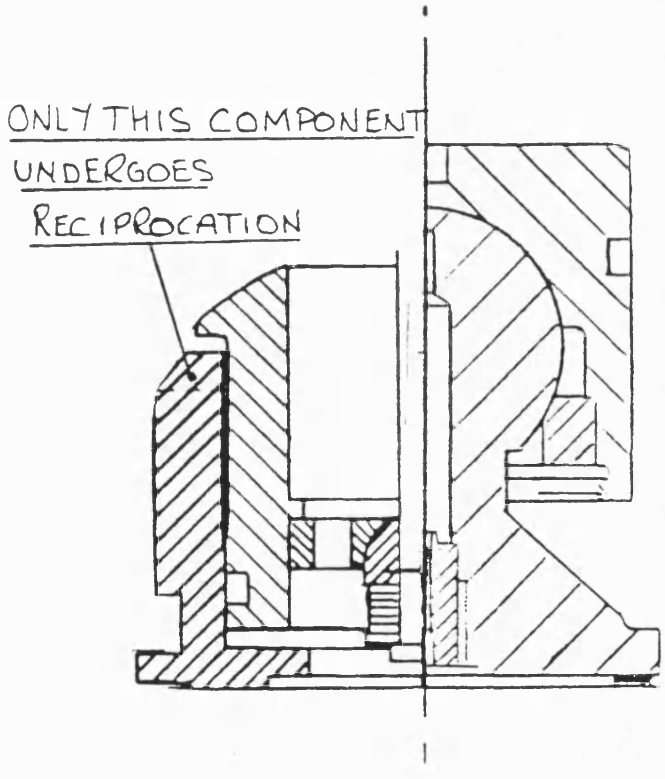

Fig 18 Comparison of the reciprocating components

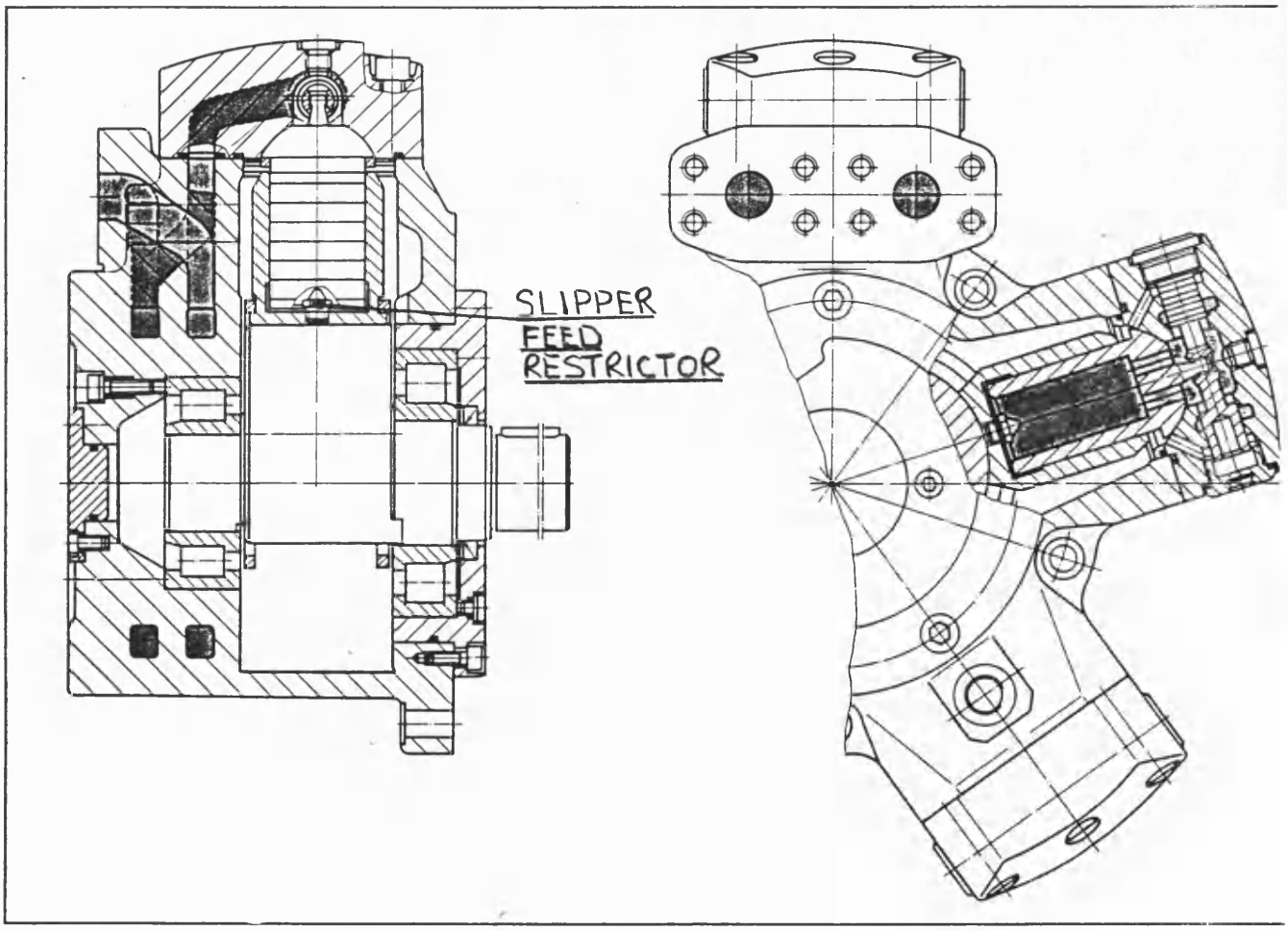

Fig 19 Pleiger motor

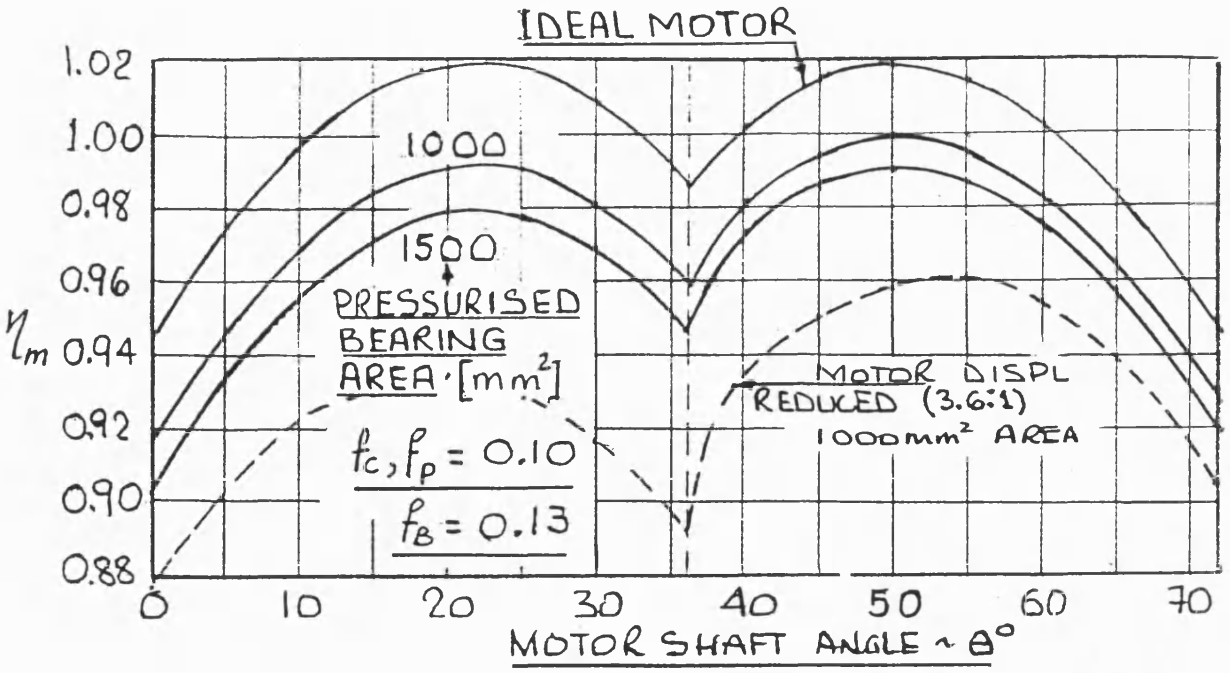

Fig 20 Predicted mechanical efficiency of the proposed motor

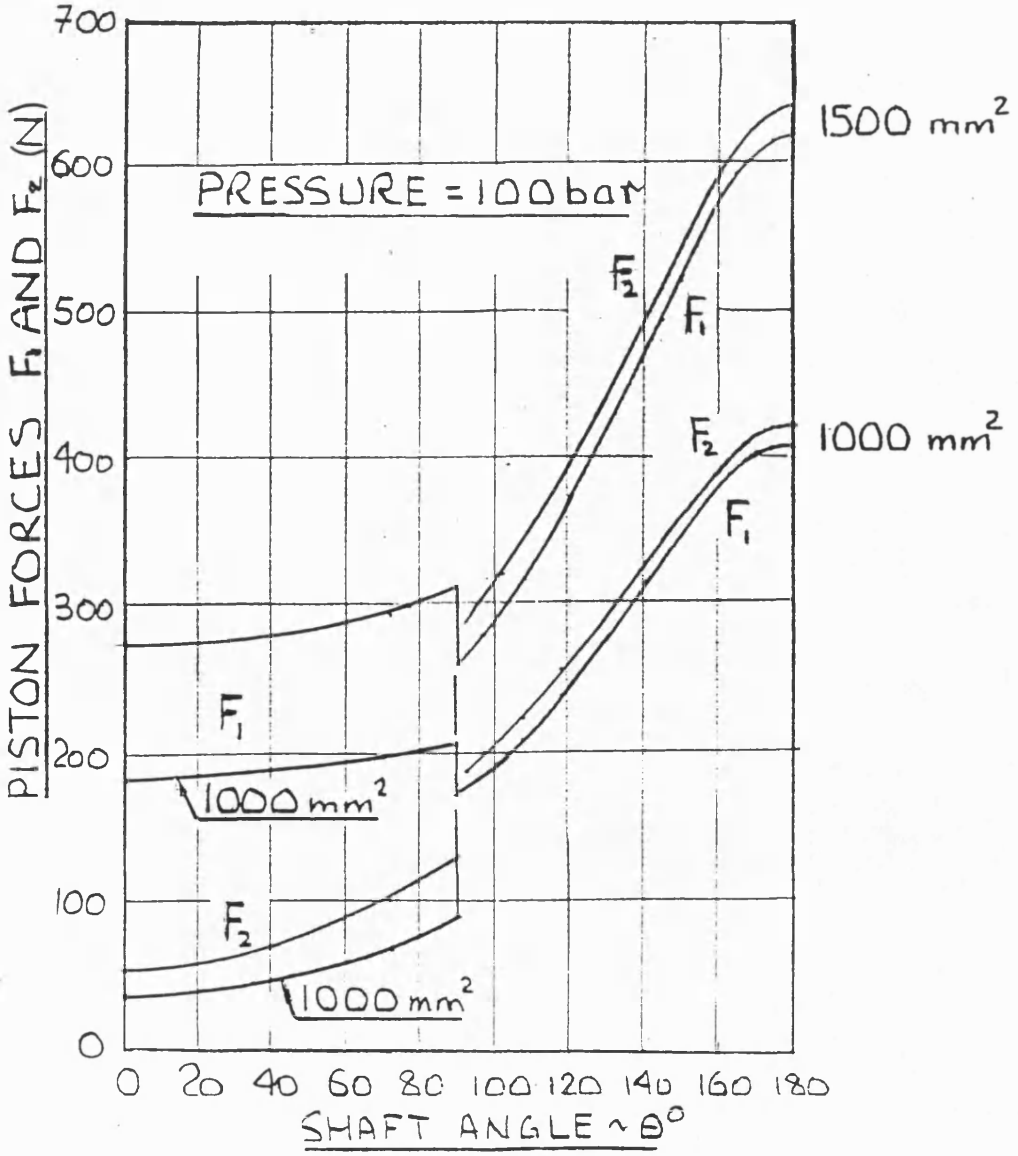

Fig 21 Predicted piston forces for the proposed motor

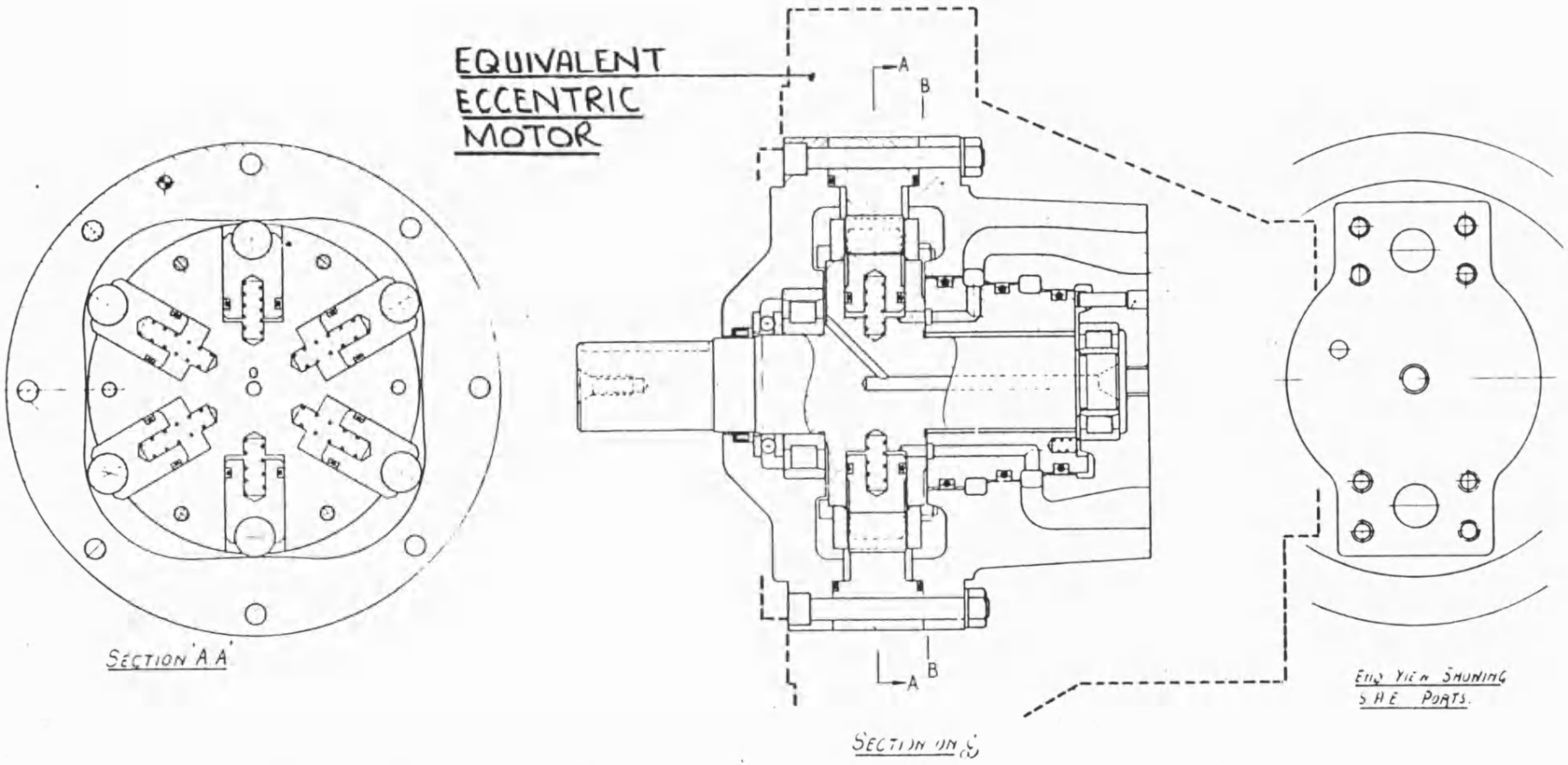

Fig 22 Design of cam motor

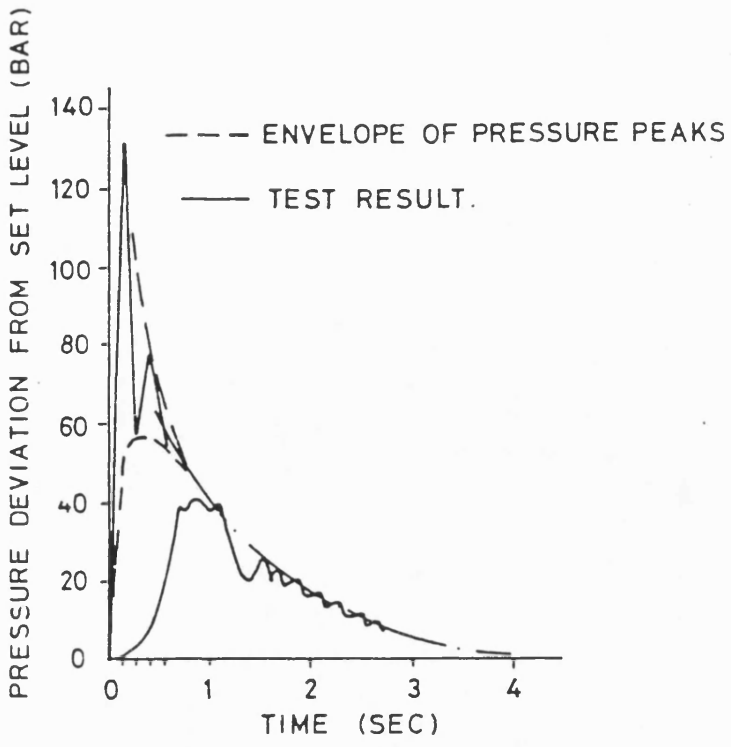

PRESSURE VARIATION FOLLOWING A STEP INCREASE IN LOAD FOR A CONTROL SETTING OF 139 BAR.

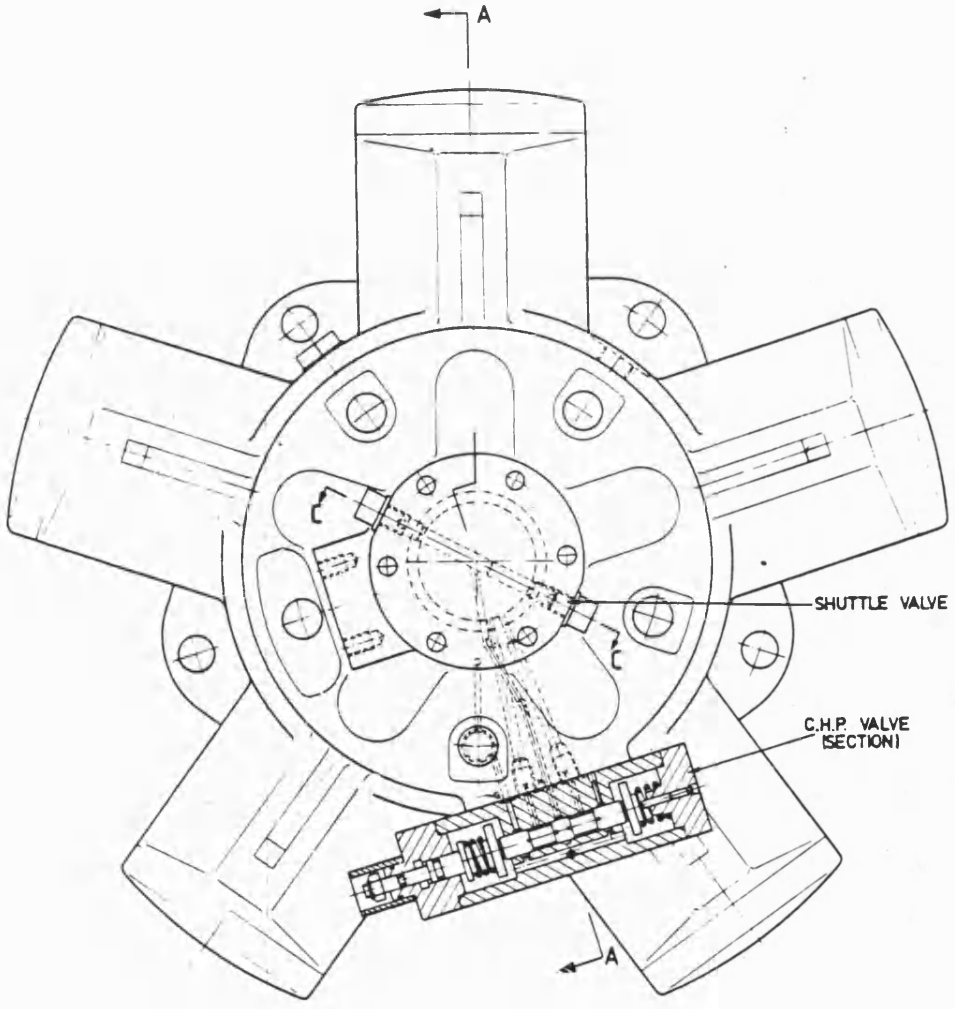

Fig 23 Constant pressure controlled motor

Appendix

For the geometry shown in Fig. 1

$$\alpha = \tan^{-1}\left(\frac{R_E \sin\theta}{L_D - R_E \cos\theta}\right) \tag{1}$$

$$X = \left(\frac{L_D - R_E \cos\theta}{\cos\theta}\right) - L_0 \tag{2}$$

For $0 < \theta < 90^o$

Slipper and piston forces

The forces for this situation are shown in Fig.2.

$$F_1 - F_2 = (f_c \cos\beta_1 + \sin\beta_1)F_{C1}$$

$$= CF_{C1} \tag{3}$$

Taking moments about O_4

$$F_1(L_2 - L_1) + \frac{Cf_p d_c}{2} = F_{C1}(L \sin\beta_1 + f_c L_5 \cos\beta_1)$$

$$\text{where} \quad L_5 = L - \frac{R_D}{\cos\beta_1} \tag{4}$$

$$\therefore F_1(L_2 - L_1) = \left(E - \frac{Cf_p d_c}{2}\right)F_{C1} \tag{5}$$

Thus from equations (3) and (5)

$$F_2 = F_1 - CF_{C1} \tag{6}$$

For the dimensions shown in Fig.3

$$A_p = \frac{\pi}{4}(d_c^2 - d_1^2)$$

For the supply pressure P the net force on the slipper piston is PA_p less the piston friction $f_p(F_1 + F_2)$ and seal friction F_s. The slipper area provides an opposing force F_u together with the normal component of F_{C1}.

$$\therefore PA_p - f_p(F_1 + F_2) - F_s = F_u + F_{C1}(\cos\beta_1 - f_c \sin\beta_1)$$

putting $A = \cos\beta_1 - f_c \sin\beta$ and substituting for F_1 and F_2 gives:-

$$F_{C1} = \frac{PA_p - F_u - F_s}{f_p\left(\frac{2E}{L_2 - L_1} - C\left(1 + \frac{f_p d_c}{L_2 - L_1}\right)\right) + A} \tag{7}$$

Upper bearing forces

For the conditions shown in Fig.4, the values of the contact force S_1 and the angle γ can be determined as follows:

Thus $$S_1 = \frac{F_N}{\cos\gamma + f_B \sin\gamma} \tag{8}$$

also $$S_1 = \frac{F_T}{\sin\gamma - f_B \cos\gamma} \tag{9}$$

These give $$\tan\gamma = \frac{F_N f_B + F_T}{F_N - F_T f_B} \tag{10}$$

Now from equation (3) $F_T = F_1 - F_2 = CF_{C1}$

From Fig.4 the area $A_B = \frac{\pi}{4}\left(d_c^2 - d_2^2\right)$

The net force maintaining the cylinder against the upper bearing is given by:

$$F_N = PA_B - F_D - F_s - f_p(F_1 + F_2) + F_K$$

where: F_D is the hydrostatic force in the bearing,

F_K is the force from the cylinder retaining spring

The angle γ can be determined from equation 10.

The moment generated by the slipper contact force that is required to overcome the friction in the upper bearing can be obtained from the geometry of Fig.2.

This force, F_{C3} is given by:

$$F_{C3} = \frac{f_B R_B S_1}{\left(f_c(L_c\cos\beta_1 - R_D) + L_c\sin\beta_1\right)} \tag{11}$$

For $90^\circ < \theta < 180^\circ$

Slipper and piston forces

The slipper and piston forces are obtained in the same way as those for $\theta \leq 90^\circ$ and are shown in Fig.5.

Thus:

$$F_1 - F_2 = (\sin\beta_2 - f_c\cos\beta_2)F_{C2} = DF_{C2} \tag{12}$$

$$F_1 = \frac{JF_{C2}}{L_2 - L_1} - \frac{DF_{c2}f_p d_c}{2(L_2 - L_1)}$$

$$F_2 = F_1 - DF_{C2} \tag{13}$$

where $J = L \sin \beta_2 - f_c L_5 \cos \beta_2$

and L_5 is as given in equation (4)

$$F_{C2} = \frac{PA_p - F_u - F_s}{f_p\left(\frac{2J}{(L_2 - L_1)} - D\left(1 + \frac{f_p d_c}{L_2 - L_1}\right)\right) + B} \tag{14}$$

where $B = \cos \beta_2 + f_c \sin \beta_2$

Upper bearing

For the geometry shown in Fig. 6:

$$S_1 = \frac{F_N}{\cos \gamma + f_B \sin \gamma} \tag{15}$$

$$\tan \gamma = \frac{F_N f_B + F_T}{F_N - F_T f_B} \tag{16}$$

The contact force required to overcome the frictional torque of the upper bearing is given by:

$$F_{C4} = \frac{f_B R_B S_1}{(L_c \sin \beta_2 - f_c(L_c \cos \beta_2 - R_D))} \tag{17}$$

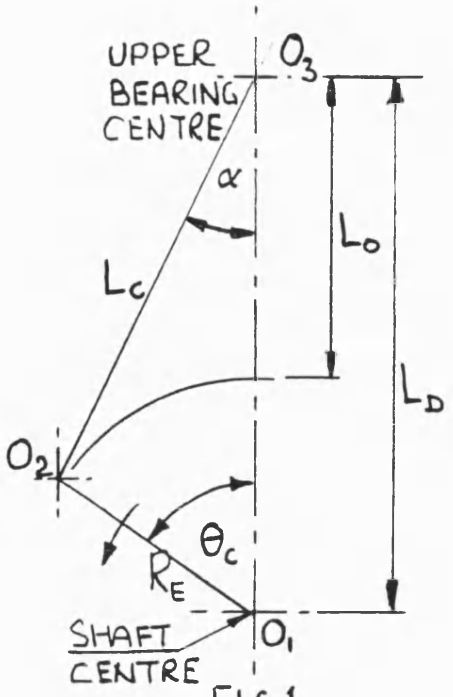

FIG1

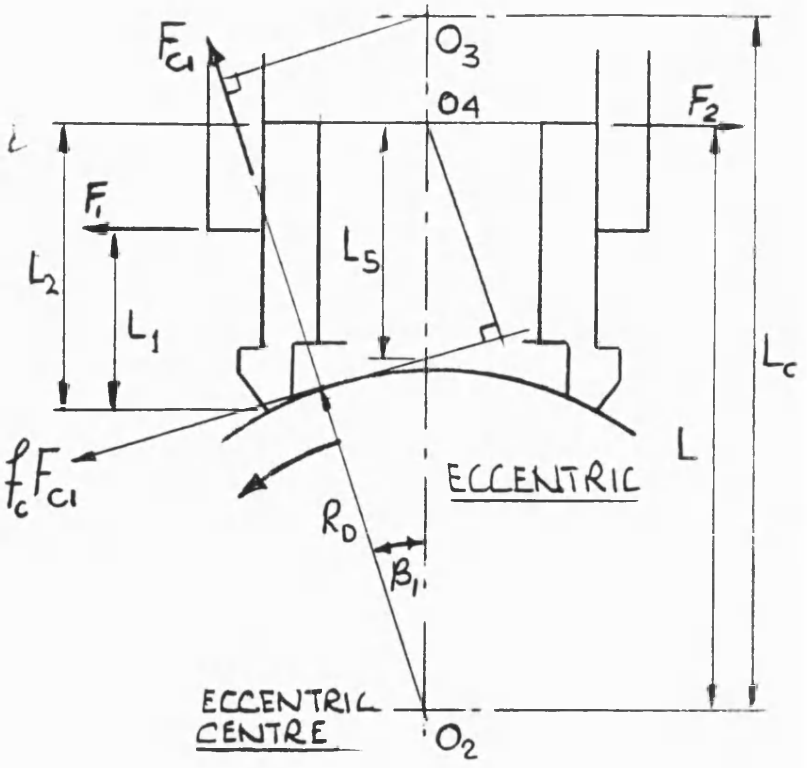

FIG2

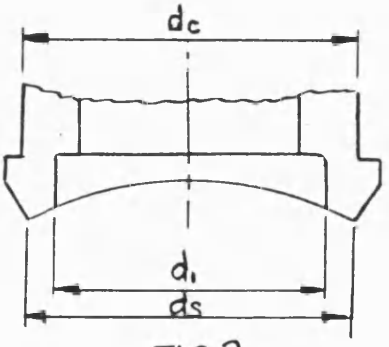

FIG3

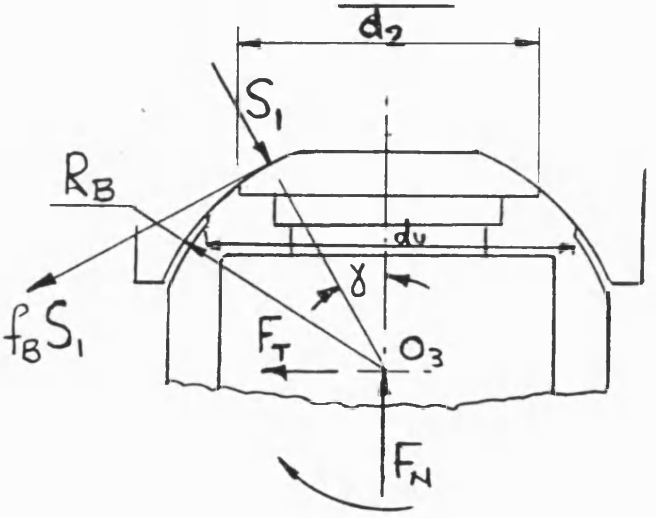

FIG4

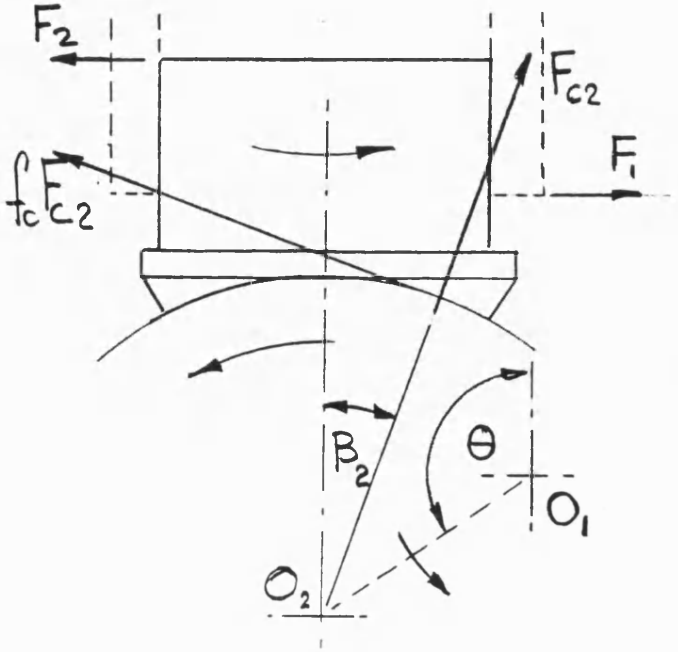

FIG5

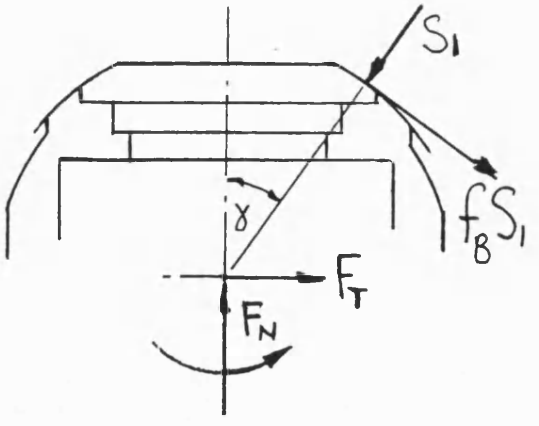

FIG6

CHAPTER 6

CONCLUSIONS

The thesis has shown that in the radial piston eccentric motor the design of the oscillating joint is of crucial importance for the achievement of high mechanical efficiency at low speeds. It is considered that hydrodynamic lubrication in the bearing surfaces is unlikely for speeds less than around 50 *rev/min*, the frictional mechanism being largely dependent on boundary lubrication.

The model predictions using constant values for the friction coefficients did not show the same variation of the mechanical losses with shaft angle that was obtained from the measured results. Different values of the coefficients obtained from the model sensitivity analysis, based on obtaining a particular loss at a particular shaft angle, produced similar variations of the losses with shaft angle. Because of the difference between these model predictions and the measured results, particularly for shaft angles above 25^0, it was concluded that the coefficients vary during the pressure cycle.

Realistic predictions were obtained from the model using coefficient values that vary with the motor geometry. The magnitude of the friction coefficients suggest that some of the bearing surfaces, notably that of the con rod, are operating at the extreme limits of boundary lubrication. This supposition was supported by the results of the very low speed test when the motor temporarily stopped rotating. Here it was considered that the con rod bearing surfaces had become almost dry.

This conclusion is also supported by the results of the theoretical squeeze film analysis. This shows that the time for the film to reduce to a thickness less than around 0.1 μm is likely to be achieved during the period when the con rod bearing is stationary at 90^0 shaft angle. The very smooth surface finish of the bearing created by only short periods of operation, together with the failure problems with water based fluids and those when operating with backpressure, demonstrate the sensitivity of this bearing to the squeeze film process.

The model has thus provided the means to determine the conditions of the bearing surfaces in the motor and gives values of the friction coefficients that were found to lie within the range of results obtained from tests of other researchers in the field. On this basis it was therefore considered that the model provides a realistic representation of the motor performance under the given operating conditions.

The model can then be used to:

a) Determine the level of the forces in the motor and their sensitivity to changes in parameters that are influenced by the design and manufacture of the components.

b) Examine the effect of changes to the design for the improvement of the motor performance.

c) Provide a basis for investigating the effect of major changes to the design concept for motors of this type.

The objective of achieving high mechanical efficiency at low speed is best served by the avoidance of bearings that have little, if any, hydrostatic support. Successful use of the ball joint type of bearing depends on the rate of reduction in the film thickness from the squeeze film that arises during the time period that the bearing is loaded and stationary. This has to be such that the film is always thick enough to provide adequate separation of the components.

This process is limiting in terms of the minimum speed of operation and is seriously affected by the type of fluid that is used. For the general application of the motors this situation is unsatisfactory and the type of motor design described by the author is intended to avoid such problems.

Other means can be employed to avoid high friction at low speeds. The author has experience of surface treatments such as TUFFTRIDING, or SULFINIZING, which reduces friction and wear. This process is used in many pumps and motors available on the market. The work by Ezato[6] on piston friction included results that had been obtained using different materials and surface treatments, some of which provided considerable improvements in performance.

There appears to be little reported work on the type of spherical joint that is used in the radial piston motor and in the high speed swash and bent axis designs. As described in Chapter 1, the increased degrees of freedom in the axial units reduce, to some extent, the oscillating requirements of the bearing as compared to that of the radial motor.

In the axial machines, the effect of friction in the ball joint creates a localised contact between the slipper and the swashplate which is probably responsible for their lower starting efficiency. At high speeds, whilst friction in the ball joint has a complex interaction with the slipper, as shown by Hooke[26,27], hydrodynamic lubrication appears to largely avoid contact between the slipper and the swashplate.

In the bent axis units friction in the ball joint has a much lower effect on the performance of the motor at low speed which is probably the reason for this type being more frequently used for motor applications than the swashplate unit.

Thus we see in the high speed machines a demarcation that is dictated by function and, probably, their cost. However, there are strong similarities in the technologies involved for the manufacture of the swash and bent axis types which enables them to be produced in the same plant.

The high torque motor manufacturer is therefore caught in the situation of having a small market base that has a wide diversity of application requirements. The main problem is the inability of the motor to operate at higher speed, for which there are various reasons that are largely dependent on the operating principles employed in the motor design.

A major cause of constraint lies in the the necessity of ensuring that the components have adequate rigidity of hydrostatic support thus ensuring good mechanical efficiency at low speed. This, however can be in direct conflict with the flexibility required to generate hydrodynamic lubrication for high speed operation.

As the model predictions have shown in the thesis, a motor design having hydrostatic support of the oscillating ball joint provides significant improvements to the low speed efficiency. The low fricton in this bearing should, then, create no particular limitation to operation at high speed. These improvements to the oscillating joint considerably reduce the unbalanced forces in the slipper. Even so, the slipper would appear to provide the obstacle to high speed operation which is largely the result of its inability to create conditions of hydrodynamic lubrication.

As was shown in Chapter 1, the use of gearbox reducers provides a considerable degree of flexibility in obtaining differing effective displacements from a given motor. Thus, for example, a motor of 150 cm^3/rev displacement operating at 2000 *rev/min* with a 7:1 reduction gearbox is equivalent to a *LSHT* motor of 1050 cm^3/rev displacement operating at 300 *rev/min*. Referring to Fig 12 Chapter 1, this speed is about three times that of most available *LSHT* motors, but the increased range of available applications could allow a considerable reduction in overall cost.

The type of hydrostatic slipper used in the high torque motor has a narrow land surrounding the slipper pocket which provides little, or no, benefit from the squeeze films that are considered necessary to allow satisfactory operation at high speeds. This relatively small area with the attendant rigidity of the slipper structure allows little, if any, scope for the generation of hydrodynamic lubrication.

The manufacture of relatively large part - circular faces at the required level of accuracy is probably more difficult to achieve than the production of smaller flat surfaces as found in the axial swashplate units. Additionally, it is practically impossible to create the type of pad with annular grooves that are used in some of these axial machines. These are considered to provide an area that allows the generation of squeeze films and, consequently, improved separation of the slipper face from that of the swashplate. It is also difficult to see how a slipper edge profile can be produced that will assist in the creation of hydrodynamic lubrication in the manner described by Hooke[27] for axial piston swashplate machines.

It is the considered view of the author that research work on the design of slippers could provide a solution to this problem. This should involve the consideration of manufacturing techniques together with the investigation of surface treatments and alternative materials in order to obtain the required performance at an optimum cost.

REFERENCES

1 Chapple,P.J., The Effect of Frictional Losses and Leakage on the Performance of Hydraulic Motors, 8th BHRA International Fluid Power Symposium, April, 1988

2 Chapple,P.J., A Performance Comparison of Hydrostatic Piston Motors -Factors affecting their Application and Use, 7th BHRA International Fluid Power Symposium, Sept, 1986

3 Proceedings of the I Mech E, 1875

4 Turnbull,D.E., Fluid Power Engineering, Newnes-Butterworths, 1976

5 Hooke,C.J., The Effects of Centrifugal Loads and Ball Friction on the Lubrication of Slippers, 6th BHRA International Fluid Power Symposium, April, 1981

6 Ezato,M. and Ikeya,M., Sliding Friction Characteristics between a piston and a cylinder for Starting and Low Speed Conditions, 7th BHRA International Fluid Power Symposium, UK, June, 1986

7 Kobayashi,S., and Ikeya,M., The Structural Analysis of Piston Balls and Hydrostatic Bearings in Swashplate Axial Piston Motors, 9th BHRA International Fluid Power Symposium, UK, April, 1990

8 Palmer,K.P., Double Row Axial Piston Pumps for Aircraft Hydraulic Systems, 5th BHRA INternational Fluid Power Symposium, Sept, 1978

9 Bowns,D.E., Rolfe,A.C., and Chapple,P.J., Computer Simulation as a first step towards Computer-aided Design of Fluid Power Systems, 5th BHRA International Fluid Power Symposium, Sept, 1978

10 Rolfe,A.C., Dynamic Characterisics of a Low Speed Hydraulic Motor, PhD Thesis, University of Bath, 1976

11 Johnson,J.L., Determining the Starting Characteristics of Hydraulic Motors, Fluid Power Testing Symposium, Milwaukee, Aug, 1975

12 Hibi,A. and Ichikawa,T., Torque Performance of Hydraulic Motor in whole operating condition from Start to Maximum Speed and its Mathematical Model, 4th BHRA International Fluid Power Symposium, April, 1975

13 Chapple,P.J., Displacement Control in Hydrostatic Motors, 6th BHRA International Fluid Power Symposium, April, 1981

14 Causemann,P., Analyse des Bewegungshaltens und der Verluste bei Radialkolbenmotoren im niedrigen Drehzahlbereich, Industrie Anzeiger, May, 1975

15 Kobayashi,S., Hirose,M., Hetsuse, and Ikeya,M., Friction Characteristics of a Ball Joint in the Swashplate Type Axial Piston Motor, 8th BHRA International Fluid Power Symposium, UK, April, 1988

16 Boinghoff,O., Untersuchungen zum Reibungsverhalten der Kugelgelenke in Axialkolbenmaschinen, Oilhydraulik und Pneumatik, 12 (1977), Nr. 11

17 INCRA Research Report International Copper Research Association, Inc, August, 1976

18 Cameron,A., Basic Lubrication Theory, Longmans, 1971

19 Thoma,J., Sealing Gaps, Hydraulic Pneumatic Power and Controls, Sept, 1963

20 Fuller,D.D., Theory and Practice of Lubrication for Engineers, Wiley,1984

21 Karelitz,G.B., Charts for Studying the Oil Film in Bearings, Trans Am Soc Mech Engrs, Vol 47, pp 1101-1122 1925

22 Needs,J.J., Effects of Side Leakage in 120^0 Centrally Supported Journal Bearings, Trans AM Soc Mech Engrs, Vol 56, pp 721-732, 1934,Vol 57, pp 135-138, 1935

23 Rabinowicz,E., The Intrinsic Variables affecting the Stick Slip Process, Proc Phys Soc, Vol 71, 1958

24 Klie,J., Untersuchungen zur Konstrukiven Optimierung von Hydrostatischen Radialkolbenmotoren mit innerer Kolbenabstutzung und ebener Spielnachstellender Steurung, PhD Thesis Aachen University, Germany, 1980

25 Clifford,M., Mobile Hydrostatic Wheel Hub Drives, SAE Paper 790883

26 Hooke,C.J., The Design of Slippers for Axial Piston Pumps and Motors, 2nd Bath International Fluid Power Workshop on Components and Systems, University of Bath, 1989

27 Hooke,C.J., The Lubrication of Slippers in Axial Piston Pumps and Motors - the Effect of Tilting Couples, Proc Instn Mech Engrs, Vol 203, 1989

BIBLIOGRAPHY

Affouard,R., Hydraulic balancing and new European design of hydraulic components, SAE 841109, 1984

Agness,J.B., Expanding the Deere family of low speed high torque hydraulic motors, SAE paper 831273, International Off - Highway Meeting and Exposition, Milwaukee, USA, September, 1983

Bowns,D.E., and Lang,I.B., Hydrostatic Drives - Present and future, Electric v. Hydraulic Drives, IMechE, October, 1983

Chapple,P.J., Displacement control in hydrostatic motors, IMechE Conference, Hydrostatic Transmissions for Vehicle Applications, September, 1981

Chapple,P.J., Cam motor Patent Application, No 81303879.1

Crook,A., and Fisher,M.J., Hydrostatic bearing operation with dilute oil-water emulsions, 2nd Fluid Power Symposium Guildford, UK January 1971

Dokoukin,A., and Rogov,A.Y., Selecting the parameters of radial piston hydraulic motors, Power, July/August, 1976

Faisandier,J., The role of the low speed motor, Fluid Power International Conference, London, 1972

Firth,D., Hydrostatic motors - Direct or indirect?, SAE 730785, September, 1973

Friedrichs,I.H., Valves - Critical elements in low speed hydraulic motors: A challenging problem and its solution, 2nd Fluid Power Symposium, Guildford, UK, January 1971

Foster,K.W.S., A load balanced port ring improves pintle valve performance, 34th NFPA National Conference on Fluid Power, Philadelphia, USA, 1978

Hahn,E.J., and Kettleborough,C.F., Thermal effects in slider bearings, IMechE Proc, Vol 183, Part 1, No 31, 1968-69

Hemingway,E.W., The measurement of film thickness in thrust bearings and the deflected shape of 'parallel' surface thrust pads, IMechE proc, Vol 180, Part 1, No 44, 1965-66

Hibbert,G., Lindsay,D.V., Turnbull,D.E., and Shute,N.A., The balancing of piston and valve plate forces in axial-piston pumps and motors, 2nd Fluid Power Symposium, Guildford, UK, Jan 1971

Hibi,A., Starting torque of swashplate type axial piston motor, Bulletin of JSME, Vol 17, No 106, April, 1974

Hibi,A., and Ichikawa,T., Measurement method of starting torque of hydraulic motors, Power, 1975

Ikeya,M., and Kato,H., Leakage characteristics of the hydraulic slipper bearing in swashplate type axial piston motor at starting and low speed, International Conference on Fluid Power, Hangzhou, China, 1985

ISO 4392.1/2/3, Hydraulic Fluid Power - Determination of Characterstics of Motors

Klie,J., Eigenschaften und merkmale von verstellbaren hydraulischen radialkolbenmotoren, Maschinenmarkt April, 1980

Klie,J., Stufenlos verstellbare radialkolbenmotoren, Der Konstrukteur, June, 1982

Martin,C., Some aspects of hydraulic motor performance, Hydraulic Pneumatic Power, August, 1972

McKeown,J., Milner,D.A., Shute,N.A., and Turnbull,D.E., Hydrodynamic factors affecting the design of valve plates and thrust bearings, IMechE Proc, Vol 181, Part 1, No 24 1966-1967

Neal,P.B., Film lubrication of plane-faced thrust pads, IMeche, Lubrication and Wear Convention, 1963

Neal,P.B., Heat transfer in pad thrust bearings, Proc IMechE, Vol 196, No 20, 1982

Nonnemacher,G., Starting Characteristics of Hydraulic Motors, 1st European Fluid Power Conference, UK, 1975

Pasynkov,R.M., Effect of angular misalignment of the cylinder block on the operation of the end face distributor in an axial reciprocating hydraulic machine, Russian Engineering Journal, Vol 56, No 10

Pinson,C.M., Introduction of a new family of small high torque, low speed motors designed for low power applications, SAE paper 831270, International Off - Highway Meeting and Exposition, Milwaukee, USA, September, 1983

Reddy,D., and Nau,B.S., The design and performance of an axial piston machine valve plate: A hybrid bearing/seal with superposed dynamic and eccentric loads, IMechE Conference on Lubrication, 1972

Rogov,A.Y., Choosing a hydraulic motor for rotary drives, Russian Engineering Journal, Vol L111, No 10

Sculthorpe,H.J., and Lemon,E.R., Hydrostatics and planetary gearing - a synergistic approach, SAE paper 780466, Earthmoving Industry Conference, Peoria, USA, April, 1978

Sodersten,B., Cam curve type radial piston motor design, Fluid Power International Conference, London, 1970

Toet,G., Start torque ratio of hydromotors, 29th National Conference on Fluid Power, Chicago, USA, September, 1971

Wang,M., and Hu,K., Studying on starting performance of high torque low speed hydraulic motors, International Conference on Fluid Power, Hangzhou, China, September, 1985

Yamaguchi,A., Bearing/seal characteristics of the fluid film between a valve plate and a cylinder block of axial pumps and motors, International Conference on Fluid Power, Hangzhou, China, September, 1985

Yamaguchi,A., and Tanioka,A., Motion of pistons in piston - type hydraulic machines, Bulletin of JSME, Vol 19, No 130, April, 1976

Yanada,H., Hibi,A., and Ichikawa,T., Low speed performance of hydraulic motors, International Conference on Fluid Power, Hangzhou, China, 1985